МИНИСТЕРСТВО НАУКИ И ВЫСШЕГО ОБРАЗОВАНИЯ РОССИЙСКОЙ ФЕДЕРАЦИИ

НАУЧНО-ТЕХНИЧЕСКИЕ ВЕДОМОСТИ

САНКТ-ПЕТЕРБУРГСКОГО ГОСУДАРСТВЕННОГО ПОЛИТЕХНИЧЕСКОГО УНИВЕРСИТЕТА

Физико-математические науки

Том 14, №3
2021

Санкт-Петербургский политехнический
университет Петра Великого
2021

НАУЧНО-ТЕХНИЧЕСКИЕ ВЕДОМОСТИ САНКТ-ПЕТЕРБУРГСКОГО ГОСУДАРСТВЕННОГО ПОЛИТЕХНИЧЕСКОГО УНИВЕРСИТЕТА. ФИЗИКО-МАТЕМАТИЧЕСКИЕ НАУКИ

Журнал с 2002 г. входит в Перечень ведущих рецензируемых научных журналов и изданий, в которых должны быть опубликованы основные результаты диссертаций на соискание ученых степеней доктора и кандидата наук.

Сведения о публикациях представлены в Реферативном журнале ВИНИТИ РАН, в международной справочной системе «Ulrich's Periodical Directory».

С 2008 года выпускается в составе сериального периодического издания «Научно-технические ведомости СПбГПУ».

Журнал зарегистрирован Федеральной службой по надзору в сфере информационных технологий и массовых коммуникаций (Роскомнадзор). Свидетельство о регистрации ПИ № ФС77-52144 от 11 декабря 2012 г.

Распространяется по Каталогу стран СНГ, Объединенному каталогу «Пресса России» и по Интернет-каталогу «Пресса по подписке». Подписной индекс 71823.

Журнал индексируется в базе данных **Web of Science** (Emerging Sources Citation Index), а также включен в базу данных «**Российский индекс научного цитирования**» (РИНЦ), размещенную на платформе Научной электронной библиотеки на сайте

http://www.elibrary.ru

Адрес редакции и издательства:
Россия, 195251, Санкт-Петербург, ул. Политехническая, д. 29.
Тел. редакции (812) 294-22-85.
http://ntv.spbstu.ru/physics

THE MINISTRY OF SCIENCE AND HIGHER EDUCATION OF THE RUSSIAN FEDERATION

ST. PETERSBURG STATE POLYTECHNICAL UNIVERSITY JOURNAL

Physics and Mathematics

VOLUME 14, No.3, 2021

Peter the Great St. Petersburg
Polytechnic University
2021

**ST. PETERSBURG STATE POLYTECHNICAL UNIVERSITY JOURNAL.
PHYSICS AND MATHEMATICS**

The journal is included in the List of leading peer-reviewed scientific journals and other editions to publish major findings of theses for the research degrees of Doctor of Sciences and Candidate of Sciences.

The publications are presented in the VINITI RAS Abstract Journal and Ulrich's Periodical Directory International Database.

The journal is published since 2008 as part of the periodical edition 'Nauchno-tekhnicheskie vedomosti SPb-GPU'.

The journal is registered with the Federal Service for Supervision in the Sphere of Telecom, Information Technologies and Mass Communications (ROSKOMNADZOR). Certificate ПИ № ФС77-52144 issued December 11, 2012.

The journal is distributed through the CIS countries catalogue, the «Press of Russia» joint catalogue and the «Press by subscription» Internet catalogue. The subscription index is **71823**.

The journal is in the **Web of Science** (Emerging Sources Citation Index) and the **Russian Science Citation Index** (RSCI) databases.

Address: 195251 Politekhnicheskaya St. 29, St. Petersburg, Russia.

Phone: (812) 294-22-85.

http://ntv.spbstu.ru/physics

Содержание

Теоретическая физика

Contents

Condensed matter physics

Simulation of physical processes

Experimental technique and devices

Physical electronics

Biophysics and medical physics

Nuclear physics

Theoretical physics

DOI: 10.18721/JPM.14301
UDC 53.08

THERMOACTIVATED CURRENT SPECTROSCOPY OF POLYETHYLENE TEREPHTHALATE FILMS IRRADIATED BY HEAVY XENON IONS

Yu.A. Gorokhovatsky[1], **D.E. Temnov**[1], **N.S. Shabanova**[1], **A.N. Nechaeff**[2], **A. Rossouw**[2]

[1] Herzen State Pedagogical University of Russia, St. Petersburg, Russian Federation;

[2] Joint Institute for Nuclear Research, Dubna of Moscow region, Russian Federation

The paper analyzes the electret state of polyethylene terephthalate (PET) films irradiated on the IC-100 cyclotron (JINR LAR) using thermostimulated spectroscopy methods. Thermally stimulated discharge currents (thermally stimulated depolarization) of PET film samples obtained at different technological stages of track membrane manufacturing are studied. The results of the analysis of thermally stimulated depolarization currents indicate a significant change in the spectra of the energy states of the electric charge accumulated during the polarization of PET films, during irradiation with accelerated heavy Xe ions, ultraviolet treatment, and alkaline etching of latent tracks. The parameters of relaxation processes (activation energy and effective frequency factor) occurring in track membranes are calculated using the Eyring method. A significant change in the energy state spectra of the electric charge accumulated during the polarization of PET films as a result of ion-track processes in them indicates the possibility of creating an electret state in PET films and track membranes irradiated with heavy ions on their basis.

Keywords: electret, track membrane, polyethylene terephthalate, thermal-stimulated discharge current, Eyring method

Citation: Gorokhovatsky Yu.A., Temnov D.E., Shabanova N.S., Nechaeff A.N., Rossouw A., Thermoactivated current spectroscopy of polyethylene terephthalate films irradiated by heavy xenon ions, St. Petersburg Polytechnical State University Journal. Physics and Mathematics. 14 (3) (2021) 8–20. DOI: 10.18721/JPM.14301

ТЕРМОАКТИВАЦИОННАЯ СПЕКТРОСКОПИЯ ПЛЕНОК ПОЛИЭТИЛЕНТЕРЕФТАЛАТА, ОБЛУЧЕННЫХ ТЯЖЕЛЫМИ ИОНАМИ КСЕНОНА

Ю.А. Гороховатский[1], **Д.Э. Темнов**[1], **Н.С. Шабанова**[1], **А.Н. Нечаев**[2], **А. Россоу**[2]

[1] Российский государственный педагогический университет им. А.И. Герцена, Санкт-Петербург, Российская Федерация;

[2] Объединенный институт ядерных исследований, г. Дубна Московской области, Российская Федерация

Методом термостимулированной токовой спектроскопии в работе проанализировано электретное состояние в облученных на циклотроне пленках полиэтилентерефталата. Изучено поведение термостимулированных токов деполяризации в образцах пленок, полученных на разных технологических стадиях изготовления трековых мембран. Результаты исследования указывают

на существенное изменение спектров энергетических состояний электрического заряда, накопленного при поляризации пленок после их облучения ускоренными тяжелыми ионами ксенона, затем последующей ультрафиолетовой обработки и щелочного травления латентных треков. С помощью метода Эйринга рассчитаны параметры релаксационных процессов (энергия активации и эффективный частотный фактор), возникающих в трековых мембранах. Указанные существенные изменения спектров свидетельствуют о возможности создания электретного состояния в облученных пленках и трековых мембран на их основе.

Ключевые слова: электрет, трековая мембрана, полиэтилентерефталат, термостимулированный ток деполяризации, метод Эйринга

Ссылка при цитировании: Гороховатский Ю.А., Темнов Д.Э., Шабанова Н.С., Нечаев А.Н., Россоу А. Термоактивационная спектроскопия пленок полиэтилентерефталата, облученных тяжелыми ионами ксенона // Научно-технические ведомости СПбГПУ. Физико-математические науки. 2021. Т. 14. № 3. С. 8–20. DOI: 10.18721/JPM.14301

Introduction

The results of fundamental and applied studies, obtained recently using heavy ion beams with low and medium energies, are clear evidence that these approaches have good prospects for the high-tech industry. Analysis of fundamental physical processes characterizing particle interaction with a solid provides the basis for the practical applications of these processes for ion-beam modification of materials [1].

Accelerated heavy ion beams can serve as a unique tool for transforming the nano- and microstructure of solids, in particular, for obtaining track membranes [2 – 4, 7].

Fabricating polymer track membranes with heavy ion accelerators is one of the major applications of ion track technologies. Track membranes based on polyester films made of polyethylene terephthalate (PET) and polycarbonate (PC) are effectively used for ultra-purification of water, in biotechnology for producing vaccines and serums, in medicine as a key filtering element of plasma filters, in analytical chemistry and environmental sanitation control [10, 11].

Modern track membranes are mainly based on polyester films such as polyethylene terephthalate (PET) and polycarbonate. PET is a polymer that is a complex thermoplastic polyester of terephthalic acid and ethylene glycol. PET films that track membranes are produced from are composites whose structure includes both amorphous and crystalline phases. PET in amorphous state is characterized by mutual random arrangement of macromolecule chains with rare isolated formations of an ordered structure. The crystalline state of PET is characterized by crystallites that are bunched macromolecules appearing as folded stacks. The crystallite size in films is about 5 – 10 nm, and the degree of crystallinity is about 40 – 50%.

The structural and physicochemical characteristics of PET-based track membranes irradiated with heavy ions depend on the parameters of the ion beam, the chemical composition of the irradiated polymer film and its structure, as well as the methods for physicochemical processing of latent tracks in it. A heavy ion track forms in a polymer material through a complex physicochemical process. A high-energy multicharged ion passing through a PET film enters into a Coulomb interaction with its electron subsystem. Amorphization of PET and a decrease in the size of crystallites are observed due to irradiation with heavy ions. In addition, the destruction of PET macromolecules is accompanied by an increase in the number of carboxyl groups in the polymer [8, 9].

Tracks in PET are capable of selective chemical etching upon exposure to aqueous solutions of alkali metals. A chemical reaction of etchant interaction occurs in ester polymers, including PET, accompanied by breaking of ester bonds, elimination of ethylene glycol and terephthalate ion molecules with carboxyl and hydroxyl groups forming on the surface, which determine the negative elec-

tric charge of the material surface. Photo-oxidation of radiolysis products in tracks exposed to soft ultraviolet (UV) radiation in the presence of oxygen is used to increase the selectivity of track etching [4, 5, 12, 15].

Notably, PET films are also used for producing electrets with a stable electrical charge. An electret is a dielectric that maintains a polarized state for a long time after the external influence is removed, leading to polarization of this dielectric and generating a quasi-static electric field in the surrounding space. The electret state is inherent to varying degrees in all dielectrics, including PET.

Analyzing the literature, we have found that the methods of ion-track electret charging of polymer films are insufficiently understood. It can be assumed that the electret properties of polymer films change under bombardment with accelerated heavy ions, similar to the above-mentioned effects of UV irradiation and alkaline etching of tracks. The reason for this is that the morphology and chemical structure of the PET film change upon exposure to both ionizing radiation processes and highly alkaline thermal hydrolysis.

We used methods of thermally stimulated depolarization to consider changes in the properties of track membranes based on polyethylene terephthalate (PET) for the purpose of analyzing the effect of ion-track etching in PET on the variaton in electret properties [17 – 21].

Thermally stimulated current spectroscopy is widely used to study the processes of electrical relaxation, in particular, the electret state in various dielectric materials [17 – 22]. One of the most popular methods of TSC spectroscopy used to study charge relaxation in electrets is the method of thermally stimulated discharge current, or thermally stimulated depolarization (TSDC). Measurement of thermally stimulated discharge currents is carried out in short-circuit mode (when the resistance of the external measuring circuit is much lower than that of the given dielectric). Analysis of the shape of the TSDC curve (temperature dependence of the initial section of the current peak, temperature position of the current maximum, etc.) allows determining the most probable activation energy of electrically active defects and their effective frequency factor based on experimental data (methods for processing TSDC data are described in detail in [21]).

The motivation behind the study was to understand how the properties of the charged surface of PET films and track membranes based on them change, in order to expand the range of their practical applications. Track membranes with electret properties can find further application in various types of transducers, for example, in sealing systems, filters, membranes, and in biomedical technologies.

Materials and methods

Samples were prepared from Hostaphan RNK PET film 30 μm thick by Mitsubishi Polyester Films (Germany). The samples were irradiated by $^{132}Xe^{+26}$ ions with a 1.16 MeV beam at +/– 35° angles sequentially on each side at the IC-100 cyclotron of the Flerov Laboratory of Nuclear Reactions (Joint Institute for Nuclear Research, Dubna, Moscow Region, Russia). The ion path length in PET was about 20 μm. The surface pore density on each side was $N = 4.5 \cdot 10^8$ cm^{-2}. Following cyclotron irradiation, all samples were exposed to UV radiation for 2 h on each side before chemical etching. UV irradiation was performed in air using LE-30 lamps (by Lisma, Saransk, Russia); the pure PET film was used as a filter and periodically replaced with a fresh one. UV radiation intensities measured with a TPK-PKM radiometer amounted to 3 – 4 W/m^2 in the UV-A range (315 – 400 nm) and 1 W/m^2 in the UV-B range (280 – 315 nm). The density of nano- and micropores on the surface was determined using a Hitachi SU8020 scanning electron microscope. Furthermore, we used the SEM microscope to examine the membrane cross-sections obtained via polymer matrix embrittlement by mild photooxidation.

In this study, we applied the TSDC method for analyzing different samples of PET films and PET-based track membranes.

Samples 1 – 6 were first irradiated with UV light; the exposure time was 2 h on each side of the film. They were then chemically etched in a thermostat at 80 °C with a concentration of sodium hydroxide (NaOH) solution equal to 1 mol/L for different periods of time: from 1 to 6 min.

Measurements of the pore diameter on the surface of the samples were carried out by SEM. The results are presented in Table 1.

A TSC-II setup from Setaram (France) was used to measure the thermally stimulated depolarization currents.

The measurement process included the following stages:

polarization of samples at a constant temperature T_p = 90 °C in an electric field of 5 kV/mm for a time t_p = 0.5 min;

cooling at a rate of 4 °C/min in an electric field until the temperature reached T_0 = 10 °C;

exposition at a temperature T_0 in the absence of an electric field for a time t_0 = 1 min;

heating at a given rate (4, 7, or 9 K/min) to a temperature T_f = 130 °C with simultaneous measurement of depolarization currents (with a Keithley 6517E electrometer).

All measurements were carried out in a vacuum chamber in a gaseous helium atmosphere in order to prevent access of oxygen to the samples.

Table 1

Structural characteristics of irradiated PET films after etching in alkaline solutions

Sample No.	Etching time, min	Average pore diameter on the surface, nm	SEM data
1	1.0	25	No etchback
2	2.0	36	
3	3.0	57	
4	4.0	78	
5	5.0	160	Etchback
6	6.0	232	

Note. Samples 7, 8, 9 were pure films, not subjected to etching; sample 8 was exposed to UV rays, sample 9 to UV rays and xenon ions.

Experimental results

We considered the samples obtained at different stages of producing track membranes (see the procedure in the previous section), comparing the results with the corresponding data on the pure PET polymer films.

Fig. 1 shows the TSDC curves for pure polymer film obtained at two different heating rates of the sample.

Several maxima associated with relaxation processes are clearly visible on the dependences presented, typically due to various molecular movements inside the polymer:

high-temperature α-process (dipole-segmental) around 90 °C, caused by orientational rotations of the polar macromolecular units when segmental motion is possible, i.e., in a highly elastic state;

β- and γ-processes (dipole-group) in the temperature ranges of 60 and 25 °C, respectively, due to the mobility of polar end and side groups of macromolecules (they can also appear in the glassy state).

A technique for finding the activation energy of these processes relies on different linear heating rates of the sample, subsequently using numerical solution methods abased on the Tikhonov – Arseniev regularization algorithms. From a mathematical standpoint, finding the required parameters,

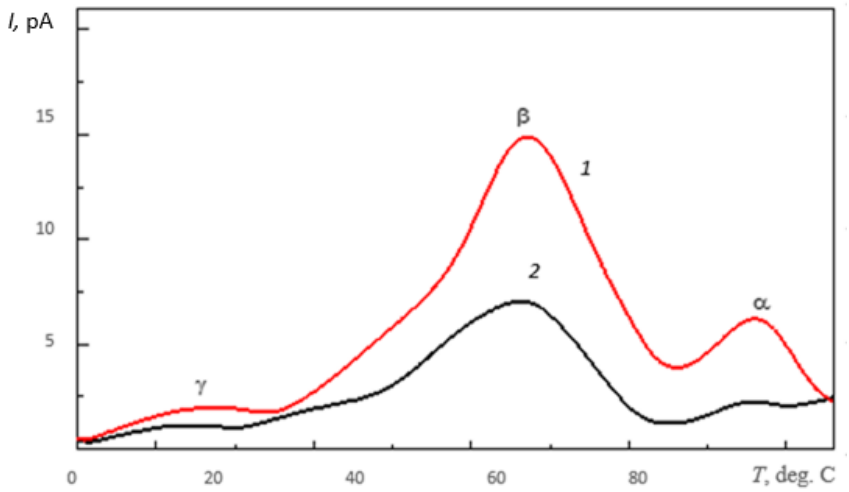

Fig. 1. TSD spectra of pure PET films at two heating rates of the samples: 9 K/min (*1*) and 7 K/min (*2*)

that is, the frequency factor ω and the activation energy E of electrically active defects (EAD) from the experimental dependence means solving the following integral equation (1):

$$j(T) \sim \int_0^{\omega_m} d\omega \int_0^{E_m} G(E,\omega)\,\xi(E,\omega,T,\beta)\,dE, \qquad (1)$$

where T is the sample temperature; β is its heating rate; $G(E,\omega)$ is the EAD distribution function; $\xi(E,\omega,T,\beta)$ is the integrand function whose specific form depends on the physical model incorporated in the theory describing the phenomenon of thermally stimulated depolarization.

Analysis of Eq. (1) confirms that this problem can only be solved if the value of the frequency factor ω is known. However, in practice, this value is unknown in advance, yielding an ambiguous solution. This difficulty can be eliminated using a method proposed in [5], comparing the energy spectra numerically reconstructed from the TSDC curves measured for a given sample at two heating rates with other conditions being equal. If the value of the frequency factor is chosen correctly, then the shapes of energy spectra should not differ for different heating rates. Conversely, the difference in the reconstructed spectra for different heating rates means that a different value has to be selected as the frequency factor.

Thus, this technique makes it possible to determine the EAD parameters in the given material with a sufficient degree of reliability even when the relaxation processes observed are not monoenergetic, and the electrically active defects have a complex energy distribution.

Processing the TSDC spectra, we discovered that the activation energies of relaxation processes turned out to be equal (in eV): 1.24, 0.93, and 0.45; they also correspond to a decrease in the maximum temperature of the depolarization peak.

Irradiation of PET films with xenon ions and UV photons significantly increases the intensity of α-relaxation, which implies an increase in the segmental mobility of polar macromolecular units in the irradiated samples (Fig. 2), which is apparently due to amorphization of the samples upon irradiation with ions [17].

Further etching of the films with the duration increased from 0.5 to 6 min considerably changes the TSDC spectrum both with respect to the temperature scale and to intensity (Fig. 3). It can be assumed that another process becomes most important for charge relaxation in this case, most likely associated with the first the formation and then the depopulation of charge traps on the track walls.

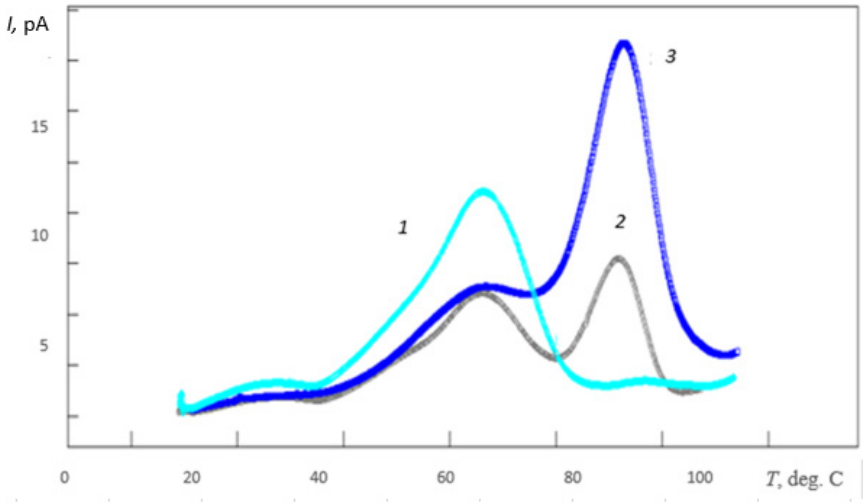

Fig. 2. TSDC spectra of pure PET films (*1*), irradiated with xenon ions (*2*) and then with UV photons (*3*) at a heating rate of 7 K/min

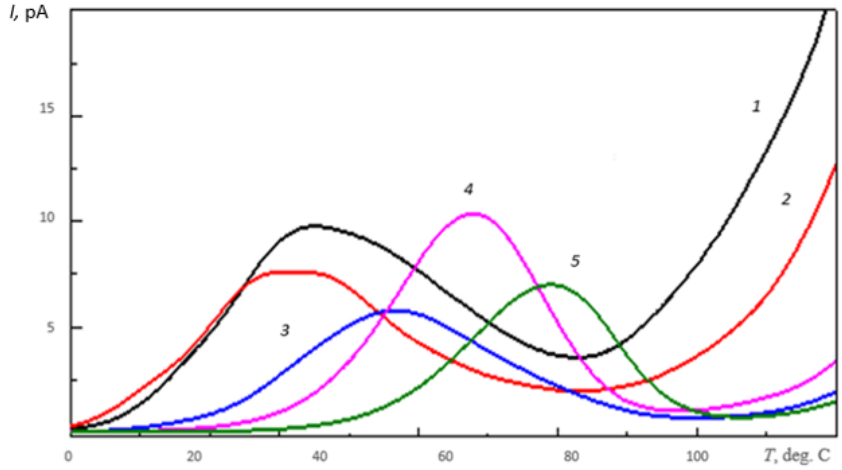

Fig. 3. TSDC spectra of PET films irradiated with xenon ions and UV photons upon subsequent chemical etching of samples 1 – 5 (curve numbers correspond to the sample numbers). Sample heating rate was 7 K/min

It can be seen from the data in Fig. 3 that the TSDC maximum shifts to the high-temperature region with an increase in the etching time, and its intensity remains approximately the same.

The parameters of this relaxation process were calculated for all etching times: the activation energy and effective frequency factor (Table 2); Eyring's method was used for this purpose [6].

It is known [4] that an increase in the etching time leads to an increase in the average diameter of the pores formed in track membranes. This is confirmed by the data given in Table 2.

Apparently, the dependence of the activation energy on the average pore diameter is practically linear (Fig. 4,*a*), and the corresponding dependence of the effective frequency factor bears a pronounced nonlinear character (Fig. 4,*b*).

A sharp increase in the frequency factor with increasing average pore diameter likely points towards the formation of through pores in PET films at an etching time sufficient for this phenomenon,

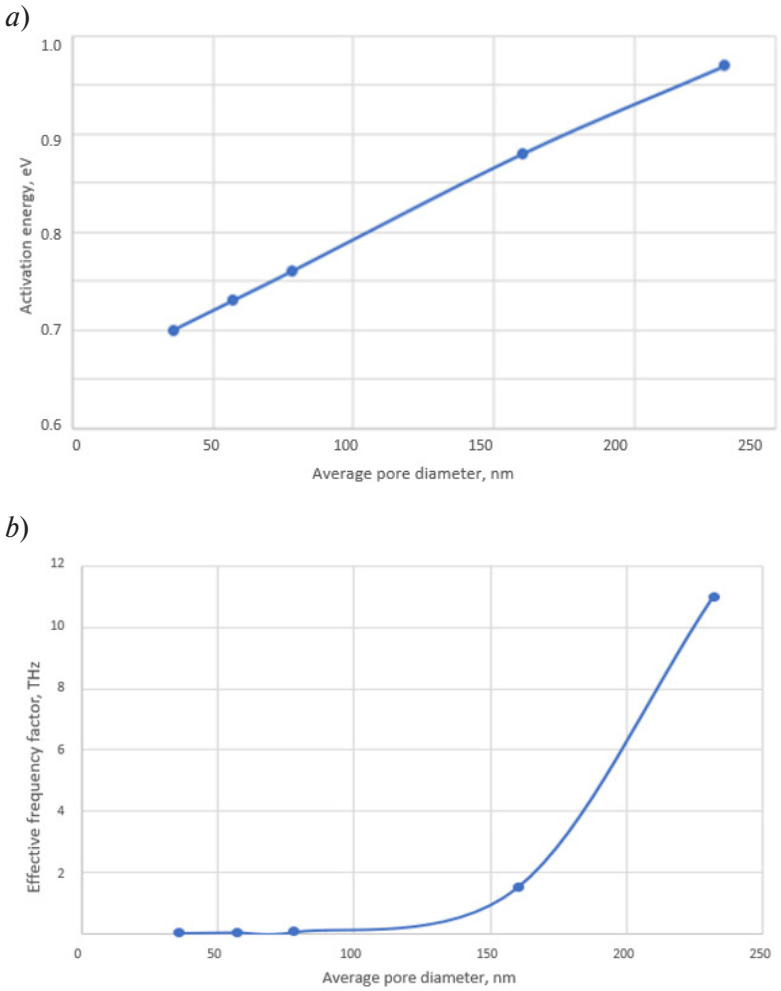

Fig. 4. Dependences of activation energy (*a*) and effective frequency factor (*b*) on average pore diameter with increasing etching time

as well as towards an increase in the free volume of the polymer. An increase in the activation energy suggests that progressively deeper charge carrier traps evolve with increased etching time.

Table 2

Parameters of dipole-group relaxation process observed in PET films at different etching times

Etching time, min	Mean diameter of pores, nm	Activation energy, eV	Effective frequency factor, 10^{10} s^{-1}
1	36	0.70	2.4
2	57	0.73	4.4
3	78	0.76	5.4
4	160	0.88	150
5	232	0.97	1100

The method of relaxation maps [7] was used to calculate the degree of disorder in the polymer system. With an increase in the etching time, it increases from 25.2 (this etching time is 1 min) to 36.6

(this time is 5 min), which means that the degree of disorder can serve as a characteristic of the total volume of the 'loose' polymer along the pore walls formed during etching.

Conclusion

The method of thermally stimulated current spectroscopy has been applied for the first time to track membranes based on PET films. We have confirmed that the processes of ion track technology, such as irradiation with heavy $^{132}Xe^{+26}$ ions, UV sensitization and etching of PET film tracks, have a major effect on the TSDC spectra. The obtained spectroscopic data were used to calculate the parameter values of the relaxers, as well as the degree of disorder of the polymer system for track membranes with different pore diameters. Several relaxation processes are clearly observed for the pure PET films, typically associated in the literature with various molecular movements inside the polymer; in particular, a high-temperature process (dipole-segmental) takes place around 90 °C, due to orientational rotations of the polar macromolecular units under the conditions when segmental motion is possible. Irradiation of PET films with xenon ions and UV photons considerably increases the intensity of α-relaxation, which means an increase in segmental mobility in irradiated samples. Further etching of the films with an increase in the etching time significantly changes the TSDC spectrum both with respect to the temperature scale and the peak intensity. It can be assumed that another process becomes most important for charge relaxation in this case, most likely associated with the formation and subsequent depopulation of charge traps on the track walls. The maximum of the TSDC spectrum shifts to the high-temperature region with increasing etching time, while the dependence of the activation energy on the average pore diameter is almost linear, and the corresponding dependence of the effective frequency factor bears a pronounced nonlinear character.

The most likely reason for the sharp increase in the frequency factor is that through pores evolve in PET films given a sufficient etching time. An increase in the activation energy suggests that progressively deeper charger carrier traps appear with increased etching time. The results may indicate that the spectrum of energy states of the electric charge accumulated during polarization of such films changes considerably and that an electret state can be generated in such materials. The relaxation parameters of track membranes can be tailored in accordance with the structural peculiarities of such objects.

Acknowledgment

The authors are grateful to the staff of the Center for Applied Physics at the Flerov Laboratory of Nuclear Reactions (Dubna, Moscow Region) for their assistance with our studies: O.M. Ivanov (irradiation of films at the IC-100 cyclotron), T.I. Mamonov (synthesis of membranes), N.V. Lizunov (SEM studies) and P.Yu. Apel (implementation of the experimental design and fruitful discussions of the experimental data).

The research was supported by the Ministry of Education of the Russian Federation as part of a state task (project No. FSZN-2020-0026).

REFERENCES

1. **Flerov G.N., Apel P.Yu., Didyk A.Yu., et al.,** Use of heavy-ion accelerators to produce nuclear membranes, Soviet Atomic Energy. 67 (4) (1989) 763–770.

2. **Bouffard S., Gervais B., Leroy C.,** Basic phenomena induced by swift heavy ions in polymers, Nucl. Instr. Meth. Phys. Res. B, Special Issue. 105 (1–4) (1995) 1–4.

3. **Li Ch., Sun Y., Jin Y., et al.,** Latent track effect of swift argon ions in polyimide, Nucl. Instr. Meth. Phys. Res. B. 135 (1–4) (1998) 234–238.

4. **Enge W.,** On the question of nuclear track formation in plastic material, Radiat. Meas. 25 (1–4) (1995) 11–26.

5. **Ditlov V.A., Gaatchegov A.U., Enge W., et al.,** The radial etching velocity for tracks in polymer films, Radiat. Meas. 28 (1–6) (1997) 137–144.

6. **Miterev A.M.,** Theoretical aspects of the formation and evolution of charged particle tracks, Physics-Uspekhi. 45 (10) (2002) 1019–1050.

7. **Apel P.Yu.,** Treki uskorennykh tyazhelykh ionov v polimerakh [Tracks of accelerated heavy ions in polymers]: Thesis for Dr. of Sci. (Chem. Sci.), Spec. 02.00.09. High Energy Chemistry, Joint Institute for Nuclear Research, Moscow, 1998 (in Russian).

8. **Apel P., Schulz A., Spohr R., et al.,** Track size and track structure in polymer irradiated by heavy ions, Nucl. Instr. Meth. Phys. Res. B. 146 (1–4) (1998) 468–474.

9. **Apel P., Spohr R., Trautmann C., Vutsadakis V.,** Track structure in polyethylene terephthalate irradiated by heavy ions: LET dependence of track diameter, Radiat. Meas. 31 (1–6) (1999) 51–56.

10. **Mchedlishvili B.V., Beryozkin V.V., Oleinikov V.A., et al.,** Structure, physical and chemical properties and applications of nuclear filters as a new class of membranes, J. Membr. Sci. 79 (2–3) (1993) 285–304.

11. **Kuznetsov V.I., Kuznetsov L.V., Shestakov V.D.,** Track membranes of the third generation (TMG-3), their properties and industrial application, Nucl. Instr. Meth. Phys. Res. B. Special Issue. 105 (1–4) (1995) 250–253.

12. **Apel P.,** Track etching technique in membrane technology, Radiat. Meas. 34 (1–6) (2001) 559–566.

13. **Kaur S.A., Amrita J.,** Track etched membranes for electronic applications, Intern. J. Sci. Res. 4 (1) (2015) 1414–1417.

14. **Martin C.R.,** Nanomaterials: A membrane based synthetic approach, Sci. 266 (5193) (1994) 1961–1966.

15. **Apel P., Spohr R.,** Introduction to ion track etching in polymers. Ion-tracks.de. Available: http://www.ion-tracks.de/ introduction1/ Retrieved 2013-01-21.

16. **Speight J.G., Lange N.A.,** Lange's handbook of chemistry, 16th edition, McGraw-Hill Education, New York, Chicago, San Francisco, Lisbon, London, Madrid, Mexico City, Milan, New Delhi, San Juan, Seoul, Singapore, Sydney, Toronto (2005) 2758–2807.

17. **Schneidearn W.A., Wendorff J.H.,** Physical mechanism of the electrical polarization of polyethylene terephthalate, Colloid and Polymer Science. 262 (10) (1984) 761–768.

18. **Cañadas J.C., Diego J.A., Mudarra M., et al.,** Effects of UV radiation on the charge trapping capability of PET, J. Phys. D. 52 (15) (2019) 155301.

19. **Gasanov A.Sh., Magerramov A.M., Nuriev M.A., Orudzhev I.A.,** Relaxation of the electret charges of PET films after the action of the aerosol particles, Surf. Eng. Appl. Electrochem. 48 (4) (2012) 343–347.

20. **Lacabanne C., Chatain D., Monpagens J.C.**, Thermally stimulated current and creep in poly(ethylene terephthalate), J. Appl. Phys. 50 (4) (1979) 2723–2731.

21. **Guzhova A.A., Temnov D.E., Galikhanov M.F.,** Influence of electreting parameters on the surface and electret properties of polyethylene terephthalate, Izvestia: Herzen University Journal of Humanities & Sciences. Physics. (157) (2013) 55–60 (in Russian).

22. **Van Turhout I.,** Thermally stimulated discharge of polymer electrets, Elsevier, Amsterdam, 1975.

23. **Vanderschuren J.G.,** Thermally stimulated relaxations in solids. Ed. by P. Briunlich, Springer-Verlag, Berlin, 1979.

24. **Gorokhovatsky Yu., Temnov D., Marat-Mendes J.N., et al.,** On the nature of thermally stimulated discharge current spectra in polyethylene terephthalate, J. Appl. Phys. 83 (10) (1998) 5337–5341.

25. **Temnov D., Fomicheva E., Tazenkov B., et al.,** Electrets properties of polyethylene films with starch and aerosol, J. Mater. Sci. Eng. A (David Publishing). 3 (7) (2013) 494–498.

26. **Gorokhovatsky Yu.A., Bordovsky G.A.,** Thermal activation current spectroscopy of high-resistance semiconductors and dielectrics, Nauka Publishing, Moscow, 1991 (in Russian).

27. **Eyring H., Gibbs P.,** Nonclassical reaction kinetics, Sci. 1951. Vol. 113 (2926) (1951) 104–105.

28. **Doulut S., Bacharan C., Demont P., et al.,** Physical aging and tacticity effects on the α relaxation mode of amorphous polymers by thermally stimulated techniques, J. Non-Cryst. Sol. 235 –237 (2 August) (1998) 645–651.

Received 15.06.2021, accepted 22.06.2021.

THE AUTHORS

GOROKHOVATSKY Yuriy A.
Herzen State Pedagogical University of Russia
48 Moyka Emb., St. Petersburg, 191186, Russian Federation
gorokh-yu@yandex.ru

TEMNOV Dmitry E.
Herzen State Pedagogical University of Russia
48 Moyka Emb., St. Petersburg, 191186, Russian Federation
tde@herzen.spb.ru

SHABANOVA Natalya S.
Herzen State Pedagogical University of Russia
48 Moyka Emb., St. Petersburg, 191186, Russian Federation
natashshabanov@yandex.ru

NECHAEFF Alexander N.
Joint Institute for Nuclear Research
6, Joliot-Curie, Dubna of Moscow region, 141980, Russian Federation
nechaeffalexander@yandex.ru

ROSSOUW Arnoux
Joint Institute for Nuclear Research
6, Joliot-Curie, Dubna of Moscow region, 141980, Russian Federation
arnoux.rossouw@gmail.com

СПИСОК ЛИТЕРАТУРЫ

1. **Флёров Г.Н., Апель П.Ю., Дидык А.Ю., Кузнецов В.И., Оганесян Р.Ц.** Использование ускорителей тяжелых ионов для изготовления ядерных мембран // Атомная энергия. 1989. Т. 67. № 4. С. 274–280.

2. **Bouffard S., Gervais B., Leroy C.** Basic phenomena induced by swift heavy ions in polymers // Nuclear Instruments and Methods in Physics Research. B. 1995. Special Issue. Vol. 105. No. 1–4. Pp. 1–4.

3. **Li Ch., Sun Y., Jin Y., Liu G., Hou M., Ma F., Patnaik A.** Latent track effect of swift argon ions in polyimide // Nuclear Instruments and Methods in Physics Research. B. 1998. Vol. 135. No. 1–4. Pp. 234–238.

4. **Enge W.** On the question of nuclear track formation in plastic material // Radiation Measurements. 1995. Vol. 25. No. 1–4. Pp. 11–26.

5. **Ditlov V.A., Gaatchegov A.U., Enge W. et al.** The radial etching velocity for tracks in polymer films // Radiation Measurements. 1997. Vol. 28. No. 1–6. Pp. 137–144.

6. **Митерев А.М.** Теоретические представления о формировании и эволюции треков заряженных частиц // Успехи физических наук. 2002. Т. 172. № 10. С. 1131–1164.

7. **Апель П.Ю.** Треки ускоренных тяжелых ионов в полимерах. Дис. ... д-ра хим. наук. Спец. 02.00.09. Химия высоких энергий. Москва: Лаборатория ядерных реакций им. Г.Н. Флёрова Объединенного института ядерных исследований, 1998. 194 с.

8. **Apel P., Schulz A., Spohr R., Trautmann C., Vutsadakis V.** Track size and track structure in polymer irradiated by heavy ions // Nuclear Instruments and Methods in Physics Research. B. 1998. Vol. 146. No. 1–4. Pp. 468–474.

9. **Apel P., Spohr R., Trautmann C., Vutsadakis V.** Track structure in polyethylene terephthalate irradiated by heavy ions: LET dependence of track diameter // Radiation Measurements. 1999. Vol. 31. No. 1–6. Pp. 51–56.

10. **Mchedlishvili B.V., Beryozkin V.V., Oleinikov V.A., Vilensky A.I., Vasilyev A.B.** Structure, physical and chemical properties and applications of nuclear filters as a new class of membranes // Journal of Membrane Science. 1993. Vol. 79. No. 2–3. Pp. 285–304.

11. **Kuznetsov V.I., Kuznetsov L.V., Shestakov V.D.** Track membranes of the third generation (TMG-3), their properties and industrial application // Nuclear Instruments and Methods in Physics Research. B. 1995. Special Issue. Vol. 105. No. 1–4. Pp. 250–253.

12. **Apel P.** Track etching technique in membrane technology // Radiation Measurements. 2001. Vol. 34. No. 1–6. Pp. 559–566.

13. **Kaur S.A., Amrita J.** Track etched membranes for electronic applications // International Journal of Science and Research. 2015. Vol. 4. No. 1. Pp. 1414–1417.

14. **Martin C.R.** Nanomaterials: A membrane based synthetic approach // Science. 1994. Vol. 266. No. 5193. Pp. 1961–1966.

15. **Apel P., Spohr R.** Introduction to ion track etching in polymers. Ion-tracks.de. Available: http://www.ion-tracks.de/ introduction1/ Retrieved 2013-01-21.

16. **Speight J.G., Lange N.A.** Lange's handbook of chemistry. 16th edition. New York, Chicago, San Francisco, Lisbon, London, Madrid, Mexico City, Milan, New Delhi, San Juan, Seoul, Singapore, Sydney, Toronto: McGraw-Hill Education, 2005. Pp. 2758–2807.

17. **Schneidearn W.A., Wendorff J.H.** Physical mechanism of the electrical polarization of polyethylene terephthalate // Colloid and Polymer Science. 1984. Vol. 262. No. 10. Pp. 761–768.

18. **Cañadas J.C., Diego J.A., Mudarra M., Parsa S.E., Sellarès J.** Effects of UV radiation on the charge trapping capability of PET // Journal of Physics. D. 2019. Vol. 52. No. 15. P. 155301.

19. **Gasanov A.Sh., Magerramov A.M., Nuriev M.A., Orudzhev I.A.** Relaxation of the electret charges of PET films after the action of the aerosol particles // Surface Engineering and Applied Electrochemistry. 2012. Vol. 48. No. 4. Pp. 343–347.

20. **Lacabanne C., Chatain D., Monpagens J.C.** Thermally stimulated current and creep in poly(ethylene terephthalate) // Journal of Applied Physics. 1979. Vol. 50. No. 4. Pp. 2723–2731.

21. **Гужова А.А., Темнов Д.Э., Галиханов М.Ф.** Влияние параметров электретирования на поверхностные и электретные свойства полиэтилентерефталата // Известия Российского государственного педагогического университета имени А.И. Герцена. 2013. № 157. С. 55–60.

22. **Van Turhout I.** Thermally stimulated discharge of polymer electrets. Amsterdam: Elsevier, 1975. 340 p.

23. **Vanderschuren J.G.** Thermally stimulated relaxations in solids. Edited by P. Briunlich. Berlin: Springer-Verlag, 1979.

24. **Gorokhovatsky Yu., Temnov D., Marat-Mendes J.N., Dias C.J.M., Das-Gupta D.K.** On the nature of thermally stimulated discharge current spectra in polyethylene terephthalate // Journal of Applied Physics. 1998. Vol. 83. No. 10. Pp. 5337–5341.

25. **Temnov D., Fomicheva E., Tazenkov B., Karulina E., Gorokhovatsky Yu.** Electrets properties of polyethylene films with starch and aerosil // Journal of Materials Science and Engineering (David Publishing). A. 2013. Vol. 3. No. 7. Pp. 494–498.

26. **Гороховатский Ю.А., Бордовский Г.А.** Термоактивационная токовая спектроскопия высокоомных полупроводников и диэлектриков. М.: Наука, 1991. 248 с.

27. **Eyring H., Gibbs P.** Nonclassical reaction kinetics // Science. 1951. Vol. 113. No. 2926. Pp. 104–105.

28. **Doulut S., Bacharan C., Demont P., Bernes A., Lacabanne C.** Physical aging and tacticity effects on the α relaxation mode of amorphous polymers by thermally stimulated techniques // Journal of Non-Crystalline Solids. 1998. Vol. 235 –237. 2 August. Pp. 645–651.

Статья поступила в редакцию 15.06.2021, принята к публикации 22.06.2021.

СВЕДЕНИЯ ОБ АВТОРЕ

ГОРОХОВАТСКИЙ Юрий Андреевич – *доктор физико-математических наук, заведующий кафедрой общей и экспериментальной физики Российского государственного педагогического университета им. А.И. Герцена, Санкт-Петербург, Российская Федерация.*

191186, Российская Федерация, г. Санкт-Петербург, наб. р. Мойки, 48

gorokh-yu@yandex.ru

ТЕМНОВ Дмитрий Эдуардович – *кандидат физико-математических наук, доцент кафедры общей и экспериментальной физики Российского государственного педагогического университета им. А.И. Герцена, Санкт-Петербург, Российская Федерация.*

191186, Российская Федерация, г. Санкт-Петербург, наб. р. Мойки, 48

tde@herzen.spb.ru

ШАБАНОВА Наталья Сергеевна – *аспирантка кафедры общей и экспериментальной физики Российского государственного педагогического университета им. А.И. Герцена, Санкт-Петербург, Российская Федерация.*

191186, Российская Федерация, г. Санкт-Петербург, наб. р. Мойки, 48

natashshabanov@yandex.ru

НЕЧАЕВ Александр Николаевич – *кандидат химических наук, ведущий научный сотрудник Лаборатории ядерных реакций им. Г.Н. Флёрова Объединенного института ядерных исследований, г. Дубна Московской области, Российская Федерация.*

141980, Российская Федерация, г. Дубна Московской области, ул. Жолио-Кюри, 6

nechaeffalexander@yandex.ru

РОССОУ Арно – *аспирант Лаборатории ядерных реакций им. Г.Н. Флёрова Объединенного института ядерных исследований, г. Дубна Московской области, Российская Федерация.*

141980, Российская Федерация, г. Дубна Московской области, ул. Жолио-Кюри, 6

arnoux.rossouw@gmail.com

DOI: 10.18721/JPM.14302
UDC 536.25, 532.517

TURBULENT MIXED CONVECTION WITHIN RAPIDLY ROTATING HEATED ANNULAR CAVITIES WITH AN AXIAL THROUGHFLOW

E.M. Smirnov, S.I. Smirnov, A.G. Abramov, S.A. Galaev

Peter the Great St. Petersburg Polytechnic University,
St. Petersburg, Russian Federation

The results of eddy-resolving numerical simulation of a turbulent mixed convection in a system of three identical, rapidly rotating annular cavities are presented. The cavities are heated from the side of the disk surfaces and from the periphery (the same distribution of the surface temperature is set for all the cavities), and heat removal proceeds by an axial air throughflow in the narrow channel, annular within the cavity system. The computations based on the Implicit LES method have been carried out in view of the conditions close to the experiments known from the literature for a single cavity; the rotational Reynolds number was 200,000, the grid dimension was 17 million cells. The complex multiscale flow structure and the influence of the input aerodynamic and thermal conditions, which are not identical for the cavities included in the system, on the local heat transfer from disk surfaces are discussed.

Keywords: mixed convection, rapidly rotating annular cavity, axial throughflow, global circulation

Citation: Smirnov E.M., Smirnov S.I., Abramov A.G., Galaev S.A., Turbulent mixed convection within rapidly rotating heated annular cavities with an axial throughflow, St. Petersburg Polytechnical State University Journal. Physics and Mathematics. 14 (3) (2021) 21–34. DOI: 10.18721/JPM.14302

ТУРБУЛЕНТНАЯ СМЕШАННАЯ КОНВЕКЦИЯ В БЫСТРОВРАЩАЮЩИХСЯ ОБОГРЕВАЕМЫХ КОЛЬЦЕВЫХ ПОЛОСТЯХ ПРИ ПРОХОЖДЕНИИ ЧЕРЕЗ НИХ ОСЕВОГО ПОТОКА

Е.М. Смирнов, С.И. Смирнов, А.Г. Абрамов, С.А. Галаев

Санкт-Петербургский политехнический университет Петра Великого,
Санкт-Петербург, Российская Федерация

Представлены результаты вихреразрешающего численного моделирования турбулентной смешанной конвекции в системе из трех одинаковых, быстровращающихся кольцевых полостей. Полости обогреваются со стороны дисковых поверхностей и с периферии (для всех полостей задано одно и то же распределение поверхностной температуры), а теплосъем осуществляется транзитным осевым потоком воздуха, протекающим по узкому (в пределах системы полостей) кольцевому каналу. Расчеты на основе метода Implicit LES проведены с учетом условий эксперимента, известных из литературы. Вращательное число Рейнольдса составляло 200 тыс., размерность сетки – 17 млн. ячеек. Обсуждается сложная многомасштабная структура течения и влияние на локальную теплоотдачу с дисковых поверхностей входных аэродинамических и тепловых условий, не являющихся идентичными для включенных в систему полостей.

Ключевые слова: смешанная конвекция, быстровращающаяся кольцевая полость, транзитный осевой поток, глобальная циркуляция

Ссылка при цитировании: Смирнов Е.М., Смирнов С.И., Абрамов А.Г., Галаев С.А. Турбулентная смешанная конвекция в быстровращающихся обогреваемых кольцевых полостях при прохождении через них осевого потока // Научно-технические ведомости СПбГПУ. Физико-математические науки. 2021. Т. 14. № 3. С. 21–34. DOI: 10.18721/JPM.14302

Introduction

While gaining a deep and reliable understanding of the mechanisms behind local heat transfer in rapidly rotating annular cavities heated from disk surfaces under axial throughflow of cooling gas is important on its own, it is also crucial in the field of turbomachinery, where such configurations are widely used for cooling rotors of axial compressors in gas turbine engines [1 – 4].

Because disk surfaces bounding the cavities are opaque and rotating rapidly, it is difficult to obtain reliable quantitative experimental data characterizing the convection that develops in these cavities, and unsteady local heat transfer. Experimental studies are typically limited to visual observations and measurements of local and integral heat transfer, averaged over time [1 – 3, 5, 6].

Much hope is therefore pinned on modern methods of computational fluid dynamics and heat transfer, as well as supercomputer technologies that allow high-precision eddy-resolving simulation. Direct numerical simulation (DNS) and the implicit large eddy simulation (LES), i.e., ILES, where the role of small-scale physical dissipation is replaced by dissipative properties of the numerical scheme, seem to show the greatest promise.

The initial experience of using the ILES method is described in [7 – 10]. The corresponding computations were carried out on grids with moderate dimensions (up to 100,000 cells) and did not yield an acceptable agreement with the experimental data for local heat transfer on disks, which was attributed to inaccurate modeling of turbulent flow in the zone where axial flow mixes with the gas circulating in the cavity.

The characteristic features of the flow structure known from the literature were successfully reproduced by computations of turbulent mixed convection in a single rapidly rotating ventilated annular cavity heated from the disks [11 – 13], carried out recently by the ILES and RANS/ILES methods (Reynolds-averaged Navier – Stokes equations) using grids with dimensions of up to several million cells. However, this left open the question about the reasons for the constant discrepancy between the simulation results and experimental data on heat transfer from disk surfaces.

Notably, it is difficult to fully reproduce the experimental conditions in the computations due to uncertainties in imposing boundary conditions. In particular, this refers to aerodynamic and thermal conditions at the inlet to the cavity: an unperturbed uniform velocity profile and a constant temperature in the inlet section of the channel supplying the coolant are generally imposed in the computations performed for a single cavity; however, the flow at the inlet to the cavity is non-uniform and turbulent in the experiments.

In view of the above, it seems particularly interesting to conduct numerical studies of mixed convection in a system of sequentially located cavities, when the experimental conditions can be simulated more accurately, which, together with detailed resolution of processes (that are significant for the problem) on refined grids, allows expecting better agreement with the measurement data. Multistage cavities are becoming the focus of increased attention in experimental studies; for example, measurements of the time-averaged temperature and local heat transfer on disk surfaces were carried out in [14] for a system of four cavities, detecting two main flow regimes characterized by two regions: forced convection at small radii and Rayleigh – Bénard convection at medium and large radii.

This paper presents the results of eddy-resolving simulations for turbulent mixed convection in a system of rapidly rotating heated annular cavities located periodically around an inner shaft of a relatively large diameter with axial throughflow of cooling air.

The computations were carried out for conditions close to the experiments in [5] but for a single cavity. We obtained a numerical solution by the ILES method on grids that were much more refined

than those used earlier [7, 8]. We analyzed structures of unsteady flow and temperature fields in the cavities and in the channel supplying the coolant, the evolution of large-scale vortex structures and turbulent fluctuations. Furthermore, we considered the influence of the conditions at the inlet to the cavity on the intensity of local heat transfer from disk surfaces.

Problem statement and computational aspects

Consider the problem of the flow and heat transfer of air (Prandtl number Pr = 0.69) in a system with three rapidly rotating interdisk cavities of the same shape, heated from both disk surfaces and from the periphery, sequentially subjected to axial throughflow of cooling gas (Fig. 1). The system rotates around the z axis with a constant angular velocity Ω.

The computational domain includes three coaxial cavities (denoted by A, B, C by order downstream) and a narrow annular channel interrupted inside each cavity, consisting of an inlet section, two short sections between the cavities and a relatively long outlet section.

The geometry of the cavities and the radial dimension of the axial channel (height) are borrowed from [5], presenting the results of experiments for a single cavity (Table 1).

A constant temperature T_{in} and a uniform axial velocity profile W_{in} (without perturbations) are set at the channel inlet (position *1* in Fig. 1), the circumferential component of relative velocity in the inlet section is assumed to be zero. Radial temperature distributions are set on the heated surfaces of disks 6 in each cavity (see Fig. 2, showing the experimental data from [5]; the radial coordinate r is measured from the central axis), somewhat different for the upstream & downstream disks [5]. Pairs of disks belonging to different cavities are identified as A1-A2, B1-B2, C1-C2 in this study. The temperature is assumed to be constant in the circumferential direction. A linear temperature distribution is set on the surfaces of cylindrical shrouds (position *4* in Fig. 1); it varies slightly between the maximum values on the disks, with $r/r_0 = 1$. The inner (*2*) and outer (*3*) cylindrical surfaces of the channels are assumed to be thermally insulated. A constant pressure is set at outlet *5* from the channel.

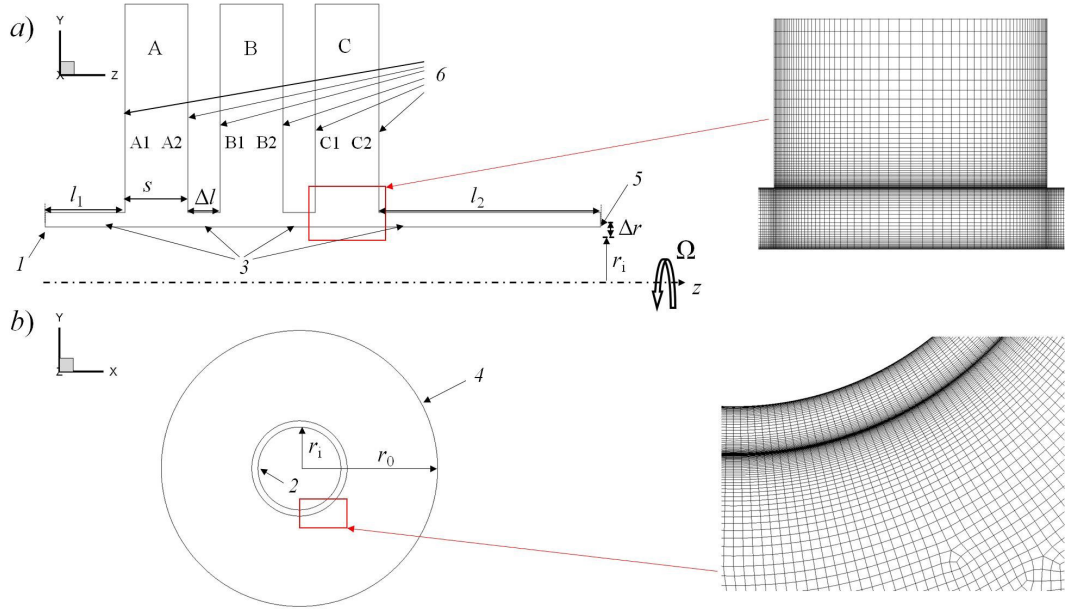

Fig. 1. Schematic illustrating the problem statement for a system of three annular cavities (A, B, C); meridional section of the system (*a*) and the axial section of one of the disks (*b*) are shown: inlet *1*; inner and outer pipe surfaces *2* and *3*; shroud *4*; outlet *5*; disk surfaces *6* (A1-A2, B1-B2, C1-C2); geometrical parameters are also given. Fragments of computational grid for one of the cavities are shown on the right.

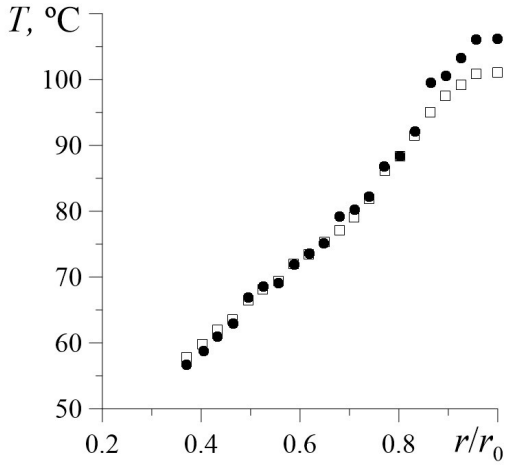

Fig. 2. Experimental radial temperature distributions along the surfaces of the disks [5]: the first (shaded circles) and the second (empty squares) disk downstream.
Radial coordinate r is measured from the central axis

Table 1

Computational geometric parameters (see Fig. 1)

Parameter	Notation	Value, m
External cavity radius	r_0	0.40
Cavity width	s	0.08
Internal radius of annular channel	r_i	0.12
Height of annular channel	Δr	0.018
Length of parts of annular channel: inlet outlet	 l_1 l_2	 0.10 0.28
Distance between cavities	Δl	0.04

Table 2

Remaining computational parameters of the problem

Parameter	Notation	Unit of measurement	Value
Axial velocity of flow	W_{in}	m/s	0.95
Angular velocity of system rotation	Ω	rad/s	14.2
Temperature at channel inlet	T_{in}	°C	25
Mean temperature at $r = r_0$	T_0		104
Temperature factor	ε_T	–	0.27
Reynolds number rotational throughflow	 Re_Ω Re_z		 $2\cdot10^5$ $2\cdot10^4$
Rossby number	Ro		0.56
Prandtl number	Pr		0.69

The numerical solution was obtained in our study for a set of parameters given in Table 2. The data in Table 2 correspond to a set of determining (dimensionless) parameters of the problem, which corresponds to one of the cases known from the literature [5, Case 4].

Traditional hydrodynamic similarity criteria (see Table 2) are defined as follows:

$$\mathrm{Re}_\Omega = \Omega r_0^2 / \nu;\ \mathrm{Re}_z = 2 r_i W_{in} / \nu;\ \mathrm{Ro} = W_{in} / \Omega r_i ,$$

where ν is the kinematic viscosity of air (for the inlet temperature).

The temperature factor is estimated by the expression

$$\varepsilon_T = \beta \Delta T,$$

where β is the coefficient of volumetric thermal expansion (also estimated for the inlet temperature), $\Delta T = T(r = r_0) - T_{in}$.

Judging from the experimental data shown in Fig. 2, the value $T_0 = T(r = r_0)$ was taken equal to 104 °C.

The computations were performed in the ANSYS Fluent 19.3 software package. The problem was solved in a relative reference frame rotating at an angular velocity Ω, based on the Boussinesq approximation with constant viscosity and thermal conductivity (estimated by the temperature at the inlet to the channel), without taking into account the action of gravity.

We used a computational algorithm based on simultaneous solution of the equations for mass balance and momentum with pressure correction. Spatial discretization of convective terms in the equations was carried out via a QUICK scheme with third-order accuracy. Diffusion terms were approximated by a central-difference scheme with second-order accuracy. The non-iterative fractional step meth-od with second-order accuracy was applied to advance in physical time. The time step was set to $4 \cdot 10^{-4}$ s, which provided a Courant number of less than unity over the entire computational domain. Representative statistics on the velocity and temperature fields and heat transfer characteristics were accumulated after a transition period (in a time corresponding to approximately 100 revolutions of the cavity system).

The unstructured computational grid whose fragments are shown in Fig. 1 consisted of hexagons, included about 17 million cells, was strongly clustered to all the walls of the computational domain. The grid used was very refined, providing, among other things, the option to reproduce the following phenomena important for satisfactorily predicting the heat transfer process with high accuracy:

flows in the mixing zones of axial stream with flow in the cavities;

evolution of multiscale vortex structures in the cavity;

their interactions with thin quasi-laminar Ekman layers formed near the disk surfaces.

Computational results and discussion

The details of the three-dimensional vortex pattern of the flow developing in the given system are illustrated in Fig. 3 using the Q-criterion isosurfaces (Q = 400 s^{-1}). Apparently, flow with two arms of highly turbulent fluid, and many separate vortical structures in the throughflow zones and at the cavity walls is generated in each of the cavities. The mechanism behind the observed turbulent arms is explained below.

Let us now focus on the particulars of throughflow in the annular channel. Recall that pronounced annular channels are only present in the inlet and outlet sections of the given configuration. Because the conditions of unperturbed uniform flow and a relatively small channel length are adopted for the inlet channel, the boundary layers do not have sufficient time to grow and turbulence does not occur here; consequently, almost uniform throughflow enters the first cavity.

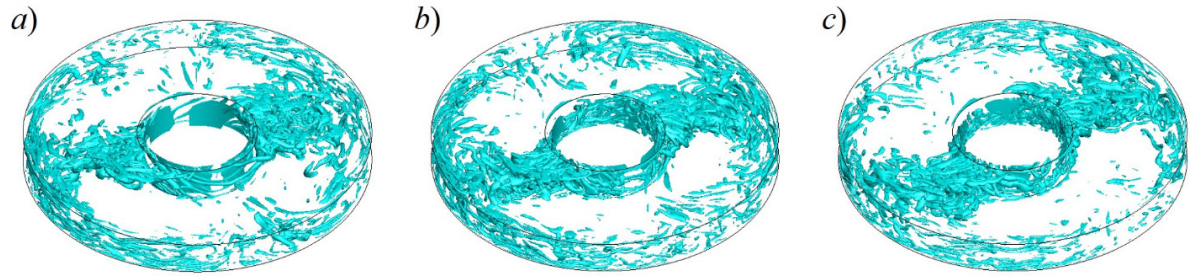

Fig. 3. Visualization of three-dimensional vortex flow through instantaneous Q-criterion isosurfaces in the cavities A (*a*), B (*b*) and C (*c*) (see Fig. 1); Q = 400 s^{-1}

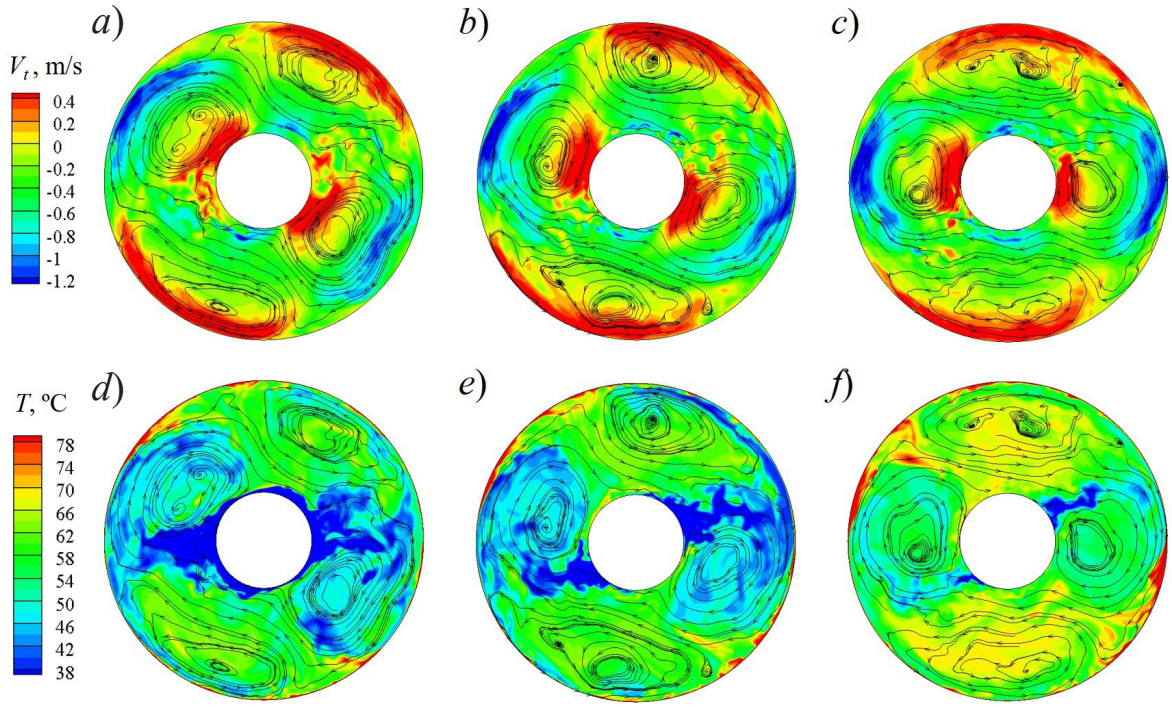

Fig. 4. Instantaneous fields of tangential velocity (*a*–*c*) and temperature (*d*–*f*) in the central axial section between the disks in the cavities A (*a*, *d*), B (*b*, *e*), C (*c*, *f*) (see Fig. 1)

However, throughflow becomes turbulent already at the outlet from the first cavity, due to its interaction with the fluid in the cavity occurring in the mixing layers. Next, throughflow passes around the sharp edge, entering a short section of the channel between the cavities, and growing considerably turbulent at the inlet to the second (and also the third) cavity.

Fig. 4 shows the instantaneous fields of relative tangential velocity and temperature in the central axial section (with streamlines plotted on them) for all cavities.

Interestingly, the 1990s experiments for cavities with a central axial tube with throughflow of cooling gas [1 – 3] yielded a general picture of fluid circulation typically distinguishing evolving large-scale cyclonic and anticyclonic vortices of the Rayleigh – Bénard type, separated by radial arms of cold gas moving towards the periphery of the region [7, 8, 11 – 13].

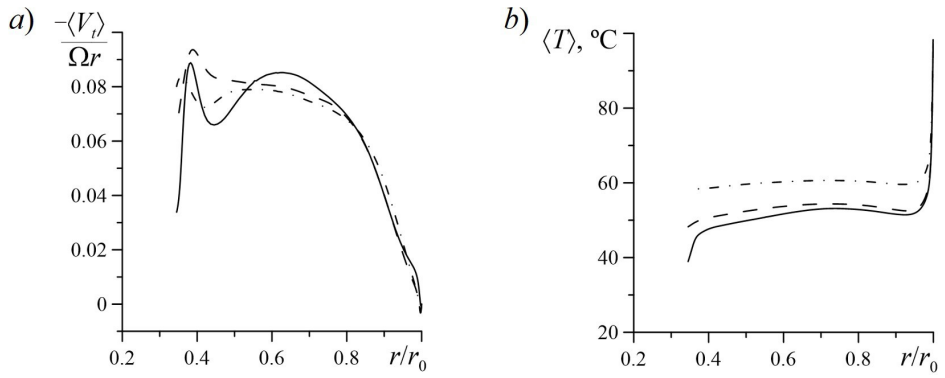

Fig. 5. Computed radial distributions of averaged tangential velocity (*a*) and temperature (*b*) in the central axial section between the disks in cavities A (solid line), B (dashed line) and C (dash-dotted line)

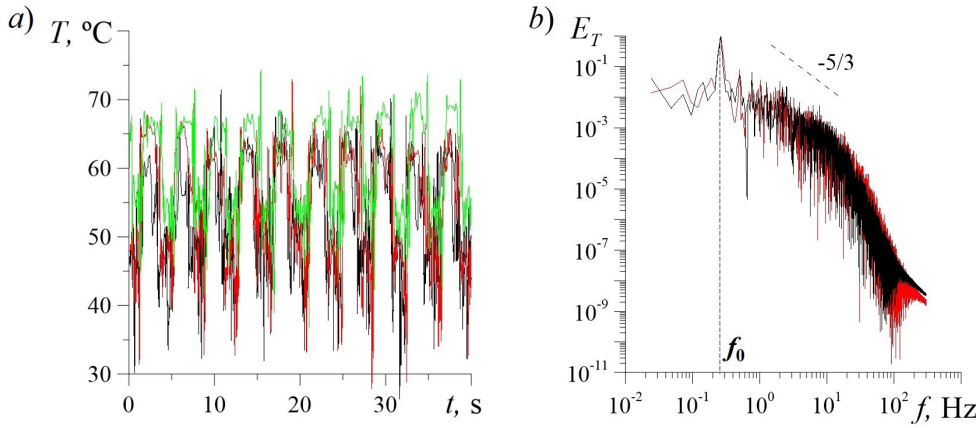

Fig. 6. Temperature fluctuations over time at the monitoring points located in the central sections of the cavities between the disks at a distance $r = 0.75r_0$ from the axis (*a*) and the corresponding energy spectrum for points in cavities A and B (*b*). Computational results are given for cavities A, B and C (black, red and green curves, respectively)

A solution obtained in our computations for an annular cavity included a 'global' anticyclonic vortex surrounding throughflow and a pair of cyclonic vortices pushed to the periphery (Fig. 4). Notably, the turbulent arms of cold gas are located inside the global anticyclonic vortex, producing a pair of local 'internal' anticyclonic vortices. The vortex structure of the flow core is generally preserved over time, with azimuthal motion (precession) in the direction opposite to the direction of rotation.

Fig. 5 shows the radial distributions of tangential velocity and temperature averaged over time and circumferential coordinate for the central section of each of the cavities (angle brackets denote averaging). On average, the flow core noticeably lags behind the translational motion of the system's global rotation (Fig. 5,*a*). We should note that measurements of circumferential velocity in [15] yielded similar levels of the lag for a related configuration with a single rapidly rotating cavity heated from only one disk; no other experimental data on the rate of lag was found.

The mean temperature of the flow core (Fig. 5,*b*) varies unevenly along the radius: it is almost con-stant in most of the cavity, while strong gradients appear near the hot shroud being in contact with regions of relatively cold gas leaking towards it.

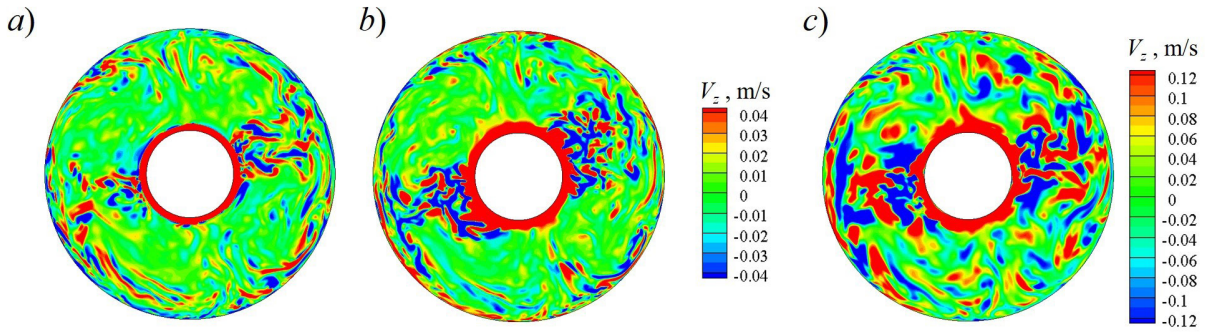

Fig. 7. Instantaneous distributions of axial velocity for the distance of 2.7 mm from the first (*a*) and the second (*b*) disk downstream, as well as in the central axial section between the disks in the first cavity (*c*)

Fig. 6 illustrates the temperature fluctuations over time for all three cavities at the monitoring points located in the central axial sections at a distance $r = 0.75r_0$ from the axis, as well as the energy spectrum of the fluctuations at the same points for the first and second cavities. The graphs presented confirm that the flow in all cavities has a pronounced turbulent character. The general structure of the fluctuations in the cavities is similar, and their amplitude reaches 0.6 of the temperature difference. The presence of low-frequency fluctuations (with the principal frequency $f_0 = 0.26$ Hz) reflects the global precession of the flow core discussed above.

Considering small-scale motion, which is largely associated with the phenomena in Ekman layers emerging on disk surfaces, let us first estimate the thickness of these layers. It is well known (see, for example, monograph [3]) that the characteristic thickness δ of the 'classical' Ekman layer can be estimated as $\delta = (\nu/\Omega)0.5$, and the total thickness of the layer δ_E is about 3δ. The corresponding estimates for the case under consideration give the values $\delta = 0.9$ mm and $\delta_E = 2.7$ mm.

Fig. 7 shows the instantaneous axial velocity distributions in the sections located in the first cavity near the disks A1 and A2 at the outer boundaries of the Ekman layers detected by these estimates, as well as in the central axial section between the disks. It can be seen from Fig. 7, a and b that longitudinally oriented vortex structures appear in the Ekman layers, which is definitive proof that hydrodynamic instabilities evolve in these layers. We obtained similar structures in recent computations of free convection in a rapidly rotating closed cavity, introducing near-axis heat sinks to simulate the heat removal effect of throughflow in the initial problem of mixed convection (see [16]). At the moment, we can only assume that given a non-isothermal Ekman layer, these structures act as a trigger giving an impetus to axial motion of the fluid across the cavity in the form of local multidirectional flows with an intensity amounting to tens of percent from the characteristic values of the relative circumferential velocity, providing effective heat transfer between the Ekman layers and the flow core. Further fundamental studies are necessary to gain more insights into this matter.

Fig. 8 shows the temperature fields averaged over time and circumferential direction in the meridional section of the given system of cavities. Evidently, the temperature of throughflow increases considerably as the fluid passes through the cavities. The increases in the mean mass temperature after passing through cavities A, B and C are 13.1, 12.9 and 9.6 ºC, respectively. Thus, the values of the temperature factor ε_T for the three cavities included in the system are different, equal to: $\varepsilon_{T,\,A} = = \varepsilon_{T,\,in} = 0.27$; $\varepsilon_{T,\,B} = 0.21$; $\varepsilon_{T,\,C} = 0.17$ (the characteristic temperature difference ΔT and the volumet-ric thermal expansion β were computed from the mass-averaged temperature at the inlet to the corre-sponding cavity to obtain estimates for the quantities $\varepsilon_{T,\,B}$ and $\varepsilon_{T,\,C}$).

Table 3 contains the computational data on the heating power from the disk (quantities Q_1 and Q_2) and outer cylindrical (Q_3) surfaces of each of the cavities. The last column of Table 3 shows the

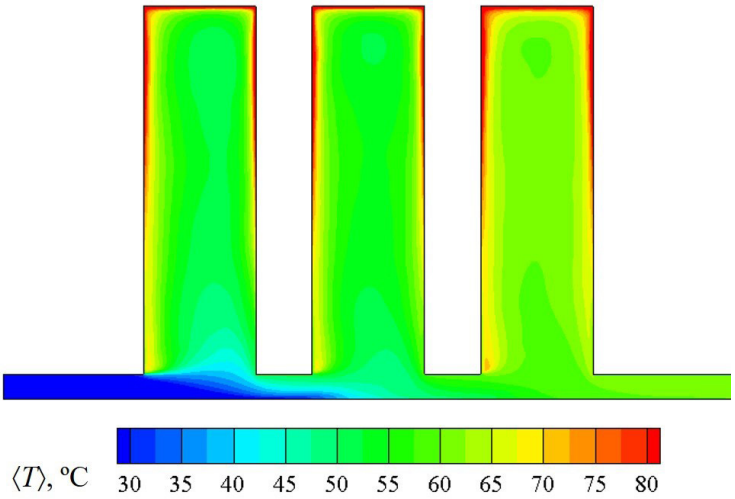

Fig. 8. Computed field of averaged temperature in the meridional section of the system

values of total heat removal Q_Σ from the cavity walls. It is noteworthy that the total amount of heat removed per unit time from the walls of the second cavity is close to the value predicted for the first one, while the flow entering the second cavity is already heated (by 13.1 °C) relative to the conditions at the inlet to the first cavity. A likely explanation for this somewhat unexpected result is that throughflow entering the second cavity is highly turbulent, while virtually no turbulent structures are observed at the inlet to the first cavity (under the given boundary conditions). As expected, much less heat is removed from the walls of the third cavity.

Another interesting finding is that integral heat removal from the disks forming the cavity becomes balanced as the flow moves from cavity A to cavity B, and then to cavity C. The difference between Q_1 and Q_2 for the first cavity is 22% (relative to the mean value), and drops to 2.5% for the third cavity.

Turning to the computational results for the local heat transfer intensity, we can observe that the local Nusselt number on the surface of the disks was computed based on the temperature difference between the local value on the wall and the mass-averaged value at the inlet, individual for each cavity.

Fig. 9 shows the computed radial distributions of the local Nusselt number, averaged over time and circumferential coordinate, over the surfaces of all six disks in comparison with the experimental data for a single cavity [5].

The local Nusselt numbers predicted for the first cavity are in fairly satisfactory agreement with the experimental data, especially taking into account their considerable scatter. The greatest discrepan-cies with the experiment are observed for the first disk downstream, where a section of 'negative' heat transfer is predicted at small radii, which is absent in the experimental data.

Table 3

Computational data on integral heating power (W) removed from the cavity surfaces

Cavity	Q_1	Q_2	Q_3	Q_Σ
A	54.4	84.7	79.7	218.8
B	61.4	71.8	81.9	215.1
C	46.3	48.6	65.1	160.0

Notations: Q_1, Q_2 are the powers removed from the disk surfaces; Q_3 is the amount of heat removed from the outer cylindrical surface; Q_Σ is a value of the total heat removal from the walls of a cavity.

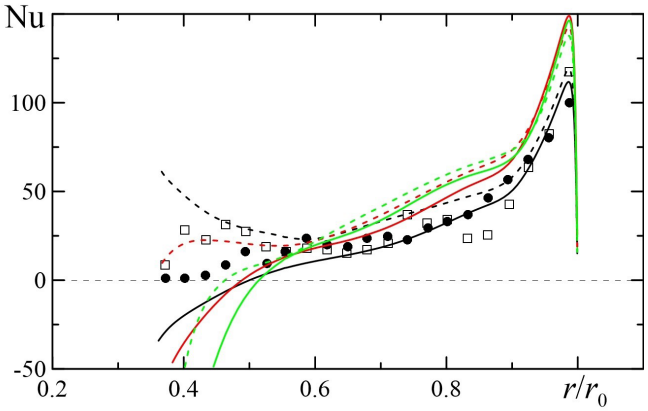

Fig. 9. Comparison of computed radial changes in the local Nusselt number (Nu) on the disk surfaces (lines) with the experimental data from [5] (symbols).
Computational results are shown for cavities A, B and C (black, red and green curves, respectively; solid lines correspond to A1, B1 and C1, dashed lines to A2, B2 and C2). The experimental data are shown similarly to Fig. 2

Moreover, the differences in the conditions at the inlet boundaries of the cavities have a major effect on the computational results. The throughflow entering the second and third cavities is strongly turbulent, contributing to increased normalized heat transfer from the disk surfaces at medium and large radii. A decrease in the temperature factor for the convection developing in the third cavity has a particular pronounced effect on the thickening of the near-surface temperature layer near disk C1 (this is clear from the temperature field shown in Fig. 8) and the appearance of a zone with 'negative' heat transfer with increasing length.

Conclusion

We have performed numerical simulation of turbulent mixed convection in a multistage system with three rapidly rotating annular cavities heated from disk surfaces and from the periphery and cooled by airflow through a narrow axial annular channel. The computations were based on Implicit Large-Eddy Simulation with a refined computational grid (17 million cells).

The simulation predicted a previously unobserved large-scale structure of the flow in cavities with a global anticyclonic eddy surrounding throughflow and cyclonic vortices localized at large radii. We believe that one of the key reasons why satisfactory agreement with experimental data was obtained was that the evolution of large-scale vortices was described correctly in the computations; small-scale structures responsible for heat transfer between the near-disk layers and the flow core were repro-duced simultaneously. Another important finding is that the heat transfer characteristics are highly sensitive to the conditions at the inlet to the cavity.

Ongoing research on this issue is aimed at further developing the eddy-resolving method for computations of this class of flows, which are more complex. This approach is expected to yield reliable and reproducible results. We plan to carry out new computations based on the compressible gas model for a system comprising two or three cavities with varying dynamic and thermal conditions at the cavity inlet, including imposing 'synthetic' turbulence at the inlet.

The study was financed by the Russian Foundation for Basic Research within the framework of Scientific Project "Eddy-resolving modeling of free and mixed convection in rapidly rotating annular cavities" No. 20-08-01090.

The computational results were obtained using the resources of the Supercomputer Center at Peter the Great Polytechnic University (www.scc.spbstu.ru).

REFERENCES

1. **Farthing P.R., Long C.A., Owen J.M., Pincombe J.R.,** Rotating cavity with axial throughflow of cooling air: Flow structure, J. Turbomach. 114 (1) (1992) 237–246.

2. **Long C.A.,** Disk heat transfer in a rotating cavity with an axial throughflow of cooling air, Int. J. Heat Fluid Flow. 15 (4) (1994) 307–316.

3. **Owen J.M., Rogers R.H.,** Flow and heat transfer in rotating-disk systems, Vol. 2: Rotating cavities, John Wiley & Sons, New York, 1995.

4. **Harmand S., Pelle J., Poncet S., Shevchuk I.V.,** Review of fluid flow and convective heat transfer within rotating disk cavities with impinging jet, Int. J. Thermal Sciences. 67 (1) (2013) 1–30.

5. **Bohn D., Deutsch G., Simon B., Burkhardt C.,** Flow visualization in a rotating cavity with axial throughflow, In: Proc. ASME Turbo Expo 2000, May 8–11, 2000, Munich, Germany, Paper No. GT2000-280.

6. **Jackson R.W., Luberti D., Tang H., et al.,** Measurement and analysis of buoyancy-induced heat transfer in aero-engine compressor rotor, J. Eng. Gas Turbines Power. 143 (6) (2021) 061004.

7. **Bohn D.E., Bouzidi F., Burkhardt C., et al.,** Numerical and experimental investigations of the air flow and heat transfer in rotating cavities, In: Proc. 9th Int. Symp. on Transport Phenomena and Dynamics of Rotating Machinery, February 10–14, 2002, Honolulu, Hawaii. Paper No. 2002.02.10-14.

8. **Kitanina E.E., Ris V.V., Smirnov E.M., Goryachev V.D.,** Numerical visualization technique for field processing of unsteady natural convection in rotating cavities, In: Proc. Eurotherm Seminar 71, October 28–30, 2002, Reims, France (2002) 275–280.

9. **Bohn D., Ren J., Tuemmers C.,** Investigation of the unstable flow structure in a rotating cavity, In: Proc. ASME Turbo Expo 2006, 8–11 May, 2006, Barcelona, Spain, Paper No. GT2006-90494.

10. **Smirnov E.M.,** Recent advances in numerical simulation of 3D unsteady convection controlled by buoyancy and rotation, In.: Proc. 12th International Heat Transfer Conference, August 18–23, 2002, Grenoble, France.

11. **Abramov A.G., Zaitsev D.K., Smirnov E.M., Smirnovsky A.A.,** An experience in eddy resolving simulation of mixed convection in a rotating annular cavity with one heated disk and axial throughflow, J. Phys.: Conf. Ser. 1683 (2020) 022089.

12. **Abramov A.G., Smirnov S.I., Kitanina E.E., Smirnov E.M.,** Non-stationary vortex structures forming in a heated rapidly rotating annular cavity with axial throughflow of cooling air, In: "Perm Hydrodynamic Scientific Readings", Proceedings of the 7-th All-Russian Conference Memorized to Prof. G.Z. Gershuny, E.M. Zhukhovitskiy and D.V. Lyubimov, Perm State University, Perm (2020) 28–37 (in Russian).

13. **Smirnov S.I., Abramov A.G., Kitanina E.E., Smirnov E.M.,** Numerical study of turbulent mixed convection in a rotating inter-disk cavity with axial throughflow of cooling air, J. Phys.: Conf. Ser. 1809 (2021) 012013.

14. **Quan Y., Han D., Xu G., et al.,** Convective heat transfer of a rotating multi-stage cavity with axial throughflow, Int. J. Heat Mass Transfer. 119 (April) (2018) 117–127.

15. **Owen J.M., Powell J.,** Buoyancy-induced flow in a heated rotating cavity, J. Eng. Gas Turbines Power. 128 (1) (2006) 128–134.

16. **Smirnov S.I., Smirnov E.M., Kolesnik E.V.,** Structure of turbulent natural convection in a heated rapidly rotating inter-disk cavity with near-axis heat sinks, J. Phys.: Conf. Ser. 1959 (2021) 012045.

Received 29.06.2021, accepted 26.07.2021.

THE AUTHORS

SMIRNOV Evgeny M.
Peter the Great St. Petersburg Polytechnic University
29 Politechnicheskaya St., St. Petersburg, 195251, Russian Federation
smirnov_em@spbstu.ru

SMIRNOV Sergei I.
Peter the Great St. Petersburg Polytechnic University
29 Politechnicheskaya St., St. Petersburg, 195251, Russian Federation
sergeysmirnov92@mail.ru

ABRAMOV Alexey G.
Peter the Great St. Petersburg Polytechnic University
29 Politechnicheskaya St., St. Petersburg, 195251, Russian Federation
abramov_ag@spbstu.ru

GALAEV Sergey A.
Peter the Great St. Petersburg Polytechnic University
29 Politechnicheskaya St., St. Petersburg, 195251, Russian Federation
galaev@spbstu.ru

СПИСОК ЛИТЕРАТУРЫ

1. **Farthing P.R., Long C.A., Owen J.M., Pincombe J.R.** Rotating cavity with axial throughflow of cooling air: Flow structure // J. Turbomach. 1992. Vol. 114. No. 1. Pp. 237–246.

2. **Long C.A.** Disk heat transfer in a rotating cavity with an axial throughflow of cooling air // Int. J. Heat Fluid Flow. 1994. Vol. 15. No. 4. Pp. 307–316.

3. **Owen J.M., Rogers R.H.** Flow and heat transfer in rotating-disk systems. Vol. 2: Rotating cavities. New York: John Wiley & Sons, 1995. 295 p.

4. **Harmand S., Pelle J., Poncet S., Shevchuk I.V.** Review of fluid flow and convective heat transfer within rotating disk cavities with impinging jet // Int. J. Thermal Sciences. 2013. Vol. 67. No. 1. Pp. 1–30.

5. **Bohn D., Deutsch G., Simon B., Burkhardt C.** Flow visualization in a rotating cavity with axial throughflow // Proc. ASME Turbo Expo 2000, May 8–11, 2000, Munich, Germany. Paper No. GT2000-280. 8 p.

6. **Jackson R.W., Luberti D., Tang H., Pountney O.J., Scobie J.A., Sangan C.M., Owen J.M., Lock G.D.** Measurement and analysis of buoyancy-induced heat transfer in aero-engine compressor rotor // J. Eng. Gas Turbines Power. 2021. Vol. 143. No. 6. P. 061004.

7. **Bohn D.E., Bouzidi F., Burkhardt C., Kitanina E.E., Ris V.V., Smirnov E.M., Wolff M.W.** Numerical and experimental investigations of the air flow and heat transfer in rotating cavities // Proc. 9th Int. Symp. on Transport Phenomena and Dynamics of Rotating Machinery; February 10–14, 2002, Honolulu, Hawaii. Paper No. 2002.02.10-14. 8 p.

8. **Kitanina E.E., Ris V.V., Smirnov E.M., Goryachev V.D.** Numerical visualization technique for field processing of unsteady natural convection in rotating cavities // Proc. Eurotherm Seminar 71; October 28–30, 2002, Reims, France. Pp. 275–280.

9. **Bohn D., Ren J., Tuemmers C.** Investigation of the unstable flow structure in a rotating cavity // Proc. ASME Turbo Expo 2006; 8–11 May, 2006, Barcelona, Spain. Paper No. GT2006-90494. 10 p.

10. **Smirnov E.M.** Recent advances in numerical simulation of 3D unsteady convection controlled by buoyancy and rotation // Proc. 12th International Heat Transfer Conference; August 18–23, 2002, Grenoble, France. 12 p.

11. **Abramov A.G., Zaitsev D.K., Smirnov E.M., Smirnovsky A.A.** An experience in eddy resolving simulation of mixed convection in a rotating annular cavity with one heated disk and axial throughflow // J. Phys.: Conf. Ser. 2020. Vol. 1683. P. 022089.

12. **Абрамов А.Г., Смирнов С.И., Китанина Е.Э., Смирнов Е.М.** Нестационарные вихревые структуры, формирующиеся в нагреваемой быстровращающейся кольцевой полости с транзитным осевым потоком охлаждающего воздуха // Пермские гидродинамические научные чтения. Материалы VII Всероссийской конференции с международным участием, посвященной памяти профессоров Г.З. Гершуни, Е.М. Жуховицкого и Д.В. Любимова. Пермь: Пермский государственный национальный исследовательский университет, 2020. С. 28–37.

13. **Smirnov S.I., Abramov A.G., Kitanina E.E., Smirnov E.M.** Numerical study of turbulent mixed convection in a rotating inter-disk cavity with axial throughflow of cooling air // J. Phys.: Conf. Ser. 2021. Vol. 1809. P. 012013.

14. **Quan Y., Han D., Xu G., Wen J., Luo X.** Convective heat transfer of a rotating multi-stage cavity with axial throughflow // Int. J. Heat Mass Transf. 2018. Vol. 119. April. Pp. 117–127.

15. **Owen J.M., Powell J.** Buoyancy-induced flow in a heated rotating cavity // J. Eng. Gas Turbines Power. 2006. Vol. 128. No. 1. Pp. 128–134.

16. **Smirnov S.I., Smirnov E.M., Kolesnik E.V.** Structure of turbulent natural convection in a heated rapidly rotating inter-disk cavity with near-axis heat sinks // J. Phys.: Conf. Ser. 2021. Vol. 1959. P. 012045.

Статья поступила в редакцию 29.06.2021, принята к публикации 26.07.2021.

СВЕДЕНИЯ ОБ АВТОРАХ

СМИРНОВ Евгений Михайлович – *доктор физико-математических наук, профессор Высшей школы прикладной математики и вычислительной физики, главный научный сотрудник Научно-исследовательской лаборатории гидроаэродинамики Санкт-Петербургского политехнического университета Петра Великого, Санкт-Петербург, Российская Федерация.*

195251, Российская Федерация, г. Санкт-Петербург, Политехническая ул., 29

smirnov_em@spbstu.ru

СМИРНОВ Сергей Игоревич – *кандидат физико-математических наук, инженер Научно-образовательного центра «Компьютерные технологии в аэродинамике и теплотехнике» Санкт-Петербургского политехнического университета Петра Великого, Санкт-Петербург, Российская Федерация.*

195251, Российская Федерация, г. Санкт-Петербург, Политехническая ул., 29

sergeysmirnov92@mail.ru

АБРАМОВ Алексей Геннадьевич – *кандидат физико-математических наук, доцент Высшей школы прикладной математики и вычислительной физики Санкт-Петербургского политехнического университета Петра Великого, Санкт-Петербург, Российская Федерация.*

195251, Российская Федерация, г. Санкт-Петербург, Политехническая ул., 29

abramov_ag@spbstu.ru

ГАЛАЕВ Сергей Александрович – *кандидат технических наук, доцент Высшей школы прикладной математики и вычислительной физики Санкт-Петербургского политехнического университета Петра Великого, Санкт-Петербург, Российская Федерация.*

195251, Российская Федерация, г. Санкт-Петербург, Политехническая ул., 29

galaev@spbstu.ru

DOI: 10.18721/JPM.14303
UDC 621.486

NUMERICAL SIMULATION OF THERMOACOUSTIC GAS OSCILLATIONS IN A PIPE WITH TOROIDAL HEAT EXCHANGE ELEMENTS

S.V. Bulovich

Peter the Great St. Petersburg Polytechnic University,
St. Petersburg, Russian Federation

The paper simulates the modes of a gas flow in a pipe closed at one end and open to the atmosphere at the other end; for this purpose, a numerical solution of the system of Navier – Stokes equations in a two-dimensional axisymmetric formulation has been used. The excitation of oscillations of gas-dynamic functions is caused by the temperature gradient in the pipe section resulting from the contact of the gas with differently heated toroidal elements inside the pipe, their temperature being maintained constant. When the specified gradient reaches the threshold value, a stable thermoacoustic oscillation of the gas column is observed in the pipe. The time dependences of the pressure and the axial component of the gas velocity, as well as the heat flows in the heat exchange unit of the resonator, were calculated. The obtained results were in good agreement with the experimental data.

Keywords: thermoacoustics, Sondhauss effect, mathematical simulation, numerical solution of Navier – Stokes equations

Citation: Bulovich S.V., Numerical simulation of thermoacoustic gas oscillations in a pipe with toroidal heat exchange elements, St. Petersburg Polytechnical State University Journal. Physics and Mathematics. 14 (3) (2021) 35–46. DOI: 10.18721/JPM.14303

ЧИСЛЕННОЕ МОДЕЛИРОВАНИЕ ТЕРМОАКУСТИЧЕСКИХ КОЛЕБАНИЙ ГАЗА В ТРУБЕ С ТЕПЛООБМЕННЫМИ ЭЛЕМЕНТАМИ ТОРОИДАЛЬНОЙ ФОРМЫ

С.В. Булович

Санкт-Петербургский политехнический университет Петра Великого,
Санкт-Петербург, Российская Федерация

В работе проведено моделирование режимов течения газа в трубе, закрытой с одного конца и открытой в атмосферу другим концом; для этого использовано численное решение системы уравнений Навье – Стокса в двумерной осесимметричной постановке. Возбуждение колебаний газодинамических функций обусловлено градиентом температуры на участке трубы, возникающим в результате контакта газа с разнонагретыми тороидальными элементами внутри трубы, температура которых поддерживается постоянной. По достижении указанным градиентом порогового значения, в трубе наблюдается устойчивое термоакустическое колебание газового столба. Рассчитаны зависимости от времени давления и осевой составляющей скорости газа, а также тепловые потоки в теплообменном блоке резонатора. Полученные результаты хорошо согласуются с экспериментальными данными.

Ключевые слова: термоакустика, эффект Зондхаусса, математическое моделирование, численное решение уравнений Навье – Стокса

Ссылка при цитировании: Булович С.В. Численное моделирование термоакустических колебаний газа в трубе с теплообменными элементами тороидальной формы // Научно-технические ведомости СПбГПУ. Физико-математические науки. 2021. Т. 14. № 3. С. 35–46. DOI: 10.18721/JPM.14303

Introduction

Many devices are available for converting thermal energy into mechanical or electrical energy. A particular focus is on the thermoacoustic engine (TAE), since acoustic energy in the form of standing or traveling waves acts as an intermediate link in this transformation. Many research groups have considered the mechanisms generating a sound field and maintaining it at a sufficient level in operation. The engine itself has a simple design, with the option to eliminate moving elements from the working fluid. External heat supply allows using any source of energy, while the motion of the working fluid in a closed system makes it possible to fabricate autonomous structures that can be used on Earth and in space.

The effect when sound is generated in a pipe closed at one end and open into the atmosphere at the other was first described by the German physicist Karl Sondhauss [1]. While the study did not explain why sound appeared, it established the general patterns behind the behavior of such characteristics as the dependence of frequency and amplitude of generated waves on the parameters. Rayleigh [2] made qualitative assessments of the phenomena when oscillations emerge and persist, ultimately laying down the foundations for the entire discipline of thermoacoustics. Expressed concisely, the concept is that if heat is given to the gas at the instant of greatest compression or is taken away from it at the instant of greatest rarefaction, this leads to an increase in acoustic oscillations. An important point in this statement is that the source driving the oscillations is identified as the time dependence of heat addition and its synchronization with pressure oscillations. Putnam and Dennis [3] provided a mathematic proof for this hypothesis, which came to be called the Rayleigh criterion. The formulation of the criterion indicates a phase shift between pressure and heat addition oscillations, whose absolute value should be less than $\pi/2$; oscillations are excited in this case. If the phase shift lies in the range from $\pi/2$ to π, the oscillations are damped.

The first TAE based on a standing wave was created in 1962 by Carter, White and Steele (USA) [4]. A stack acting as a heat exchanger with thermal inertia was placed between the heat supply and heat removal sections in the experiments, similar to regenerative Stirling engines. This improvement made it possible to significantly enhance the thermoacoustic effect in the Sondhauss pipe. A particularly interesting prototype was built at the Los Alamos National Laboratory in the 1990s [5]. An experimental setup was constructed at the same time at the National Center for Physical Acoustics of the University of Mississippi to study a stationary thermoacoustic wave in a wide range of parameters [6]. Further experimental studies were aimed at producing a system consisting of a stack combining an acoustic prime mover and an acoustic refrigerator, united by a common resonator [7]. Changing the rectilinear resonator to a *U*-shape and using a liquid piston in the resonator made it possible to significantly reduce the size of the twin setup [8].

The idea that an analogy can be drawn between a Stirling engine and a thermoacoustic engine has been further developed, leading to revision of the basic theory describing the generation of stationary waves in a resonator. Ring-shaped resonators with the operating principle based on traveling waves were constructed as a result [9, 10].

Notably, even though the basic principles of thermoacoustic effects are fairly well-understood, with extensive experimental experience accumulated in creating functional devices, the issues of theoretical analysis and mathematical modeling are far from fully resolved. Because the processes occur on different scales, either an extremely simplified formulation is obtained, allowing to describe the object 'as a whole', or the analysis focuses on the unsteady heat transfer mechanism neglecting the processes outside the near-wall layer of the heat exchanger.

Let us consider an experiment with a Sondhauss tube without a regenerator. In a sense, this formulation is more complicated, since the presence of a regenerator in some modes stabilizes the unsteady gas flow. Let us rely on the results of the experimental study [11], which returns us to the basic formulation of the Sondhauss pipe problem.

A plane channel of length L with a square section $d \times d$ was described in [11]. One end of the channel was closed, the other open, and the gas in the channel interacted with the atmosphere. A heater was located inside the channel at a distance σ from the closed end; a cooler was located at a distance l ($l << \sigma$) from the heater. The heater and cooler were grids consisting of an equal number N of cylindrical rods of the same radius a. The heater had a constant temperature T^+, and the cooler T^-. All rods were parallel to each other. It was confirmed experimentally that the threshold at which self-oscillations occurred in the resonator was a function of two parameters: the temperature difference and the distance between the heat exchangers. Another parameter is the location of the heat exchangers relative to the closed end of the pipe.

The main difficulties in theoretical analysis of thermoacoustic self-oscillations, the main difficulties are caused by complex mathematical description of feedback mechanisms accounting for nonlinear properties; besides, nonlinear partial differential equations have to be solved for this purpose. Therefore, linearizing the system of differential equations by some method provides certain insights into the laws of thermoacoustics.

We should note that early studies were based on a one-dimensional approximation in a nonlinear formulation. Friction and heat transfer were represented by closing relations depending on the flow regime. However, this approach turned out to be ineffective for describing periodic processes because it is impossible to correctly reflect the phase shifts of the signal in the closing relations.

The Rott equation was later formulated [12, 13] based on a linearized system of equations for the balance of mass, momentum and energy in the one-dimensional approximation; a software version of the solution to this equation is available: DeltaEC [14] (free access). The range of applicability is determined for this model by the 3% pressure deviation from its baseline value. Many examples assessing the performance of devices using this software are given in literature [15 – 17]. As linear theory was applied in practice, the understanding of thermoacoustic oscillations was supplemented with the knowledge that a critical temperature gradient must be exceeded to excite oscillations if the heat source and sink are separated in space [5].

A different approach was used in [18], based on the system of boundary layer equations. This made it possible to construct a mathematical model based on the behavior of functions towards the wall, gaining new data on possible losses of acoustic energy. Losses are accounted for as an energy balance, which consequently sets not only the threshold level of the temperature gradient when gas oscillations occur, but also the possible parameter values of traveling or standing waves. Taken together, this information made it possible to achieve better agreement between experimental results and theoretical estimates. Monograph [19] describes the specifics of problems related to heat addition during combustion.

However, it is fundamentally impossible to model some effects within the framework of linearized theory. This primarily refers to the evolutionary process of oscillation generation. Linearized theory can only characterize the state of oscillations that are already established.

Turbulence is another important issue. Changing the direction in which the gas moves leads to the fact that the turbulence model should describe the transition phenomena when turbulent flow is generated and vice versa. The appearance and destruction of turbulent structures are characterized by a relaxation time scale, which is not represented in any way in the Rott equation. Notably, the problem of describing transitions within turbulence models has not been solved completely even for the so-called canonical flows on plates, in pipes, or in the wake.

Finally, the third aspect are different oscillation modes emerging for gas-dynamic functions. In the general case, they are not described by the simplest dependences in the form of harmonic functions, which are the solution to linearized equations. In particular, the problem on oscillatory flow around a cylinder is constructed by two regime parameters: the Keulegan – Carpenter number (the ratio of the hydrodynamic to the geometric scale that is the cylinder diameter) and the Stokes number (the estimate of the boundary layer width as a fraction of the geometric scale). According to the generally accepted classification, up to six zones with completely different flow structures are identified on the regime map in the vicinity of the cylinder [20]. A tandem of two cylinders complements the picture with another parameter, i.e., the distance between the cylinders. This generates an interference pattern, which can be accompanied by both an increase and a decrease in the friction factor of the pair.

Many of these problems can be solved by mathematical modeling via numerical solution of a system of differential equations. Various approaches to numerical study of the problem were considered in a number of works, for example, in [21 – 27].

Let us consider some of these studies in more detail. It was confirmed in [21] that the self-oscillation mode could be obtained by numerically solving a system of Navier – Stokes equations in a two-dimensional formulation. A particular assumption made by the authors is that plates of zero thickness are used as heaters in the calculations. The results of numerical integration in [22] simulate the operation of some of the engine elements. The problem is solved in a two-dimensional formulation, examining heat transfer on a plate in oscillatory flow caused by external excitation. The performance characteristics of a high-frequency (300 Hz) engine with flat heat exchangers were calculated in [24] in a two-dimensional formulation assuming a turbulent flow regime. The mathematical model was closed by the (k-ε) turbulence model. The temperature was set on the channel wall and on the stack connecting the heat exchangers. The authors investigated the influence from the lengths of the resonator and the stack connecting the flat heat exchangers, comparing the data with linear theory. The results of numerical simulation revealed an oscillatory mode of gas-dynamic functions with decreasing amplitude. The LS-FLOW solver, developed by the Japan Aerospace eXploration Agency for analysis of three-dimensional compressible flows within the Navier – Stokes system of equations, was used in [26]. The computations were carried out on an unstructured grid in a two-dimensional formulation. It was found that a short trigger pulse injected from the open end of the computational domain was required to induce oscillations in the system. However, a deviation of the numerical solution from linear theory was observed.

To summarize, mathematical modeling of thermoacoustic self-excitation in the given system by numerically integrating the system of Navier – Stokes differential equations imposes stricter requirements on all aspects of the computational process. Constructing the solution to the problem by the control volume method involves tailoring the size of the domain where the desired functions are defined, the shapes of the discretization elements of the computational domain, the method for approximating the function at the element boundary, the time integration scheme. The computations in all of the above studies were performed in a two-dimensional formulation without accounting for the interaction with the pipe wall. For this reason, this work contains the solution of a two-dimensional problem including the interaction with the pipe wall.

Problem statement and computational aspects

The solution of the problem from [11] requires three coordinate directions. If a channel with a square cross-section is replaced with a cylindrical pipe, and the heat exchanging rods with toroidal elements, then, assuming that the gas-dynamic functions are homogeneous in the circumferential direction, axial symmetry appears in the problem formulation, making it possible to reduce the number of spatial coordinates to 2. This geometric modification does not fundamentally affect the excitation of thermoacoustic oscillations under consideration, allowing to consider not only unsteady heat

transfer on the surface of heat exchangers but also the interaction of the gas with the pipe wall, which is commonly excluded from balance relations in the two-dimensional formulation.

The system of Navier – Stokes equations for the problem formulated in an axisymmetric setting consists of four partial differential equations:

mass balance,

energy balance,

balance of momentum written as projections on two axes, z and r.

The system should be supplemented with two equations of state:

thermodynamic (in the form of the Mendeleev – Clapeyron equation),

caloric, establishing the relationship between internal energy and temperature.

A diagram of the computational domain and explanations for the problem formulation are shown in Fig. 1, the values of the parameters used in the calculations are summarized in Table.

Parameters of stagnant gas values at the open end of the pipe: $P^0 = 0.1$ MPa, $T^0 = 300$ K. The temperature of the cooler surface $T = 300$K. The given quantitative values of the problem parameters correspond to the sizes selected in [11]. Judging by the results of that study for the selected distance between the heat exchangers, the self-excitation mode should occur at the temperature $T^+ = 850$ K and higher at the heater surface. Thus, it can be established through a series of calculations with varying heater temperature that the mathematical model can reproduce the important conclusions of the experimental study.

The boundary conditions at the permeable boundary of the computational domain are imposed in a simplified formulation. Firstly, the boundary of the computational domain coincides with the exit section of the pipe, which excludes the influence from the so-called synthetic jet arising outside the resonator on the solution [28]. Secondly, when gas enters the computational domain, the steady-state values of gas-dynamic functions are obtained by isentropic formulas; the value P^0 is used for gas outflow.

The side wall of the pipe is divided into three zones to maintain the thermodynamic balance in the system. The pipe wall temperatures in the sections to the left and to the right of the heat exchanger are T^+ and T^-, respectively. The condition of thermal insulation is imposed between these zones, on the pipe wall section (1.0 cm long), centered relative to the location of the heat exchangers. An identical boundary condition is imposed at the end of the pipe.

The no-slip condition is imposed on the surface of the toroidal elements and on the pipe walls.

The results in this study were obtained using the ANSYS FLUENT 2021R1 package, allowing to solve two-dimensional problems in the axisymmetric formulation. The pressure-based solver in the implicit formulation with the coupled algorithm was used to construct the solution. Reconstructions with third-order accuracy (Third-Order MUSCL) were used to produce the values of functions on the control surfaces. The time integration was performed by an implicit scheme with second-order

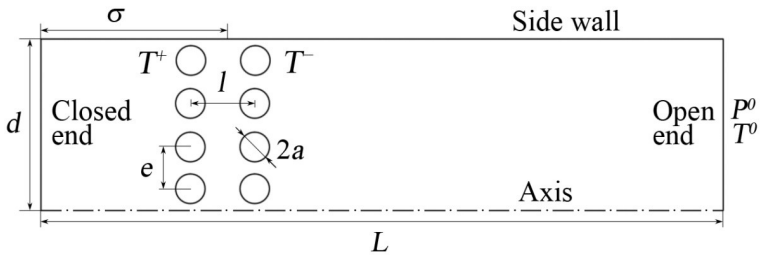

Fig. 1. Schematic of computational domain (geometric proportions are not reproduced):
Side wall of the pipe; Closed & Open ends of the pipe; Axis of symmetry;
T^+, T^- are the temperatures of the heater and the cooler; see also table

Table

Computational parameters of the problem and their values

Parameter	Notation	Unit	Value
Length of computational domain	L	m	1.0
Radius of computational domain	d	cm	3.2
Radius of cylindrical rods	a	mm	1.0
Distance from grid to closed wall of pipe	σ	cm	20
Distance between grid rows	l	mm	6.0
Number of elements in grid	N	–	4
Grid spacing	e	mm	4.0
Gas pressure	P^0	MPa	0.1
Temperature of gas of cooler surface	 T^0 T	K	300

Notes. 1. The values given correspond to the selected dimensions from [11]. 2. The grid spacing is the distance between the central lines of the torus generators. 3. The compressed medium is air.

accuracy. Discretization was carried out on an unstructured mesh consisting of quadrangular elements. The mesh provided clustering to all impermeable boundaries of the computational domain. This made it possible to resolve the structure of the temperature and dynamic boundary layer on the pipe wall and on the surfaces of the heat exchangers.

The results in the study (see below) were obtained on a mesh containing about 40,000 elements, while the time integration step was $\Delta t = 0.1$ ms.

Computational results and discussion

Initial data. The computations were carried out for the initial state of the gas, when its pressure in the pipe was P^0, and its velocity was equal to zero. The stepwise dependence on the axial coordinate was taken as the initial state of the temperature. It was assumed that the temperature to the left and right of the gratings coincides with the temperature of the heat exchangers. The temperature in the section where the thermal insulation condition was imposed on the pipe wall was determined by the half-sum of the selected temperature levels. The gas density was taken in accordance with the ideal gas equation of state. This local state, which is unsteady with respect to temperature between the heat exchangers and the air around them, is essentially sufficient to excite natural oscillations of the gas column in the system.

The excitation of oscillations starts as a temperature field is generated in the vicinity of the heat exchangers. The process is accompanied by pressure gradients appearing, along with a nonzero value of the velocity vector. Pressure and velocity waves are characterized by small amplitude and natural oscillation frequency. This state of gas (oscillations with small amplitude) can last rather long and count more than one hundred oscillation periods. Both an unsteady solution and a steady heat transfer regime can be established depending on the magnitude of the temperature gradient. Let us give the results for four temperatures of the heater (K): 600, 800, 900 and 1200.

Fig. 2 shows the time dependences of the mean cross-sectional velocity at the open end of the pipe and the magnitude of the pressure deviation from the initial value at its closed end at different temperatures of the heater.

Judging from the data presented, the arising oscillations of gas-dynamic functions are completely damped in a time interval of less than 1 s at a heater temperature $T^+ = 600$ K.

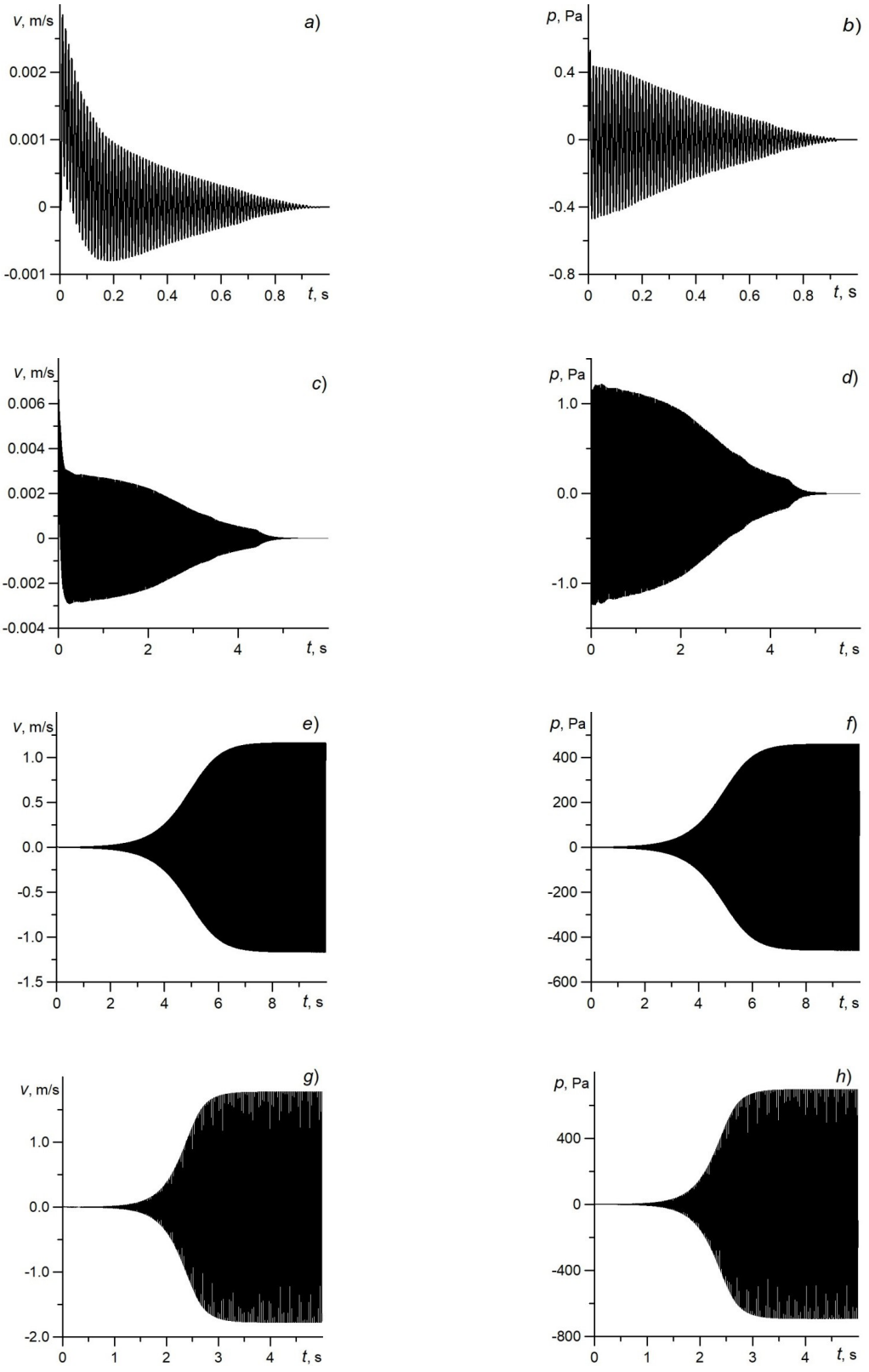

Fig. 2. Time dependences of axial velocity component, averaged over the section, at the open end of the pipe (*a*, *c*, *e*, *g*) and pressure deviation from the initial level at the closed end of the pipe (*b*, *d*, *f*, *h*) at heater temperature $T^+ = 600$ K (*a*, *b*), 800 K (*c*, *d*), 900 K (*e*, *f*) and 1200 K (*g*, *h*)

The damping scenario of natural oscillations undergoes changes at a heater temperature $T^+ = 800$ K, namely, the process proceeds much more slowly. For the given initial state of the functions, the transition to steady state occurs in a time interval exceeding 4 s. A possible explanation for this behavior of the functions is that the selected combination of problem parameters produces a regime that is outside the boundaries of oscillation self-excitation. The heater temperature does not precisely coincide with the temperature at which the self-oscillations of gas-dynamic functions are observed in the experiment: this can be related to the change in the channel shape and simplified description given to the behavior of the functions at the open end of the pipe.

The threshold values of the temperature gradient are exceeded at a heater temperature $T^+ = 900$ K, therefore, a continuous oscillatory gas flow evolves. Steady flow is established in the pipe in several stages. First, a time interval exists with small-amplitude oscillations, when the signal magnitude increases by a linear law; secondly, there is an 'avalanche-like' resonant mode of increasing the oscillation amplitude, when there is positive feedback between the change in pressure and the specific heat flux in the heat exchangers; thirdly, the transition to steady non-stationary oscillation mode uis observed. The oscillation amplitude of gas-dynamic functions (third stage) is stabilized due to two factors. The first is the work of the frictional forces of the gas against the pipe wall performed during oscillatory flow, and the second is the radiation that occurs the open end of the pipe, generating a synthetic jet.

The flow regime in the resonator at heater temperature $T^+ = 1200$K is characterized by a shorter transition time to steady oscillations. The amplitude of velocity oscillations at the open end of the pipe and the pressure deviation from the initial value at its closed end is higher than for the case $T^+ = 900$ K. The natural frequency of the gas column is 87.0 ± 0.7 Hz up to the selected time integration step.

Let us focus on the behavior of functions over time for one oscillatory period in steady state. Fig. 3 shows the dependence of the specific heat flux averaged over the entire surface of the grid and the pressure deviation from the initial state for one oscillatory period for the cases $T^+ = 900$ and 1200 K.

The zero value of the pressure deviation from the initial one in the heat exchangers is taken as the beginning of the cycle. The behavior of the specific heat flux function indicates that the maximum heat addition is synchronized with the maximum pressure increase across the heater. In turn, the maximum heat removal in the cooling grid is also in the vicinity of the minimum pressure. Thus, a situation that falls under the Rayleigh criterion happens with both heat exchangers. Notably, the sig-

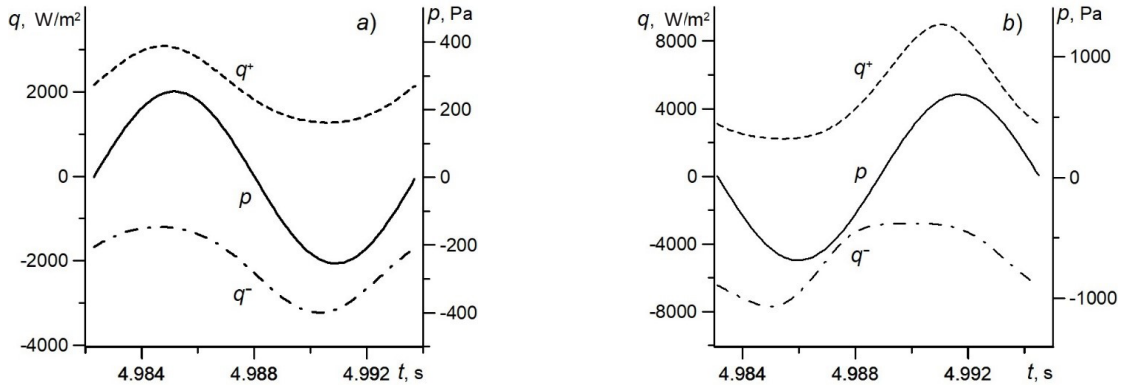

Fig. 3. Time dependences of pressures p (solid line), specific heat fluxes q^+ (dashed line) and q^- (dash-dotted line) for the oscillatory period in the heater and cooler, respectively, for cases $T^+ = 900$ K (a) and 1200 K (b)

nals increase in amplitude and lose their sinusoidal shape with the distance from the parameter values setting the excitation boundary of thermoacoustic oscillations.

Conclusion

The solution to the problem on self-excitation of oscillations in a structure reproducing the Sondhauss effect has been obtained by numerical integration of the system of differential Navier – Stokes equations for compressible gas. Depending on the temperature difference in the heat exchangers, the mode established is either oscillation damping, or a stable unsteady mode of oscillatory flow of a gas column in a pipe closed at one end. The result of mathematical modeling is in good agreement with the experimental data.

REFERENCES

1. **Sondhauss C.,** Über die Schallschwingungen der Luft in erhitzten Glassrohen und gedeckten Pfeifen von ungleicher Weite, Pogg. Ann. Phys. und Chem. 79 (1850) 1–34.

2. **Strutt J.W., Baron Rayleigh,** The theory of sound, Vol. 2, Macmillan and Co., London, 1878.

3. **Putnam A.A., Dennis W.R.,** A survey of organ-pipe oscillations in combustion systems, J. Acoust. Soc. Am. 28 (2) (1956) 246–259.

4. **Feldman K.T.,** Review of the literature on Sondhauss thermoacoustic phenomena, J. Sound Vib. 7 (1) (1968) 71–82.

5. **Swift G.W.,** Thermoacoustics: a unifying perspective for some engines and refrigerators, 2nd Ed., Springer, Heidelberg, Germany, 2017.

6. **Arnott W.P., Bass H.E., Raspet R.,** Specific acoustic impedance measurements of an air-filled thermoacoustic prime mover, J. Acoust. Soc. Am. 92 (6) (1992) 3432–3434.

7. **Hariharan N.M., Sivashanmugam P., Kasthurirengan S.,** Influence of operational and geometrical parameters on the performance of twin thermoacoustic prime mover, Int. J. Heat Mass Transfer. 64 (September) (2013) 1183–1188.

8. **Sugita H., Matsubara Y., Kushino A., et al.,** Experimental study on thermally actuated pressure wave generator for space cryocooler, Cryogenics. 44 (6–8) (2004) 431–437.

9. **Ceperley P.H.,** A pistonless Stirling engine – The travelling-wave heat engine, J. Acoust. Soc. Am. 66 (5) (1979) 1508–1513.

10. **Yazaki T., Iwata A., Maekawa T., Tominaga A.,** Travelling-wave thermoacoustic engine in a looped tube, Phys. Rev. Lett. 81 (15) (1998) 3128–3131.

11. **Katto Y., Takano K.,** Study of the oscillation of a gas column caused by heat conduction in a tube. Bulletin of ISME. 20 (147) (1977) 1169–1173.

12. **Rott N.,** Damped and thermally driven acoustic oscillations in wide and narrow tubes, Z. Angew. Math. Phys. 20 (2) (1969) 230–243.

13. **Rott N.,** Thermally driven acoustic oscillations, part III: Second-order heat flux, Z. Angew. Math. Phys. 26 (1) (1975) 43–49.

14. **Ward B., Clark J., Swift G.W.,** Design environment for low-amplitude thermoacoustic energy conversion. DeltaEC, Version 6.2, Users Guide, Los Alamos National Laboratory, USA, 2008.

15. **Yang R., Wang Y., Tan J., et al.,** Numerical and experimental study of a looped travelling-wave thermoacoustic electric generator for low-grade heat recovery, Int. J. Energy Res. 43 (11) (2019) 5735–5746.

16. **Kalra S., Desai K.P., Naik H.B., Atrey M.D.,** Theoretical study on standing wave thermoacoustic engine, Physics Procedia, 67 (Proc. of the 25th Intern. Cryog. Eng. Conf. and Intern. Cryog. Mater. Conf. 2014) (2015) 456–461.

17. **Gorshkov I.B., Petrov V.V.,** Numerical simulation of a looped tube 4-stage traveling-wave thermoacoustic engine, Izvestiya of Sarat. Univ. Physics. 18 (4) (2018) 285–296 (in Russian).

18. **Galiullin R.G., Revva I.P., Khalimov G.G.,** Teoriya termicheskikh avtokolebaniy [Thermal self-oscillations theory], Kazan University Publishing, Kazan, 1982 (in Russian).

19. **Larionov V.M., Zaripov R.G.,** Avtokolebaniya gaza v ustanovkakh s goreniyem [Gas self-oscillations in the plants with combustion], Kazan State Techn. University Publishing, Kazan, 2003 (in Russian).

20. **Nuriyev A.N., Zaytseva O.N.,** Resheniye zadachi ob ostsilliruyushchem dvizhenii tsilindra v vyazkoy zhidkosti v pakete OpenFOAM [Solving the problem on the oscillating motion of a cylinder in the viscous fluid using the OpenFOAM packet], Vestnik Kazanskogo Tekhnologicheskogo Universiteta. 16 (8) (2013) 116–123 (in Russian).

21. **Jeffrey F.Z., Vipperman S., Schaefer L.A.,** Advancing thermoacoustics through CFD simulation using FLUENT, Proc. ASME 2008 Intern. Mech. Eng. Congr. and Expos. Vol. 8 (Energy Systems: Analysis, Thermodynamics and Sustainability; Sustainable Products and Processes) Boston, Massachusetts, USA. Oct. 31–Nov. 6 (2008) 101–110.

22. **Tasnim S.H., Fraser R.A.,** Computation of the flow and thermal fields in a thermoacoustic refrigerator, Intern. Commun. Heat Mass Transf. 37 (7) (2010) 748–755.

23. **Guoyao Yu., Dai W., Luo E.,** CFD simulation of a 300 Hz thermoacoustic standing wave engine, Cryogenics. 50 (9) (2010) 615–622.

24. **Muralidharan H., Hariharan N.M., Perarasu V.T., et al.,** CFD simulation of thermoacoustic heat engine, Progress in Computational Fluid Dynamics. 14 (2) (2014) 131–137.

25. **Dar Ramdanel M.Z., Khorsi A.,** Numerical investigation of a standing-wave thermoacoustic device, Thermophysics and Aeromechanics. 22 (3) (2015) 313–318.

26. **Kuzuu K., Hasegawa S.,** Numerical investigation of heated gas flow in a thermoacoustic device, Appl. Therm. Eng. 110 (5 January) (2017) 1283–1293.

27. **Hariharan N.M., Arun S., Sivashanmugam P., Kasthurirengan S.,** CFD simulation on the performance of twin thermoacoustic prime mover for various resonator lengths and operating pressures, Heat Transfer – Asian Res. 47 (2) (2018) 337–346.

28. **Bulovich S.V.,** Mathematical simulation of a gas flow in the vicinity of the open end of a tube for harmonic oscillations of a piston at the resonance frequency at the other end of the tube, Technical Physics. 62 (11) (2017) 1634–1638.

Received 07.05.2021, accepted 21.06.2021.

THE AUTHOR

BULOVICH Sergei V.
Peter the Great St. Petersburg Polytechnic University
29 Politechnicheskaya St., St. Petersburg, 195251, Russian Federation
bulovic@yandex.ru

СПИСОК ЛИТЕРАТУРЫ

1. **Sondhauss C.** Über die Schallschwingungen der Luft in erhitzten Glassrohen und gedeckten Pfeifen von ungleicher Weite // Pogg. Ann. Phys. und Chem. 1850. Band 79. S. 1–34.

2. **Дж.В. Стрэтт (Лорд Рэлей).** Теория звука. Т. 2. М.: Гостехиздат, 1955. 300 с.

3. **Putnam A.A., Dennis W.R.** A survey of organ-pipe oscillations in combustion systems // Journal of the Acoustical Society of America. 1956. Vol. 28. No. 2. Pp. 246–259.

4. **Feldman K.T.** Review of the literature on Sondhauss thermoacoustic phenomena // Journal of Sound and Vibration. 1968. Vol. 7. No. 1. Pp. 71–82.

5. **Swift G.W.** Thermoacoustics: a unifying perspective for some engines and refrigerators. 2nd edition. Heidelberg, Germany: Springer, 2017. 326 p.

6. **Arnott W.P., Bass H.E., Raspet R.** Specific acoustic impedance measurements of an air-filled thermoacoustic prime mover // Journal of the Acoustical Society of America. 1992. Vol. 92. No. 6. Pp. 3432–3434.

7. **Hariharan N.M., Sivashanmugam P., Kasthurirengan S.** Influence of operational and geometrical parameters on the performance of twin thermoacoustic prime mover // International Journal of Heat and Mass Transfer. 2013. Vol. 64. September. Pp. 1183–1188.

8. **Sugita H., Matsubara Y., Kushino A., Ohnishi T., Kobayashi H., Dai W.** Experimental study on thermally actuated pressure wave generator for space cryocooler // Cryogenics. 2004. Vol. 44. No. 6–8. Pp. 431–437.

9. **Ceperley P.H.** A pistonless Stirling engine – The travelling-wave heat engine // Journal of the Acoustical Society of America. 1979. Vol. 66. No. 5. Pp. 1508–1513.

10. **Yazaki T., Iwata A., Maekawa T., Tominaga A.** Travelling-wave thermoacoustic engine in a looped tube // Physical Review Letters. 1998. Vol. 81. No. 15. Pp. 3128–3131.

11. **Katto Y., Takano K.** Study of the oscillation of a gas column caused by heat conduction in a tube // Bulletin of the ISME. 1977. Vol. 20. No. 147. Pp. 1169–1173.

12. **Rott N.** Damped and thermally driven acoustic oscillations in wide and narrow tubes // Zeitschrift für angewandte Mathematik und Physik. 1969. Vol. 20. No. 2. Pp. 230–243.

13. **Rott N.** Thermally driven acoustic oscillations, part III: Second-order heat flux // Zeitschrift für angewandte Mathematik und Physik. 1975. Vol. 26. No. 1. Pp. 43–49.

14. **Ward B., Clark J., Swift G.W.** Design environment for low-amplitude thermoacoustic energy conversion. DeltaEC Version 6.2 Users Guide. USA: Los Alamos National Laboratory, 2008.

15. **Yang R., Wang Y., Tan J., Luo J., Jin T.** Numerical and experimental study of a looped travelling-wave thermoacoustic electric generator for low-grade heat recovery // International Journal of Energy Research. 2019. Vol. 43. No. 11. Pp. 5735–5746.

16. **Kalra S., Desai K.P., Naik H.B., Atrey M.D.** Theoretical study on standing wave thermoacoustic engine // Physics Procedia. 2015. Vol. 67. Proceedings of the 25th International Cryogenic Engineering Conference and International Cryogenic Materials Conference, 2014. Pp. 456–461.

17. **Горшков И.Б., Петров В.В.** Численное моделирование кольцевого четырехступенчатого термоакустического двигателя с бегущей волной // Известия Саратовского ун-та. Новая серия. Серия Физика. 2018. Т. 18. № 4. С. 285–296.

18. **Галиуллин Р.Г., Ревва И.П., Халимов Г.Г.** Теория термических автоколебаний. Казань: Изд-во Казан. ун-та, 1982. 155 с.

19. **Ларионов В.М., Зарипов Р.Г.** Автоколебания газа в установках с горением. Казань: Изд-во Казан. гос. техн. ун-та, 2003. 227 с.

20. **Нуриев А.Н., Зайцева О.Н.** Решение задачи об осциллирующем движении цилиндра в вязкой жидкости в пакете OpenFOAM // Вестник Казанского технологического университета. 2013. № 8. С. 116–123.

21. **Jeffrey F.Z., Vipperman S., Schaefer L.A.** Advancing thermoacoustics through CFD simulation using FLUENT // Proceedings of the ASME 2008 International Mechanical Engineering Congress and Exposition. Vol. 8: Energy Systems: Analysis, Thermodynamics and Sustainability; Sustainable Products and Processes. Boston, Massachusetts, USA. October 31 – November 6, 2008. Pp. 101–110.

22. **Tasnim S.H., Fraser R.A.** Computation of the flow and thermal fields in a thermoacoustic refrigerator // International Communications in Heat and Mass Transfer. 2010. Vol. 37. No. 7. Pp. 748–755.

23. **Guoyao Yu., Dai W., Luo E.** CFD simulation of a 300 Hz thermoacoustic standing wave engine // Cryogenics. 2010. Vol. 50. No. 9. Pp. 615–622.

24. **Muralidharan H., Hariharan N.M., Perarasu V.T., Sivashanmugam P., Kasthurirengan S.** CFD simulation of thermoacoustic heat engine // Progress in Computational Fluid Dynamics. 2014. Vol. 14. No. 2. Pp. 131–137.

25. **Dar Ramdane M.Z., Khorsi A.** Numerical investigation of a standing-wave thermoacoustic device // Thermophysics and Aeromechanics. 2015. Vol. 22. No. 3. Pp. 313–318.

26. **Kuzuu K., Hasegawa S.** Numerical investigation of heated gas flow in a thermoacoustic device // Applied Thermal Engineering. 2017. Vol. 110. 5 January. Pp. 1283–1293.

27. **Hariharan N.M., Arun S., Sivashanmugam P., Kasthurirengan S.** CFD simulation on the performance of twin thermoacoustic prime mover for various resonator lengths and operating pressures // Heat Transfer – Asian Research. 2018. Vol. 47. No. 2. Pp. 337–346.

28. **Булович С.В.** Математическое моделирование течения газа в окрестности открытого торца трубы при колебаниях поршня на другом конце трубы по гармоническому закону на резонансной частоте // Журнал технической физики. 2017. Т. 87. № 11. С. 1632–1636.

Статья поступила в редакцию 07.05.2021, принята к публикации 21.06.2021.

СВЕДЕНИЯ ОБ АВТОРЕ

БУЛОВИЧ Сергей Валерьевич – *кандидат физико-математических наук, доцент Высшей школы прикладной математики и вычислительной физики Санкт-Петербургского политехнического университета Петра Великого, Санкт-Петербург, Российская Федерация.*

195251, Российская Федерация, г. Санкт-Петербург, Политехническая ул., 29

bulovic@yandex.ru

DOI: 10.18721/JPM.14304
UDC 004.94

AN INFLUENCE ANALYSIS OF CREEP AND PLASTICITY CHARACTERISTICS ON THE SPARK PLASMA SINTERING PROCESS

V.A. Borisenko[1], **A.S. Semenov**[1], **T. Wallmersperger**[2]

[1] Peter the Great St. Petersburg Polytechnic University,
St. Petersburg, Russian Federation;

[2] Dresden University of Technology,
Dresden, Germany

In the paper, the spark plasma sintering (SPS) process for metal particles has been simulated based on experimental data and using the finite element method in the thermo-electro-mechanical formulation with taking into account the temperature influence on parameters of materials (nickel and copper). A comparison of obtained results with experimental data made it possible to create a computational model of the SPS process, the model being convenient to evaluate the influence of creep and plasticity parameters on the size of the interparticle neck forming in SPS. It was found that the creep effect significantly dominated over the plasticity influence on the process of forming the sintering neck at high temperatures. In this case, the variation of creep parameters in simulation also actively affects the formation of the neck.

Keywords: spark plasma sintering, metal, finite-element modelling, plasticity, creep, coupled fields

Citation: Borisenko V.A., Semenov A.S., Wallmersperger T., An influence analysis of creep and plasticity characteristics on the spark plasma sintering process, St. Petersburg Polytechnical State University Journal. Physics and Mathematics. 14 (3) (2021) 47–59. DOI: 10.18721/JPM.14304

АНАЛИЗ ВЛИЯНИЯ ХАРАКТЕРИСТИК ПОЛЗУЧЕСТИ И ПЛАСТИЧНОСТИ НА ПРОЦЕСС ИСКРОВОГО ПЛАЗМЕННОГО СПЕКАНИЯ

В.А. Борисенко[1], **А.С. Семенов**[1], **Т. Вальмерспергер**[2]

[1] Санкт-Петербургский политехнический университет Петра Великого,
Санкт-Петербург, Российская Федерация;

[2] Технический университет Дрездена,
г. Дрезден, Германия

На основе экспериментальных данных в работе промоделирован процесс искрового плазменного спекания (ИПС) металлических частиц методом конечных элементов в термоэлектромеханической постановке с учетом влияния температуры на параметры материалов (никеля и меди). Сравнение результатов моделирования с экспериментом позволило создать вычислительную модель процесса ИПС, удобную для оценки влияния параметров ползучести и пластичности на размер межчастичной шейки, образующейся при проведении ИПС. Установлено, что для высоких температур эффект ползучести в несколько раз превосходит влияние пластичности на процесс образования шейки спекания. При этом изменение параметров ползучести при моделировании также активно влияет на формирование шейки.

Ключевые слова: искровое плазменное спекание, металл, конечно-элементное моделирование, пластичность, ползучесть, связанные поля

Ссылка при цитировании: Борисенко В.А., Семенов А.С., Вальмерспергер Т. Анализ влияния характеристик ползучести и пластичности на процесс искрового плазменного спекания // Научно-технические ведомости СПбГПУ. Физико-математические науки. 2021. Т. 14. № 3. С. 47–59. DOI: 10.18721/JPM.14304

Introduction

Detailed experimental and theoretical studies [1, 2], as well as simulations [3 – 5] have been carried out for sintering and compaction of powder metallurgy products, aimed at improving their properties. The technology for obtaining metal powders and manufacturing products from them offers several benefits [6, 7], in particular, making it possible to synthesize materials that are difficult or impossible to obtain by other methods; furthermore, it helps save metal and significantly reduces the production costs. Additionally, using pure starting powders yields sintered materials with a lower impurity content, better corresponding to a given composition compared to conventional cast alloys. Sintered materials have better mechanical properties compared to cast ones with the same composition and density; for instance, the preferred orientation of the crystal grains of the metal (texture), which is characteristic for cast equivalents, has a smaller adverse effect. The size and shape of the structural elements of sintered materials are easier to control, and even more importantly, it is possible to produce such types of mutual arrangement and shape of grains that are unattainable for cast metal.

Due to these structural peculiarities, sintered metals are more heat-resistant, better tolerate the effects of cyclic fluctuations in temperature and stress, as well as nuclear radiation, which is crucial for the materials used in novel devices.

Spark Plasma Sintering/Field Assisted Sintering Technology (SPS/FAST) is an effective method for obtaining defect-free blanks from powder materials, combining pressing with an intense electrical discharge, allowing to obtain compact materials in a very short time. Recently, there has been an increase in the number of studies on spark plasma sintering (see, for example, [11 – 13]). The essence of this method for consolidating powder materials is that substances are heated by electric current pulses passing through it. This way, the temperature and sintering time are greatly reduced compared to conventional high-temperature sintering and hot pressing.

The difficulties with simulating the given class of problems are due to different sintering mechanisms (plasticity, creep, thermal migration, etc.). In addition, the sintering process consists of multiple pronounced stages: neck growth, formation and subsequent shrinkage of closed pores. Moreover, fields of different nature interact in this case: electrical, thermal, chemical and mechanical. The nontrivial dependence of electrical and mechanical constants on the temperature of the material can cause problems with the convergence of the solution during simulation. This convergence also strongly depends on the parameters of the contact, namely the thermal and electrical conductivity of the zone of contacting elements. Finite element modeling (FEM) is a valuable tool for gaining a better understanding of the process. FEM was mainly used previously to study macroscopic temperature gradients in samples during a fast process [14 – 16] but recently more and more works [4, 5] consider FEM of particle deformation, as well as microscopic distribution of current and temperature upon particle contact as the simplest representative volume of powder.

It was established in [5] that using elastic and viscoelastic models of the sintered material in simulating such processes does not yield a good correlation with experimental data. In this case, the best accuracy was obtained by simultaneously taking into account both viscous and plastic effects.

The goal of this study consisted in analyzing the potential offered by FEM of spark plasma sintering by comparing the results with experimental data.

To solve this problem, it was necessary to analyze the influence of a number of key factors and, first of all, creep, on the diameter of the interparticle neck formed in the process of the studied technology.

Experimental setup and mathematical model

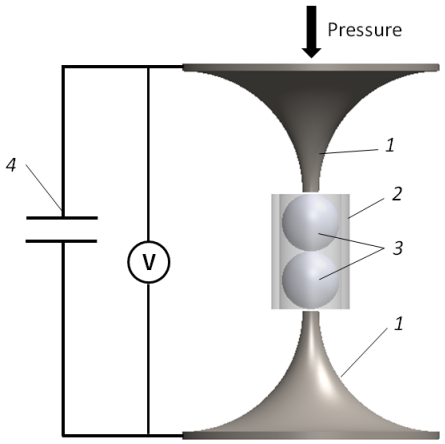

Fig. 1. Schematic of experimental setup: copper punches *1*, thick-walled glass tube *2*, nickel balls *3*, electrolytic capacitors *4*

The experiments carried out at the Dresden University of Technology (Germany) [4, 5] involved balls made of commercially pure nickel 1 mm in diameter. To remove oxides from nickel spheres, the balls were placed in a citric acid solution for several hours and rinsed with distilled water and ethanol before they were inserted into the setup. An experimental setup was developed and built specifically to study the initial stages of contact formation under spark plasma sintering. The diagram is shown in Fig. 1.

Copper punches *1* 1 mm in a diameter are located at the top and bottom of the setup. Thick-walled glass tube *2* with a 1 mm internal diameter is attached to the lower punch to prevent balls *3* from falling out. Two nickel balls are placed between the fitting punches. A mechanical load (Pressure) is applied to the upper punch using a 1 kg weight providing an axial compressive force of 12.5 MPa in the cross section of the copper punches, and, accordingly, in the equatorial section of the balls. An electrode containing two series-connected electrolytic capacitors *4* is attached to the upper punch. The second electrodes of the capacitor are connected to the lower punch via a current rectifier that serves as a switch controlled by a microcontroller. The capacitors were charged to a voltage from 1 to 8 V (the value depended on the experimental conditions).

Mathematical model

We consider a related thermoelectromechanical axisymmetric problem for analyzing the deformations, emerging stresses, as well as the evolution of the temperature field and contact resistance. Elastic, plastic and viscous parameters of the material are used for simulating the mechanical component of the problem. Given that there are no reliable data for nickel plasticity curves at high temperatures, a plasticity model with linear hardening was used to simulate plastic deformations. The von Mises condition was considered as a condition for the onset of plasticity, due to the isotropy of the material. The heat balance equation taking into account the Fourier law was used for non-stationary processes accompanying the changes in the thermal field.

The complete system of equations for a coupled thermoelectromechanical initial boundary-value problem has the following form for the given conditions:

$$\begin{cases} \rho(T)C(T)\dfrac{\partial T}{\partial t} - \nabla\cdot\left(\lambda(T)\,\mathbf{E}\cdot\nabla T\right) - q_v = 0, \\ \nabla\cdot\left({}^4\mathbf{C}(T)\cdot\cdot\left((\nabla\mathbf{u})^s - \boldsymbol{\alpha}(T)\left(T - T_{ref}\right) - \boldsymbol{\varepsilon}^P - \boldsymbol{\varepsilon}^c\right)\right) = 0, \\ \nabla\cdot\left(\boldsymbol{\varepsilon}_n\cdot\nabla\dfrac{\partial\varphi}{\partial t}\right) + \nabla\cdot\left[\boldsymbol{\sigma}(T)\cdot\nabla\varphi\right] = 0, \end{cases} \quad (1)$$

where λ is the thermal conductivity, T is the temperature, T_{ref} is the initial temperature, $\boldsymbol{\varepsilon}^P$ is the plastic deformation tensor, $\boldsymbol{\varepsilon}^c$ is the deformation creep, ρ is the density, C is the specific heat, q_v is the volumetric heat transfer, φ is the scalar electric potential, $\boldsymbol{\sigma}$ is the electrical conductivity tensor, ε_p the dielectric permittivity tensor of the medium, $\mathbf{f}_v$ is the volumetric force vector, $\mathbf{u}$ is the displacement vector, $^4\mathbf{C}$ is the stiffness tensor, $\boldsymbol{\alpha}$ is the tensor of linear thermal expansion coefficients.

Volume forces and inertial terms are absent from the equilibrium equation of system (1) in the given problem statement. The values of elastic, thermal and electrical constants of the material depending on temperature are given in Table 1 for nickel and copper (taken from [4, 5]); the dimensions of the given constants correspond to a certain system of units: millimeters, gigagrams, seconds (mm, Gg, s). Table 1 also lists the values of the yield stress σ_y and the plastic modulus H_0 corresponding to the model of plasticity with linear hardening. The data presented indicate that the characteristics of materials are considerably dependent on temperature. In SPS, a current passing through the material causes it to heat up, leading to a change in the material constants, for example, resistivity. A change in the latter in turn leads to a change in the current and density of the heat released in the given section. This chain reflects how the material constants are related to the temperature field, and how, in turn, the temperature field depends on these constants.

Norton's law based on the similarity hypothesis was used to account for creep. In general, Norton's law is written as

$$\boldsymbol{\varepsilon}^c = A\sigma_i^{n-1}\mathbf{S}\cdot t\cdot\exp\left(-\frac{\Delta H}{RT}\right), \tag{2}$$

where ΔH is the creep activation energy; R is the Boltzmann constant; t is the time; T is the temperature; σ is the stress; n and A are the power and linear creep indicators; $\mathbf{S}$ is the stress tensor deviator.

The values of the creep constants were taken from monograph [17]:

$A = 80.4$ MPa$^{-4.6}$/s, $n = 4.6$, $\Delta H = 284$ kJ for nickel;

$A = 2.45$ MPa$^{-4.8}$/s, $n = 4.8$, $\Delta H = 197$ kJ for copper.

Since the problem is symmetric with respect to the contact plane of the balls, it seems reasonable to consider only the upper part of the structure in the FE simulation (see Fig. 1); it is shown in a horizontal position in Fig. 2, *a*,*b*. The FE model is shown in Fig. 2,*a*. It contains 1524 elements and 4491 nodes. The model was constructed in the ANSYS FEA package using PLANE 223 type elements in a thermoelectromechanical setting.

The contact between the balls in this symmetric statement is modeled as the contact between the upper ball and an absolutely rigid plane. Since boundary conditions in the given problem should be imposed taking into account the experimental procedure, they should be mechanical, electrical and thermal in nature. The mechanical component should reflect the restricted displacements and the fact that pressure is applied to the upper copper punch. A restriction on displacement of the contact surface was imposed in the symmetric problem statement. The electrical component accounted for the potential difference applied to the electrodes of the test setup. The function of the potential over time was taken to be equal to half the voltage between the capacitor plates changing over time. An exponential curve was combined with its piecewise-linear point approximation for the FE simulation (Fig. 2,*c*).

The following boundary conditions were imposed on the free surface of the ball and the punch: zero normal stress and electric current ($\sigma_n = 0$, $J_n = 0$), thermal radiation by the Stefan – Boltzmann law (the ball material was assumed to be a blackbody with the emissivity $\varepsilon = 1$) $q_n = \varepsilon\cdot\sigma_{SB}\cdot\left(T^4 - T_0^4\right)$. Restrictions on the radial components of displacement, electric current and heat flux were imposed on the boundary of axial symmetry: $u_n = 0$, $J_n = 0$, $q_n = 0$. The boundary conditions of zero displacement, potential and heat flux were imposed on the contact boundary of the balls: $u_n = 0$, $\varphi = 0$, $q_n = 0$.

Table 1

Values of elastic, thermal and electrical constants of nickel and copper depending on temperature [4, 5]

T, K (^{o}C)	300 (27)	500 (227)	700 (427)	900 (627)	1100 (827)	1400 (1127)	1728 (1455)
Values for nickel							
ρ, Gg/mm^3	8.90e–12	8.82e–12	8.74e–12	8.65e–12	8.55e–12	8.40e–12	8.10e–12
C_p, J/(Gg·K)	4.44e+8	5.24e+8	5.24e+8	5.43e+8	5.77e+8	6.09e+8	6.25e+8
λ, W/(mm·K)	0.0904	0.0721	0.0609	0.0662	0.0735	0.0767	0.0785
ρ_e, Ω·mm	7.37e–5	18.0e–5	32.0e–5	38.7e–5	44.5e–5	52.4e–5	59.0e–5
α, 1/K	13e–6	14e–6	15e–6	16.5e–6	17e–6	19e–6	13e–6
E, GPa	218	199	195	192	171	141	–
ν	0.28	0.28	0.28	0.30	0.31	0.34	–
σ_y, MPa	185	180	140	80	50	–	–
H_0, MPa	1800	1400	1100	1000	750	–	–
Values for copper							
ρ, Gg/mm^3	8.93e–12	8.63e–12	8.73e–12	8.62e–12	8.51e–12	8.39e–12	7.96e–12
C_p, J/(Gg·K)	3.85e+8	4.08e+8	4.25e+8	4.41e+8	4.64e+8	5.07e+8	5.14e+8
λ, W/(mm·K)	0.402	0.385	0.370	0.355	0.338	0.322	0.184
ρ_e, Ω·mm	1.73e–5	3.09e–5	4.51e–5	6.04e–5	7.72e–5	9.59e–5	23.4e–5
α, 1/K	16e–6	18e–6	19e–6	20e–6	24e–6	29e–6	–
E, GPa	130	115	103	89.7	76.8	63.7	–
ν	0.35	0.35	0.35	0.36	0.38	0.40	–
σ_y, MPa	220	190	100	40	–	–	–
H_0, MPa	500	400	200	200	–	–	–

Notations: T is the temperature, ρ is the density, C_p is the heat capacity at constant pressure, λ is the thermal conductivity, ρ_e is the resistivity, α is the thermal expansion coefficient, E is Young's modulus, ν is Poisson's ratio, σ_y is the yield stress, H_0 is the plastic modulus.

The following boundary conditions were imposed on the upper boundary of the punch: pressure versus time $\sigma_n = p(t)$, potential versus time $\varphi = V(t)/2$ and initial temperature $T = T_0$. The general form of the boundary conditions is shown in Fig. 2,*b*.

The penalty function method was used. The following parameter values were given:

normal contact stiffness factor equal to 1.0;

penetration tolerance factor equal to 0.1;

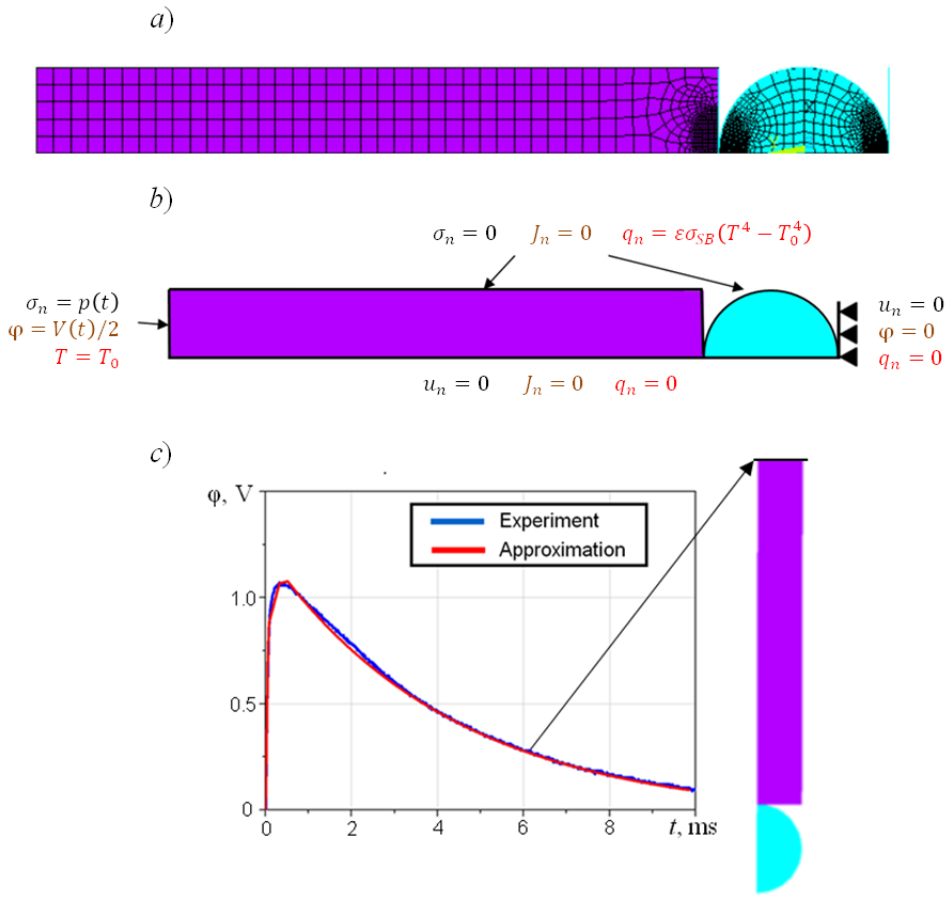

Fig. 2. Schematic representation of FE model
of spark plasma sintering for copper punch (purple) and nickel ball (blue):
a corresponds to partition of objects into finite elements, *b* illustrates the boundary conditions
of the problem statement, *c* is the graph of the electric potential applied to the upper boundary of the punch

thermal contact conductivity equal to 1 kW/K;
electrical contact conductivity equal to 1 MS.

Computational results and discussion

A series of simulations by the finite element method was performed to assess the influence of the yield parameters on the results of SPS. Virtual experiments differed by the initial charge of the capacitor and, accordingly, the dependence of the passing current on time. We selected three cases of initial voltage on the capacitor before the start of the SPS process were chosen: 2, 3, and 5 V. The input data for the mathematical model was the dependence of the voltage in the setup on time, recorded in a real experiment. The creep parameters were varied in addition to the change in the initial voltage on the capacitor plates, namely, its power exponent n and its activation energy ΔH.

We only analyzed the results obtained for the first 10 ms of the computational experiment, since the main changes in the thermal and electric fields were basically finished by the end of this time interval, and the process was observed to reach steady behavior.

The problem was solved in two thermoelectromechanical statements to assess the effect of creep on the temperature of the interparticle neck during sintering: without creep and taking it into account. The results obtained in [4] were used for verification, where the FE model was considered in a thermoelectric statement without mechanical deformations taken into account. The radius of the neck

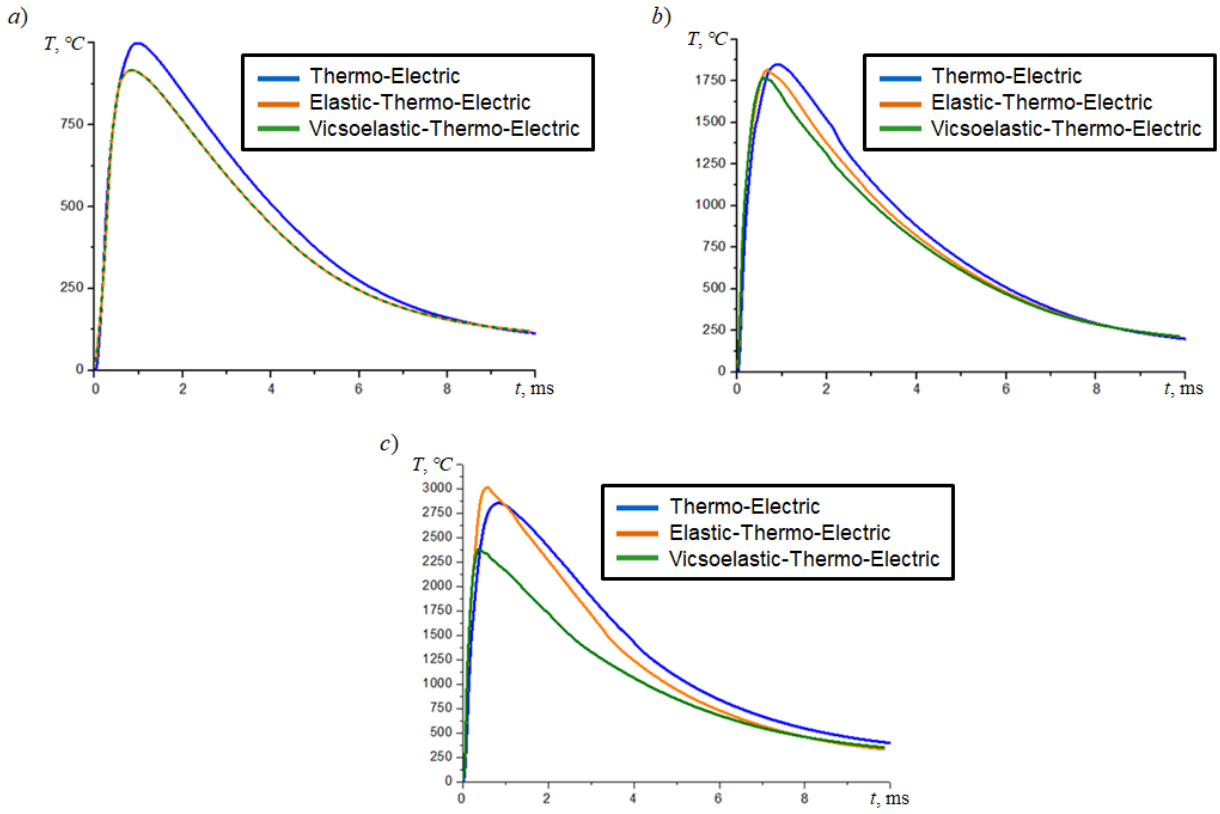

Fig. 3. Comparison of temperature evolution in the interparticle neck at initial voltages on capacitor plates equal to 2 V (*a*), 3 V (*b*) and 5 V (*c*), obtained in two thermoelectromechanical statements and compared with the thermoelectric statement (blue curves) [4]

contact was set in this model according to the experimental results and did not change throughout the entire simulation.

The graphs below are given for the dependence of the temperature of the neck material on time during sintering for three experiments differing in the initial voltage on the capacitor plates: 2, 3, and 5 V (Fig. 3). Apparently, accounting for creep at an initial voltage of 2 V does not affect the temperature change.

In addition, we compared the diameters of the sintering neck for the computational cases with and without accounting for the creep of its material, with different initial voltages on the capacitor plates (Table 2). The maximum diameter of the contact between spherical particles was taken as the neck diameter in the mathematical model.

Analyzing the data in Table 2, we can conclude that accounting for the creep at high initial voltages on the capacitor plates (3 and 5 V) makes it possible to refine the neck diameter and approach the experimental data, while the magnitude of the creep practically does not affect the growth of the neck at low temperatures.

The effect of creep at a high temperature provides a large area of contact between the particles, and, therefore, the peak temperature is lower. This result is consistent with the dependences shown in Fig. 4.

Significant differences between the simulation results and experimental data can be explained by increasing influence of other factors governing the formation of the interparticle neck, for example, the phenomena of surface and grain-boundary diffusion, which can develop at high capacitor volt-

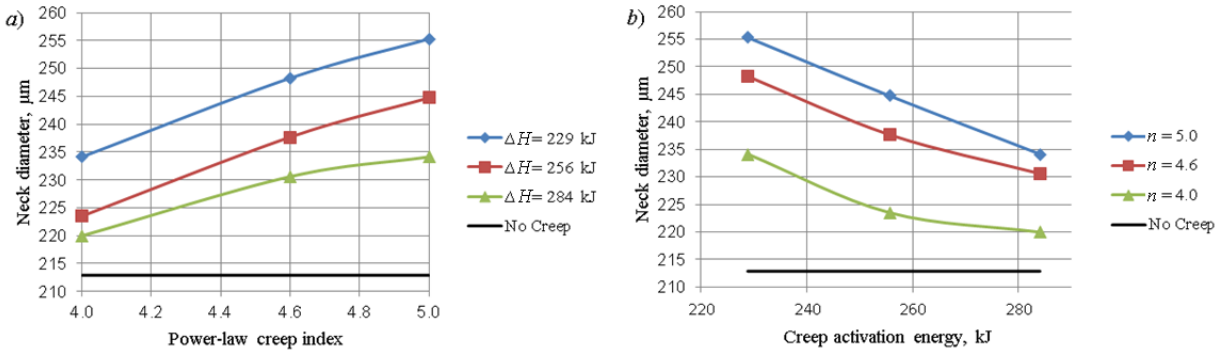

Fig. 4. Neck diameter depending on creep exponent n (*a*) and creep activation energy ΔH (*b*)

Table 2

Comparison of diameters of interparticle neck in spark plasma sintering, obtained experimentally and by the FEM method

Method	Neck diameter, μm			Deviation, %		
	2 B $T = 258$ K	3 B	5 B	2 B $T = 258$ K	3 B	5 B
		$T = 267$ K			$T = 267$ K	
Experiment	148	171	293	–		
FEM in elastic statement	147	158	213	–0.7	–7.6	–27
FEM accounting for creep	147	164	227	–0.7	–4.1	–23

Notes. 1. Data are given for three values of the initial voltage on the capacitor plates and two values of temperature.
2. Deviations of the computed results from the experiment are shown.

ages, and, consequently, with greater heating. Unfortunately, such effects are not implemented yet in the ANSYS FEA package.

To assess the influence of necking mechanisms, we considered the dependence of plastic and creeping deformations on the voltage set on the capacitor plates (Fig. 5). Analysis of the dependences plotted confirms that plasticity is the main mechanism behind the formation of an interparticle neck at low capacitor voltages before discharge (which is equivalent to a lower current passing through the system), while the main factor at higher voltages is creep.

Because creep has a considerable influence on the processes occurring at high initial voltages V on the capacitor plates, we estimated the influence of the parameters of the Norton creep law on the obtained diameter of the sintering neck was estimated for a value $V = 5$ V. The following set of parameters of Norton's creep law was selected:

the values $n = 5$ and 4 corresponding to deviations of +9 and –13% from the initial tabular value were taken for the creep exponent n, in addition to the tabular value $n = 4.6$ [17];

the values $\Delta H = 255.6$ and 228.9 kJ corresponding to deviations of 10 and 20% from the initial tabular value were taken for the creep activation energy ΔH, in addition to the tabular value $\Delta H =$ = 284 kJ [17].

The dependences for neck diameter on the creep exponent n and creep activation energy ΔH are shown in Fig. 4.

In addition to the above, we estimated the influence of the yield stress on the resulting neck size for the given tabular values of the creep parameters $n = 4.6$ and $\Delta H = 284$ kJ [17]. The following values of the yield stress (in MPa) were taken: 160, 180, 200, 220 and 240. The resulting dependence of the

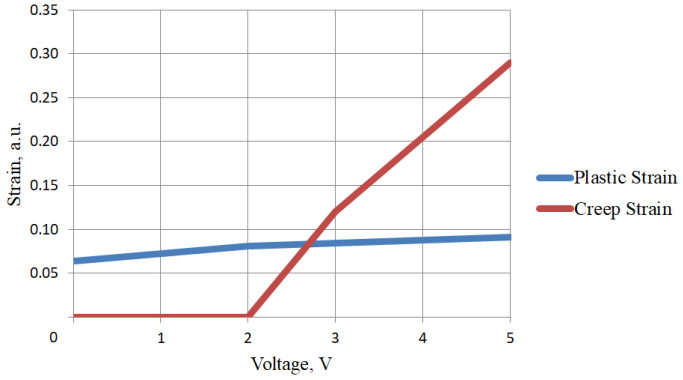

Fig. 5. Levels of plastic and creeping deformations
in the SPS interparticle neck depending on voltage on the capacitor plates

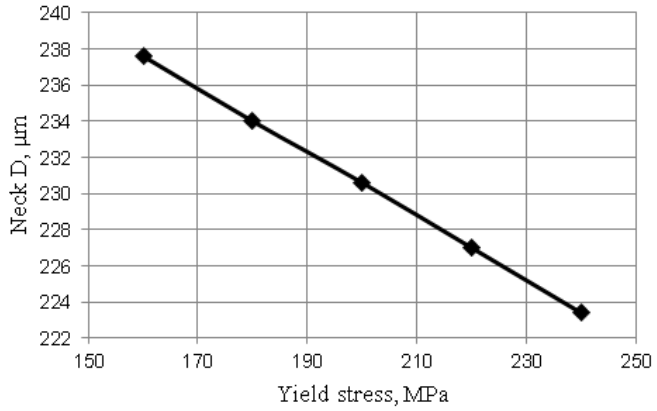

Fig. 6. Sintering neck diameter depending on yield stress of the ball material

sintering neck diameter on the yield stress is shown in Fig. 6. Evidently, the nature of the plotted dependence is actually linear for the given parameter values.

It was found that a 9% increase in the exponent results in an increase in the neck diameter by 3%, while taking into account the contribution of creep deformations results in an increase in the neck diameter by 50%. At the same time, its decrease by 13% leads to a decrease in the neck diameter by 3.1%. Furthermore, a decrease in the creep activation energy ΔH by 10% leads to an increase in the neck diameter by 5%, and taking into account the contribution of creep deformations to an increase in the neck diameter by 75%; a decrease in ΔH by 20% leads to an increase in the neck diameter by 10%, and taking into account the contribution of creep deformations to an increase in the neck diameter by 150%. In addition, a 20% increase in the yield stress results in a 3% decrease in the neck diameter.

These dependences confirm our conclusions about the predominant contribution of creeping deformations to the SPS process, in comparison with the influence of plastic deformations.

Conclusion

Based on the results obtained, we can argue that the behavior of sintered particles can be described fairly satisfactorily for low voltages on capacitor plates during spark plasma sintering. However, if higher voltages are set, the given thermoelectromechanical concepts of microparticle sintering mechanisms turn out to be insufficient for reliably modeling this process.

It was found that the creep effect on the sintering neck growth is several times greater for high temperatures than the effect of plasticity. At the same time, the change in the creep parameters during modeling also actively affects the formation of the neck. A deviation of the creep activation energy from the tabulated values by only 10% can produce an increase in creep deformations by 75% and an increase in neck diameter by 5%.

According to the data in monograph [18], the diffusion mechanism has a major effect on the sintering process along with the creep phenomenon. The influence of high temperatures (over 1500 °C) on the process of grain-boundary and surface diffusion was estimated in [19, 20].

Accounting for these necking mechanisms as well as creep and plasticity can give a more accurate agreement between the simulated results for high-current sintering and the available experimental data.

REFERENCES

1. **Anselmi-Tamburini U., Garay J.E., Munir Z.A.,** Fundamental investigations on the spark plasma sintering/synthesis process: III. Current effect on reactivity, Mater. Sci. Eng. A. 407 (1–2) (2005) 24–30.

2. **Trapp J., Semenov A.S., Nöthe M., et al.,** Fundamental principles of spark plasma sintering of metals: part III – densification by plasticity and creep deformation, Powder Metallurgy. 63 (5) (2020) 329–337.

3. **Wei Li,** Constitutive modeling and simulation of spark plasma sintering with applications to fabrication of functionally structured mono-carbides, Ph. D. thesis, University of California, San Diego, USA, 2013.

4. **Semenov A.S., Trapp J., Nöthe M., et al.,** Experimental and numerical analysis of the initial stage of field-assisted sintering of metals, J. Mater. Sci. 52 (3) (2017) 1486–1500.

5. **Semenov A.S., Trapp J., Nöthe M., et al.,** Thermo-electro-mechanical modeling, simulation and experiments of field-assisted sintering, J. Mater. Sci. 54 (15) (2019) 10764–10783.

6. **Barinov V.Yu., Rogachev A.S., Vadchenko S.G., et al.,** Iskrovoye plazmennoye spekaniye izdeliy slozhnoy formy s ispolzovaniyem kvaziistaticheskogo pressovaniya [Spark plasma sintering of complex-shaped products using quasi-static pressing], Mezhdunarodnyy zhurnal prikladnykh i fundamentalnykh issledovaniy [International Journal of Applied and Fundamental Research]. (1-3) (2016) 312–315 (in Russian).

7. **Grigoryev E.G., Kalin B.A.,** Elektroimpulsnaya tekhnologiya formirovaniya materialov iz poroshkov [Spark-discharge technology of material forming from powders], Moscow Engineering and Physical Institute (MEPhI), Moscow, 2008 (in Russian).

8. **Kolerov O.K.,** Characteristics of primary recrystallization and its role in the sintering of metal powders, Soviet Powder Metallurgy and Metal Ceramics. 12 (3) (1973) 192–195.

9. **Petrushina M.V., Pogudo E.L., Chivel Yu.A.,** Simulation of the process of sintering of spherical powders under the effect of pulsed laser radiation, High Temperature. 44 (1) (2006) 151–155.

10. **Mishra D.D., Agarwala V., Agarwala R.C.** Sintering behavior of mechanically alloyed Ti-48Al-2Nb aluminides, High Temperature. 52 (1) (2014) 65–71.

11. **Maniere C., Durand L., Weibel A., Estournes C.,** Spark plasma sintering and finite element method: from the identification of the sintering parameters of a submicronic α-alumina powder to the development of complex shapes, Acta Materialia. 102 (1 January) (2016) 169–175.

12. **Munir Z.A., Anselmi-Tamburini U., Ohyanagi M.,** The effect of electric field and pressure on the synthesis and consolidation of materials: a review of the spark plasma sintering method, J. Mater. Sci. 41 (3) (2006) 763–777.

13. **Olevsky E., Froyen L.,** Constitutive modeling of spark-plasma sintering of conductive materials, Scripta Materialia. 55 (12) (2006) 1175–1178.

14. **Orru R., Licheri R., Locci A.M., et al.,** Consolidation/synthesis of materials by electric current activated/assisted sintering, Mater. Sci. Eng. R: Reports. 63 (4–6) (2009) 127–287.

15. **Allen J., Walter C.,** Numerical simulation of the temperature and stress field evolution applied to the field assisted sintering technique, ISRN Mater. Sci. 2012 (2012) ID 698158. 1–9.

16. **Zinoviev V.E.,** Teplofizicheskiye svoystva metallov pri vysokikh temperaturakh [Thermophysical properties of metals at high temperatures (Handbook)], Metalurgia, Moscow, 1989 (in Russian).

17. **Frost H.J., Ashby M.F.,** Deformation-mechanism maps: the plasticity and creep of metals and ceramics, Pergamon Press, Oxford [Oxfordshire], New York, 1982.

18. **Kang S.-J. L.,** Sintering: densification, grain growth and microstructure, Elsevier Butterworth-Heinemann, 2005.

19. **Borisenko V.A., Semenov A.S.,** Issledovaniye deformirovaniya mezhchastichnoy sheyki metallicheskikh mikrochastits putem diffuzii [Studies in straining the interparticle neck of metal microparticles through diffusion], SPbPU Science Week, Materials of Scientific Conference with International Participation, November 13–19, 2017, Institute of Applied Mathematics and Mechanics, Polytechnical Institute Publishing, St. Petersburg (2017) 103–105 (in Russian).

20. **Borisenko V.A., Semenov A.S.,** Modelirovaniye protsessa rosta sheyki mezhdu dvumya sfericheskimi chastitsami pri spekanii [Simulation of the process of a neck growth between two spherical particles during sintering], SPbPU Science Week, Materials of Scientific Conference with International Participation, November 19–24, 2018, Institute of Applied Mathematics and Mechanics, Polytechnical Institute Publishing, St. Petersburg (2018) 80–83 (in Russian).

Received 13.04.2021, accepted 18.06.2021.

THE AUTHORS

BORISENKO Vladislav A.
Peter the Great St. Petersburg Polytechnic University
29 Politechnicheskaya St., St. Petersburg, 195251, Russian Federation
vladborisenko1995@gmail.com

SEMENOV Artem S.
Peter the Great St. Petersburg Polytechnic University
29 Politechnicheskaya St., St. Petersburg, 195251, Russian Federation
Semenov.Artem@googlemail.com

WALLMERSPERGER Thomas
Dresden University of Technology
3c, George-Bähr-Straße, Dresden, 01069, Saxony, Germany
servicecenter.studium@tu-dresden.de

СПИСОК ЛИТЕРАТУРЫ

1. **Anselmi-Tamburini U., Garay J.E., Munir Z.A.** Fundamental investigations on the spark plasma sintering/synthesis process: III. Current effect on reactivity// Materials Science and Engineering. A. 2005. Vol. 407. No. 1–2. Pp. 24–30.

2. **Trapp J., Semenov A.S., Nöthe M., Wallmersperger T., Kieback B.** Fundamental principles of spark plasma sintering of metals: part III – densification by plasticity and creep deformation // Powder Metallurgy. 2020. Vol. 63. No. 5. Pp. 329–337.

3. **Wei Li.** Constitutive modeling and simulation of spark plasma sintering with applications to fabrication of functionally structured mono-carbides. Ph. D. thesis. San Diego, USA: University of California, 2013. 271 p.

4. **Semenov A.S., Trapp J., Nöthe M., Eberhardt O., Wallmersperger T., Kieback B.** Experimental and numerical analysis of the initial stage of field-assisted sintering of metals // Journal of Materials Science. 2017. Vol. 52. No. 3. Pp. 1486–1500.

5. **Semenov A.S., Trapp J., Nöthe M., Eberhardt O., Wallmersperger T., Kieback B.** Thermo-electro-mechanical modeling, simulation and experiments of field-assisted sintering // Journal of Materials Science. 2019. Vol. 54. No. 15. Pp. 10764–10783.

6. **Баринов В.Ю., Рогачев А.С., Вадченко С.Г., Московских Д.О., Колобов Ю.Р.** Искровое плазменное спекание изделий сложной формы с использованием квазистатического прессования // Международный журнал прикладных и фундаментальных исследований. 2016. № 1-3. С. 312–315.

7. **Григорьев Е.Г., Калин Б.А.** Электроимпульсная технология формирования материалов из порошков. М.: Изд-во МИФИ, 2008. 152 с.

8. **Колеров О.К.** Особенности первичной рекристаллизации и ее роль при спекании металлических порошков // Порошковая металлургия. 1973. № 3. С. 18–22.

9. **Петрушина М.В., Погудо Е.Л., Чивель Ю.А.** Моделирование процесса спекания сферических порошков под действием импульсного лазерного излучения // Теплофизика высоких температур. 2006. Т. 44. № 1. С. 148–152.

10. **Mishra D.D., Agarwala V., Agarwala R.C.** Sintering behavior of mechanically alloyed Ti-48Al-2Nb aluminides // Теплофизика высоких температур. 2014. Т. 52. № 1. С. 65–71.

11. **Maniere C., Durand L., Weibel A., Estournes C.** Spark plasma sintering and finite element method: from the identification of the sintering parameters of a submicronic α-alumina powder to the development of complex shapes // Acta Materialia. 2016. Vol. 102. 1 January. Pp. 169–175.

12. **Munir Z.A., Anselmi-Tamburini U., Ohyanagi M.** The effect of electric field and pressure on the synthesis and consolidation of materials: a review of the spark plasma sintering method // Journal of Materials Science. 2006. Vol. 41. No. 3. Pp. 763–777.

13. **Olevsky E., Froyen L.** Constitutive modeling of spark-plasma sintering of conductive materials // Scripta Materialia. 2006. Vol. 55. No. 12. Pp. 1175–1178.

14. **Orru R., Licheri R., Locci A.M., Cincotti A., Cao G.** Consolidation/synthesis of materials by electric current activated/assisted sintering // Materials Science and Engineering. R: Reports. 2009. Vol. 63. No. 4–6. Pp. 127–287.

15. **Allen J., Walter C.** Numerical simulation of the temperature and stress field evolution applied to the field assisted sintering technique // ISRN Materials Science. 2012. Vol. 2012. Article ID 698158. Pp. 1–9.

16. **Зиновьев В.Е.** Теплофизические свойства металлов при высоких температурах. М.: Металлургия, 1989. 384 с.

17. **Фрост Г.Дж., Эшби М.Ф.** Карты механизмов деформации. Пер. с англ. Челябинск: Металлургия, 1989. 328 с.

18. **Kang S.-J.L.** Sintering: densification, grain growth and microstructure. Oxford: Elsevier Butterworth-Heinemann, 2005. 265 p.

19. **Борисенко В.А., Семенов А.С.** Исследование деформирования межчастичной шейки металлических микрочастиц путем диффузии // Неделя науки СПбПУ. Материалы научной конференции с международным участием. Институт прикладной математики и механики. 13–19 ноября 2017 г., СПб.: Изд-во Политехн. ун-та, 2017. С. 103–105.

20. **Борисенко В.А., Семенов А.С.** Моделирование процесса роста шейки между двумя сферическими частицами при спекании // Неделя науки СПбПУ. Материалы научной конференции с международным участием. Институт прикладной математики и механики. 19–24 ноября 2018 г., СПб.: Изд-во Политехн. ун-та, 2018. С. 80–83.

Статья поступила в редакцию 13.04.2021, принята к публикации 18.06.2021.

СВЕДЕНИЯ ОБ АВТОРАХ

БОРИСЕНКО Владислав Андреевич – *инженер-исследователь Института передовых производственных технологий Санкт-Петербургского политехнического университета Петра Великого, Санкт-Петербург, Российская Федерация.*

195251, Российская Федерация, г. Санкт-Петербург, Политехническая ул., 29

vladborisenko1995@gmail.com

СЕМЕНОВ Артем Семенович – *кандидат физико-математических наук, доцент Высшей школы механики и процессов управления, заведующий кафедрой сопротивления материалов Санкт-Петербургского политехнического университета Петра Великого, Санкт-Петербург, Российская Федерация.*

195251, Российская Федерация, г. Санкт-Петербург, Политехническая ул., 29

Semenov.Artem@googlemail.com

ВАЛЬМЕРСПЕРГЕР Томас – *доктор технических наук, профессор Технического университета Дрездена, г. Дрезден, Саксония, Германия.*

01062, Германия, г. Дрезден

servicecenter.studium@tu-dresden.de

DOI: 10.18721/JPM.14305
UDC 533.1; 621.791

THE CONDITION FOR APPLICATION OF THE CROCCO INTEGRAL IN THE MATHEMATICAL DESCRIPTION OF A LASER WELDING PLASMA PLUME

S.O. Dudoladov[1], **N.V. Larionov**[1,2]

[1] Peter the Great St. Petersburg Polytechnic University, St. Petersburg, Russian Federation;

[2] St. Petersburg State Marine Technical University, St. Petersburg, Russian Federation

Based on the theoretical approach developed in the article by G.A. Turichin et al. (High Temperature. 2006. Vol. 44. No. 5. Pp. 647–655), the characteristics of the plasma plume forming in the keyhole laser welding have been investigated. A condition corresponding to the existence of the Crocco integral was defined, making it possible to simplify the system of gas dynamics equations and obtain analytical solutions for a plasma plume in the form of a classical submerged jet. These solutions were analyzed for a wide range of metal vapor velocities and temperatures at the keyhole top. For some of the selected values, an agreement with the numerical calculations of other authors was found.

Keywords: gas dynamics equations, plasma plume, laser welding, shear layer, submerged jet

Citation: Dudoladov S.O., Larionov N.V., The condition for application of the Crocco integral in the mathematical description of a laser welding plasma plume, St. Petersburg Polytechnical State University Journal. Physics and Mathematics. 14 (3) (2021) 60–75. DOI: 10.18721/JPM.14305

УСЛОВИЕ ПРИМЕНЕНИЯ ИНТЕГРАЛА КРОККО ПРИ МАТЕМАТИЧЕСКОМ ОПИСАНИИ ПЛАЗМЕННОГО ФАКЕЛА ПРИ ЛАЗЕРНОЙ СВАРКЕ

С.О. Дудоладов[1], **Н.В. Ларионов**[1,2]

[1] Санкт-Петербургский политехнический университет Петра Великого, Санкт-Петербург, Российская Федерация;

[2] Санкт-Петербургский государственный морской технический университет, Санкт-Петербург, Российская Федерация

На основе теоретического подхода, разработанного в статье Туричина Г.А. и др. (ТВТ, 2006. Т. 44, № 5. С. 655–663), исследуются характеристики плазменного факела, образующегося при лазерной сварке с глубоким проплавлением. Находится условие, которое отвечает существованию интеграла Кракко и позволяет упростить систему газодинамических уравнений, дающую аналитические решения для плазменного факела в виде классической затопленной струи. Полученные решения анализируются для широкого интервала значений скорости и температуры паров металла на вылете из парогазового канала. Для некоторых выбранных значений найдено согласие с численными расчетами других авторов.

Ключевые слова: газодинамические уравнения, плазменный факел, лазерная сварка, слой смешения, затопленная струя

Ссылка при цитировании: Дудоладов С.О., Ларионов Н.В. Условие применения интеграла Кракко при математическом описании плазменного факела при лазерной сварке // Научно-технические ведомости СПбГПУ. Физико-математические науки. 2021. Т. 14. № 3. С. 60–75. DOI: 10.18721/JPM.14305

Introduction

The essence of keyhole laser welding is that a laser beam directed at a metal workpiece causes the welded metal to heat and evaporate with a vapor-gas channel (the so-called keyhole) forming. The interaction between the vapor pressure of the material, hydrostatic forces of the surrounding liquid metal and surface tension forces prevent the keyhole from closing [1]. A jet of metal vapors escapes from the keyhole (KH) into the shielding gas atmosphere, propels it and mixes with it, attenuating at a certain height due to viscosity. The interaction of the laser beam with the evaporated metal can lead to partial ionization of these vapors, generating plasma above the surface treated, i.e., a plasma plume and plasma inside the KH [2 – 4]. The plasma plume serves as a convenient medium for transferring energy from laser radiation to the workpiece. However, it also affects the welding process, due to absorption and scattering of laser radiation, as well as heating of the laser head.

The interactions between the plasma plume, laser beam and shielding gas paint a complex picture of gas flow and heat/mass transfer [5 – 7]. When the absorbed energy becomes comparable to the energy losses due to conduction, convection and radiation of the plasma plume, the plume becomes capable of maintaining a stationary shape with respect to the laser beam. The spatial distributions of the gas temperature and particle concentration in the plasma plume are always non-uniform. The presence of density gradients within the plasma plume leads to refraction and defocusing of the laser beam, reducing the power density of laser radiation and thus affecting the laser welding process.

Combustion of the plasma plume during welding can be accompanied by different complex processes depending on the specific type of material processing. For example, condensed-phase clusters can evolve in the plasma plume during hybrid laser-arc welding of metallic materials due to expansion and cooling of metal vapors, reducing the mean energy of electrons in the plasma and affecting the course of kinetic processes [8, 9].

As new methods need to be developed for controlling the processes occurring during keypoint laser welding in order to improve the quality of material processing and obtain welds with the required properties, studies into the distributions of temperature, density and concentration of particles in a plasma plume are of paramount importance.

Turichin et al. [5] considered the characteristics of a plasma plume appearing during welding in a helium-iron atmosphere using a solid-state neodymium-doped yttrium aluminum garnet laser (Nd:YAG). The absorption of laser radiation by the plume in this particular case is typically very insignificant. The authors then used a system of gas-dynamic equations to solve the problem on a jet of hot iron vapors ejected into an atmosphere of cold helium acting as the shielding gas [10 – 12]. The influence of insignificant volumetric heat release due to absorption of laser radiation by the plume was taken into account by introducing an appropriate source into the energy balance equation. The properties of the source were determined from the solution of the kinetic equation for the energy spectrum of plasma electrons [13].

Analytical solutions of the system of gas-dynamic equations corresponding to the problem of a laminar submerged jet [10] were obtained in [5] taking the approximation of an axially symmetric boundary layer and neglecting the heat source. Several assumptions were made to obtain these solutions, allowing, in particular, to introduce the Crocco integral, but the authors did not investigate the condition for its existence in detail.

In view of the above, one of the main goals of this study was to identify the domain where the values of the observed quantities can be described by analytical solutions obtained in [5]. An additional task was to analyze the characteristics of the plasma plume in a wide range of velocities and temperatures

of metal vapors ejected from the keyhole, comparing the results with the data of numerical calculations obtained by other authors [6, 7].

Theoretical description of a plasma plume

We consider the stationary case, i.e., neglect all the transient processes associated with the initial instants when the laser is switched on and the plume starts to form. Assuming that welding is performed by a Nd: YAG laser in a helium atmosphere, we will also neglect the heat source (similar to [5]), associated with the absorption of laser radiation by the plume.

Fig. 1 schematically shows the plasma plume, which is a metal vapor (MV) jet escaping from the keyhole (KH) into an atmosphere of shielding helium gas (HG). The vapors advance the shielding gas, mixing with it, and the jet attenuates at some distance from the surface due to viscosity. The axes of the Cartesian coordinate system are located so that the axis z is directed along the keyhole axis, which can be represented as a cylinder with a small depth Δz.

Let us denote the density of the mixture consisting of metal vapors with shielding gas as ρ, the mass fraction of metal atoms in the mixture as C. Then the densities of metal vapors ρ_V and shielding gas ρ_g are expressed as

$$\begin{cases} \rho = \rho_V + \rho_g, \\ \rho_V = C\rho,\ \rho_g = (1-C)\rho. \end{cases} \tag{1}$$

Some of the properties that mainly determine the properties of a stabilized plasma plume occur in the layer where metal vapors are mixed with shielding gas atoms. We consider the edge of the mixing layer, where the concentration of heavy metal atoms in the mixture is low, i.e., the region where the heavy gas diffuses in the light one. In this case, the properties of the plume can be described in the approximation of the boundary layer. We assume that the boundary layer is laminar (see the estimate of the Reynolds number below, in the description of the results).

Let us take two length scales: longitudinal $\sim z$ (along the direction in which metal vapors are ejected) and transverse $\sim r = \sqrt{x^2 + y^2}$ (across the keyhole axis). Similar to theory of the boundary layer, the transverse scale is assumed to be much smaller than the longitudinal one.

The complete system of gas dynamic equations for the given binary mixture, written in the approximation of an axially symmetric boundary layer, has the form [10, 11]:

$$\begin{cases} \rho\left\{v_r \dfrac{\partial v_z}{\partial r} + v_z \dfrac{\partial v_z}{\partial z}\right\} = \dfrac{1}{r}\dfrac{\partial}{\partial r}\left(r\mu \dfrac{\partial v_z}{\partial r}\right) - \dfrac{\partial p}{\partial z}, \\ \rho\left\{v_r \dfrac{\partial C}{\partial r} + v_z \dfrac{\partial C}{\partial z}\right\} = \dfrac{1}{r}\dfrac{\partial}{\partial r}\left(r\rho D_{gV} \dfrac{\partial C}{\partial r}\right), \\ \rho\left\{v_r \dfrac{\partial h}{\partial r} + v_z \dfrac{\partial h}{\partial z}\right\} = \dfrac{1}{r}\dfrac{\partial}{\partial r}\left(r\dfrac{\kappa}{C_p}\dfrac{\partial h}{\partial r}\right) + v_z \dfrac{\partial p}{\partial z} + \mu\left(\dfrac{\partial v_z}{\partial r}\right)^2 + q, \\ \dfrac{\partial}{\partial r}(r\rho v_r) + \dfrac{\partial}{\partial z}(r\rho v_z) = 0, \\ \dfrac{\partial p}{\partial r} = 0, \end{cases} \tag{2}$$

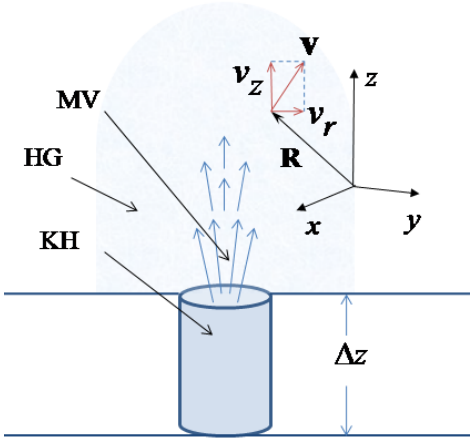

Fig. 1. Schematic of plasma plume and velocity field $\mathbf{v}(\mathbf{R})$, where $\mathbf{R} = (r, \varphi, z)$: metal vapors MV; shielding helium gas HG; keyhole KH, its depth Δz. A laser beam (not shown in the figure) falls along the normal to the surface of the metal workpiece

where v_r, v_z are the cylindrical components of the velocity field $\mathbf{v}$; μ is the dynamic viscosity; D_{gV} is the interdiffusion coefficient; κ is the thermal conductivity; C_p is the heat capacity of the mixture, $C_p = (1-C)\cdot C_{p_g} + C\cdot C_{p_V}$ (C_{p_g}, C_{p_V} are the specific heat capacities of helium and metal vapors); $h = C_p T$ is the enthalpy written in terms of temperature T; p is the pressure.

The source q (which we are going to neglect below) is the volumetric heat release related to the absorption of laser radiation energy by the mixture.

System of equations (2) is written in the cylindrical coordinate system (r, φ, z) with the axis z along the keyhole top (see Fig. 1). Assuming axial symmetry for the problem implies that the velocity field $\mathbf{v}$ is independent of the angle φ and that the rotational component v_φ of the velocity is equal to zero, i.e.,

$$\mathbf{v}(r,z) = \mathbf{e}_r v_r(r,z) + \mathbf{e}_z v_z(r,z).$$

The first equation in system (2) is obtained from the main dynamic equation (Navier – Stokes equations), the second and third are derived from the convective diffusion equation and the general energy balance equation, respectively. The fourth equation in system (2) is the continuity equation, and the fifth equation is the well-known condition of constant pressure across the boundary layer.

System (2) differs from a similar system of equations given in [5] by a quadratic term $\sim (\partial v_z/\partial r)^2$, characterizing the action of viscous forces in the equation for enthalpy. The authors of [5] assumed in advance that this term was small and omitted it. On the other hand, we preserved this term for the sake of generality; we are going to explain at the end of the section why it can be neglected. Below we make a natural assumption about the constant pressure [10], in the same manner as it was done in [5], i.e., we take $\partial p/\partial z = 0$ in system (2).

We use the Mendeleev – Clapeyron equation as an equation of state closing system (2):

$$p = \left(\frac{C}{M_V} + \frac{1-C}{M_g}\right)\rho RT, \tag{3}$$

where M_i is the molar mass for the i^{th} component of the mixture, R is the universal gas constant.

System (2), (3) can be solved by finding the transfer coefficients μ, D_{gV}, κ. These coefficients contain the free path lengths λ_g, λ_V (for helium and metal, respectively), which can be estimated as follows based on molecular kinetic theory [14, 15]:

$$\begin{cases} \lambda_g = \dfrac{1}{n_g \sigma_{gg}\sqrt{2} + n_V \sigma_{gV}\sqrt{1 + m_g/m_V}}, \\ \lambda_V = \dfrac{1}{n_V \sigma_{VV}\sqrt{2} + n_g \sigma_{Vg}\sqrt{1 + m_V/m_g}}, \end{cases} \tag{4}$$

where m_g, m_V are the masses of helium and metal atoms, respectively; n_g, n_V are the corresponding concentrations; σ_{gg}, σ_{gV}, σ_{Vg}, σ_{VV} are the effective cross sections of gas – gas, gas – metal, metal – gas and metal – metal interactions.

The mass of a helium atom is $m_g \approx 4$ amu; we took the mass of an iron atom $m_V \approx 56$ amu as the mass of the metal atom; concentrations $n_g = \rho_g/m_g$, $n_V = \rho_V/m_V$.

The effective cross sections are expressed as

$$\sigma_{gg} = 4\pi r_g^2, \sigma_{gV} = \pi\left(r_g + r_V\right)^2, \sigma_{VV} = 4\pi r_V^2,$$

where r_g, r_V are the effective radii of the atoms.

The Van der Waals radii were chosen as these radii [16, 17]: $r_g \approx 140$ pm, $r_V \approx 210$ pm.

Therefore,

$$\sigma_{gg} \approx 2.46\cdot 10^5 \text{ (pm)}^2,\ \sigma_{gV} \approx 3.85\cdot 10^5 \text{ (pm)}^2,\ \sigma_{VV} \approx 5.54\cdot 10^5 \text{ (pm)}^2 \tag{5}$$

and

$$\lambda_g \approx \gamma\lambda_V, \tag{6}$$

where the value of γ lies in the range from 2 to 4. The number 2 corresponds to the $C \to 1$ limit, and 4 corresponds to the $C \to 0$ or $C \to 0.5$ limit.

The expressions for the transfer coefficients have the following form [14, 15]:

$$\begin{cases} \nu = \dfrac{1}{3}\left[C\lambda_V\left\langle v_V\right\rangle + (1-C)\lambda_g\left\langle v_g\right\rangle\right], \\ D_{gV} = \dfrac{1}{3}\left[(1-C)\lambda_V\left\langle v_V\right\rangle + C\lambda_g\left\langle v_g\right\rangle\right], \\ \alpha = \dfrac{C_v}{3C_p}\left[C\lambda_V\left\langle v_V\right\rangle + (1-C)\lambda_g\left\langle v_g\right\rangle\right], \end{cases} \tag{7}$$

where $\nu = \mu/\rho$ is the kinematic viscosity; $\alpha = \kappa/(\rho C_p)$ is the thermal diffusivity coefficient; $\left\langle v_V\right\rangle, \left\langle v_g\right\rangle$ are the mean thermal velocities of iron and helium atoms, respectively.

The mass fraction C of iron atoms in the mixture should be less than 0.6 in the region of the mixing layer under consideration, with predominant diffusion of heavy gas in light one; this value corresponds to the approximate equality $n_g \approx 10\, n_V$. Let us consider a particular case $C \approx 0.5$. The reason why we have chosen it will become clear later on.

Then, taking into account relation (6), as well as the ratio of thermal velocities $\left\langle v_g\right\rangle \Big/ \left\langle v_V\right\rangle = \sqrt{m_V/m_g} \approx 4$, we can rewrite the expressions for the transfer coefficients as follows:

$$\begin{cases} \nu \approx \nu_\infty \dfrac{\rho_\infty}{\rho}\left(\dfrac{h}{h_\infty}\right)^{1/2}(1-C), \\ D_{gV} \approx \nu_\infty \dfrac{\rho_\infty}{\rho}\left(\dfrac{h}{h_\infty}\right)^{1/2} C,\ \alpha \approx \alpha_\infty \dfrac{\rho_\infty}{\rho}\left(\dfrac{h}{h_\infty}\right)^{1/2}(1-C), \end{cases} \tag{8}$$

where

$$\nu_\infty = \frac{4\left(kT_\infty\right)^{3/2}}{3p\sigma_{gg}\left(\pi m_g\right)^{1/2}},\ \alpha_\infty = \frac{3\nu_\infty}{5},\ h_\infty = C_pT_\infty;$$

T_∞, ρ_∞ are the temperature and density at infinity, i.e., the parameters of the shielding gas away from the plume; k is the Boltzmann constant.

Let us rewrite system (2) in view of the remarks made and the transfer coefficients (8) obtained:

$$\begin{cases} \left\{v_r\frac{\partial v_z}{\partial r}+v_z\frac{\partial v_z}{\partial z}\right\} = \nu_\infty\frac{\rho_\infty}{\rho}\frac{1}{r}\frac{\partial}{\partial r}\left(r\left(1-C\right)\left(\frac{h}{h_\infty}\right)^{1/2}\frac{\partial v_z}{\partial r}\right), \\ \left\{v_r\frac{\partial C}{\partial r}+v_z\frac{\partial C}{\partial z}\right\} = \nu_\infty\frac{\rho_\infty}{\rho}\frac{1}{r}\frac{\partial}{\partial r}\left(rC\left(\frac{h}{h_\infty}\right)^{1/2}\frac{\partial C}{\partial r}\right), \\ \left\{v_r\frac{\partial h}{\partial r}+v_z\frac{\partial h}{\partial z}\right\} = \alpha_\infty\frac{\rho_\infty}{\rho}\frac{1}{r}\frac{\partial}{\partial r}\left(r\left(1-C\right)\left(\frac{h}{h_\infty}\right)^{1/2}\frac{\partial h}{\partial r}\right)+ \\ +\nu_\infty\frac{\rho_\infty}{\rho}\left(1-C\right)\left(\frac{h}{h_\infty}\right)^{1/2}\left(\frac{\partial v_z}{\partial r}\right)^2, \\ \frac{\partial}{\partial r}\left(r\rho v_r\right)+\frac{\partial}{\partial z}\left(r\rho v_z\right)=0. \end{cases} \quad (9)$$

The first two equations are almost identical with respect to two different variables for values of C close to 0.5, and the boundary conditions of the solutions are similar up to a constant value: $C \to 0$, $v_z \to 0$ at $r \to \infty$, and C, v_z tend to some constant values depending on z at $r \to 0$.

Thus, the Crocco integral can be introduced for $C \approx 0.5$:

$$C = av_z + f$$

(a and f are constants), allowing to exclude the equation for C from system (9).

Notably, the refined condition for using the Crocco integral, $C \approx 0.5$, can be regarded as the main result of this section.

Because it was not discussed in [5] whether the Crocco integral could be used in system (2), it was impossible to find the domain where the analytical solutions obtained would give a more accurate result. For example, the value of ν differs from D_{gV} by about ten times for $C << 1$, making it impossible to introduce the Crocco integral that linearly relates the quantities C and v_z.

Let us solve the system of three equations with respect to the unknown fields v_r, v_z and h in the same way as it was done in [5]. Let us write down the main steps of the solution.

Step 1. Transition to Dorodnitsyn variables x, y [10]:

$$\begin{cases} ydy = \dfrac{\rho}{\rho_\infty} rdr, \\ x = z. \end{cases} \tag{10}$$

Step 2. Assumption of a weak dependence of the density ρ on its argument r, i.e., $\partial\rho/\partial r \approx 0$ [5]. The basis for this important assumption is that the escaping metal vapors are heavy but hot, while the surrounding helium gas is, on the contrary, light but cold.

Then,

$$y^2 = \frac{1}{\rho_\infty}\left(r^2\rho - \int_0^r r^2 \frac{\partial\rho}{\partial r} dr\right) \approx \frac{\rho}{\rho_\infty} r^2, \ \frac{\partial y}{\partial r} \approx \left(\frac{\rho}{\rho_\infty}\right)^{1/2}. \tag{11}$$

Step 3. Introducing new velocities U, $\tilde{V}$ dependent on x, y, and their stream function ψ:

$$\begin{cases} V = v_r, \ U = v_z, \\ \tilde{V} = \left(V\dfrac{\partial y}{\partial r} + U\dfrac{\partial y}{\partial z}\right); \end{cases} \begin{cases} U = \dfrac{1}{y}\dfrac{\partial\psi}{\partial y}, \\ \tilde{V} = -\dfrac{1}{y}\dfrac{\partial\psi}{\partial x}. \end{cases} \tag{12}$$

Step 4. Linearization of equations, corresponding to the following substitutions with respect to system (9):

$$(1-C)\left(\frac{h}{h_\infty}\right)^{1/2} \to \frac{1}{2}\left(\frac{h_0}{h_\infty}\right)^{1/2}, \ C\left(\frac{h}{h_\infty}\right)^{1/2} \to \frac{1}{2}\left(\frac{h_0}{h_\infty}\right)^{1/2}, \tag{13}$$

where h_0 is the characteristic value of the enthalpy in the given region.

Step 5. Introducing the self-similar variable $\xi = y\Big/\left(x\tilde{\nu}_\infty^{1/2}\right)$ and writing the stream function and enthalpy in terms of the new variables ξ, x:

$$\psi(\xi, x) = \tilde{\nu}_\infty x \cdot c(\xi), \ h = \frac{\tilde{\nu}_\infty}{x} d(\xi), \tag{14}$$

where

$$\tilde{\nu}_\infty = \frac{\nu_\infty}{2}\left(\frac{h_0}{h_\infty}\right)^{1/2}, \ \tilde{\alpha}_\infty = \frac{\alpha_\infty}{2}\left(\frac{h_0}{h_\infty}\right)^{1/2}.$$

Step 6. Transition to differential equations for functions $c(\xi)$, $d(\xi)$:

$$\begin{cases} \xi^2 c''' + \xi(c-1)c'' + \xi(c')^2 - (c-1)c' = 0, \\ \left(\tilde{\alpha}_\infty \xi \cdot d'' + (\tilde{\alpha}_\infty + \tilde{\nu}_\infty c)d' + \tilde{\nu}_\infty c' \cdot d\right)\xi^3 + \dfrac{1}{x}(\xi c'' - c')^2 = 0. \end{cases} \tag{15}$$

The solution of the first equation for the function $c(\xi)$ is known, corresponding to the solution for a laminar submerged jet of incompressible gas [10]. The second equation for the function $d(\xi)$ defines the enthalpy and contains a term proportional to $1/x$. Omitting this term assuming that it is small ($x = z$ is a large scale) is equivalent to omitting the term $\sim (\partial v_z/\partial r)^2$ in the original equations (9). Notice that the equation for $d(\xi)$ can be solved exactly and its solution is expressed in quadratures. Here, following [5], we do not take the influence of this term into account, considering it a correction of higher order $\sim 1/x^2$.

Let us write down the final solutions for the field of velocities, enthalpy, and the fraction of metal vapors in the mixture:

$$U = \frac{2b^2}{x}\cdot\frac{1}{\left(1+\frac{1}{4}b^2\xi^2\right)^2},\ \tilde{V} = \frac{\tilde{\nu}_\infty^{1/2}b}{x}\cdot\frac{b\xi\left(1-\frac{1}{4}b^2\xi^2\right)}{\left(1+\frac{1}{4}b^2\xi^2\right)^2},$$
$$h = \frac{\tilde{\nu}_\infty}{x}\frac{b_1}{\left(1+\frac{1}{4}b^2\xi^2\right)^{\frac{2\tilde{\nu}_\infty}{\tilde{\alpha}_\infty}}},\ C = aU. \qquad (16)$$

Here the constants a, b_1, b are found from the boundary conditions for the function $c(\xi)$ and from the conditions for preserving the corresponding total fluxes. The explicit expressions for these constants take the form

$$a = \frac{I_0}{J_0},\ b_1 = \frac{C_p H_0}{8\pi\tilde{\nu}_\infty^2}\left(1+2\frac{\nu_\infty}{\alpha_\infty}\right),\ b = \left(\frac{3J_0}{16\pi\tilde{\nu}_\infty\rho_\infty}\right)^{1/2}, \qquad (17)$$

where J_0, I_0, C_p, H_0 are the total fluxes (along the jet) of mixture momentum, metal vapor mass, and enthalpy, respectively.

We should emphasize that the described procedure for solving system (9) is borrowed from [5]; therefore, solutions (16) completely coincide in their structure with the solutions obtained in [5].

However, the slight difference is in the constants in $\tilde{\alpha}_\infty$, $\tilde{\nu}_\infty$ (14) (see Eq. (11) in [5]), which are half the size of the similar constants given in [5]. The reason for this difference is that we refined the condition for using the Crocco integral above.

To write the quantities U, $\tilde{V}$, h, C found in terms of the 'physical coordinates' r, z, we should first make a transition from the coordinates x, ξ to coordinates x, y, and then perform the inverse Dorodnitsyn transformation. The dependence of the variable y on ρ should be taken into account.

The solutions found are diverging at $z \to 0$, which is typical for the self-similar case. The origin along the jet axis was shifted deep into the keyhole by Δz in this example to eliminate the divergence.

Results and discussion

We analyze solutions (16) considering the following problem statement. The KH has a shape close to a straight cylinder with a small depth Δz of the order of several millimeters (see Fig. 1). The latter was estimated provided that $h(r = 0, z = \Delta z) = h_m$, where $h_m = C_p T_m$ is the maximum enthalpy corresponding to the temperature in the center of the keyhole top. The KH radius r_k corresponds to the radius of the laser spot on the surface of the workpiece and is approximately equal to $r_k \approx 1.5\cdot10^{-4}$ m for the given case [6]. The temperature of the side walls and the bottom is considered constant and equal to the boiling point T_b of the welded material, which is iron in our case. The maximum veloc-

ity of metal vapors U_m is reached in the center of the keyhole top, where, accordingly, the mixture temperature reaches its maximum T_m. Welding is performed in a shielding helium gas under normal conditions, i.e., at a temperature of 298 K and a pressure of 101.325 kPa.

A pair of boundary values (T_m, U_m) was set using the calculated data from [6], presenting numerical studies of keyhole laser welding of an iron workpiece. Let us give the values for these pairs of quantities used below:

13800 K, 360 m/s; 14100 K, 690 m/s;

14400 K, 920 m/s; 14500 K, 1120 m/s.

The quantities H_0, I_0, J_0 included in solutions (16) were estimated from the above values of temperature, velocity, pressure, and radius of the keyhole.

The table lists the boundary values of various characteristics of the iron-helium mixture used in the calculations.

Table

Boundary values for characteristics of iron-helium mixture

T_b	3200 K
T_∞	298 K
C_{pV} at T_b	480.8 J/(kg·K)
C_{pg} at T_∞	5193 J/(kg·K)
μ_∞ at T_∞	$1.99 \cdot 10^{-5}$ Pa·s
κ_∞ at T_∞	0.157 W/(m·K)
ρ_∞ at T_∞	0.164 kg/m^3

Setting explicit values for temperature, velocity and pressure, we can now estimate the Reynolds number Re for our problem. Let us choose U_m as the characteristic velocity, and estimate the characteristic linear dimensions by the KH diameter $2r_k$. We calculate the dynamic viscosity of metal vapors using the Enskog equation [15]:

$$\mu_V = 1{,}016 \frac{5}{16\left(2r_V\right)^2}\left(\frac{m_V k T_m}{\pi}\right)^{1/2},$$

then, taking into account the equation of state, we find the kinematic viscosity $\nu_V = \mu_V / \rho_V \approx$ $\approx 3 \cdot 10^{-3}$ m^2/s. Therefore,

$$\mathrm{Re} = \frac{2r_k U_m}{\nu_V} \approx 20.$$

The obtained Reynolds number is less than the typical value at which a steady laminar jet loses its stability [18, 19].

Let us now move on to the results. Fig. 2 shows the radial dependences of the temperature and mass fraction of iron atoms in the mixture at a distance of 5 mm from the surface of the workpiece,

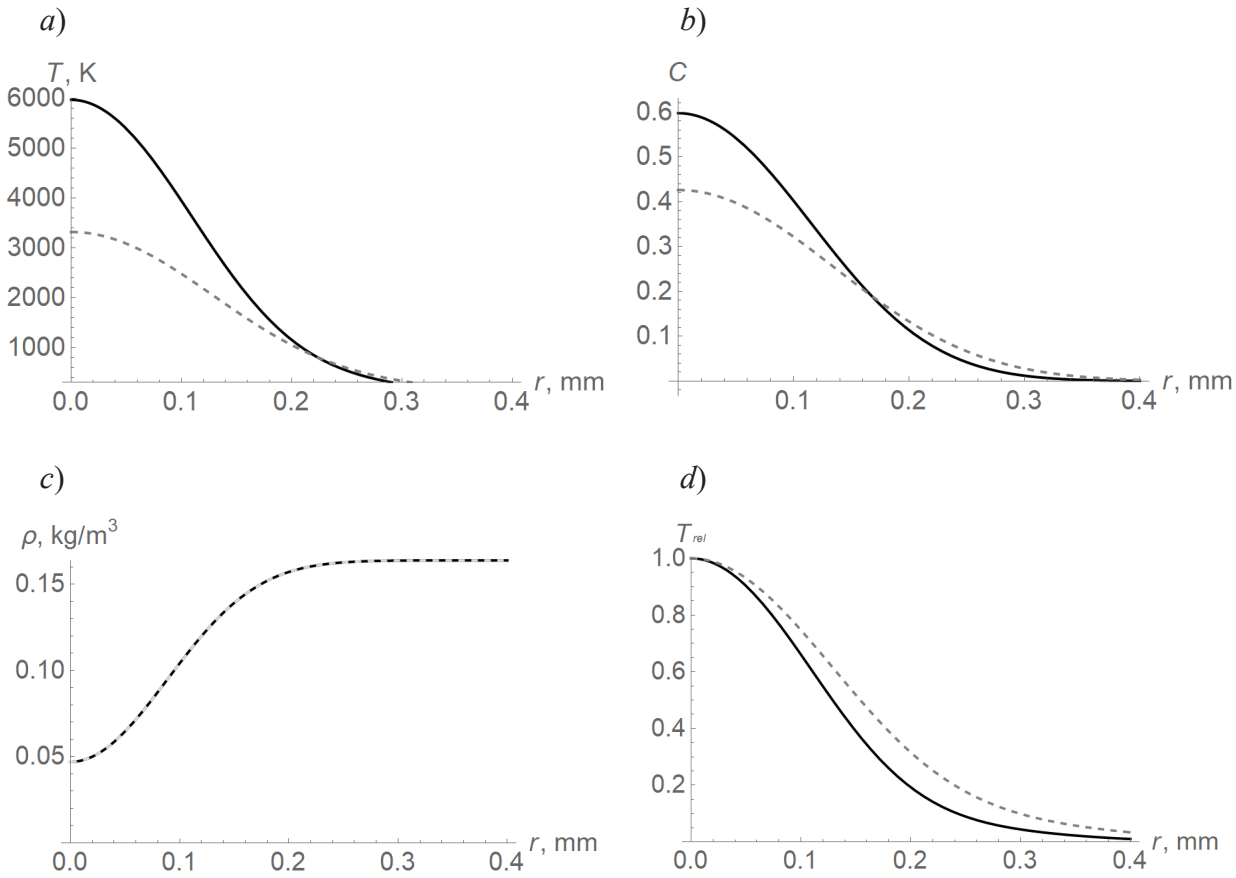

Fig. 2. Radial distributions for jet temperature (*a*) and mass fraction of iron atoms in the jet (*b*) at a distance of 5 mm from the workpiece surface; radial distributions of mixture density at KH top (*c*) and radial distributions normalized to the maximum temperature T_{rel} (*d*).
Fig. 2,*d* corresponds to Fig. 2,*a* but each curve is normalized to its maximum.
The values shown are α_∞, ν_∞ (solid lines) and $2\alpha_\infty$, $2\nu_\infty$ (dashed lines), see Table

as well as the density of the mixture at the KH top. The dependences are constructed by Eqs. (16). The maximum velocity and the corresponding temperature at the KH top are equal to 1120 m/s and 14500 K, respectively.

Analyzing the graphs in Fig. 2, we can conclude that the transfer processes decide the final width of the submerged jet. The characteristic radius of jet attenuation can be estimated by equating the temperature of the mixture to the temperature of the shielding gas; it turns out that this radius is approximately equal to 0.3 – 0.4 mm.

The dashed lines in Fig. 2 correspond to the curves obtained following [5], i.e., the quantities α_∞, ν_∞ included in Eqs. (16) turn out to be doubled. As expected in this case, the absolute value of the temperature decreases due to the viscosity preventing the jet from propagating, while the width increases due to thermal conductivity (see Fig. 2,*d*). The maximum temperature is approximately halved. A similar dependence is observed for the quantity C, however, the maximum value decreases by only 1.5 times, which is associated with the upward motion of cooled iron atoms.

The submerged jet of iron vapor in the shielding helium gas attenuates at a certain distance from the treated surface. The attenuation height depends on many factors, including the velocity at which the vapor is ejected from the keyhole.

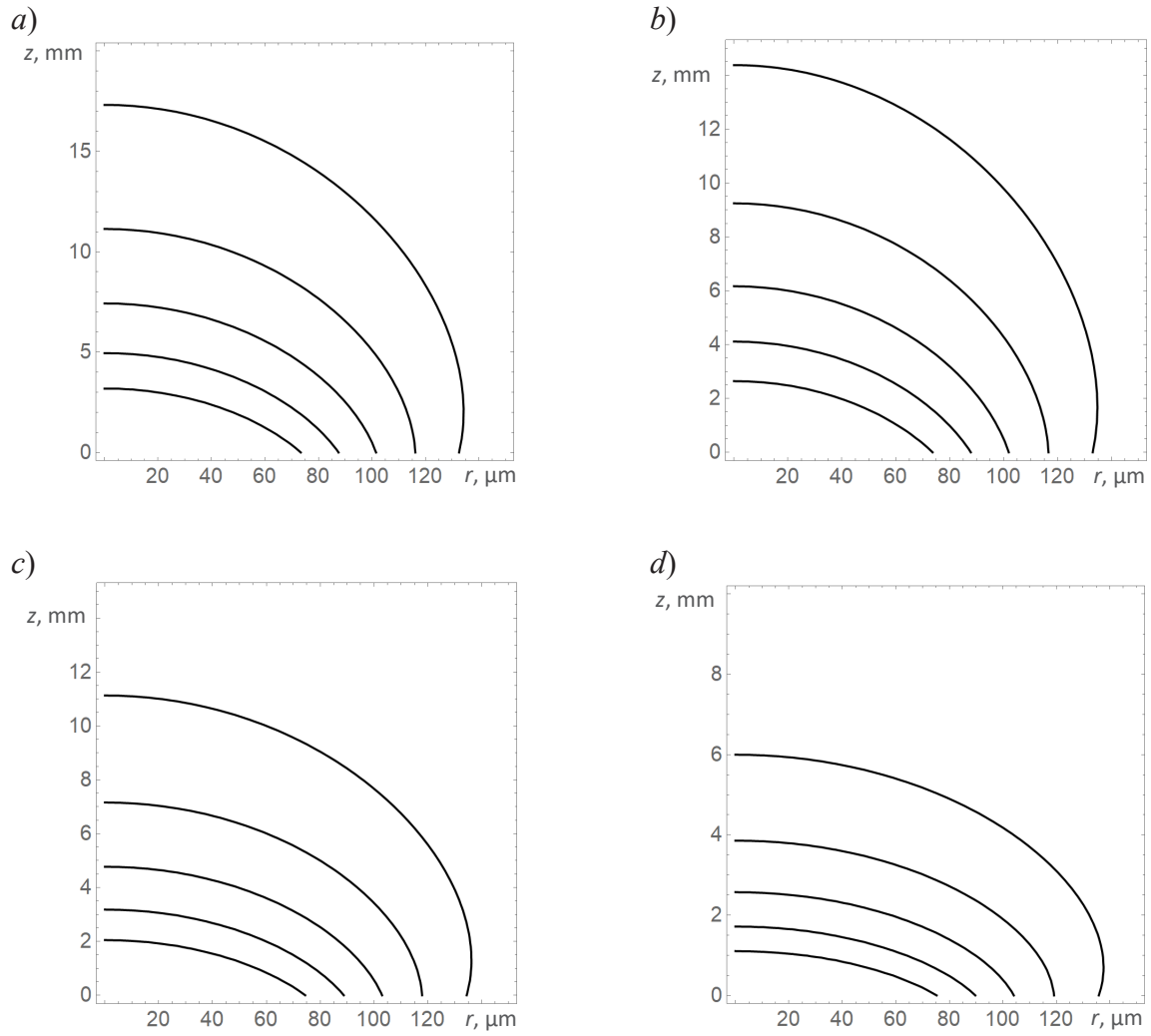

Fig. 3. Family of isolines $C(r, z) = C_0$ for different pairs of parameter values (T_m, K and U_m, m/s): 14500 and 1120 (*a*), 14400 and 920 (*b*), 14100 and 690 (*c*), 13800 and 360 (*d*); the values taken are $C_0 = 0.3$; 0.4; 0.5; 0.6 and 0.7

We use Eqs. (16) to analyze the behavior of the plasma plume with varying boundary values of maximum velocity U_m and temperature T_m.

Fig. 3 shows a family of isolines for the same mass fractions of iron atoms in the mixture for different pairs (T_m, K and U_m, m/s):

$$C(r, z) = C_0 \ (C_0 = 0.3 - 0.7 \text{ with a step } 0.1).$$

The graphs show an approximately linear relationship between the maximum velocity U_m and the penetration depth of iron atoms into the shielding gas. For example, the isoline point with $C_0 = 0.5$ at $r = 0$ for $U_m = 1120$ m/s is located at a height of $z \approx 7.5$ mm, and the height of the same point decreases by three times for a velocity three times less ($U_m = 360$ m/s): $z \approx 2.5$. This linear dependence is an obvious consequence from introducing the Crocco integral in our problem. A similar picture is observed for the isotherms of the gas mixture $T(r, z) = T_0$, K: $T_0 = (1 - 14)\cdot 10^3$ K at a step of 10^3 K (see Fig. 4).

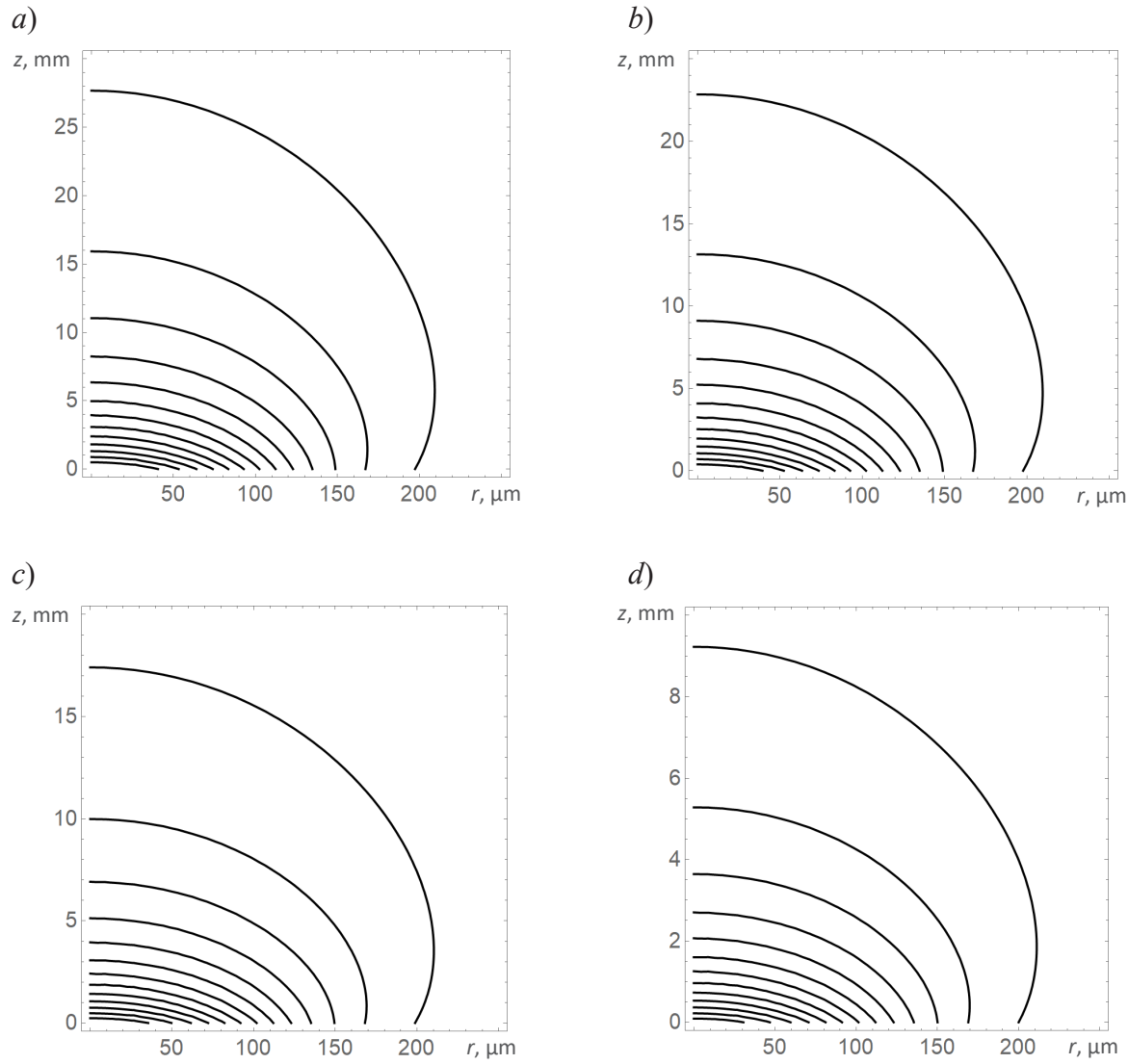

Fig. 4. Family of gas mixture isotherms $T(r, z) = T_0$
for the same pairs of parameter values (T_m, K and U_m, m/s) as in Fig. 3.
The values taken are T_0, K: 1000, 2000, 3000, etc.

The results we obtained were compared with the numerical data from [6]. considering the process of laser keyhole welding of an iron workpiece in shielding argon gas. A system of gas-dynamic equations was solved taking into account the heat source associated with absorption of laser radiation. Although a slightly different model is considered in [6], some patterns obtained in it are described by solutions (16): the penetration depth of iron atoms into the shielding gas along the direction in which iron vapor is ejected is linearly related to the maximum velocity U_m (of course, with the corresponding temperature T_m); a similar linear dependence was observed for the temperature of the gas mixture.

Conclusion

We used the analytical solutions of the system of gas-dynamic equations written in the boundary-layer approximation to analyze the characteristics of a plasma plume generated under keyhole welding of an iron workpiece with a neodymium-doped (Nd:YAG) laser in shielding helium gas.

Analysis of the transfer coefficients included in the system of gas-dynamic equations made it possible to find the condition for using the Crocco integral. This condition corresponds to the mass fractions C of metal vapors in the mixture close to 0.5. The kinematic viscosity for such values becomes practically equal to the diffusion coefficient, and the equation for the velocity field v_z is written in the same form as the diffusion equation (see system (9)), allowing to introduce the Crocco integral and consequently solve a system with a smaller number of equations. The solutions (16) obtained in this case for the field of velocities, enthalpy and mass fraction of metal vapors in the mixture completely coincide in their structure with the solutions obtained in [5]. There is, however, a slight difference in that the transfer coefficients for the shielding gas are redefined. For example, it is necessary to substitute α_∞, $\nu_\infty \to 2\alpha_\infty$, $2\nu_\infty$ in the final solutions (16) to make a transition from solutions (16) presented here to the corresponding solutions in [5], producing in particular noticeable changes in the radial dependences of the mixture temperature and mass fraction of metal vapors in the mixture. The reason why this difference between the solutions appears is that the Crocco integral was introduced in [5] without rigorous analysis of the conditions under which it can be used.

The dependences of the mass fraction of iron atoms in the gas mixture and the mixture temperature have been considered for various boundary values of velocity and temperature of the vapors at the keyhole top. We have found a linear relationship (natural, due to the Crocco integral introduced) between the maximum velocity of iron vapor ejected from the keyhole and the penetration depth of iron atoms into the shielding gas (a similar dependence was found for the mixture temperature). The same linear relationship between these quantities was observed in [6], where the system of gas-dynamic equations was solved numerically for a similar problem.

To conclude, we should note that the estimate of the Reynolds number in our problem yielded $\mathrm{Re} \approx 20$, which is less than the typical value at which a laminar stationary jet becomes unstable [18, 19]. The Reynolds number grows larger for higher velocities of metal vapors U_m, and the assumption that the jet in the mixture is laminar and steady may become inapplicable. In this case, the problem will have to be solved relying on the theory of a turbulent boundary layer [20].

REFERENCES

1. **Grigoryants A.G., Shiganov I.N., Misyurov A.I.,** Tekhnologicheskiye protsessy lazernoy obrabotki [Laser treatment technologies], Bauman University Publishing, Moscow, 2006 (in Russian).

2. **Gong J., Peng G., Li L., et al.,** Effect of plasma plume produced by vacuum laser welding on energy transmission, Opt. Laser Technol. 136 (April) (2021) 106744.

3. **Luo Y., Tang X., Lu F., et al.,** Effect of subatmospheric pressure on plasma plume in fiber laser welding, J. Mater. Process. Technol. 215 (January) (2015) 219–224.

4. **Xu W., Chen A., Wang Q., et al.,** Characteristics of laser-induced aluminum plasma plumes after increasing sample temperature and spatial confinement, J. Anal. At. Spectrom. 34 (11) (2019) 2288–2294.

5. **Turichin G.A., Grigor'ev A.M., Zemlyakov E.V., et al.,** Special features of formation of plasma torch under conditions of hybrid laser-arc welding, High Temperature. 44 (5) (2006) 647–655.

6. **Chen X., Wang H.-X.,** Prediction of the laser-induced plasma characteristics in laser welding: a new modelling approach including a simplified keyhole model, J. Phys. D: Appl. Phys. 36 (13) (2003) 1634–1643.

7. **Wang H.-X., Chen X.,** Three-dimensional modelling of the laser-induced plasma plume characteristics in laser welding, J. Phys. D: Appl. Phys. 36 (6) (2003) 628–639.

8. **Turichin G.A., Zemlyakov E.V.,** Kinetika formirovaniya nanoklasterov kondensirovannoy fazy v plazmennom fakele pri gibridnom lazerno-dugovom vozdeystvii na metallicheskiye materialy [Generation kinetics of condensed-phase nanoclusters in the plasma torch under hybrid laser-arc impact on metal

materials], Proceedings of the 6-th International Conference "Beam Technologies and Laser Application", Edited by Prof. G. Turichin. Polytechnical University Publishing, St. Petersburg (2009) 146–148 (in Russian).

9. **Turichin G., Zemlyakov E., Pozdeyeva E., Norman E.,** Volume condensation in the plasma torch at laser-arc materials impact, Photonics Russia. (1) (2009) 12–15 (in Russian).

10. **Loitsyanskii L.G.,** Boundary layer, National Advisory Committee for Aeronautics, Washington, 1956.

11. **Loitsyanskii L.G.,** Mechanics of liquids and gases (International Series of Monographs in Aeronautics and Astronautics, Vol. 6, Pergamon Press, Oxford, London, Edinburg, New York, 1966.

12. **Landau L.D., Lifshits E.M.,** Fluid mechanics, Course of theoretical physics, Vol. 6, Pergamon Press, Oxford, New York, 2013.

13. **Dilthey U., Goumeniouk A., Lopota V., Turichin G.,** Kinetic description of keyhole plasma in laser welding, J. Phys. D: Appl. Phys. 33 (21) (2000) 2747–2753.

14. **Kikoin A., Kikoin I.,** Molecular physics, Translated by G. Leib, Central Books Ltd, Dadenham, Great Britain,1979.

15. **Golubev I.F.,** Viscosity of gases and gas mixtures, A handbook, National Science Foundation, Washington, 1970.

16. **Batsanov S.S.,** Van der Waals radii of elements, Inorg. Mater. 37 (9) (2000) 871–885.

17. CRC handbook of chemistry and physics, By Lide D.R. (Editor), 90th ed., American Chemical Society, USA, 2009–2010.

18. **Sinha A., Bharadwaj K.K., Das D.,** Instability of a low Reynolds number round jet, Proc. 39-th Nation. Conf. on Fluid Mech. & Fluid Power, 2012, December 13–15, SVNIT Surat. Gujarat, India (2012) FMFP2012-160.

19. **Dmitrenko A.V.,** Determination of critical Reynolds number in the jet based on the theory of stochastic equations and equivalence of measures, J. Phys. Conf. Ser. 1705 (2020) 012015.

20. **Abramovich G.N.,** Applied gas dynamics, 2-nd edition, Project-Nerd Publishing, USA, 1973.

Received 20.06.2021, accepted 26.07.2021.

THE AUTHORS

DUDOLADOV Savelii O.
Peter the Great St. Petersburg Polytechnic University
29 Politechnicheskaya St., St. Petersburg, 195251, Russian Federation
sava2312@yandex.ru

LARIONOV Nikolay V.
Peter the Great St. Petersburg Polytechnic University
29 Politechnicheskaya St., St. Petersburg, 195251, Russian Federation
St. Petersburg State Marine Technical University
3 Lotsmanskaya St., St. Petersburg, 190121, Russian Federation
larionov.nickolay@gmail.com

СПИСОК ЛИТЕРАТУРЫ

1. **Григорьянц А.Г., Шиганов И.Н., Мисюров А.И.** Технологические процессы лазерной обработки. М.: Изд-во МГТУ им. Н.Э. Баумана, 2006. 664 с.

2. **Gong J., Peng G., Li L., Xia H., Meng Sh., Wang J.** Effect of plasma plume produced by vacuum laser welding on energy transmission // Optics & Laser Technology. 2021. Vol. 136. April. P. 106744.

3. **Luo Y., Tang X., Lu F., Chen Q., Cui H.** Effect of subatmospheric pressure on plasma plume in fiber laser welding // Journal of Materials Processing Technology. 2015. Vol. 215. January. Pp. 219–224.

4. **Xu W., Chen A., Wang Q., Zhang D., Li S., Jiang Y., Gao X., Jin M.** Characteristics of laser-induced aluminum plasma plumes after increasing sample temperature and spatial confinement // Journal of Analytical Atomic Spectrometry. 2019. Vol. 34. No. 11. Pp. 2288–2294.

5. **Туричин Г.А., Григорьев А.М., Земляков Е.В., Валдайцева Е.А., Дилтей У., Гуменюк А.** Особенности формирования плазменного факела при гибридной лазерно-дуговой сварке // Теплофизика высоких температур. 2006. Т. 44. № 5. С. 655–663.

6. **Chen X., Wang H.-X.** Prediction of the laser-induced plasma characteristics in laser welding: a new modelling approach including a simplified keyhole model // Journal of Physics D: Applied Physics. 2003. Vol. 36. No. 13. Pp. 1634–1643.

7. **Wang H.-X., Chen X.** Three-dimensional modelling of the laser-induced plasma plume characteristics in laser welding // Journal of Physics D: Applied Physics. 2003. Vol. 36. No. 6. Pp. 628–639.

8. **Туричин Г.А., Земляков Е.В.** Кинетика формирования нанокластеров конденсированной фазы в плазменном факеле при гибридном лазерно-дуговом воздействии на металлические материалы // «Лучевые технологии и применение лазеров». Материалы 6-й Международной конференции. Под ред. проф. Г.А. Туричина. СПб.: Изд-во СПбГПУ, 2009. С. 146–148.

9. **Туричин Г., Земляков Е., Поздеева Е., Норман Е.** Объемная конденсация в плазменном факеле при лазерно-дуговом воздействии на материалы // Фотоника. 2009. № 1. С. 12–15.

10. **Лойцянский Л.Г.** Ламинарный пограничный слой. М.: Физматлит, 1962. 480 с.

11. **Лойцянский Л.Г.** Механика жидкости и газа. 7-е изд., испр. М.: Дрофа, 2003. 840 с.

12. **Ландау Л.Д., Лифшиц Е.М.** Гидродинамика. Изд. 5-е. (Теоретическая физика. Т. VI). М.: Физматлит, 2001. 736 с.

13. **Dilthey U., Goumeniouk A., Lopota V., Turichin G.** Kinetic description of keyhole plasma in laser welding // Journal of Physics D: Applied Physics. 2000. Vol. 33. No. 21. Pp. 2747–2753.

14. **Кикоин А.К., Кикоин И.К.** Молекулярная физика. Изд. 2-е, перераб. М.: Наука, 1976. 480 с.

15. **Голубев И.Ф.** Вязкость газов и газовых смесей. М.: Физматгиз, 1959. 376 с.

16. **Batsanov S.S.** Van der Waals radii of elements // Inorganic Materials. 2001. Vol. 37. No. 9. Pp. 871–885.

17. CRC handbook of chemistry and physics. Lide D.R. (Editor). 90th ed. USA: American Chemical Society, 2009–2010. 2804 p.

18. **Sinha A., Bharadwaj K.K., Das D.** Instability of a low Reynolds number round jet // Proceedings of the 39-th National Conference on Fluid Mechanics and Fluid Power. 2012. December 13–15. SVNIT Surat. Gujarat, India. FMFP2012-160.

19. **Dmitrenko A.V.** Determination of critical Reynolds number in the jet based on the theory of stochastic equations and equivalence of measures // Journal of Physics: Conference Series. 2020. Vol. 1705. P. 012015.

20. **Абрамович Г.Н.** Прикладная газовая динамика. Изд. 5-е. М.: Наука. Гл. ред. физ.-мат. литры, 1991. 600 с.

Статья поступила в редакцию 20.06.2021, принята к публикации 26.07.2021.

СВЕДЕНИЯ ОБ АВТОРАХ

ДУДОЛАДОВ Савелий Олегович – *студент бакалавриата Института металлургии, машиностроения и транспорта Санкт-Петербургского политехнического университета Петра Великого, Санкт-Петербург, Российская Федерация.*

195251, Российская Федерация, г. Санкт-Петербург, Политехническая ул., 29

sava2312@yandex.ru

ЛАРИОНОВ Николай Владимирович – *кандидат физико-математических наук, доцент Высшей школы прикладной физики и космических технологий Санкт-Петербургского политехнического университета Петра Великого; старший научный сотрудник Санкт-Петербургского государственного морского технического университета, Санкт-Петербург, Российская Федерация.*

195251, Российская Федерация, г. Санкт-Петербург, Политехническая ул., 29

larionov.nickolay@gmail.com

DOI: 10.18721/JPM.14306
UDC 538.913

A COMPARISON OF POTENTIAL FUNCTIONS FOR MOLECULAR DYNAMIC SIMULATION OF METHANE SORPTION IN THE SILICALITE

D.S. Kutsova, E.V. Bogatikov, A.N. Shebanov, E.N. Bormontov

Voronezh State University,
Voronezh, Russian Federation

In order to make the best choice, two types of a force field have been studied to access a possibility of application of one of them to simulation of adsorption and transport processes in the silicalite (synthetic zeolite)-methane system. To accomplish this, the molecular dynamic technique implemented in the LAMMPS package was used. Priority criteria of the choice were retention of the structure completeness during long simulation runs, the system's stability, the possibility of simulation of a separate good-sized zeolite cluster without using periodic boundary conditions for multiplying zeolite's lattice in space. For the force-field, which met these requirements, some structural, thermodynamic and transport characteristics of the system were calculated. Radial and angular distribution functions for different atom pairs and triplets were obtained for both the pure zeolite and the silicalite-methane system. A good agreement of all obtained characteristics with literature data of numerical and natural experiments was achieved.

Keywords: silicalite, ZSM-5 zeolite, methane, molecular dynamic, sorption, potential function

Citation: Kutsova D.S., Bogatikov E.V., Shebanov A.N., Bormontov E.N., A comparison of potential functions for molecular dynamic simulation of methane sorption in the silicalite, St. Petersburg Polytechnical State University Journal. Physics and Mathematics. 14 (3) (2021) 76–89. DOI: 10.18721/JPM.14306

СРАВНЕНИЕ ПОТЕНЦИАЛЬНЫХ ФУНКЦИЙ ДЛЯ МОЛЕКУЛЯРНО-ДИНАМИЧЕСКОГО МОДЕЛИРОВАНИЯ СОРБЦИИ МЕТАНА В СИЛИКАЛИТЕ

Д.С. Куцова, Е.В. Богатиков, А.Н. Шебанов, Е.Н. Бормонтов

Воронежский государственный университет,
г. Воронеж, Российская Федерация

С целью оптимального выбора, в работе исследованы два вида силового поля для оценки возможности их применения к моделированию процессов поглощения и переноса в системе силикалит (синтетический цеолит) – метан; для этого использован метод молекулярной динамики, реализованный в пакете LAMMPS. Приоритетными критериями выбора были сохранение целостности структур при длительных расчетах, стабильность системы, возможность моделирования отдельного кластера цеолита большого размера без использования периодических граничных условий для размножения решетки в пространстве. Для потенциала, удовлетворившего этим требованиям, проведен расчет структурных, термодинамических и транспортных характеристик системы. Рассчитаны радиальная и угловая функции распределения частиц для различных пар и троек атомов для чистого цеолита и для двухкомпонетной системы силикалит – метан. Достигнуто хорошее согласие всех полученных характеристик с литературными данными численных и натурных экспериментов.

Ключевые слова: силикалит, цеолит ZSM-5, метан, молекулярная динамика, сорбция, потенциальная функция

Ссылка при цитировании: Куцова Д.С., Богатиков Е.В., Шебанов А.Н., Бормонтов Е.Н. Сравнение потенциальных функций для молекулярно-динамического моделирования сорбции метана в силикалите // Научно-технические ведомости СПбГПУ. Физико-математические науки. 2021. Т. 14. № 3. С. 76–89. DOI: 10.18721/JPM.14306

Introduction

Zeolite materials are sorbents widely used in the oil, construction, and chemical industries, medicine and agriculture. These aluminosilicates are capable of absorbing various substances due to their specific composition and framework structure. Synthetic substances are of particular interest, because samples with clearly reproducible characteristics can be obtained during their production.

Silicalite is a synthetic zeolite with a ZSM-5 type structure, is capable of absorbing small diameter molecules [1], including hydrocarbons [2]. This feature makes it possible to use silicalite as a material for the gas-sensitive layer in methane sensors [3].

The mechanisms behind absorption, emission and transport of sorbed molecules should be understood to fabricate such devices. Studies of these processes at the microscopic level are especially informative, allowing to study the mechanisms of interparticle interaction and construct mathematical models of similar phenomena based on these mechanisms. Because zeolite structures have a complex geometry, computer simulation has been increasingly used instead of classical theoretical methods [4]. The molecular dynamics (MD) method has proven advantageous for modeling a variety of physical processes; in particular, it can be used to successfully study the behavior of the silicalite – methane system under different conditions [5 – 10].

The main component of the model in the MD method is the function of potential interaction of particles. The specific representation of the potential is chosen depending on a range of phenomena that are supposed to be reproduced in the simulation.

The goal of this study is to find the form of this function that is best suited for analysis of sorption/desorption processes in the silicalite – methane system.

Two force field models were chosen for solving this problem. The criteria selected as the most important were that the structures could preserve integrity during long computations, the system could remain stable, and it would be possible to simulate an individual zeolite cluster consisting of a large number of unit cells, without using periodic boundary conditions for lattice multiplication in space. An additional condition imposed was for the specific force field to reproduce a number of main characteristics of the system and give good agreement with experimental data [11, 12].

The main parameters estimated for the system considered in the study were its structural, thermodynamic and transport characteristics.

Parameters of the system

The silicalite – methane system was considered in the study. Two type of zeolite channels are present: sinusoidal and straight; they are located along the [100] and [010] crystallographic directions, respectively. The channels are formed by 10-membered rings, whose diameters are 5.1 × 5.5 Å for sinusoidal types and 5.3 × 5.6 Å for straight types. The channels mutually intersect, allowing for three-dimensional diffusion in the inner space of the silicalite despite the absence of channels along the [001] direction. The maximum diameter of the spheres along which diffusion can occur is 4.70 Å along the [100] crystallographic direction, 4.46 Å along the [010] and [001] directions. The critical diameter for methane molecules is 3.8 Å, making it possible for them to move in all crystallographic directions inside the zeolite interior.

We considered different properties of the system for lattices of different sizes whose parameters are given in Table 1.

Table 1

Structural parameters and composition of ZSM-5 zeolite with different crystal lattice sizes

Zeolite size along the crystal axes, unit cells	Zeolite size along the axis, Å			Number of atoms		
	a	*b*	*c*	Total	Si	O
1 × 1 × 1	20.09	19.738	26.284	288	96	192
1 × 1 × 2	20.09	19.738	26.284	576	192	384
2 × 2 × 2	40.18	39.476	65.709	2304	768	1536
5 × 5 × 5	100.45	98.689	26.284	36000	12000	24000

Parameters of computational experiments

The experiments in this study were carried out by means of molecular dynamics (MD) computations. The computations were performed in the free LAMMPS package (Large-scale Atomic/Molecular Massively Parallel Simulator) [13]. Periodic boundary conditions were imposed in all experiments; the potential cutoff radius r_s was 12.5 Å. Either microcanonical (NVE) or canonical (NVT) modeling ensembles were used depending on the problem (N is the amount of substance, V is the volume, E is the energy, T is the temperature). The average temperature of the system corresponded to 298 K. The simulation step was dt = 1 fs, the number of steps was from 1 to 2 million. The initial velocities followed a normal distribution for an average temperature of 298 K. Before the main computations were started, the energy minimization procedure was performed using the conjugate gradient method. After the desired accuracy was reached for energy, the system was equilibrated for 100 ps (10^5 simulation steps) in the NVE ensemble using the Langevin thermostat to allow the system to achieve the temperature T = 298 K.

Problems of force field model

The processes of absorption and transfer of molecules inside the sorbent substance are often well described by the potential represented as additive functions of the interparticle distance:

$$U(r) = U_{inter}(r) + U_{intra}(r), \tag{1}$$

where $U_{inter}(r)$ and $U_{intra}(r)$ describe inter- and intramolecular interactions, respectively.

Because the methane molecule is nonpolar and there are no cations in the silicalite lattice, the silicalite molecule is generally electrically neutral; therefore, the intermolecular interaction of unbound particles can be described by the Lennard – Jones potential for the interaction of unbound particles without using the Coulomb potential.

We used the Lennard – Jones (12-6) potential:

$$U_{inter}(r) = \sum 4\varepsilon_{ij}\left[\left(\frac{\sigma_{ij}}{r_{ij}}\right)^{12} - \left(\frac{\sigma_{ij}}{r_{ij}}\right)^{6}\right], \tag{2}$$

where r_{ij}, Å, is the distance between the atoms i and j; ε_{ij}, kcal/mol, is the characteristic interaction energy of the ith and jth atoms; σ_{ij}, Å, is the characteristic length of such interaction.

Intramolecular interaction is often described by an additive potential consisting of two-, three-, and four-particle terms:

$$U_{intra}(r) = U_{stratch}(r) + U_{bend}(r) + U_{tor}(\varphi), \tag{3}$$

$$U_{stretch}(r) = \sum k_r \left(r_{ij} - r_0\right)^2, \tag{4}$$

$$U_{bend}(\theta) = \sum k_\vartheta \left(\theta_{ijk} - \theta_0\right)^2, \tag{5}$$

$$U_{tor}(\varphi) = \sum k_\varphi \left[1 + d\cos\left(n\varphi_{ijkl}\right)\right]. \tag{6}$$

The potentials $U_{ŝtretch}(r)$ and $U_{bend}(\theta)$ are harmonic. They describe the deviation of the bond length r between a pair of atoms relative to the equilibrium value r_0 and the angle θ formed by three atoms from its equilibrium value θ_0. The term $U_{tor}(\varphi)$ is the torsion potential, which is periodic and simulates the change in the dihedral angle φ formed by four atoms of the same molecular structure. Potential parameters k_r, k_θ, k_φ are the stiffness constants of linear, angular and dihedral bonds, respectively; $d = \pm 1$ (depends on the specific implementation of the potential); n is the symmetry coefficient, represented by an integer.

The first model of the force field is represented by Eqs.(1) – (6) with the coefficients given in Table 2. A factor of 1/2 is already included in the stiffness constants. The coefficients ε and σ for atoms of different types were found by the formulas of the geometric and arithmetic mean, respectively (the Lorentz – Berthelot combining rule).

Most studies generally consider zeolite samples consisting of 2 – 8 unit cells [6 – 8]; the authors impose periodic boundary conditions, where the boundaries of the simulation box coincide with the boundaries of the lattice, to provide an infinite extension of the zeolite framework in space.

We considered a system of the following composition and configuration to reproduce the processes of sorption on zeolite from a state of complete freedom from sorbate molecules to maximum occupancy at a given temperature, as well as further desorption to minimum possible occupancy. A ZSM-5 type zeolite was represented by a lattice of 5 × 5 × 5 unit cells, surrounded by 10,000 methane molecules at the initial instant. The total number of particles in such a system is two orders of magnitude greater than the number typically considered.

The first force-field model was used for this system. Experimental computations of the interaction of particles revealed unstable behavior of the zeolite framework, where an excessively large vibrational amplitude of lattice atoms led to its subsequent decay. This behavior was detected over long simulation times of 2 million steps (for an NVT ensemble).

The second potential consists of terms (1) – (5). Its parameters coincide with the values given in Table 2, with the exception of the constants describing the binding potentials of zeolite. The following values were used for them [16]:

k_r (Si – O) = 298.53 kcal/(mol·Å^2),
r_0 (Si – O) = 1.59 Å,
k_θ (O – Si – O) = 69.03 mol·rad^2,
θ_0 (O – Si – O) = 109.5°,

Table 2

Parameters of particle interaction function (1) – (6)

Substance	Atom	σ, Å	ε, kcal/mol
ZSM-5	Si	4.009	0.1274
	O	2.890	0.1547
CH_4	C	3.400	0.05565
	H	2.963	0.06618
–	Bonds	k_r, kcal/(mol·Å^2)	r_0, Å
ZSM-5	O – Si	298.75	1.649
CH_4	C – H	170	1.09
–	–	k_θ, kcal/(mol·rad^2)	θ_0, degrees
ZSM-5	O – Si – O	69.0897	109.47
	Si – O – Si	5.427	141.00
CH_4	H – C – H	17.5	109.50
–	–	k_φ, kcal/mol	$d = +1$
ZSM-5	Si – O – Si – O	–0.35	$n = 3$

Note. All parameters related to the ZSM-5 zeolite were taken from [14], those related to methane (CH_4) from [15].

k_θ (Si – O – Si) = 9.06 mol·rad^2,
θ_0 (Si – O – Si) = 149°.

The mutual influence of atoms is reduced in this form of force field due to limited simulated degrees of freedom, namely, by eliminating the four-particle interaction potential. At the same time, the system particles are still described realistically. This potential function is called the simplified general valence force field and was used in [16], analyzing the reproduction of the structural characteristics in several types of zeolites, including silicalite, as well as their infrared and Raman spectra.

No problems with maintaining the system integrity were uncovered in computations using the second potential [17]. Since it is sorption/desorption and transport processes in a multicomponent system that interest us in this study, we had to ascertain not only that the structure of the lattice was preserved, but also whether the dynamics of interaction between sorbate and sorbent particles within the sorbent lattice was described realistically, and the processes of substance transfer were reproduced. For this reason, we carried out comprehensive analysis of this potential to assess whether it could be applied to the silicalite – methane system, including computations of its structural, thermodynamic and transport characteristics.

Computation of structural characteristics of pure silicalite

The radial (RDF) and angular (ADF) functions characterizing the distributions of particles in the system were chosen as the estimated structural characteristic of the particle system. These parameters were estimated both for a pure silicalite lattice and for a two-component silicalite – methane system.

RDF and ADF were computed separately for a silicalite lattice of different sizes (in unit cells): 1 × 1 × 2, 2 × 2 × 2, and 5 × 5 × 5. The compositions of these silicalite samples are given in Table 1. Since the topology of silicalite is represented by the junction of tetrahedral complexes of oxygen and silicon, the following pairs and triplets of atoms acted as arguments for the distribution functions:

Si – O, Si – O – Si, O – Si – O.

Only the sizes of the ZSM-5 zeolite sample differed in this series of computations: it was placed in a simulation box with the boundaries corresponding to the boundaries of the zeolite. The microcanonical NVE simulation ensemble was used.

The radial particle distribution function was plotted for a cutoff radius of 10 Å with an accuracy of 0.01 Å. The function $g(r)$ for Si and O atoms was computed assuming silicon to be the central atom. The angular distribution functions for the combinations of Si – O – Si and O – Si – O atoms were plotted with an accuracy of 1°.

The plots obtained as a result of the computations have characteristic peaks corresponding to the most probable mutual arrangement of atoms in the structure. The peak on the RDF curve for Si – O pairs of particles is sharp and narrow, which corresponds to a highly ordered system. Its maximum falls on the distance between the particles equal to 1.59 Å (Fig. 1). This value is consistent with the structural data presented in the database of zeolite materials [18].

The peaks on the ADF curve for Si – O – Si and O – Si – O atom triplets correspond to the angles $\theta = 145.1°$ and $\theta = 109.5°$, respectively. The values of the O – Si – O angle forming a tetrahedral complex were obtained in [19, 20] and lie in the ranges of 107.9 – 110.9° and 107.1 – 111.5°, respectively. The location of the first peak on the distribution of Si – O – Si triplets coincides with the position of the peak in the range from 145.7 to 177.7°, obtained experimentally in [20], while the values from [19], where the distribution functions were computed theoretically, have a much larger scatter: from 140 to 180°. We can conclude then that the stability and integrity of the lattice is preserved for different sizes of silicalite samples.

We performed several numerical experiments to assess the influence of the simulation boundaries on the relative position of the lattice. Namely, the boundaries were either set according to the dimensions of the simulation box, or were taken so as to exceed its dimensions by 3, 5, and 7 times, respectively. Since it was established that the sizes of the silicate lattice do not affect the reproduction of its structural characteristics, we considered the ZSM-5 sample only with a lattice consisting of 2 × 2 × 2 unit cells.

The computed results for the RDF and ADF functions in the cases of all possible two- and three-particle interactions have shown that the position of the simulation boundaries relative to the given structure does not affect the positions of the peaks. The only changes observed were in the height of the peaks on the function plots, which is explained by the peculiarities of RDF and ADF computa-

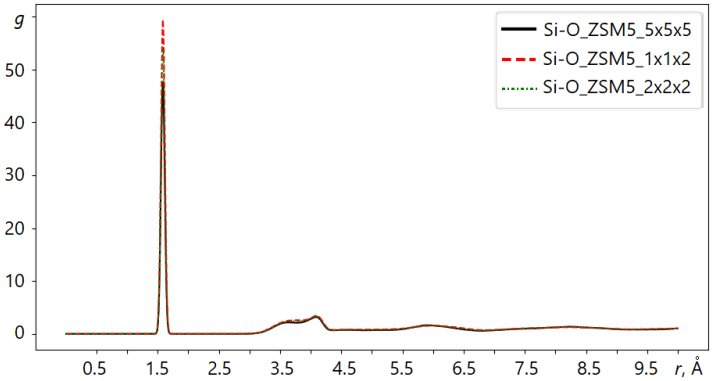

Fig. 1. Radial distribution function (RDF) for pairs of Si – O particles
for ZSM-5 zeolite with crystalline lattices with 1 × 1 × 2, 2 × 2 × 2 and 5 × 5 × 5 unit cells

tions, namely, their dependence on the total volume of the system. Therefore, it is possible to simulate a zeolite cluster located far from the boundary of the simulation box without structural distortions of the lattice.

Computation of structural characteristics of the silicalite – methane system

The following systems were prepared to test the interaction potential of the silicalite lattice with absorbed methane molecules:

silicalite with a size of 1 × 1 × 2 unit cells with a different number of methane molecules inside: 8, 16, 24 and 32, which corresponds to 1, 2, 3 and 4 molecules per channel intersection in silicalite. These sizes were chosen for comparison with the literature data [6 – 8].

In each case, a ZSM-5 zeolite was placed in the center of the simulation box. Methane molecules were randomly distributed inside the zeolite using the Packmol package. The microcanonical NVE simulation ensemble was used. Similar to the case of pure silicalite, the cutoff radius and the accuracy with which the RDF of the particles was computed were 10 and 0.01 Å, respectively.

The distribution of methane molecules in zeolite was estimated by computing the radial distribution function RDF for pairs of O – C atoms, since carbon and oxygen atoms are central for the methane molecule and the tetrahedral complex of the zeolite lattice, respectively.

The resulting graph has three peaks. The first one corresponds to the range of distances between molecules from 3.9 to 4.1 Å, the second one to the range from 5.7 to 5.9 Å, and the third lies in the range from 8.1 to 8.3 Å. These values are close to those of the radii of silicalite channels, which indicates the preferred arrangement of the molecules in the center of the channels. A slight difference in the positions of the peaks for different degrees of zeolite loading is fairly characteristic and is explained by the shift in the energy minimum with a change in the number of absorbed molecules. The shift in the peaks towards decreasing distance is the most pronounced at loading close to the limit. The shape of the curves is consistent with the data obtained earlier by computer simulation [6 – 8].

The RDF for a pair of C – C atoms (Fig. 2) was computed to assess the peculiarities of mutual arrangement of methane molecules in the interior of the zeolite. It is evident from Fig. 2 that the main peak lies in the range from 4.1 to 4.4 Å. Its position shifts towards smaller distances with increased zeolite loading with adsorbate molecules. Our result is consistent with the data obtained by the molecular dynamics method in [7]. The location of the first peak strongly depends on the concentration

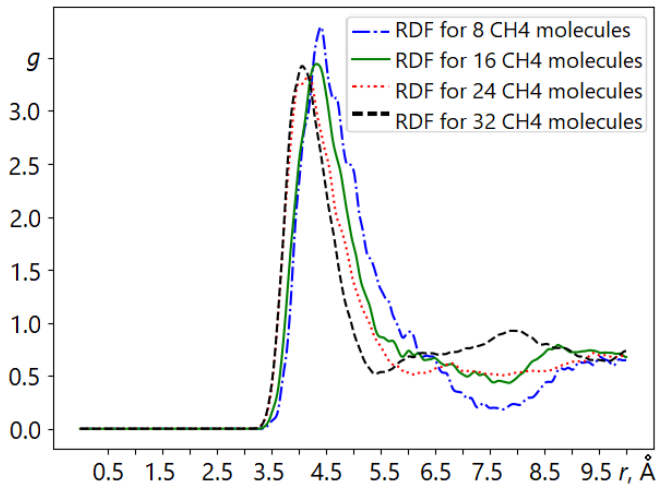

Fig. 2. Radial distribution function for pairs of C – C atoms for different numbers of methane molecules inside the crystal lattice of ZSM-5 zeolite with 1 × 1 × 2 unit cells

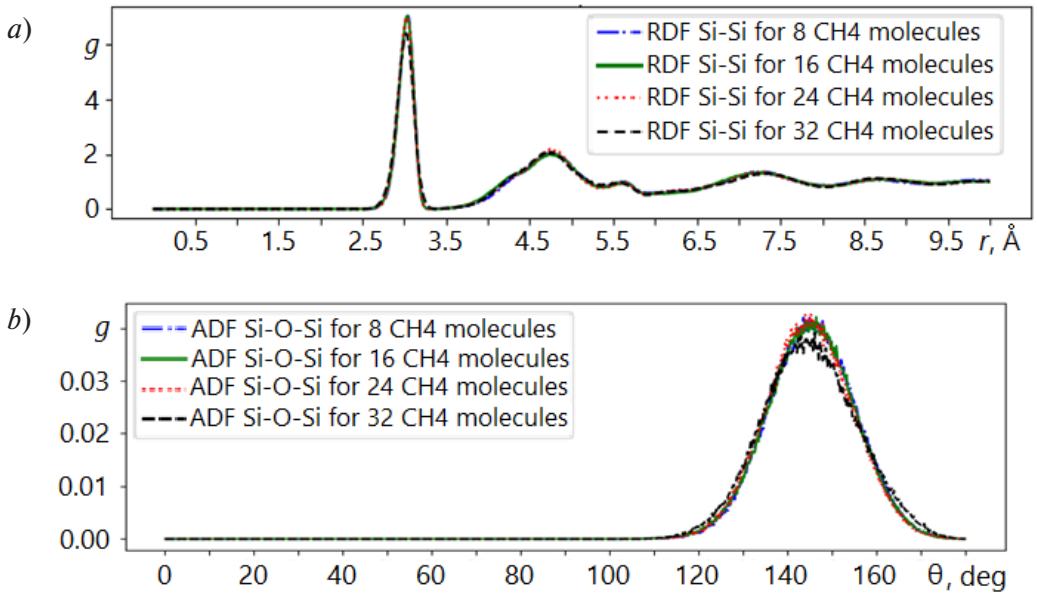

Fig. 3. The RDF of a pair of Si – Si atoms (*a*) and the ADF of a triplet of Si – O – Si atoms (*b*) with different numbers of methane molecules inside the crystal lattice of ZSM-5 zeolite with 1 × 1 × 2 unit cells

of methane (CH4) molecules, since the RDF value, according to [7], essentially depends on the Lennard – Johnson interaction between its molecules.

In addition to the above data, RDF and ADF were computed for groups of C – H and H – C – H methane atoms, as well as for combinations of Si – O, O – O, Si – Si, O – Si – O, Si – O – Si silicalite atoms. The single peaks on the function plots for methane atoms have a sharp shape, and their position coincides with the equilibrium value of the bond length of 1.09 Å and the angle of 109.5°. This allows us to conclude that the harmonic potential with the parameters used satisfactorily reproduces the structure of the methane molecule.

The curves of $g(r)$ and $g(\theta)$ dependences for zeolite atoms, whose examples are shown in Fig. 3, indicate that no structural changes occur in the zeolite framework at the given values of silicalite loading with methane molecules, and the actual presence of adsorbate molecules does not distort the lattice topology. Thus, the simulation potentials used ensure the stability of the zeolite lattice structure during sorption processes.

Computation of adsorption heat

The adsorption heat was computed to assess whether the thermodynamic properties of the silicalite – methane system were reproduced correctly. We used a method based on computing the energy difference between the (sorbent + single sorbed molecule) system and the pure sorbent system in the canonical ensemble (NVT) [21]. Adsorption heat ΔH was computed by the following formula:

$$-q = \Delta H = \langle U_1 \rangle - \langle U_0 \rangle - \langle U_g \rangle - \frac{1}{\beta}, \tag{7}$$

where $\beta = 1/(k_B T)$ (k_B is the Boltzmann constant); U_0, kcal/mol, is the sorbent energy in the absence of a guest molecule; U_1, kcal/mol, is the total energy of the sorbent with one guest molecule; U_g, kcal/mol, is the energy of an isolated guest molecule in the absence of sorbent; the notation $\langle \cdots \rangle$ corresponds to averaging over the ensemble at constant temperature and volume.

The quantity U_g depends only on the temperature T and can be computed once. Eq. (7) is applied in the zero-occupancy approximation, which implies ideal gas behavior.

This method requires simulation of different systems to obtain the energies used in Eq. (7). Therefore, the following systems were used for the computations:

silicalite with 1 × 1 × 2 unit cells with one methane molecule inside;

silicalite of the same size in the absence of other molecules;

one methane molecule placed in a simulation box corresponding in size to the silicalite sample used.

The minimum number of methane molecules meets the requirement for low zeolite loading (zero-occupancy approximation). The boundaries of the simulation box correspond to the boundaries of a cell in the ZSM-5 zeolite of the given size (they remain unchanged for an individual methane molecule). The methane molecule was placed in the center of the simulation box, which coincided (with an accuracy of 2 Å) with the location of the straight channel of the zeolite and the large cavity. According to [7, 9, 22], this position is energetically favorable for the methane – silicalite system. Configurations were created using the Packmol utility. The simulation was conducted in the canonical NVT ensemble. A series of statistical simulations was carried out to minimize the possible computational inaccuracies: 5 experiments for each system, differing in initial conditions (velocities).

The computed value of adsorption heat was –6.7 kcal/mol. A computational method similar to that in our study was used in [7, 9]. The values obtained by the authors were –4.2 and –5.8 kcal/mol, respectively. Values of –5.0, –6.1 and –6.7 kcal/mol were obtained by experimental procedures such as the calorimetric method [22, 23] and the vacuum microbalance method combined with the Clausius – Clapeyron equation [23]. The reason for such a wide value range is that techniques yielding different accuracies were used, with several aspects affecting the results. Thus, the value of adsorption heat computed in this paper is consistent with the literature data and is closer to the threshold values obtained in the full-scale experiment. Consequently, the given force field potential correctly reproduces the thermodynamic characteristics of the silicalite – methane system.

Computation of self-diffusion coefficient

The standard parameter characterizing transport phenomena in sorbent – sorbate systems is the self-diffusion coefficient of the sorbate in sorbent pores. Unlike ordinary diffusion, self-diffusion occurs under equilibrium conditions in the system, in particular, without a concentration gradient of the diffusing substance. We found the self-diffusion coefficient D_s of methane in silicalite using a method based on the relationship between diffusion and standard deviation:

$$D_s = \frac{1}{2dN} \lim_{\Delta t \to \infty} \frac{d}{dt} \left\langle \left(\sum_{i=1}^{N} r_i(t + \Delta t) - r_i(t) \right)^2 \right\rangle, \quad (8)$$

where r_i, Å, is the position of the particle i at a certain instant; t, s, is the time; N is the number of molecules; d is the dimension of the system.

This method is widely accepted and provides good agreement between the results and experimental data.

The experiment involved a system consisting of silicalite with 1 × 1 × 2 unit cells with 8 methane molecules inside, which corresponds to one molecule per intersection. Methane molecules were randomly positioned inside the zeolite using the Packmol package. The boundaries of the simulation box coincided with the boundaries of the silicalite lattice. Energy conservation in the system was ensured by using the microcanonical NVE ensemble.

The self-diffusion coefficient of methane in silicalite was determined for the given parameters of the system over a time interval from $2 \cdot 10^5$ to 10^6 steps to ensure stable diffusion flow in the system.

The obtained value of the coefficient D_s was $1.1 \cdot 10^{-10}$ m^2/s. Experimental techniques were used for computing D_s in [24 – 26], yielding values of $1.1 \cdot 10^{-8}$, $1.1 \cdot 10^{-10}$ and $1.3 \cdot 10^{-10}$ m^2/s, using pulsed field gradient NMR, membrane technique and pulsed gas chromatography, respectively. Computer simulations by the MD method in [5, 27] yielded the range from $9.0 \cdot 10^{-10}$ to $1.1 \cdot 10^{-8}$ m^2/s. Consequently, the value of the self-diffusion coefficient of methane in silicalite that we have found is in agreement with the literature data obtained both in a full-scale experiment and as a result of computer simulation. Such a small value of the self-diffusion coefficient indicates that the configurational mechanism of substance transfer is predominant under equilibrium conditions, which is typical for porous substances where the channel sizes are comparable to the sizes of absorbed molecules.

Conclusions

The most probable mutual positions of the given pairs and triplets of atoms, computed through their radial and angular distribution functions, respectively, agree with the theoretical and experimental values (within the error). This applies both to the structure of the silicalite lattice and to the methane molecule. Furthermore, we have established that the position of the modeling boundaries relative to the zeolite lattice does not affect the integrity of the structures, and the presence of methane molecules in the interior of the crystal lattice introduces only slight distortions if limiting values of sorbent occupancy are taken. This confirms that the potential function is suitable for modeling the interaction between the lattice atoms of silicalite and methane. In addition, reproducing the position of the peaks on the curves of the RDF and ADF functions eliminates the influence from the size of the computational cell and confirms the stability of the selected simulation potential with the parameters used.

We have established for the given force field that it is possible to simulate a sufficiently large silicalite sample adopting the position of the simulation boundaries significantly exceeding the boundaries of the zeolite.

The adsorption heat of methane on silicalite, computed in the study, was equal to –6.7 kcal/mol, which is close to the known experimentally obtained value and is in agreement with the computational data. Thus, the potential used for the force field satisfactorily reproduces the thermodynamic properties of the given system.

We have computed a crucial characteristic of transport processes, which is the self-diffusion coefficient D_s of the absorbed substance for the silicalite – methane system. The obtained value of $1.1 \cdot 10^{-10}$ m^2/s does not contradict the data found in the literature, allowing us to conclude that transport processes proceed mainly along the configuration mechanism for normal conditions and zeolite occupancy, equal to 4 molecules per unit cell.

To summarize, the computed structural, thermodynamic, and transport characteristics of the silicalite – methane system using the potential of a simplified general valence force field are consistent with the data presented in literature, giving reason to believe that it is correct to use the potential function we have chosen to simulate the sorption/desorption processes.

REFERENCES

1. **Berezovsky V., Öberg S.,** Computational study of the CO adsorption and diffusion in zeolites: validating the Reed – Ehrlich model, Adsorption. 24 (4) (2018) 403–413.

2. **Gautam S., Liu T., Cole D.,** Sorption, structure and dynamics of CO_2 and ethane in silicalite at high pressure: a combined Monte Carlo and molecular dynamics simulation study, Molecules. 24 (1) (2019) 99.

3. **Kutsova D.S., Bogatikov E.V., Shebanov A.N., et al.,** Analysis of the composition of a complex gas mixture by a sensor based on zeolite, Journal of Nano- and Microsystem Technique. 9 (2016) 591–592.

4. **Matera S., Schneider W.F., Heyden A., Savara A.,** Progress in accurate chemical kinetic modeling, simulations and parameter estimation for heterogeneous catalysis, ACS Catalysis. 9 (8) (2019) 6624–6647.

5. **Goodbody S.J., Watanabe K., MacGowan D., et al.,** Molecular simulation of methane and butane in silicalite, J. Chem. Soc., Faraday Trans. 87 (13) (1991) 1951–1958.

6. **Bussai C., Fritzsche S., Haberlandt R., Hannongbua S.,** A molecular dynamic (MD) study of methane in silicalite-1: A novel Møller – Plesset potential energy surface, Studies in Surface Science and Catalysis, Book Series, Proc. of the 14-th Intern. Zeolite Conf.; 25 – 30 April, 2000, Cape Town, South Africa. 154 (Part B) (2004) 2104–2109.

7. **Nicholas J.B., Trouw F.R., Mertz J.E., et al.,** Molecular dynamics simulation of propane and methane in silicalite, J. Phys. Chem. 97 (16) (1993) 4149–4163.

8. **Demontis P., Suffritti G.B., Fois E.S., Quartieri S.,** Molecular dynamics studies on zeolites. 6. Temperature dependence of diffusion of methane in silicalite, J. Phys. Chem. 96 (3) (1992) 1482–1490.

9. **June R.L., Bell A.T., Theodorou D.N.,** Molecular dynamics study of methane and xenon in silicalite, J. Phys. Chem. 94 (21) (1990) 8232–8240.

10. **Cheng X., Li Z., He Y.-L.,** Effect of temperature and pore structure on the release of methane in zeolite nanochannels, RSC Advances. 9 (17) (2019) 9546–9554.

11. **Van Gunsteren W.F., Daura X., Hansen N., et al.,** Validation of molecular simulation: an overview of issues, Angewandte Chemie International Edition. 57 (4) (2018) 884–902.

12. **Merz P.T., Shirts M.R.,** Testing for physical validity in molecular simulations, PLoS ONE. 13 (9) (2018) 1–22.

13. LAMMPS Molecular Dynamics Simulator. Access mode: https://lammps.sandia.gov, Application date: May 6, 2016.

14. **Choi S.G., Lee S.H.,** Preliminary molecular dynamics simulation studies of H-Y zeolite in a non-rigid zeolite framework, Bull. Korean Chem. Soc. 20 (4) (1999) 445–450.

15. **Vela S., Huarte-Larrañaga F.,** A molecular dynamics simulation of methane adsorption in single walled carbon nanotube bundles, Carbon. 49 (13) (2011) 4544–4553.

16. **Smirnov K.S., Bougeard D.,** Molecular dynamics study of the vibrational spectra of siliceous zeolites built from sodalite cages, J. Phys. Chem. 97 (37) (1993) 9434–9440.

17. **Kutsova D.S., Bogatikov E.V., Shebanov A.N., et al.,** Simulation of methane sorption and desorption in silicalite, Bulletin of Voronezh State Technical University. 13 (5) (2017) 108–112 (in Russian).

18. **Baerlocher Ch., McCusker L.B.,** Database of zeolite structures, Access mode: http://www.iza-structure.org/databases, Application date: May, 20, 2016.

19. **Astala R., Auerbach S.M., Monson P.A.,** Density functional theory study of silica zeolite structures: stabilities and mechanical properties of SOD, LTA, CHA, MOR, and MFI, J. Phys. Chem. B. 108 (26) (2004) 9208–9215.

20. **Van Koningsveld H.** High-temperature (350 K) orthorhombic framework structure of zeolite H-ZSM-5, Acta Cryst. B46 (6) (1990) 731–735.

21. **Vlugt T.J.H., Garcia-Perez E., Dubbeldam D., et al.,** Computing the heat of adsorption using molecular simulations: The effect of strong coulombic interaction, J. Chem. Theory Comput. 4 (6) (2008) 1007–1118.

22. **Vigne-Meader F., Auroux A.,** Potential maps of methane, water and methanol in silicalite, J. Phys. Chem. 94 (1) (1990) 316–322.

23. **Papp H., Hinsen W., Do N.T., Baerns M.,** The adsorption on methane on H-ZSM-5 zeolite, Thermochimica Acta. 82 (1) (1984) 137–148.

24. **Caro J., Bulow M., Schirmer W., et al.,** Microdynamics of methane, ethane and propane in ZSM-5 type zeolites, J. Chem. Soc., Faraday Trans. 1: Phys. Chem. in Cond. Phases. 81 (10) (1985) 2541–2550.

25. **Hayhurst D.T., Paravar A.R.,** Diffusion of C_1 to C_5 normal paraffins in silicalite, Zeolites. 8 (1) (1988) 27–29.

26. **Chiang A.S., Dixon A.G., Ma Y.H.,** The determination of zeolite crystal diffusivity by gas chromatography – II. Experimental, Chem. Eng. Sci. 39 (10) (1984) 1461–1468.

27. **June R.L., Bell A.T., Theodorou D.N.,** Molecular dynamics studies of butane and hexane in silicalite, J. Phys. Chem. 96 (3) (1992) 1051–1060.

Received 30.03.2021, accepted 03.06.2021.

THE AUTHORS

KUTSOVA Daria S.
Voronezh State University
1, Universitetskaya Sq., Voronezh, 394006, Russian Federation
potanina.ds@gmail.com

BOGATIKOV Evgenii V.
Voronezh State University
1, Universitetskaya Sq., Voronezh, 394006, Russian Federation
evbogatikov@yandex.ru

SHEBANOV Alexandr N.
Voronezh State University
1, Universitetskaya Sq., Voronezh, 394006, Russian Federation
anshebanov@hotmail.com

BORMONTOV Evgenii N.
Voronezh State University
1, Universitetskaya Sq., Voronezh, 394006, Russian Federation
me144@phys.vsu.ru

СПИСОК ЛИТЕРАТУРЫ

1. **Berezovsky V., Öberg S.** Computational study of the CO adsorption and diffusion in zeolites: validating the Reed – Ehrlich model // Adsorption. 2018. Vol. 24. No. 4. Pp. 403–413.

2. **Gautam S., Liu T., Cole D.** Sorption, structure and dynamics of CO_2 and ethane in silicalite at high pressure: a combined Monte Carlo and molecular dynamics simulation study// Molecules. 2019. Vol. 24. No. 1. P. 99.

3. **Куцова Д.С., Богатиков Е.В., Шебанов А.Н., Смирнова К.Г., Глушков Г.И.** Анализ состава сложной газовой смеси сенсором на основе цеолита // Нано- и микросистемная техника. 2016. Т. 18. № 9. С. 589–591.

4. **Matera S., Schneider W.F., Heyden A., Savara A.** Progress in accurate chemical kinetic modeling, simulations and parameter estimation for heterogeneous catalysis // ACS Catalysis. 2019. Vol. 9. No. 8. Pp. 6624–6647.

5. **Goodbody S.J., Watanabe K., MacGowan D., Walton J.P.R.B., Quirke N.** Molecular simulation of methane and butane in silicalite // J. Chem. Soc., Faraday Trans. 1991. Vol. 87. No. 13. Pp. 1951–1958.

6. **Bussai C., Fritzsche S., Haberlandt R., Hannongbua S.** A molecular dynamic (MD) study of methane in silicalite-1: A novel Møller – Plesset potential energy surface // Studies in Surface Science and Catalysis. Book Series. Proc. of the 14-th Intern. Zeolite Conf.; 25 – 30 April, 2000. Cape Town, South Africa. 2004. Vol. 154. Part B. Pp. 2104–2109.

7. **Nicholas J.B., Trouw F.R., Mertz J.E., Iton L.E., Hopfinger A.J.** Molecular dynamics simulation of propane and methane in silicalite // J. Phys. Chem. 1993. Vol. 97. No. 16. Pp. 4149–4163.

8. **Demontis P., Suffritti G.B., Fois E.S., Quartieri S.** Molecular dynamics studies on zeolites. 6. Temperature dependence of diffusion of methane in silicalite // J. Phys. Chem. 1992. Vol. 96. No. 3. Pp. 1482–1490.

9. **June R.L., Bell A.T., Theodorou D.N.** Molecular dynamics study of methane and xenon in silicalite // J. Phys. Chem. 1990. Vol. 94. No. 21. Pp. 8232–8240.

10. **Cheng X., Li Z., He Y.-L.** Effect of temperature and pore structure on the release of methane in zeolite nanochannels // RSC Advances. 2019. Vol. 9. No. 17. Pp. 9546–9554.

11. **Van Gunsteren W.F., Daura X., Hansen N., Mark A.E., Oostenbrink C., Riniker S., Smith L.J.** Validation of molecular simulation: an overview of issues // Angewandte Chemie International Edition. 2018. Vol. 57. No. 4. Pp. 884–902.

12. **Merz P.T., Shirts M.R.** Testing for physical validity in molecular simulations // PLoS ONE. 2018. Vol. 13. No. 9. Pp. 1–22.

13. LAMMPS Molecular Dynamics Simulator. Режим доступа: https://lammps.sandia.gov (Дата обращения: 06.05.2016).

14. **Choi S.G., Lee S.H.** Preliminary molecular dynamics simulation studies of H-Y zeolite in a non-rigid zeolite framework // Bull. Korean Chem. Soc. 1999. Vol. 20. No. 4. Pp. 445–450.

15. **Vela S., Huarte-Larrañaga F.** A molecular dynamics simulation of methane adsorption in single walled carbon nanotube bundles // Carbon. 2011. Vol. 49. No. 13. Pp. 4544–4553.

16. **Smirnov K.S., Bougeard D.** Molecular dynamics study of the vibrational spectra of siliceous zeolites built from sodalite cages // J. Phys. Chem. 1993. Vol. 97. No. 37. Pp. 9434–9440.

17. **Куцова Д.С., Богатиков Е.В., Шебанов А.Н., Куликов Д.Г., Бормонтов Е.Н.** Моделирование процессов сорбции-десорбции метана силикалитом // Вестник Воронежского государственного технического университета. 2017. Т. 13. № 5. С. 108–112.

18. **Baerlocher Ch., McCusker L.B.** Database of zeolite structures. Режим доступа: http://www.iza-structure.org/databases (Дата обращения 20.05.2016).

19. **Astala R., Auerbach S.M., Monson P.A.** Density functional theory study of silica zeolite structures: stabilities and mechanical properties of SOD, LTA, CHA, MOR, and MFI // J. Phys. Chem. B. 2004. Vol. 108. No. 26. Pp. 9208–9215.

20. **Van Koningsveld H.** High-temperature (350 K) orthorhombic framework structure of zeolite H-ZSM-5 // Acta Cryst. Section B. 1990. Vol. B46. No. 6. Pp. 731–735.

21. **Vlugt T.J.H., Garcia-Perez E., Dubbeldam D., Ban S., Calero S.** Computing the heat of adsorption using molecular simulations: The effect of strong coulombic interaction // J. Chem. Theory Comput. 2008. Vol. 4. No. 6. Pp. 1007–1118.

22. **Vigne-Meader F., Auroux A.** Potential maps of methane, water and methanol in silicalite // J. Phys. Chem. 1990. Vol. 94. No. 1. Pp. 316–322.

23. **Papp H., Hinsen W., Do N.T., Baerns M.** The adsorption on methane on H-ZSM-5 zeolite // Thermochimica Acta. 1984. Vol. 82. No. 1. Pp. 137–148.

24. **Caro J., Bulow M., Schirmer W., Karger J., Heink W., Preifer H., Zdanov S.P.** Microdynamics of methane, ethane and propane in ZSM-5 type zeolites // J. Chem. Soc., Faraday Trans. 1: Phys. Chem. in Cond. Phases. 1985. Vol. 81. No. 10. Pp. 2541–2550.

25. **Hayhurst D.T., Paravar A.R.** Diffusion of C_1 to C_5 normal paraffins in silicalite // Zeolites. 1988. Vol. 8. No. 1. Pp. 27–29.

26. **Chiang A.S., Dixon A.G., Ma Y.H.** The determination of zeolite crystal diffusivity by gas chromatography – II. Experimental // Chem. Eng. Sci. 1984. Vol. 39. No. 10. Pp. 1461–1468.

27. **June R.L., Bell A.T., Theodorou D.N.** Molecular dynamics studies of butane and hexane in silicalite // J. Phys. Chem. 1992. Vol. 96. No. 3. Pp. 1051–1060.

Статья поступила в редакцию 30.03.2021, принята к публикации 03.06.2021.

СВЕДЕНИЯ ОБ АВТОРАХ

КУЦОВА Дарья Сергеевна – *аспирантка кафедры физики полупроводников и микроэлектроники Воронежского государственного университета, г. Воронеж, Российская Федерация.*

394006, Российская Федерация, г. Воронеж, Университетская пл., 1

potanina.ds@gmail.com

БОГАТИКОВ Евгений Васильевич – *кандидат физико-математических наук, доцент кафедры физики полупроводников и микроэлектроники Воронежского государственного университета, г. Воронеж, Российская Федерация.*

394006, Российская Федерация, г. Воронеж, Университетская пл., 1.

evbogatikov@yandex.ru

ШЕБАНОВ Александр Николаевич – *ассистент кафедры физики полупроводников и микроэлектроники Воронежского государственного университета, г. Воронеж, Российская Федерация.*

394006, Российская Федерация, г. Воронеж, Университетская пл., 1.

anshebanov@hotmail.com

БОРМОНТОВ Евгений Николаевич – *доктор физико-математических наук, профессор, заведующий кафедрой физики полупроводников и микроэлектроники Воронежского государственного университета, г. Воронеж, Российская Федерация.*

394006, Российская Федерация, г. Воронеж, Университетская пл., 1.

me144@phys.vsu.ru

DOI: 10.18721/JPM.14307
UDC 532.517

THERMAL MANIKIN SHAPE INFLUENCE ON AIRFLOW AND HEAT TRANSFER IN THE MODEL ROOM WITH DISPLACEMENT VENTILATION

E.D. Stepasheva, M.A. Zasimova, N.G. Ivanov

Peter the Great St. Petersburg Polytechnic University,
St. Petersburg, Russian Federation

The paper presents the results of numerical modeling of turbulent flow and heat transfer in the model room with displacement ventilation. The goal of the study is to assess the shape influence of the thermal manikin placed in the room on the computed airflow structure. Three manikin shapes have been considered: a detailed one (close to a human shape) and ones simplified partially and completely. The problem formulation was close to the test conditions of P.V. Nielsen et al. (2003). The RANS approach based on the standard k-ε turbulence model was applied. The study revealed solution sensitivity to the dimension and topology of the mesh used, as well as the solution dependence on the uncertainty of the inlet velocity distribution. The calculated results were shown to agree generally with the experimental data. The simplification of the manikin shape had a significant impact on the local parameter prediction accuracy.

Keywords: ventilation, thermal manikin, turbulent airflow and heat transfer, natural convection

Citation: Stepasheva E.D., Zasimova M.A., Ivanov N.G., Thermal manikin shape influence on airflow and heat transfer in the model room with displacement ventilation, St. Petersburg Polytechnical State University Journal. Physics and Mathematics. 14 (3) (2021) 90–106. DOI: 10.18721/JPM.14307

ВЛИЯНИЕ ФОРМЫ ТЕПЛОВОГО МАНЕКЕНА НА ТЕЧЕНИЕ И ТЕПЛООБМЕН В МОДЕЛЬНОМ ПОМЕЩЕНИИ С ВЫТЕСНЯЮЩЕЙ ВЕНТИЛЯЦИЕЙ

Е.Д. Степашева, М.А. Засимова, Н.Г. Иванов

Санкт-Петербургский политехнический университет Петра Великого,
Санкт-Петербург, Российская Федерация

В работе представлены результаты численного моделирования турбулентного течения и теплообмена в модельном помещении с вытесняющей вентиляцией, в котором размещен нагретый тепловой манекен. Цель работы – оценить влияние формы манекена на структуру течения воздуха, предсказываемую расчетами. Рассмотрены три формы манекена: детальная (приближена к форме человека), а также частично и полностью упрощенные. Постановка задачи приближена к условиям тестового эксперимента P.V. Nielsen и др. (2003). Моделирование турбулентности осуществлялось с помощью RANS-подхода с привлечением стандартной k-ε модели турбулентности в сочетании с методикой разрешения пристенной области. В результате исследования выявлена степень чувствительности решения к размерности и топологии используемой сетки, а также влияние на решение неопределенности входного распределения скорости. Показано, что расчетные результаты в целом согласуются с данными эксперимента; упрощение формы манекена оказывает существенное влияние на точность предсказания локальных параметров.

Ключевые слова: вентиляция, тепловой манекен, турбулентное течение и теплообмен, естественная конвекция

Ссылка при цитировании: Степашева Е.Д., Засимова М.А., Иванов Н.Г. Влияние формы теплового манекена на течение и теплообмен в модельном помещении с вытесняющей вентиляцией // Научно-технические ведомости СПбГПУ. Физико-математические науки. 2021. Т. 14. № 3. С. 90–106. DOI: 10.18721/JPM.14307

Introduction

Ventilation systems must provide thermally comfortable characteristics, maintaining a microclimate that is suitable for humans in ventilated rooms. The following characteristics are commonly used to assess the thermal comfort in practice [1, 2]:

draft rating (DR),

predicted mean vote for the quality of air (PMV),

predicted percentage dissatisfied with the temperature of the environment (PPD),

predicted percentage dissatisfied with the vertical temperature gradient (Percentage Dissatisfied).

When it comes to ventilation systems that have already been put into operation, these characteristics are assessed from interviews with people in the room using a special technique. The characteristics of thermal comfort can also be estimated based on initial data on airflow: local and/or integral velocities, velocity fluctuations and (for non-isothermal problems) temperatures, using the empirical relations listed in the standards.

Formulating and solving applied ventilation problems generates a large number of parameters that are difficult (and often impossible) to define unambiguously. These are, in particular, the following parameters:

person's position in the room and its variation over time,

shape of the person's body (individual geometry, positions of individual body parts),

individual heat transfer characteristics (local and integral),

thermal insulation of the clothing, etc.

While the above parameters significantly affect the flow and heat transfer characteristics, and, as a consequence, the thermal comfort characteristics, all of them can be fully taken into account only in some simple cases. It is often convenient, and sometimes in fact necessary to simplify the problem statement for both physical modeling and computational fluid dynamics (CFD). This decision needs to be substantiated in each case.

Physical experiments considering the characteristics of thermal comfort in a room with people widely employ thermal manikins simulating humans, including heat release and breathing. Computational studies of ventilation flow also frequently involve 'virtual' thermal manikins (see, for example, [3 – 5]). Ref. [6] thoroughly reviews the state of the art in numerical simulation of airfllow and heat transfer near a thermal manikin [6].

Numerical simulation, especially in fundamental studies, is best performed with a simplified shape of the thermal manikin rather than the detailed geometry of the human body, since this allows controlling the conditions of the computational experiment more precisely (for example, the quality of the mesh near a solid surface). Example computations are given in [7, 8] for flow and heat transfer in the vicinity of a thermal manikin with a simplified shape; the results were obtained based on an eddy-resolving method for Large Eddy Simulation. However, standard thermal manikins are typically used in modern physical experiments: they have a detailed shape, so additional comprehensive studies are required to directly compare the computational results obtained for a simplified manikin with the experimental data.

The degree to which the shape of the thermal manikin influences the structure of the flow in the room was previously assessed for various configurations both in experimental studies [9, 10] and based

on CFD [8, 11, 12]. Conclusions on the effect that the shape of the manikin has on the local characteristics of the flow were drawn in [8 – 12] for particular cases in each of the given problems.

Experimental data have been accumulated in the literature for two test configurations corresponding to two types of ventilation: mixing [10, 13] and displacement [13]. In the first case, the air supplied through the inlets is mixed well in the room, for example, due to global circulation. With displacement ventilation (second case), fresh air is supplied to the bottom of the room, and the exhaust openings are located near the ceiling, which minimizes global mixing. Experiments in [10, 13] considered a test room containing a heated manikin with controlled heat release from the skin surface. The experiments measuring the velocity and temperature fields, carried out in several sections of the room, were interpreted by the authors as benchmarks. The results of experimental measurements, well documented and posted by the authors as a database at http://www.cfd-benchmarks.com/, have been repeatedly used to validate the computational data [8, 14 – 16]: Refs. [8, 14] present the computational results for a room with displacement ventilation, and Refs. [15, 16] discuss a room with mixing ventilation.

This paper provides the results for numerical study of flow and heat transfer near a thermal manikin for the test conditions with displacement ventilation [13].

Our goal was to assess the degree of sensitivity of the flow structure in the room to changes in the geometric shape of the thermal manikin.

The computations were carried out for three shapes of the manikin: detailed (close to the shape of the human body and largely corresponding to the one adopted in the experiment), partially simplified (consisting of parallelepiped blocks), and completely simplified (one solid parallelepiped). Turbulence was simulated using the RANS approach with the standard k-ε turbulence model, which is the most widespread in studies of jet flows.

Problem statement

Geometric model. We consider a ventilated room (Fig. 1,*a*); its height, width and length (in meters) are $H = 2.7$, $W = 3.0$ and $L = 3.5$, respectively. The coordinate system used is shown on the schematic the room, the origin of the coordinate system is located in its bottom left corner. One of the end sides has a rectangular inlet opening near the floor, with the height $h_{in} = 0.2$ m and the width $w_{in} = 0.4$ m. The equivalent inlet diameter $D_e = (4h_{in}w_{in}/\pi)^{1/2} = 0.3$ m. The outlet has a square shape $h_{out} = w_{out} = 0.3$ m and is located on the opposite end wall near the ceiling of the room. The inlet and outlet are centered along the z coordinate.

A thermal manikin is located in the center of the room; its surface is h = 0.05 m above the floor. We considered three shapes of the thermal manikin: parallelepiped, block and detailed (see also Table 1). The manikin is in an upright position, facing the inlet. The simplest of the given shapes is a parallelepiped (Fig. 1,*b*) with the following dimensions: height $h_m = 1.7$ m, width $w_m = 0.4$ m and thickness $l_m = 0.1$ m. The surface area of the manikin is $S_m = 1.78$ m^2.

The geometric parameters of the block shape (Fig. 1,*c*) are the same as in [8]. The block-shaped manikin is made up of parallelepipeds, which taken together imitate the real shape of the human body to some degree. The manikin also has the following separate parts: head, two arms, torso and two legs (Table 2). The surface area of the manikin is $S_m = 1.48$ m^2 (see Table 1).

The detailed shape of the manikin (Fig. 1,*d*) is close to that used in the experiment. The manikin geometry was produced with the MakeHuman software (official website: *makehumancommunity.org*).

Note that the area of the thermal manikin used in the experimental study [13] is $S_m = 1.47$ m^2. This value is 7% less than for the detailed shape of the manikin discussed in this paper. The reason for this is that the shape of the manikin used in [13] cannot be reproduced completely because the geometry was described insufficiently, even though the measurement results were fairly well documented. While the experiments in [13] were carried out for both the sitting and standing positions of the manikin

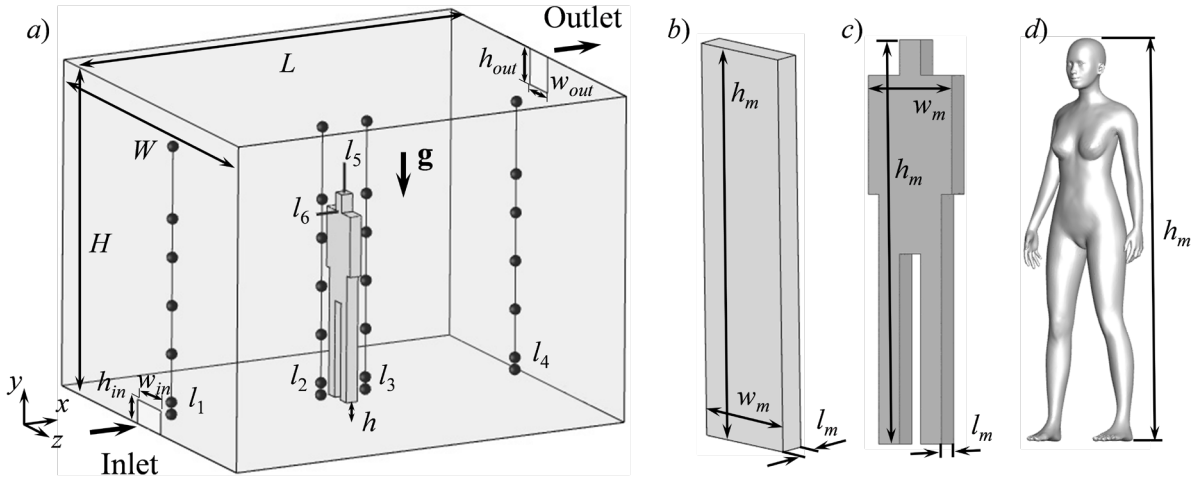

Fig. 1. Schematic of the room (*a*) and different shapes of the manikin: parallelepiped (*b*), block (*c*), detailed (*d*).
Inlet and outlet of the airflow, and geometric parameters are shown;
lines $l_1 - l_6$ mark the positions of the sections for which experimental data are available

Table 1

Compugational configurations accounting for manikin shape and external factors

Manikin shape (S_m, m^2)	q_w, W/m^2	Computational grid, mln	Element type	y_p, mm	$\langle y^+ \rangle$
Parallelepiped (1.78)	21	0.79	Hexagonal	1.0	1.12
		0.97		0.5	0.58
		0.24	Polyhedral	5.0	4.74
		1.16		1.0	1.05
Block (1.48)	26	1.04		1.0	1.05
Detailed (1.57)	24	1.62		1.0	1.02

N o t a t i o n s: S_m is the surface area, q_w is the specific heat flux, y_p is the height of the first near-wall cell at the surface of the manikin, $\langle y^+ \rangle$ is the averaged dimensionless distance from the manikin surface to the center of the first near-wall cell.

(the latter is also considered in our study), the geometry on http://www.cfd-benchmarks.com/ is only given for the sitting position.

Lines $l_1 - l_6$ shown in Fig. 1,a demonstrate the positions of the sections for which experimental data are available in [13]. All lines are located in the central plane of the room: for $z = 1.5$ m. Lines $l_1 - l_4$ are located at distances 0.20, 1.55, 1.95 and 3.30 meters from the inlet. The symbols in the figure mark the positions of the points where the magnitudes of velocity (measured with an ultrasonic anemometer) and temperature (measured with a thermocouple) were captured along the lines. The database contains velocities obtained by Particle Image Velocimetry (PIV) for lines l_5, l_6 (their positions are $x = 1.75$ m and $y = 1.60$ m).

Physical parameters of the environment and boundary conditions. The physical properties of the air were taken constant and corresponded to a temperature of 22 °C:

density $\rho = 1.194$ kg/m^3,

Table 2

Geometrical parameters for three manikin shapes

Parameter of manikin/part	Size for shape, m		
	parallelepiped	block	detailed
Height h_m	1.70	1.70	1.70
Maximum width w_m	0.40	0.40	0.59
Thickness l_m	0.10	0.30	0.30
Head	–	0.15×0.10	MakeHuman software used
Body		0.75×0.30	
Arm (two)		0.50×0.05	
Leg (two)		0.80×0.10	
Distance between legs		0.10	

N o t e. The sizes of the manikin parts for the block shape are given in the *yz* plane.

dynamic viscosity $\mu = 1.789 \cdot 10^{-5}$ kg/(m·s),
specific heat $C_p = 1006$ J/(kg·K),
thermal conductivity $\lambda = 0.024$ W/(m·K).
The Prandtl number with such parameters equals $\mathrm{Pr} = \mu C_p/\lambda = 0.69$.

According to documentation for the experiment in [13], it is preferable to set a uniform velocity profile $V_{in} = 0.2$ m/s at the inlet to the room. This condition was reproduced in the main series of computations, which corresponds to a volumetric flow rate of 57.6 m^3/h. The Reynolds number plotted from the equivalent diameter and inlet velocity is in this case $\mathrm{Re} = \rho D_e V_{in}/\mu = 4300$.

In addition to recommendations, the appendix to the experimental data in [13] on the website contains a table (in Excel format) of measured magnitudes of the inlet velocity. According to these data, the mean flow velocity at the inlet is 0.181 m/s. Additional computations were performed for the configuration with a block-shaped manikin, with a uniform velocity profile given at the inlet $V_{in} = 0.181$ m/s (the corresponding flow rate was 52.1 m^3/h). Another series of computations were performed for a non-uniform velocity profile at the inlet, obtained from the solution to the problem of flow in a channel with the corresponding section, where the mean flow rate was $V_{in} = 0.181$ m/s.

Soft boundary conditions (constant pressure) were imposed at the inlet from the computational domain. The no-slip condition was imposed on the walls of the ventilated room and on the surface of the manikin.

The following thermal boundary conditions were imposed in accordance with the experimental conditions in [13]:
inlet temperature was constant and equal to $T_{in} = 22$ °C,
the walls of the room were adiabatic.

The integral heat removal from the manikin surface was taken equal to $Q_w = 38$ W for all geometric configurations, which corresponds to 50% of the value adopted in the standards for a person standing still. If the computations for the thermal manikin do not account for the radiative heat transfer (as is the case in this study), a customary technique is to reduce the typical heat release for a person by approximately two times. A constant value of the specific heat flux was given on the surface of the manikin, defined as $q_w = Q_w/S_m$. The values of the specific heat flux used for different geometric shapes of the manikin are given in Table 1.

Mathematical and computational models. Turbulence was simulated by the RANS approach (solving the Reynolds-averaged Navier – Stokes equations); for more details see, for example, mono-

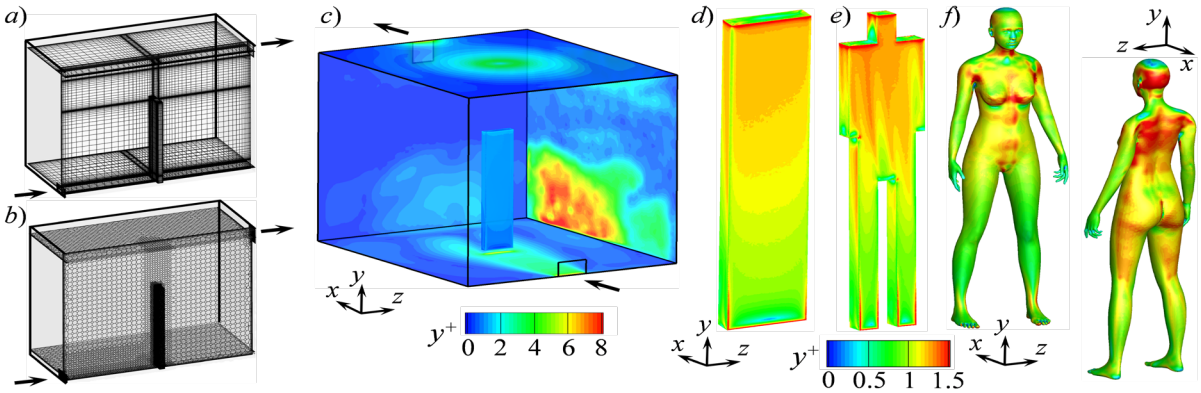

Fig. 2. General view of computational meshes with hexagonal elements (0.79 million) (*a*) and polyhedral elements (1.16 million) (*b*) for parallelepiped-shaped manikin; distribution of y^+ along room wall surfaces (mesh of 1.16 million cells) (*c*) and along surfaces of three shapes of manikins: parallelepiped (*d*), block (*e*) and detailed (*f*)

graph [17]. The equations are closed by the standard semi-empirical *k*-ε turbulence model [18] combined with the Enhanced Wall Treatment technique for resolving the near-wall region. The following turbulence characteristics were adopted in the computations at the inlet to the room:

turbulent intensity $I = 30\%$,

ratio of turbulent to molecular viscosity $\mu_t/\mu = 44$.

The buoyancy force was taken into account in the Boussinesq approximation. The gravitational acceleration vector **g**, whose magnitude equals $g = 9.81$ m/s^2, is directed vertically down towards the floor of the room (see Fig. 1,*a*). The volumetric thermal expansion coefficient was given as $\beta = 3.39 \cdot 10^{-3}$ K^{-1}.

The computations used quasi-structured meshes with hexagonal elements, constructed in the ICEM CFD 2019 R3 mesh generator, as well as unstructured meshes with polyhedral elements obtained in ANSYS Fluent by transforming computational meshes with tetrahedral elements built in ICEM CFD. The sizes and some other characteristics of the computational meshes used in the study are given in Table 1. The appearance of meshes with hexagonal and polyhedral elements is shown in Fig. 2,*a*,*b*. The meshes are clustered towards the walls of the computational domain, as well as towards the surface of the manikin.

Meshes with hexagonal elements were used for the simplest form of a manikin, i.e., a parallelepiped. Two types of mesh with hexagonal elements were constructed, with varying height y_p of the first near-wall cell at the surface of the manikin (see Table 1): this dimension was 1 mm for the first type, the total size of the mesh was 790,000 (82 × 109 × 90) cells, and 0.5 mm for the second type (half as much), while the total mesh size was 970,000 (98 × 111 × 92) cells. The value of the dimensionless distance y^+ from the manikin surface to the center of the first near-wall cell (see Fig. 2,*a*), is, on average, 1.12 and 0.58 for the types, respectively.

Two meshes consisting of polyhedral elements were also constructed for the parallelepiped-shaped manikin. A more economical mesh containing 240,000 elements in total had five prismatic layers without clustering near the walls perpendicular to the axes *x* and *y* or near the manikin surface; the transverse size of the cells in the layers was $y_p = 5$ mm. The rest of the area, that is, the inner part of the room, was divided into identical polyhedral cells with the characteristic size of 10 cm. This mesh topology is often used in engineering practice because it is very easy to generate. The second polyhedral mesh, with a total of 1.16 million elements, was clustered around the near-wall jet, as well as in the region above the manikin (see Fig. 2,*b*). The characteristic size of polyhedral elements was 5 cm

in the refined regions, and 10 cm in the rest of the domain. Ten prismatic layers were given near the manikin surface with a clustering coefficient of 1.1 to the surface of the manikin; the height of the first near-wall layer y_p = 1 mm. The distribution of y^+ for this configuration of the computational mesh is shown in Fig. 2,*c*,*d*. The value of y^+ does not exceed 10 on the walls of the room, averaging to 1.05 over the manikin surface.

The computational mesh for the block and detailed shapes of the manikin consisted of prismatic layers and polyhedral cells with characteristics similar to the polyhedral mesh with clustering for the parallelepiped-shaped manikin. The distribution of y^+ on the surface of the manikins for these cases is shown in Fig. 2,*d*,*f*. The values of y^+ on the surface of the manikin also amounted to about 1 on average (see Table 1).

All computations were performed in the ANSYS Fluent 2019 R3 CFD package. The equations were approximated with second-order precision. The SIMPLE method was chosen to organize the iterative process. The resources of the Hydroaerodynamics Research Laboratory cluster (maximum of 24 cores) were used.

Computational results and discussion

Sensitivity of solution to the mesh used. Fig. 3 shows the velocity profiles in six sections of the room $l_1 - l_6$, obtained in computations for the parallelepiped-shaped manikin with meshes of different dimensions and topology (see Table 1).

The graphs for the sections l_1 and l_2 (Fig. 3,*a*,*b*) show a zone where a near-wall inlet jet propagates (at $y < 0.6$ m). The jet intensity decreases downstream; the velocity magnitude changes from the inlet value, equal to 0.20 m/s, to the corresponding value in front of the manikin surface, equal to 0.15 m/s. The velocity profiles shown in the sections l_1 and l_2 vary little as the computational

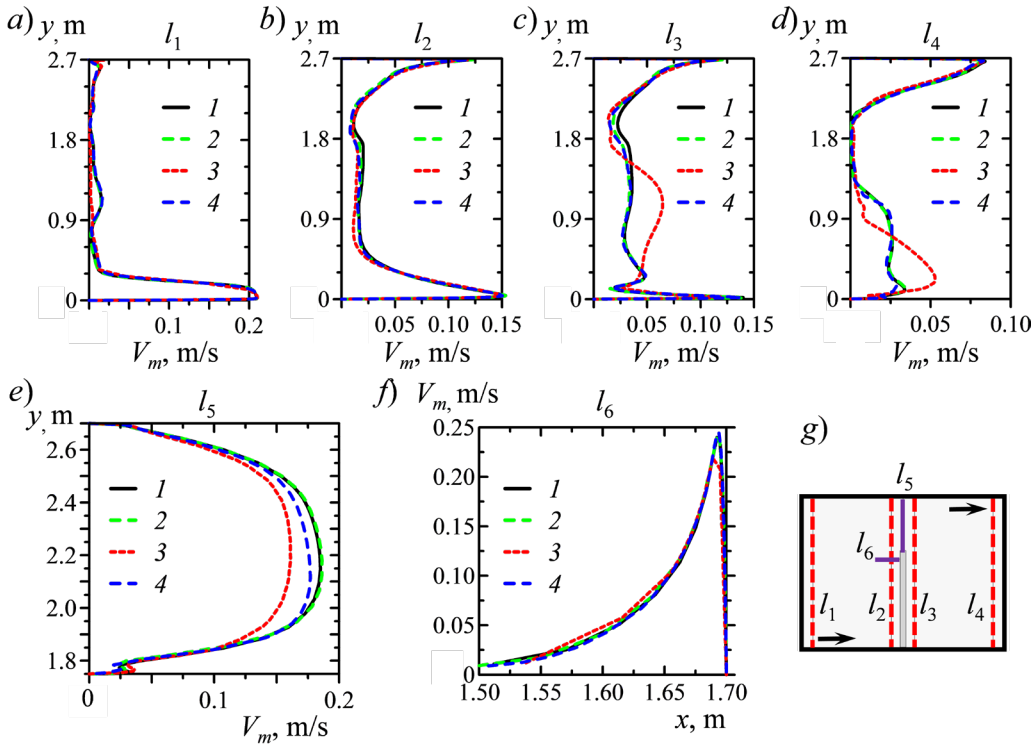

Fig. 3. Velocity profiles (*a* – *f*) plotted along lines $l_1 - l_6$ (see Fig. 1) obtained in solutions with meshes of different dimensions: 0.79 (*1*), 0.97 (*2*), 0.24 (*3*) and 1.16 (*4*); *g* shows the layout of the sections

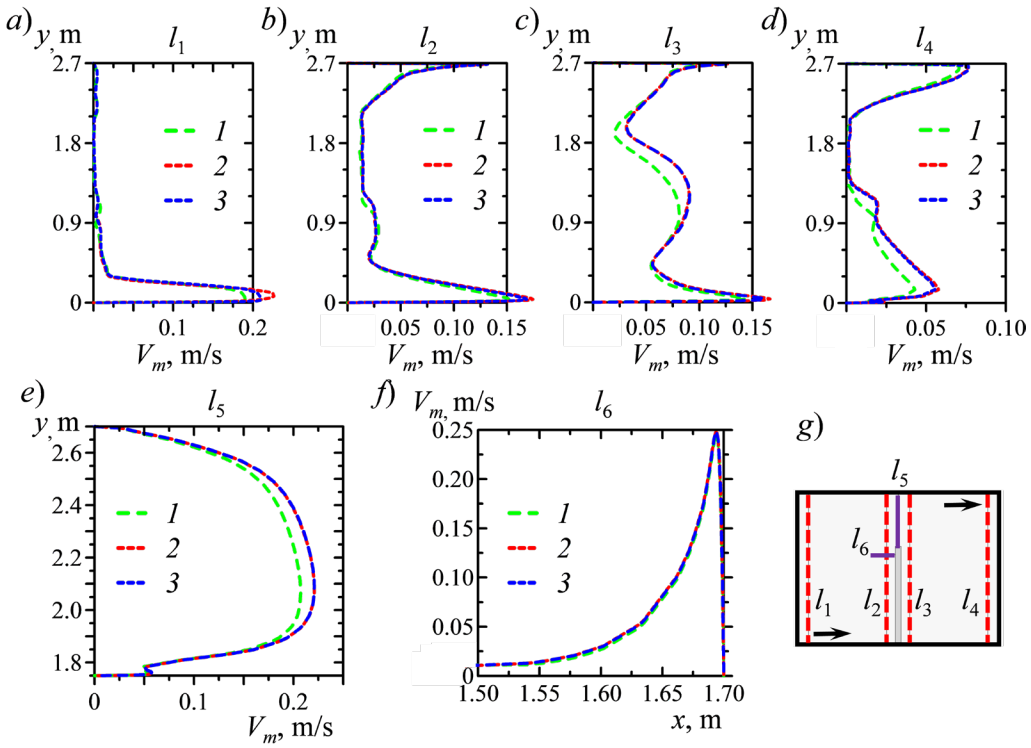

Fig. 4. Velocity profiles (a – f) plotted along the lines $l_1 - l_6$ (see Fig. 1) obtained for different inlet velocity distributions: uniform, equal to 0.181 m/s (*1*); non-uniform profile with a mean flow rate of 0.181 m/s (*2*); uniform, equal to 0.200 m/s (*3*); g is the layout of the sections

mesh is altered, although the solution on the coarsest mesh *3* is apparently somewhat different from the others. The obtained solution is considerably sensitive to the computational mesh used, which is manifested in the wake behind the manikin, as evident from the velocity graphs in the sections l_3 and l_4 for the bottom of the room at $y < 1.8$ m (Fig. 3,*c*,*d*). The flow here is characterized by reduced velocities. The solution obtained with a mesh with fewer elements (240,000) is markedly different from the solutions obtained on more refined meshes.

Velocity graphs plotted in sections l_5 and l_6 (Fig. 3,*e*,*f*), as well as in the top of the room in sections l_2 and l_3 at $y \geq 1.8$ m (Fig. 3,*b*,*c*) illustrate free-convection flow evolving near the surface of the thermal manikin and in the thermal plume above it due to buoyancy. A free-convection boundary layer emerges near the manikin surface, where the characteristic velocities in the upper part of the manikin reach 0.25 m/s (Fig. 3,*f*). A weak dependence of the solution on the dimension of the mesh used in the computations is observed in this region. The solution is somewhat sensitive to the mesh near the thermal plume generated above the manikin. Analyzing the data for the velocity distribution shown in Fig. 3,*e*, we can conclude that the velocities in this region, computed on a mesh with 240,000, are 15% lower than for other meshes. Importantly, the temperature fields obtained in the computations with all meshes considered practically coincide.

Notice that the three solutions obtained on two hexagonal meshes and on a mesh with clustered polyhedral elements are nearly the same. This means that the solution obtained on a mesh with clustered polyhedral cells can be considered weakly dependent on the mesh. Because of this, meshes with similar topology and dimensions were used for the configurations with the block-shaped and detailed manikins.

Sensitivity of the solution to the inlet velocity distribution. This sensitivity was considered for the configuration with the block-shaped manikin. Three inlet distributions were given:

uniform velocity distribution $V_{in} = 0.2$ m/s, recommended in [13];

uniform velocity distribution $V_{in} = 0.181$ m/s (mean value according to the experimental data given in the appendix to [13]);

velocity distribution obtained by additionally computing the flow in a rectangular channel $h_{in} \times w_{in}$ with a length of $15h_{in}$, with the mean flow rate of 0.181 m/s.

Fig. 4 shows the velocity profiles in the sections $l_1 - l_6$, obtained in solutions with different inlet velocity distributions. The graph in Fig. 4,*a* for the section l_1 shows the differences in the solutions obtained: the maximum velocities in the region of the near-wall jet (at $y < 0.6$ m) are in the range of 0.19 – 0.23 m/s. The velocity profiles in the remaining sections in Fig. 4 ($l_2 - l_6$), away from the inlet, only differ slightly: there are some differences in the region with reduced velocities in the sections l_3 and l_4, as well as in the thermal plume zone above the manikin (section l_5). The data presented in Fig. 4 indicate that the obtained solution changes little within the given range of inlet flow rates. A uniform distribution of $V_{in} = 0.2$ m/s was used in the main series of computations.

Effect of manikin shape on flow and heat transfer

Description of the flow structure. Fig. 5 illustrates the flow structure in a ventilated room, showing streamlines colored by velocity magnitude (Fig. 5,*a*,*c*,*d*), as well as the velocity fields in several sections of the room (Fig. 5,*b*,*e*,*f*), constructed for three manikin shapes.

The solutions obtained allow distinguishing two regions in the flow. The first one is where the near-wall jet propagates in the bottom of the room, interacting with the manikin. The second is the region with buoyancy-induced free-convection upward airflow. This flow evolves near and above the surface of the heated manikin, producing a thermal plume initiating secondary flow in the top of the room. Both regions have comparable velocities and interact little with each other.

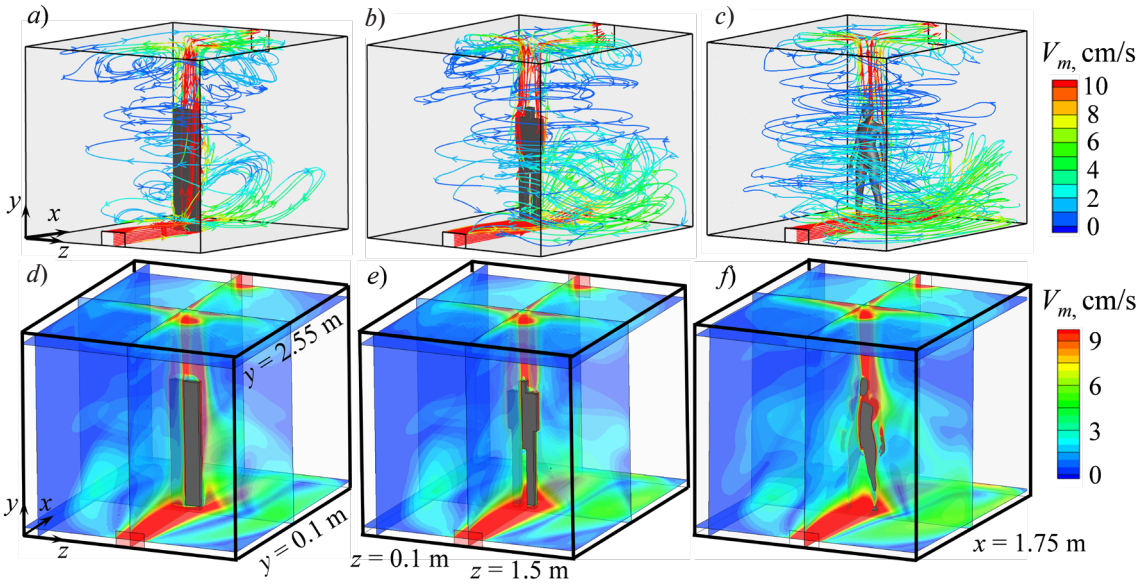

Fig. 5. Streamlines ($a - c$) colored by velocity magnitude; velocity magnitude fields ($d - f$) in several sections of the room, obtained in computations with three manikin shapes: parallelepiped (*a*, *d*), block (*b*, *e*), detailed (*c*, *f*)

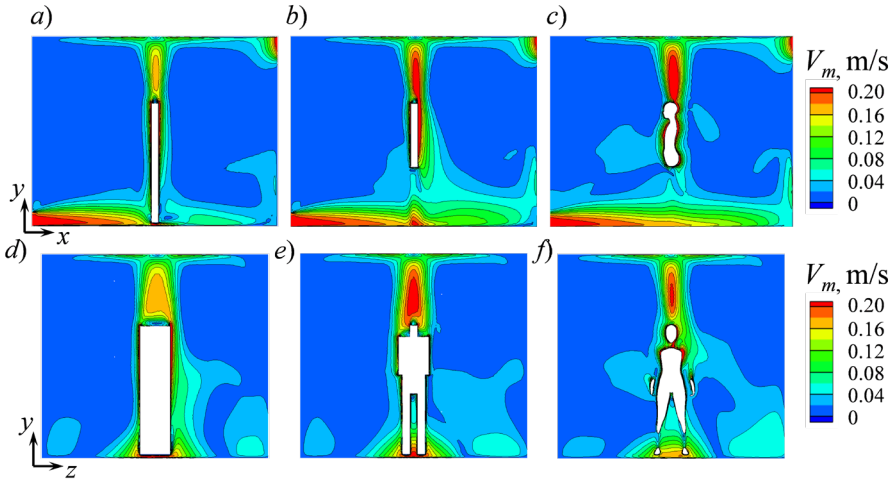

Fig. 6. Velocity magnitude distributions in two sections of the room: $z = 1.50$ m ($a - c$) and $x = 1.75$ m ($d - f$) computed for three manikin shapes: parallelepiped (a, d), block (b, e), detailed (c, f)

Fig. 6 shows the velocity fields in two central sections of the room: $z = 1.50$ m and $x = 1.75$ m (the velocity fields in Fig. 5,*d*,*e*,*f* are shown in isometric projection for the same sections). The flow structure obtained in the computations for all shapes of the manikin was asymmetric relative to the central plane $z = 1.5$ m. The near-wall jet spreads from the inlet along the floor, interacts with the manikin, attenuates and collides with the end wall opposite from the inlet. When the jet interacts with the wall, the flow rate is distributed unevenly, and, after turning around, the backflow along one of the bottom corners of the room appears to be more intense than along the opposite corner. This is evident from the local maximum velocities in the bottom right part of the room (Fig. 6,*d*,*e*,*f*). Notably, an asymmetric solution was obtained for both topologies of the computational mesh used for the parallelepiped-shaped manikin.

Figs. 5 and 6 show the results for the solution with the jet attaching to the right side wall, which is not unique, apparently. Two steady solutions (converging by residuals) were obtained for the parallelepiped-shaped manikin, with the jet attaching to the opposite side walls of the ventilated room. It was found for both computational mesh topologies that the solution was not unique.

The data obtained show that the global flow structure evolving in the room changes little with the change in the manikin shape. However, the local flow characteristics change depending on the manikin shape. For example, differences in the velocity fields are observed in the jet flow zone where the jet interacts with the manikin (Fig. 6). Differences in the characteristic velocities in the thermal plume above the manikin are observed in the region with free-convection flow. The maximum velocities in the thermal plume were 0.180 m/s for the parallelepiped-shaped manikin, 0.230 m/s for the block shape, 0.255 m/s for the detailed one. Thus, the intensity of free-convection flow is higher for manikins with detailed and block shapes than for the parallelepiped-shaped manikin.

Comparison of computational and experimental data. The results of numerical simulation were compared with the experimental data from [13] (Fig. 7). Fig. 7,*a* schematically shows the locations of sections I and II where PIV measurements were carried out in [13]. Both sections are in the center of the room ($z = 1.5$ m): section I above the manikin, and section II in front of it, near the face. Fig. 7,*b*,*c* shows the distribution of the velocity magnitude near the manikin surface in sections I and II based on experimental data from [13]. The velocity magnitude is constructed by two components V_x and V_y, however, the position of the coordinate axes x', y' is not described exactly

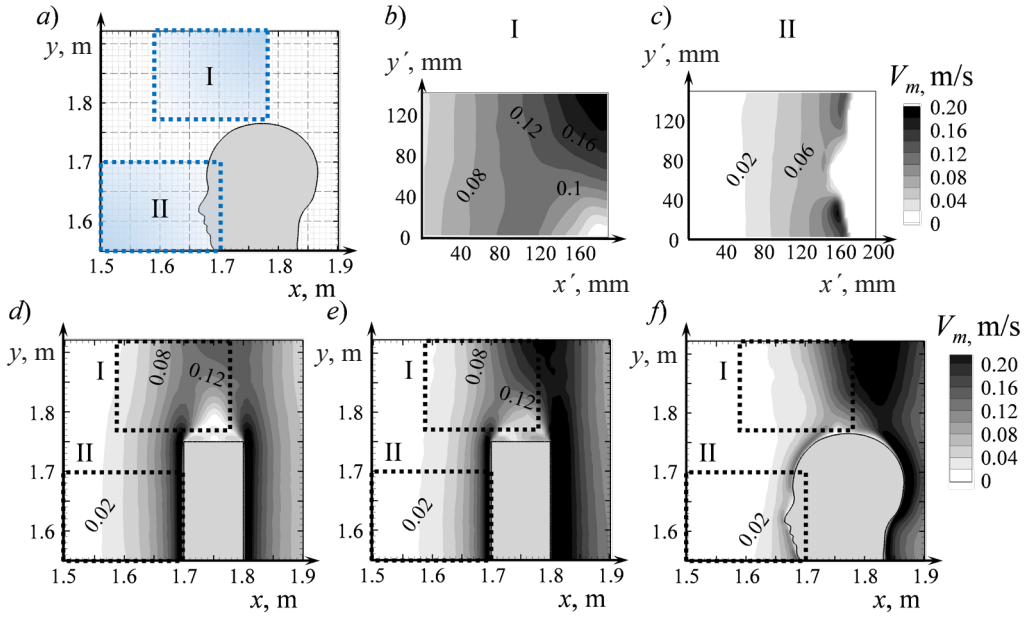

Fig. 7. Layout of sections I and II (*a*); comparison of velocity magnitude distributions in sections I (*b*) and II (*c*) based on the experimental data in [13] with the computational results for three manikin shapes: parallelepiped (*d*), block (*e*), detailed (*f*)
(central plane $z = 1.5$ m is shown)

in [13] for the experimental data given. The velocity fields obtained from the numerical simulation data for the cases with different manikin shapes are shown in Fig. 7,*d*,*e*,*f*. The velocity magnitude is constructed by three components but the contribution of the velocity component V_z in the central section is minimal.

As the shape of thermal manikin changes, the structure of upward flow near its surface changes considerably: the characteristic values velocities in front of the manikin (at $x < 1.7$ m) are noticeably higher for the cases with the block and parallelepiped shapes than for the detailed shape. The statement in the case of a simplified (flat) manikin shape, in the absence of any inhomogeneities on the surface, is close to the problem of free-convection flow near a heated plate, where the upward velocity increases upstream. Complex three-dimensional free-convection upward flow evolves near the front of the torso in the case with the detailed manikin shape; this flow changes direction around the manikin's shoulders, and, judging from the streamlines (see Fig. 5,*d*), the air rising near the torso flows over the shoulders to the back of the manikin, subsequently movinh upward along the back of the head. Thus, the velocities in the facial region are noticeably lower for a detailed manikin than those obtained for simplified manikins (parallelepiped and block).

Fig. 8 shows the velocity distributions in several sections of the room, obtained in the experiment and through computations for three manikin shapes. Fig. 8,*c* shows the velocity distribution along line l_6 located in section II; the coordinate x' is measured from the surface of the manikin's face. The computed flow structure near the detailed manikin in section II (near the face) agrees with the flow structure obtained in the experiment both qualitatively (see Fig. 7) and quantitatively (Fig. 8,*c*). The velocities in this region appear to be overestimated by approximately two times for simpler manikin shapes (both block and parallelepiped).

The velocities in section I can be used to estimate the intensity of the thermal plume emerging above the manikin. The velocity distribution along the line l_5 in this section is shown in Fig. 8,*b*. As noted above, changing the shape of the manikin substantially changes the position of the thermal plume and the characteristic velocities of the upward flow. The data on the velocity in section I

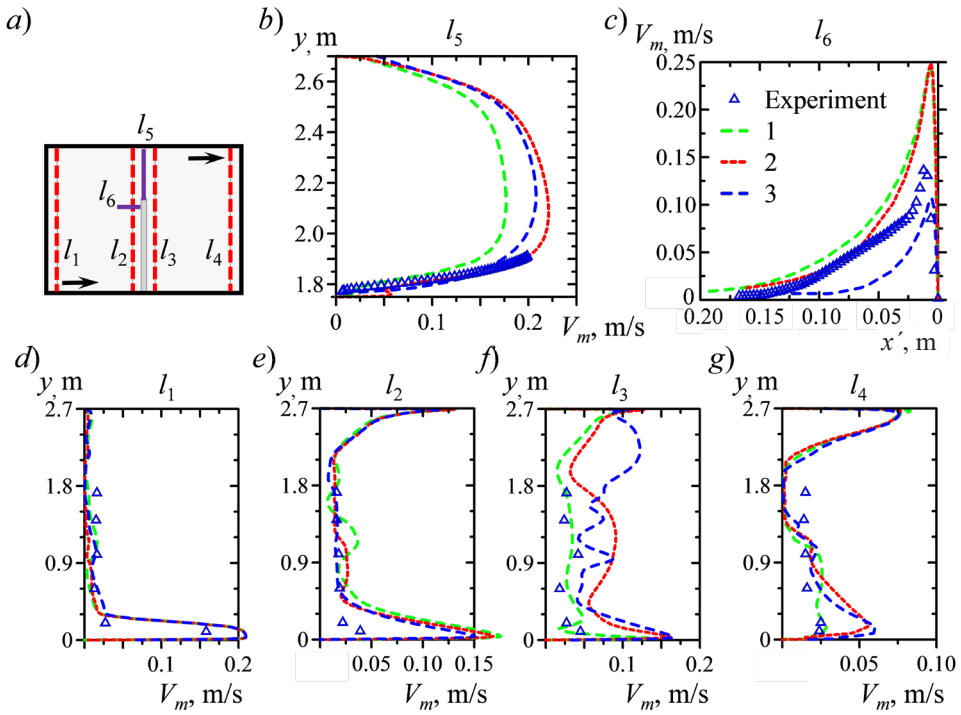

Fig. 8. Layout of the sections (*a*); velocity profiles plotted along the lines $l_1 - l_6$ ($b - g$), obtained in solutions using three manikin shapes:
parallelepiped (*1*), block (*2*) and detailed (*3*)

that are closest to the experiment can be obtained using both the detailed and block shapes of the manikin.

The velocity distributions away from the manikin surface are shown in Fig. 8,*d*,*e*,*g*. Analyzing the graphs, we can see satisfactory agreement between the computational results and experimental data in the region of the near-wall jet (sections l_1 and l_2 at $y < 0.3$ m): however, the computed velocities are somewhat higher than experimental data. The characteristic velocities amount to 0.025 m/s in the region of low-velocity flow in front of manikin (section l_1 at $y > 0.3$ m and l_2 at $0.6 < y < 2.1$ m). Here, the computational data generally agree with the experimental velocities. Changing the shape of the manikin apparently has a rather weak effect on the flow structure in this region.

The shape of the manikin has a more pronounced effect on the flow structure in the section l_3, located directly behind the manikin near the surface (Fig. 8,*f*). The variation range of characteristic velocities does not exceed 0.1 m/s in this region. Experimental velocities are lower than those computed for all manikin shapes. Evidently, the reason for the differences between the computational and experimental data in this region is that the position of the manikin's legs is not reproduced exactly in numerical simulation, even in the case of detailed geometry. At the same time, the computational results related to velocity for three different cases of the manikin shape coincide both with each other and with the experimental data in section l_4 (Fig. 8,*g*). There are some differences in the data in the lower corner of the room with $y < 0.6$ m.

Parameters of heat release from the manikin surface. The temperature distributions T_w over the surface of the thermal manikin obtained for cases with a different manikin shape are shown in Fig. 9,*a*–*c*. The corresponding distributions of dimensionless heat transfer, the Nusselt number

$$\mathrm{Nu} = q_w l_w / \lambda \left(T_{in} - T_w \right),$$

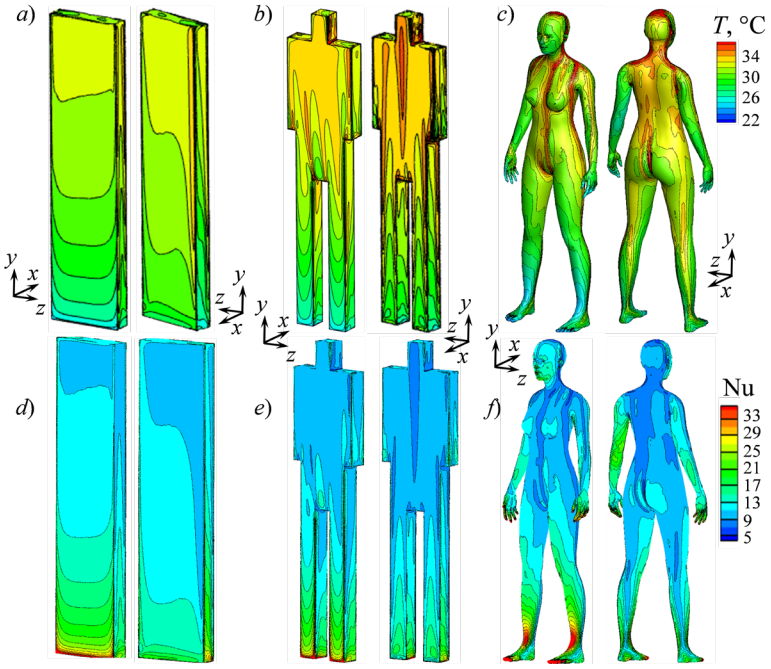

Fig. 9. Computed distributions of temperature ($a - c$) and Nusselt number ($d - f$) over the surfaces of manikins with different shapes: parallelepiped (a, d), block (b, e) and detailed (c, f)

where $l_m = 0.1$ m for all manikin shapes, are shown in Fig. 9,*d*,*e*,*f*.

Table 3 shows the limits within which the temperature varies over the surfaces of manikins with different shapes: minimum $T_{w,\min}$, maximum $T_{w,\max}$; the temperatures $\langle T_w \rangle$ and Nusselt numbers $\langle \mathrm{Nu} \rangle$ averaged over the manikin surface are also shown.

The temperature distributions for the upwind (opposite to the direction of the x axis) and downwind (along the direction of the x axis) sides differ for all manikin shapes considered. The temperatures are higher from the downwind than from the upwind side; acccordingly, the heat release is lower from this side. There are local differences in temperature distributions for different manikin shapes. In particular, the distribution is almost uniform in the z-direction for the simplest shape (parallelepiped), while a non-uniform distribution is observed for the detailed shape.

Notably, the temperature increases and the heat transfer decreases along the height of the thermal manikin. The minimum temperature on the surface of the manikin is in its lower part. This value is close to the temperature of the inlet air jet $T_{in} = 22$°C, varying slightly from one shape of the manikin to another. The maximum temperature is observed in the upper part of the manikin, near the curved surface. The value $T_{w,\max}$ greatly depends on the shape of the manikin, amounting to 33.6 °C for the parallelepiped, 41.7 °C for the block and 51.4 °C for the detailed shape (see Table 3). The wide variation range of the maximum temperatures corresponding to the detailed shape of the manikin confirms that simplifying the shape of the manikin can produce large errors for the estimated local parameters of thermal comfort. We should note, however, that given such high local temperatures detected on the surface of the detailed manikin, mechanisms of thermostatic control are engaged in the real conditions; neglecting these mechanisms can produce substantially larger uncertainties.

The mean temperature is an integral parameter for the given problem, weakly depending on the geometric shape of the manikin used and amounting to about 31 °C. Importantly, the experimental value of the mean temperature is consistent with the computed one.

Table 3

Comparison of computed and experimental parameter values for heat transfer from the surfaces of manikins with different shapes

Parameter	Computed value for			Experiment
	parallelepiped	block	detailed	detailed
$T_{w,\min}$, °C	23.18	23.21	22.33	–
$T_{w,\max}$, °C	33.60	41.70	51.40	–
$\langle T_w \rangle$, °C	30.50	31.30	30.70	32.2
$\langle \mathrm{Nu} \rangle$	13.2	12.1	12.6	10.6

Conclusion

We have carried out a numerical study on the influence that the shape of a heated thermal manikin has on the flow and heat transfer of air in a model room with displacement ventilation. We have considered three shapes of the manikin: parallelepiped, block and detailed. The computations were performed based on the RANS approach using the standard k-ε turbulence model.

The sensitivity of the solution to topology and dimension of the computational mesh was examined for the simplest shape, the parallelepiped. It was confirmed that a mesh comprised of polyhedral elements with a dimension of about one million cells, refined near the air jet and the thermal plume, making it possible to obtain a solution that weakly depends on the mesh parameters. We have examined the influence of the dynamic conditions at the inlet on the obtained solution: the flow structure in the vicinity of the manikin was found to be weakly sensitive to the inlet velocity profile in the given velocity range.

The computations indicate that the global flow structure evolving in the room is not symmetrical with respect to the central plane. Two converging solutions were obtained for one of the geometrical configurations, where the jet deflects towards the opposite side walls.

Apparently, the intensity of free-convection flow was higher in the cases when the detailed and block-type shapes of the manikin was used compared to the configuration with the manikin with the simplest shape, a parallelepiped. Furthermore, the simplification of the manikin shape significantly affects the local characteristics of flow and heat transfer. On the other hand, the integral parameters only weakly depend on the shape of the manikin used.

As a whole, we can conclude that using a simplified shape of the manikin is reasonable in the cases when it is necessary and does not produce any significant distortion of the solution.

The study was financed by the Russian Foundation for Basic Research, grant no. 20-58-18013.

REFERENCES

1. **Fanger P.O., Melikov A.K., Hanzawa H., Ring J.,** Air turbulence and sensation of draught, Energy and Buildings. 12 (1) (1988) 21–39.

2. ANSI/ASHRAE Standard 62.1–2019. Ventilation for acceptable indoor air quality. 2019. https://www.ashrae.org/technical-resources/bookstore/standards-62-1-62-2

3. **Pei J., Rim D.,** Quality control of computational fluid dynamics (CFD) model of ozone reaction with human surface: Effects of mesh size and turbulence model, Building and Environment. 189 (February) (2021) 107513.

4. **Al Assaad D., Ghali K., Ghaddar N., et al.,** Evaluation of different personalized ventilation air terminal devices: Inhalation vs. clothing-mediated exposures, Building and Environment. 192 (April) (2021) 107637.

5. **Ma J., Qian H., Nielsen P.V., et al.,** What dominates personal exposure? Ambient airflow pattern or local human thermal plume, Building and Environment. 196 (June) (2021) 107790.

6. **Liu J., Zhu S., Kim M.K., Srebric J.,** A review of CFD analysis methods for personalized ventilation (PV) in indoor built environments, Sustainability. 11 (15) (2019) 4166.

7. **Berrouk A.S., Lai A.C.K., Cheung A.C.T., Wong S.L.,** Experimental measurements and large eddy simulation of expiratory droplet dispersion in a mechanically ventilated enclosure with thermal effects, Building and Environment. 45 (2) (2010) 371–379.

8. **Taghinia J.H., Rahman M.M., Lu X.,** Effects of different CFD modeling approaches and simplification of shape on prediction of flow field around manikin, Energy and Buildings. 170 (1 July) (2018) 47–60.

9. **Zukowska D., Melikov A., Popiolek Z.,** Thermal plumes above a simulated sitting person with different complexity of body geometry, Proceedings of Roomvent 2007, The Tenth International Conference on Air Distribution in Rooms, Helsinki, Finland, June 13–15, 3 (2007) 191–198.

10. **Topp C., Hesselholt P., Trier M.R., Nielsen P.V.,** Influence of geometry of thermal manikins on room airflow, Proceedings of ISIAQ 7th International Conference "Healthy Buildings 2003", Singapore, December 7–22, 2003.

11. **Brohus H., Nielsen P.V.,** CFD models of persons evaluated by full-scale wind channel experiments, Proceedings of Roomvent'96, The Fifth International Conference on Air Distribution in Rooms, Yokohama, Japan, July 17–19, 1996. 2 (1996) 137–144.

12. **Yan Y., Li X., Yang L., Tu J.,** Evaluation of manikin simplification methods for CFD simulations in occupied indoor environments, Energy and Buildings. 127 (1 September) (2016) 611–626.

13. **Nielsen P.V., Murakami S., Kato S., et al.,** Benchmark tests for a computer simulated person, Indoor Environmental Engineering, Aalborg University, Aalborg, Denmark, 2003.

14. **Deevy M., Sinai Y., Everitt P., et al.,** Modelling the effect of an occupant on displacement ventilation with computational fluid dynamics, Energy and Buildings. 40 (3) (2008) 255–264.

15. **Martinho N., Lopes A., Silva M.,** CFD modelling of benchmark tests for flow around a detailed computer simulated person, Proceedings of the 7th International Thermal Manikin and Modelling Meeting (at University of Coimbra), September, 2008.

16. **Martinho N., Lopes A., da Silva M.G.,** Evaluation of errors on the CFD computation of air flow and heat transfer around the human body, Building and Environment. 58 (December) (2012) 58–69.

17. **Wilcox D.C.,** Turbulence modeling for CFD, 3-th Ed., DCW Industries, Inc., La Cañada, California, 2006.

18. **Launder B.E., Spalding D.B.,** Lectures in mathematical models of turbulence. Academic Press, London, 1972.

Received 27.06.2021, accepted 20.08.2021.

THE AUTHORS

STEPASHEVA Ekaterina D.
Peter the Great St. Petersburg Polytechnic University
29 Politechnicheskaya St., St. Petersburg, 195251, Russian Federation
momoirin@yandex.ru

ZASIMOVA Marina A.
Peter the Great St. Petersburg Polytechnic University
29 Politechnicheskaya St., St. Petersburg, 195251, Russian Federation
zasimova_ma@spbstu.ru

IVANOV Nikolay G.
Peter the Great St. Petersburg Polytechnic University
29 Politechnicheskaya St., St. Petersburg, 195251, Russian Federation
ivanov_ng@spbstu.ru

СПИСОК ЛИТЕРАТУРЫ

1. **Fanger P.O., Melikov A.K., Hanzawa H., Ring J.** Air turbulence and sensation of draught // Energy and Buildings. 1988. Vol. 12. No. 1. Pp. 21–39.

2. ANSI/ASHRAE Standard 62.1–2019. Ventilation for acceptable indoor air quality. 2019. https://www.ashrae.org/technical-resources/bookstore/standards-62-1-62-2

3. **Pei J., Rim D.** Quality control of computational fluid dynamics (CFD) model of ozone reaction with human surface: Effects of mesh size and turbulence model // Building and Environment. 2021. Vol. 189. February. P. 107513.

4. **Al Assaad D., Ghali K., Ghaddar N., Katramiz E., Ghani S.** Evaluation of different personalized ventilation air terminal devices: Inhalation vs. clothing-mediated exposures // Building and Environment. 2021. Vol. 192. April. P. 107637.

5. **Ma J., Qian H., Nielsen P.V., Liu L., Li Y., Zheng X.** What dominates personal exposure? Ambient airflow pattern or local human thermal plume // Building and Environment. 2021. Vol. 196. June. P. 107790.

6. **Liu J., Zhu S., Kim M.K., Srebric J.** A review of CFD analysis methods for personalized ventilation (PV) in indoor built environments // Sustainability. 2019. Vol. 11. No. 15. P. 4166.

7. **Berrouk A.S., Lai A.C.K., Cheung A.C.T., Wong S.L.** Experimental measurements and large eddy simulation of expiratory droplet dispersion in a mechanically ventilated enclosure with thermal effects // Building and Environment. 2010. Vol. 45. No. 2. Pp. 371–379.

8. **Taghinia J.H., Rahman M.M., Lu X.** Effects of different CFD modeling approaches and simplification of shape on prediction of flow field around manikin // Energy and Buildings. 2018. Vol. 170. 1 July. Pp. 47–60.

9. **Zukowska D., Melikov A., Popiolek Z.** Thermal plumes above a simulated sitting person with different complexity of body geometry // Proceedings of Roomvent 2007, The Tenth International Conference on Air Distribution in Rooms. Helsinki, Finland, June 13–15, 2007. Vol. 3. Pp. 191–198.

10. **Topp C., Hesselholt P., Trier M.R., Nielsen P.V.** Influence of geometry of thermal manikins on room airflow // Proceedings of ISIAQ 7th International Conference "Healthy Buildings 2003". Singapore, December 7–22, 2003. 6 p.

11. **Brohus H., Nielsen P.V.** CFD models of persons evaluated by full-scale wind channel experiments // Proceedings of Roomvent'96, The Fifth International Conference on Air Distribution in Rooms. Yokohama, Japan, July 17–19, 1996. Vol. 2. Pp. 137–144.

12. **Yan Y., Li X., Yang L., Tu J.** Evaluation of manikin simplification methods for CFD simulations in occupied indoor environments // Energy and Buildings. 2016. Vol. 127. 1 September. Pp. 611–626.

13. **Nielsen P.V., Murakami S., Kato S., Topp C., Yang J.-H.** Benchmark tests for a computer simulated person. Aalborg, Denmark: Indoor Environmental Engineering, Aalborg University, 2003. 7 p.

14. **Deevy M., Sinai Y., Everitt P., Voigt L., Gobeau N.** Modelling the effect of an occupant on displacement ventilation with computational fluid dynamics // Energy and Buildings. 2008. Vol. 40. No. 3. Pp. 255–264.

15. **Martinho N., Lopes A., Silva M.** CFD modelling of benchmark tests for flow around a detailed computer simulated person // Proceedings of the 7th International Thermal Manikin and Modelling Meeting (at University of Coimbra). September, 2008. 6 p.

16. **Martinho N., Lopes A., da Silva M.G.** Evaluation of errors on the CFD computation of air flow and heat transfer around the human body // Building and Environment. 2012. Vol. 58. December. Pp. 58–69.

17. **Wilcox D.C.** Turbulence modeling for CFD. 3-th Ed. La Cañada, California: DCW Industries, Inc., 2006. 515 p.

18. **Launder B.E., Spalding D.B.** Lectures in mathematical models of turbulence. London: Academic Press, 1972. 169 p.

Статья поступила в редакцию 27.06.2021, принята к публикации 20.08.2021.

СВЕДЕНИЯ ОБ АВТОРАХ

СТЕПАШЕВА Екатерина Дмитриевна – *студентка Физико-механического института Санкт-Петербургского политехнического университета Петра Великого, Санкт-Петербург, Российская Федерация.*

195251, Российская Федерация, г. Санкт-Петербург, Политехническая ул., 29

momoirin@yandex.ru

ЗАСИМОВА Марина Александровна – *кандидат физико-математических наук, ассистент Высшей школы прикладной математики и вычислительной физики Санкт-Петербургского политехнического университета Петра Великого, Санкт-Петербург, Российская Федерация.*

195251, Российская Федерация, г. Санкт-Петербург, Политехническая ул., 29

zasimova_ma@spbstu.ru

ИВАНОВ Николай Георгиевич – *кандидат физико-математических наук, доцент Высшей школы прикладной математики и вычислительной физики, заведующий научно-исследовательской лабораторией гидроаэродинамики Санкт-Петербургского политехнического университета Петра Великого, Санкт-Петербург, Российская Федерация.*

195251, Российская Федерация, г. Санкт-Петербург, Политехническая ул., 29

ivanov_ng@spbstu.ru

DOI: 10.18721/JPM.14308
UDC 53.07, 538.9

PROJECTING CLASSICAL MOTT POLARIMETER

V.N. Petrov[1], **P.G. Gabdullin**[1], **A.V. Pavlov**[1],
A.B. Ustinov[1], **V.N. Strocov**[2], **J.H. Dil**[2]

[1] Peter the Great St. Petersburg Polytechnic University,
St. Petersburg, Russian Federation;

[2] Paul Scherrer Institute,
Brugg, Switzerland

In this paper we describe a new spin detector designed and manufactured at SPbPU. This device makes it possible to analyze the polarization of the secondary electron flux conserving the information about the electrons' spatial distribution. The main stages of development, construction and testing the detector are discussed in details. As a result, the possibility of implementing such devices has been proved in principle. At the same time, both high spatial resolution of this device and its efficiency were demonstrated. Combining such detectors with hemispherical energy analyzers will make it possible to obtain spin-resolved dispersion images of the structure under study.

Keywords: Mott detector, spin, electron spectroscopy, secondary electron polarization

Citation: Petrov V.N., Gabdullin P.G., Pavlov A.V., Ustinov A.B., Strocov V.N., Dil J.H., Projecting classical Mott polarimeter, St. Petersburg Polytechnical State University Journal. Physics and Mathematics. 14 (3) (2021) 107–115. DOI: 10.18721/JPM.14308

ПРОЕКЦИОННЫЙ КЛАССИЧЕСКИЙ ДЕТЕКТОР МОТТА

В.Н. Петров[1], **П.Г. Габдуллин**[1], **А.В. Павлов**[1],
А.Б. Устинов[1], **В.Н. Строков**[2], **Ж.Х. Дил**[2]

[1] Санкт-Петербургский политехнический университет Петра Великого,
Санкт-Петербург, Российская Федерация;

[2] Институт Пауля Шеррера,
г. Бругг, Швейцария

В работе описывается новый спиновый детектор, разработанный, сконструированный и изготовленный в СПбПУ. Такой прибор позволяет анализировать поляризацию потока вторичных электронов, сохраняя информацию об их пространственном распределении. Представлены основные этапы создания и тестирования разработанного устройства, продемонстрированы результаты испытаний его отдельных узлов. В результате доказана принципиальная возможность реализации подобных устройств. При этом продемонстрированы как высокое пространственное разрешение данного прибора, так и его эффективность. Совмещение таких детекторов с полусферическими энергоанализаторами современных электронных спектрометров позволит получать спин-разрешенные дисперсионные зависимости исследуемой структуры.

Ключевые слова: детектор Мотта, спин, электронная спектроскопия, поляризация вторичных электронов

Ссылка при цитировании: Петров В.Н., Габдуллин П.Г., Павлов А.В., Устинов А.Б., Строков В.Н., Дил Ж.Х. Проекционный классический детектор Мотта // Научно-технические ведомости СПбГПУ. Физико-математические науки. 2021. Т. 14. № 3. С. 107–115. DOI: 10.18721/JPM.14308

Introduction

The spin configuration of a certain ensemble of particles is important for describing many physical processes and phenomena. A physical quantity known as polarization P is used to characterize the experimentally measured spin structure. Polarization relative to a specific quantization axis follows the expression

$$P = (N^{\uparrow} - N^{\downarrow})/(N^{\uparrow} + N^{\downarrow}),$$

where $N^{\uparrow}$, $N^{\downarrow}$ are the numbers of electrons with spin parallel or antiparallel to quantization axis, respectively. The projection of spin can take values $+\hbar/2$ and $-\hbar/2$.

The spin degree of freedom can be used to describe a variety of physical phenomena. The results of spin measurements made a major contribution to understanding such physical phenomena as giant magnetoresistance [1], formation of magnetic domains [2, 3], Rashba effect [4], and appearance of topologically protected states in solids [5].

Polarization of particle fluxes can be detected directly, for example, by using the classical Mott polarimeter [6, 7]. Electrons in such a device are accelerated to energies of the order of 40 – 100 keV, and subsequently scattered by gold foil. Due to spin-orbit interaction, a spin-dependent scattering occurs on the gold foil, allowing electrons with a spin projection parallel to the the quantization axis to be slightly more probably scattered into one of the detectors, and electrons with an opposite spin projection to the other.

The resulting scattering asymmetry A can be expressed as

$$A = (N_1 - N_2)/(N_1 + N_2),$$

where N_1, N_2 are the numbers of electrons captured by the first and second detectors, respectively.

Since the potential of the spin-orbit interaction depends linearly on spin projection, it can be assumed that asymmetry is proportional to the polarization value, i.e., $A \sim P$. This allows calculating the polarization as follows: $P = A/S$, where S is the Sherman function. The value of Sherman function is determined by the false asymmetry arising from imperfection of the experimental setup.

Angle-resolved photoemission spectroscopy (ARPES) is an important modern experimental technique [8]. Using this method, it is possible to obtain angle-resolved secondary electron spectra emitted from a sample [8]. Since the emission angle of electrons in a solid is related to the value of electron momentum, ARPES can be used to directly measure the electronic band dispersion for electrons $E(\mathbf{k})$ (E is the electron energy, $\mathbf{k}$ is the wave vector).

The available devices typically operate as follows: the secondary electrons are emitted from the sample, then fall to the energy analyzer, where they are separated by their energy and entrance angle. The electron flux is then amplified by means of a microchannel plate. After passing the microchannel plate, the electrons fall on the fluorescent screen, where they are converted into visible radiation subsequently recorded by a camera outside the vacuum chamber.

Such energy analyzers allow simultaneous measurement of the number of particles, their momenta and energies in a wide range, thus significantly reducing the time required to accumulate data. A hemispherical energy analyzer used in ARPES in combination with a Mott

polarimeter makes it possible to experimentally measure spin and angle-resolved electronic dispersion (SARPES) [9]. This method serves as an indispensable tool for studying new materials.

A serious drawback of available SARPES devices is that the existing Mott polarimeters are single-channel devices, which means that only a small portion of the secondary electron flux is recorded at each moment in time, with the energy and momentum projection in a narrow range. This outweighs the potential benefits that spatially sensitive energy analyzers could provide. This fact significantly reduces the effectiveness of the experiments conducted.

This problem may be solved using a Mott polarimeter which combines spin analysis with the spatially sensitive electron detectors. The first proposal for such a device was presented in [10]. In this work, we describe process of creating and testing a multichannel polarization detector based on the classical Mott polarimeter.

Design and development

The multichannel polarization detector was developed based on the classical Mott polarimeter, with changes introduced to ensure spatial resolution.

Fig. 1 shows a schematic representation of the Mott polarimeter constructed. The construction allowed for assembling the device right after the exit aperture of the PHOBOS 150 hemispherical energy analyzer (by SPECS, Germany).

The device operates as follows. After passing through the energy analyzer, the electron flux propagates through the entrance aperture *1* of the Mott polarimeter. Then the electron flux passes through a focusing four-section electrostatic lens *2*. The focused electron beam is then accelerated by a 40 kV potential and enters drift space *3*. This beam can then scatter either on the CCD matrix or gold foil *5* (this is selected by turning the vacuum manipulator).

The first mode (the CCD matrix is in the center of the detector) is required to adjust the electro-optical lens of the detector. The image is obtained by the CCD matrix located at the center of detector, right after electrostatic lens (Fig. 2). In the second mode, electrons are scattered by gold foil. In this case, due to spin-dependent scattering on the gold foil, the electrons have a

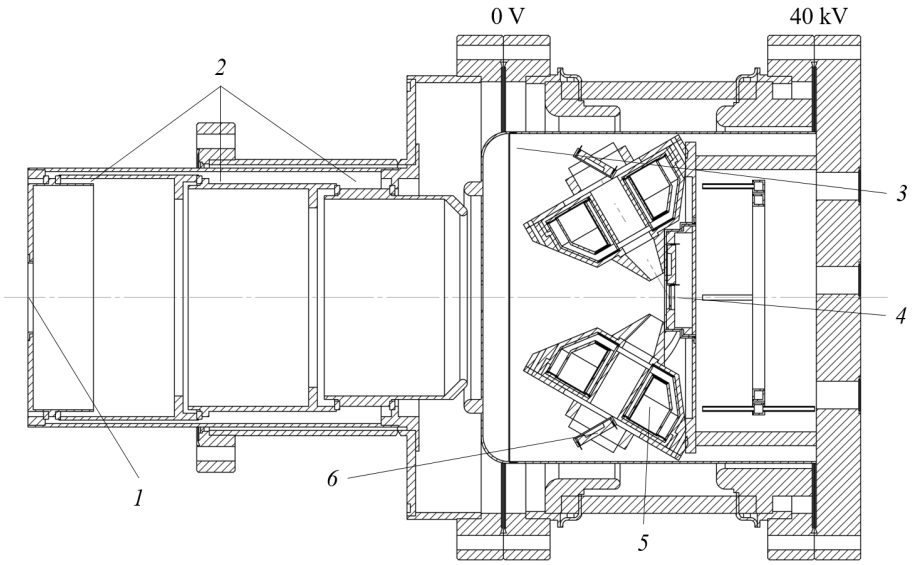

Fig. 1. Scheme of multichannel Mott polarimeter:
1: entrance aperture, *2*: focusing electrostatic lens, *3*: electrostatic screen, *4*: gold foil (or CCD matrix), *5*: magnetic lens, *6*: CCD array. The captions '0 V' and '40 kV' correspond to the potentials applied to the respective parts of the device

higher probability of falling into one of four detectors depending on spin orientation (two detectors for each spin projection). Thus, the device is capable of analyzing the polarization of the electron flux.

After scattering on gold foil, the electrons enter the detector, which consists of a magnetic focusing lens (position *5* in Fig. 1) and CCD matrix *6*, which is capable of detecting high-energy electrons. The magnetic lens is designed to focus the scattered electrons, and the matrix serves as a detector recording not only the arrival of the particle but also the position of the pixel that captures it. Hamamatsu S7170 sensors (Japan) were chosen as the detector, as they have neither a protective layer nor an ultraviolet filter, which allows them to effectively detect high-energetic charged particles. Thus, the device records collision events between accelerated secondary electrons and the CCD matrix. Figs. 2 and 3 show images of the aperture located inside the energy analyzer, obtained on a CCD array in secondary electron counting mode. The size of each pixel (px) in such an array is 24 μm × 24 μm, its resolution is 512 px × 512 px.

So, such device consequently would not only be capable of spin analysis of the electron flux but can also detect the electrons' spatial distribution. In particular, it can measure the spin-resolved electron dispersions $E(\mathbf{k})$.

Testing and calibration of the Mott polarimeter

Construction of a device is a complex process comprising several stages and procedures such as making drawings of the device, manufacturing, welding and assembling its componentss, conducting vacuum tightness tests. A series of tests is then carried out for dielectric strength for the insulators that are used in the detector.

In a device which functions correctly, the electron flux is supposed to be focused on the gold foil without any distortion, then the electron flux reflects from the foil focused and then collected on the CCD matrix. Since each point in the cross section of the electron beam carries information about the physical properties of the given sample, the level of distortion should be kept to a minimum.

To adjust the electrostatic and magnetic optics, a plate with a pattern made up of holes 0.50 and 0.25 mm in diameter was placed inside the energy analyzer. After electrons passed through the energy analyzer, they were distributed in space in accordance with their energy and emission angle. Traveling through the aperture, this electron flux was converted into an image of a point array, where inside each point the electrons had similar energies and emission angles.

A CCD matrix was installed in the center of the Mott polarimeter (instead of the gold foil) to test the electrostatic lens. An example of an image obtained in secondary electron counting mode is shown in Fig. 2. Here the X axis is parallel to the direction along the energy axis of the analyzer, and the Y axis is parallel to the direction along which the emission angle of electrons in the beam was measured. A sharp image of the aperture on the CCD matrix corresponds to optimal focusing of the electrostatic lens. Adjusting the electron optics and changing the accelerating voltage made it possible to choose an amplification factor of the lens suitable for the experiment.

After a sharp image was obtained on the CCD matrix in the center of the Mott polarimeter, the voltages at the electrodes of the electrostatic lens were recorded, and gold foil was installed in the center of the polarimeter.

The magnetic lenses were adjusted by varying the value of the current flowing through the coils. This current generates a magnetic field where the electron trajectories are twisted around the axis of the lens. This provides the required focusing, but inevitably produces some distortion to the image.

Fig. 3 shows images of the aperture on the CCD matrix located behind the magnetic lens. The im-ages on the left and right arrays of the Mott polarimeter should be rotated in different directions if the direction of current is the same in both lenses. Slight blurring of the images is due to the aberrations in the complex electron-optical system, and they can be further minimized by finer adjustment of the optics and image post-processing.

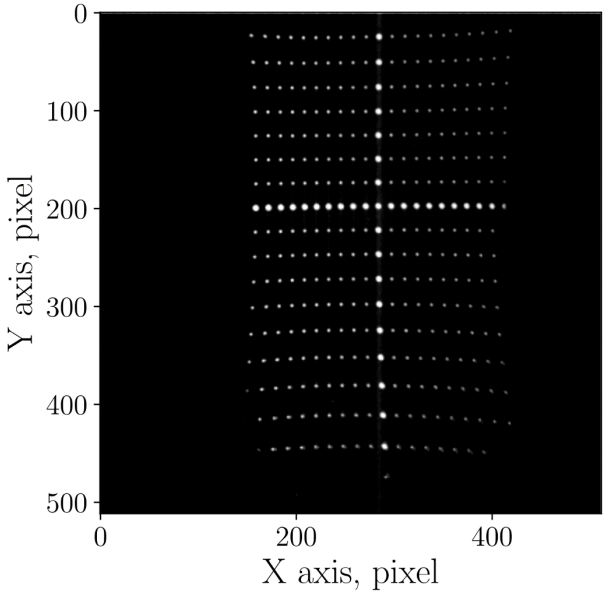

Fig. 2. Images of aperture inside the energy analyzer taken on the CCD matrix in the center of the Mott polarimeter.
The intensity at each point is proportional to the number of electrons hitting a given pixel of the matrix The background corresponding to the dark current of the CCD matrix and illumination from inelastic electrons was subtracted from the image

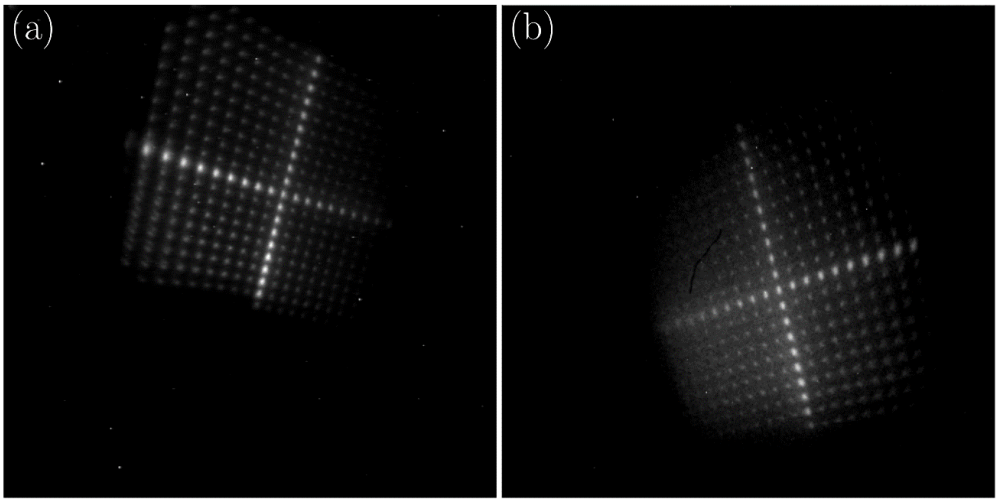

Fig. 3. Images of the aperture installed in the same location as in Fig. 2 but obtained on the first (*a*) and the second (*b*) CCD detectors behind the magnetic lenses (see also explanations to Fig. 2)

As the last test of the system, we measured the asymmetry of electron beam from a magnetized sample by the Mott polarimeter. An amorphous iron boride (FeB) sample has been chosen as a magnetic target. As a soft magnetic with a rectangular hysteresis loop, this material has stable surface magnetism, which makes it convenient for experiments. The sample was irradiated with a beam of primary electrons, while the flux of secondary electrons was directed to the energy analyzer to determine the energy dispersion, and then into the Mott polarimeter for spin analysis.

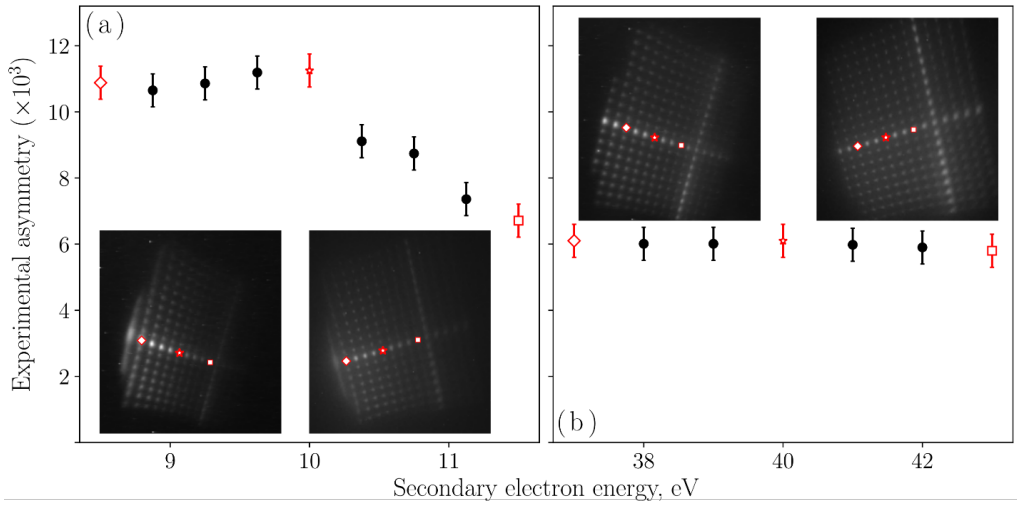

Fig. 4. Asymmetry of electron flux depending on the energy of low- (*a*) and high-energy (*b*) secondary electrons emitted from a magnetized FeB sample (measurements were carried out by a Mott polarimeter). The insets show images from two CCD matrices (see Fig. 3), where diamonds, stars and boxes mark the points serving as the sources of the signal used to calculate the asymmetry (marked with the same symbols on the graphs)

Fig. 4 demonstrates the dependencies of asymmetry on the energy of secondary electrons for two energy ranges: 8.5 – 11.5 and 37 – 43 eV (central values of energy are 10 and 40 eV, respectively). As noted above, the electron flux is converted into a point array by aperture as it passes through the energy analyzer. In this case, the electrons inside each point have close values of energy and similar emission angles. This can be used to obtain the asymmetry of the electron beam as a function of energy. The empty symbols in Fig. 4 correspond to the points whose signal level (see images in the inset) was used to calculate the asymmetry. Analyzing the data in Fig. 4, we can conclude that low-energy electrons have higher polarization compared to higher-energy ones, which is in good agreement with the literature data [11, 12].

Further experiments will allow to find find the value of the Sherman function S for this Mott polarimeter. After all calibration and adjustment procedures, it will be possible to measure the spin-resolved electronic band dispersions.

Conclusions

In this paper, we present the details of the process of creating and testing a novel prototype of a classical projecting Mott polarimeter. Individual units of the device have been tested at various construction stages.

While the final adjustments remain to be introduced before the device can be put into operation, it has been established that implementing such devices is possible in principle. High spatial resolution of this device and its efficiency have been confirmed.

REFERENCES

1. **Baibich M.N., Broto J.M., Fert A., et al.,** Giant magnetoresistance of (001) Fe/(001)Cr magnetic superlattices, Phys. Rev. Lett. 61 (21) (1988) 2472.

2. **Kirschner J., Rebenstorff D., Ibach H.,** High-resolution spin-polarized electron-energy-loss spectroscopy and the stoner excitation spectrum in nickel, Phys. Rev. Lett. 53 (21) (1988) 698.

3. **Vaterlaus A., Stamm C., Maier U., et al.,** Two-step disordering of perpendicularly magnetized ultrathin films, Phys. Rev. Lett. 84 (10) (2000) 2247.

4. **Hoesch M., Muntwiler M., Petrov V.N., et al.,** Spin structure of the Shockley surface state on Au (111), Phys. Rev. B. 69 (24) (2004) 241401.

5. **Hasan M.Z., Kane Ch.L.,** Colloquium: topological insulators // Rev. Mod. Phys. 82 (4) (2010) 3045.

6. **Petrov V.N., Galaktionov M.S., Kamochkin A.S.,** Comparative tests of conventional and retarding-potential Mott polarimeters, Rev. Sci. Instr. 72 (9) (2001) 3728–3730.

7. **Petrov V.N., Grebenshikov V.V., Grachev B.D., Kamochkin A.S.,** New compact classical 40 kV Mott polarimeter, Rev. Sci. Instr. 74 (3) (2003) 1278–1281.

8. **Shikin A.M.,** Vzaimodeystaiye fotonov i elektronov s tverdym telom [Interaction of photons and electrons with solids], BBM Publishing, St. Petersburg, 2008 (in Russian).

9. **Hoesch M., Greber T., Petrov V.N., et al.,** Spin-polarized Fermi surface mapping, J. Electron Spectrosc. Relat. Phenom. 124 (2–3) (2002) 263–279.

10. **Strocov V.N., Petrov V.N., Dil J.H.,** Concept of a multichannel spin-resolving electron analyzer based on Mott scattering, J. Synchrotron Rad. 22-3 (May) (2015) 708–716.

11. **Penn D.R., Apell S.P., Girvin S.M.,** Theory of spin-polarized secondary electrons in transition metals, Phys. Rev. Lett. 55 (5) (1985) 518.

12. **Oepen H.P., Frömter R.,** Scanning electron microscopy with polarisation analysis, Handbook of Magnetism and Advanced Magnetic Materials (Eds. H. Kronmüller, S. Parkin, R. Wiesendanger, G. Guntherodt). Wiley Online Library, 2007. https: //doi.org/10.1002/9780470022184. hmm309

Received 28.06.2021, accepted 05.07.2021.

THE AUTHORS

PETROV Vladimir N.
Peter the Great St. Petersburg Polytechnic University
29 Politechnicheskaya St., St. Petersburg, 195251, Russian Federation
petrov@physics.spbstu.ru

GABDULLIN Pavel G.
Peter the Great St. Petersburg Polytechnic University
29 Politechnicheskaya St., St. Petersburg, 195251, Russian Federation
gabdullin_pg@spbstu.ru

PAVLOV Alexander V.
Alferov University of RAS
8-3 Khlopin St., St. Petersburg, 194021, Russian Federation
a.pavlov@physics.spbstu.ru

USTINOV Alexander B.
Peter the Great St. Petersburg Polytechnic University
29 Politechnicheskaya St., St. Petersburg, 195251, Russian Federation
ustinov@physics.spbstu.ru

STROCOV Vladimir N.
Paul Scherrer Institute
111, Forschungsstrasse, Villigen PSI, 5232, Switzerland
vladimir.strocov@psi.ch

DIL Jan Hugo
Paul Scherrer Institute
111, Forschungsstrasse, Villigen PSI, 5232, Switzerland
jan-hugo.dil@psi.ch

СПИСОК ЛИТЕРАТУРЫ

1. **Baibich M.N., Broto J.M., Fert A., et al.** Giant magnetoresistance of (001) Fe/(001)Cr magnetic superlattices // Physical Review Letters. 1988. Vol. 61. No. 21. P. 2472.

2. **Kirschner J., Rebenstorff D., Ibach H.** High-resolution spin-polarized electron-energy-loss spectroscopy and the stoner excitation spectrum in nickel // Physical Review Letters. 1984. Vol. 53. No. 7. P. 698.

3. **Vaterlaus A., Stamm C., Maier U., Pini M.G., Politi P., Pescia D.** Two-step disordering of perpendicularly magnetized ultrathin films // Physical Review Letters. 2000. Vol. 84. No. 10. P. 2247.

4. **Hoesch M., Muntwiler M., Petrov V.N., Hengsberger M., Patthey L., Shi M., Falub M., Greber T., Osterwalder J.** Spin structure of the Shockley surface state on Au (111) // Physical Review B. 2004. Vol. 69. No. 24. P. 241401.

5. **Hasan M.Z., Kane Ch.L.** Colloquium: topological insulators // Reviews of Modern Physics. 2010. Vol. 82. No. 4. P. 3045.

6. **Petrov V.N., Galaktionov M.S., Kamochkin A.S.** Comparative tests of conventional and retarding-potential Mott polarimeters // Review of Scientific Instruments. 2001. Vol. 72. No. 9. Pp. 3728–3730.

7. **Petrov V.N., Grebenshikov V.V., Grachev B.D., Kamochkin A.S.** New compact classical 40 kV Mott polarimeter // Review of Scientific Instruments. 2003. Vol. 74. No. 3. Pp. 1278–1281.

8. **Шикин А.М.** Взаимодействие фотонов и электронов с твердым телом. СПб.: Издательство ВВМ, 2008. 11 с.

9. **Hoesch M., Greber T., Petrov V.N., Muntwiler M., Hendsberger M., Auwarter W., Osterwalder J.** Spin-polarized Fermi surface mapping // Journal of Electron Spectroscopy and Related Phenomena. 2002. Vol. 124. No. 2–3. Pp. 263–279.

10. **Strocov V.N., Petrov V.N., Dil J.H.** Concept of a multichannel spin-resolving electron analyzer based on Mott scattering // Journal of Synchrotron Radiation. 2015. Vol. 22. Part 3. May. Pp. 708–716.

11. **Penn D.R., Apell S.P., Girvin S.M.** Theory of spin-polarized secondary electrons in transition metals // Physical Review Letters. 1985. Vol. 55. No. 5. P. 518.

12. **Oepen H.P., Frömter R.** Scanning electron microscopy with polarization analysis // Handbook of Magnetism and Advanced Magnetic Materials (Eds. H. Kronmüller, S. Parkin, R. Wiesendanger, G. Guntherodt). Wiley Online Library, 2007. https: //doi.org/10.1002/9780470022184. hmm309

Статья поступила в редакцию 28.06.2021, принята к публикации 05.07.2021.

СВЕДЕНИЯ ОБ АВТОРАХ

ПЕТРОВ Владимир Никифорович – *доктор физико-математических наук, профессор кафедры физики Института физики, нанотехнологий и телекоммуникаций Санкт-Петербургского политехнического университета Петра Великого, Санкт-Петербург, Российская Федерация.*

195251, Российская Федерация, г. Санкт-Петербург, Политехническая ул., 29
petrov@physics.spbstu.ru

ГАБДУЛЛИН Павел Гарифович – *кандидат физико-математических наук, доцент Высшей инженерно-физической школы Санкт-Петербургского политехнического университета Петра Великого, Санкт-Петербург, Российская Федерация.*

195251, Российская Федерация, г. Санкт-Петербург, Политехническая ул., 29

gabdullin_pg@spbstu.ru

ПАВЛОВ Александр Валерьевич – *преподаватель кафедры общей физики Санкт-Петербургского национального исследовательского академического университета имени Ж.И. Алфёрова РАН, Санкт-Петербург, Российская Федерация.*

194021, Российская Федерация, г. Санкт-Петербург, ул. Хлопина, 8, к. 3

a.pavlov@physics.spbstu.ru

УСТИНОВ Александр Борисович – *кандидат физико-математических наук, доцент Высшей инженерно-физической школы Санкт-Петербургского политехнического университета Петра Великого, Санкт-Петербург, Российская Федерация.*

195251, Российская Федерация, г. Санкт-Петербург, Политехническая ул., 29

ustinov@physics.spbstu.ru

СТРОКОВ Владимир Николаевич – *доктор физико-математических, наук, научный сотрудник Института Пауля Шеррера, г. Бругг, Швейцария.*

5232, 111, Forschungsstrasse, Villigen PSI, Switzerland

vladimir.strocov@psi.ch

ДИЛ Жан Хьюго – *PhD, глава научной группы COPHEE Института Пауля Шеррера, г. Бругг, Швейцария.*

5232, 111, Forschungsstrasse, Villigen PSI, Switzerland

jan-hugo.dil@psi.ch

DOI: 10.18721/JPM.14309
UDC 621.455.4; 621.455.34

A MODEL OF AN ION PLASMA ELECTRICALLY POWERED SPACECRAFT PROPULSION WITH A REMOTE MONITORING AND A CONTROL SYSTEM

D.B. Dyubo[1], S.B. Makarov[1], Yu.V. Kuleshov[2], P.S. Goncharov[2], N.A. Shunevich[2], V.V. Martynov[2], O.Yu. Tsybin[1]

[1] Peter the Great St. Petersburg Polytechnic University, St. Petersburg, Russian Federation;

[2] Military Space Academy Named after A.F. Mozhaysky, St. Petersburg, Russian Federation

This paper continues the publication cycle on developing the ion plasma electrically powered spacecraft propulsion (EPSP) of the spacecraft. For monitoring and control of the EPSP operation, a feedback system based on a signal proportional to the EPSP plasma radiation intensity has been proposed to be used. It was assumed that the radiation intensity in the ultraviolet, visible and infrared ranges being proportional to the instantaneous thrust value of the EPSP. Accordingly, the introduction of a signal from the radiation registration detector into the feedback loop should allow to create an onboard closed system for monitoring and control of the EPSP operation. A photodetector based on a dynamic *pin*-diode integrator was considered for use in this system.

Keywords: ion plasma thruster, acceleration, neutralization, plasma radiation, photodetector, automatic control

Citation: Dyubo D.B., Makarov S.B., Kuleshov Yu.V., Goncharov P.S., Shunevich N.A., Martynov V.V., Tsybin O.Yu., A model of an ion plasma electrically powered spacecraft propulsion with a remote monitoring and a control system, St. Petersburg Polytechnical State University Journal. Physics and Mathematics. 14 (3) (2021) 116–125. DOI: 10.18721/JPM.14309

МОДЕЛЬ ИОННО-ПЛАЗМЕННОГО ЭЛЕКТРИЧЕСКОГО РАКЕТНОГО ДВИГАТЕЛЯ С СИСТЕМОЙ УДАЛЕННОГО КОНТРОЛЯ И УПРАВЛЕНИЯ

Д.Б. Дюбо[1], С.Б. Макаров[1], Ю.В. Кулешов[2], П.С. Гончаров[2], Н.А. Шуневич[2], В.В. Мартынов[2], О.Ю. Цыбин[1]

[1] Санкт-Петербургский политехнический университет Петра Великого, Санкт-Петербург, Российская Федерация;

[2] Военно-космическая академия имени А.Ф. Можайского, Санкт-Петербург, Российская Федерация

Данная статья продолжает цикл публикаций о создании ионно-плазменного электрического ракетного двигателя (ИЭРД) космического аппарата. С целью контроля и управления работой двигателя предлагается использовать систему с обратной связью, основанную на сигнале, пропорциональном интенсивности излучения плазмы ИЭРД. Предполагается, что интенсивность такого излучения в ультрафиолетовом, видимом и инфракрасном диапазонах пропорциональна мгновенной силе тяги ИЭРД. Соответственно, введение сигнала с датчика регистрации излучения в цепь обратной связи позволит создать бортовую замкнутую систему контроля и управления работой ИЭРД. Для использования в данной системе рассматривается фотоприемник на основе динамического *p–i–n*-диода-интегратора.

Ключевые слова: ионно-плазменный электрический ракетный двигатель, нейтрализация, излучение плазмы, фотоприемник, автоматическое управление

Ссылка при цитировании: Дюбо Д.Б., Макаров С.Б., Кулешов Ю.В., Гончаров П.С., Шуневич Н.А., Мартынов В.В., Цыбин О.Ю. Модель ионно-плазменного электрического ракетного двигателя с системой удаленного контроля и управления // Научно-технические ведомости СПбГПУ. Физико-математические науки. 2021. Т. 14. № 3. С. 116–125. DOI: 10.18721/JPM.14309

Introduction

Space exploration has made great strides in recent years. Large spacecraft are increasingly constructed instead of small ones, with multiple rather than single spacecraft launched. The exploration of deep space, as well as interplanetary missions, also open vast new opportunities. New requirements are thus imposed on electrically powered propulsion systems (EPSs) in spacecraft, aimed at accelerating vehicles in outer space [1 – 4]. Particles are first ionized in propellant flow in such engines, with the resulting ions subsequently accelerated by an electric field. Accelerated ions are neutralized upon leaving the accelerating system in the EP; flow of the neutrals produced then expands freely into outer space. Electrical energy is consequently converted into kinetic energy of spacecraft motion. The efficiency of the engine can be characterized by a parameter determining the efficiency of converting electrical energy into kinetic energy of propellant flow [4]. The thrust generated by the electric prop system is fundamentally limited because, on the one hand, high values of electrical power are required to obtain large momenta, and, on the other hand, the power cannot exceed that of the solar arrays powering the spacecraft electrical system. Xenon is the most popular propellant for EPSs: its advantages are chemical inertness and a relatively large atomic mass. However, xenon has a high cost, its production is limited, and reserves on Earth are insufficient.

Due to these drawbacks of xenon, new EP engines running on alternative propellants need to be constructed. Novel EPSs should be simple, fuel-efficient, stable, easy to control, reliable and durable at an acceptable cost. The EPS should be designed to endure multiple switching cycles and pauses in operation. Besides, as EPSs are installed in an increasing number of spacecraft, the motion control systems should be improved. Modern EPSs in spacecraft include an onboard power supply/control (PSC) unit. The system of telemetric control (STC) sends the data on the operation of the EPS to the mission control center of the spacecraft, which processes the data and sends control signals to the spacecraft (via the onboard controller integrated in the PSC unit).

The set of basic operating parameters of the EPS includes the thrust F, the mass flow rate $\dot{m}_p$ of the propellant, the ion beam current I_i, the velocity v_i of accelerated ions at the exit from the accelerator, the acceleration voltage U_k of each k^{th} electrode, the velocity v_{ex} of accelerated neutrals in the beam, the neutral flux $\dot{m}_{ex}$ in the exiting beam, and some others. Since each individual parameter does not completely describe the operation of the EPSP, all parameters must be measured simultaneously and logically combined in commands. The latter involves a fairly complicated step-by-step procedure where errors and false signals can be generated.

Assuming that the plume is a mono-velocity flux of neutral particles, the thrust can be found from the simplified formulation of the momentum conservation law [1 – 4]:

$$F = \frac{d\left(mv\right)_{ex}}{dt} = \dot{m}_{ex} v_{ex}, \dot{v}_{ex} = 0, \quad (1)$$

where $\dot{m}_{ex}$ is the mass flow rate of propellant, v_{ex} is the outflow velocity of propellant particles.

The parameters $\dot{m}_{ex}$, v_{ex} in Eq. (1) correspond only to the ejected neutral plume. Because a magnetic mirror is produced in the spacecraft as charged particles escape, ions cannot completely leave, generating thrust. It is typically impossible to simply measure the parameters $\dot{m}_{ex}$, v_{ex} on board. The simplified theory assumes that the parameter $\dot{m}_{ex}$ is equal to the flow rate of the propellant, the velocity v_{ex} corresponds to the potential difference passed by the ion U from the injection plane to the equipotential region where neutralization occurs. An ideal EPS in this representation provides the thrust F created by the ion beam current I_i of singly charged ions accelerated by the electric voltage U [4]:

$$F = I_i \sqrt{\frac{2\mu_i U}{e}}, \tag{2}$$

where μ_i is the ion mass, e is the elementary ion charge. Eq. (2) is derived for the ideal case, when each ion must be instantly neutralized in the plane where it is ejected from the accelerator. The correction can be introduced with two additional parameters η_m, η_n that the thrust $F(t)$ depends on:

$$F(t) = \eta_m \eta_n I_i(t) \sqrt{\frac{2\mu_i U}{e}}. \tag{3}$$

The conversion efficiency η_m of propellant mass is the ratio used to measure the ionization efficiency of the neutral propellant flow. The mass conversion efficiency η_n is the ratio used to measure the neutralization efficiency of the ionized propellant flow. Moreover, each parameter in relation (3) can be unstable, depending on time. In addition, a fraction of the electrical power of the ion flux is spent on electromagnetic radiation. Apparently, the relationship between plasma electromagnetic radiation and the thrust and jet power of the EPSP has not been described in literature. The goal of our study is to formulate a model for a plasma ion electrically powered spacecraft propulsion with a remote monitoring and control system, using plasma radiation from the EPSP to generate signal and transmit it to the onboard control system and telemetrically to the mission control center.

Plasma radiation in EPS

We suggest to monitor and control the EPS, in particular, to stabilize the thrust, by measuring the integral control the signal from the sensor recording the intensity of plasma radiation in the system and using it to automatically regulate the feedback loop. The control signal is proportional to the thrust F.

Mechanical thrust is generated based on the principle that charges induced on the surfaces of the surfaces of accelerator electrodes produce the force of attraction between the electrodes and the accelerated ions. Induced charges are created by the electric field of external sources together with the intrinsic electric field of the accelerated ions. Ions can produce positive traction on a given electrode during the period they spend in the accelerating electric field from the side of this electrode. The traction produced by an ion becomes zero immediately after this ion is neutralized, since the neutralized particles do not interact with the EPS electrodes.

The voltage U in Eqs. (2, 3) is the potential difference between point where the ion is injected from the ionizer into the interelectrode gap of the accelerator and the accelerating electrode (the ejection plane of the ion from the accelerator). If an ion settles on any electrode of the accelerator before neutralization, its overall contribution to the thrust vanishes. Moreover, the thrust decreases if the ions are not neutralized completely. Thus, the ion current I in Eqs. (2, 3) neither has a measurable magnitude nor is exactly related to the thrust F. The value of the thrust can be estimated more correctly by measuring the parameters of the plasma generated in the neutralizer.

Intense ultraviolet, visible, infrared and microwave radiation is generated from a flux of accelerated ions during operation [7 – 10]. EPS plasma provides high radiative luminosity at the stage of neutralization, allowing diagnostics by optical and microwave spectroscopy [7 – 9]. Photographs of the bright luminous flux accompanying the operation of the EPS are given in many studies, in particular, [10].

The plasma plume starts to glow, mainly due to recombination resulting from neutralization of the ion charge, collisions and resonant charge exchange, spontaneous relaxation of excitation. The predominant mechanisms governing radiation depend on both the individual properties of charged and neutral particles contained in the plasma and by its collective properties, primarily bearing a vibration-wave nature. The radiation of individual particles is generated by electron transitions in atoms or ions between discrete energy levels; electron deceleration in an ion cloud; cyclotron radiation of electrons in a magnetic field.

Structure of onboard remote monitoring/control system

Remote monitoring and control of the EPS should be carried out via a photodetector recording the luminous intensity of plasma [11, 12]. Accordingly, the electromagnetic radiation intensity of the plasma can serve as a parameter for rapid monitoring of the EPS parameters during operation. The intensity of ultraviolet, visible and infrared radiation $I_{rad}(\omega, t)$ can be represented as following integral parameter:

$$I_{rad}(\omega,t) = \eta_{rad}(\omega) I_i(t). \tag{4}$$

Relation (4) contains the generation efficiency of frequency-dependent radiation $\eta_{rad}(\omega)$, which is smaller than unity, $\eta_{rad}(\omega) < 1$. When the onboard detector receives radiation $I_{rad}(\omega, t)$ emanating from the neutralizer, the parameter $\eta_{rad}(\omega)$ indicates the neutralization efficiency of the operating ion current $I_i(t)$ as the main source of radiation. The radiation intensity $I_{rad}(\omega, t)$ can be represented by a time-dependent signal $S(\omega, t)$, accounting for the fluctuations in all parameter values: vacuum conditions and temperature, power source, propellant flow, ionizer, particle losses in the accelerator, instability of ion flux neutralization.

The signal $S(\omega, t) = kI_{rad}(\omega, t)$ can also be used as a complex signal for monitoring and control of the EPS. Accordingly, Eqs. (2, 4) prove that the signal $S(\omega, t)$ is proportional to the thrust $F(t)$:

$$S(\omega,t) = \left[\left(k \cdot \eta_{rad} / \eta_n \eta_m \right) \left(e / 2\mu_i U \right)^{1/2} \right] \cdot F(t) = \text{const}(\omega) F(t), \tag{5}$$

and can be used to control the magnitude of thrust $F(t)$ in the onboard monitoring system.

Fig. 1 shows a simplified block diagram describing the operation of the EPS with a closed system for remote monitoring and control. The design of the EPS, the spatial characteristics of ion and electron beams in an independent electric field, and the induced surface electric charge were calculated using the Computer Science Technology (CST) Particle Studio package [5, 6].

The block diagram shows the propellant flow, the accelerated ion and electron fluxes combined inside the neutralizer, and a neutral exhaust plume.

This layout is commonly used for ion-electron neutralization in widespread grid and Hall-effect EPSP.

EPS with the closed system for remote monitoring and control includes a photodetector, a modulator, a power supply/control unit (PSCU), a power source and a propellant flow controller. The PSCU-controlled power source supplying electric energy generates the voltage applied to the electrodes. Plasma radiation, photodetector, modulator, PSCU, power source and flow controller comprise a closed loop providing automated control of the EPSP. The photodetector generates instanta-

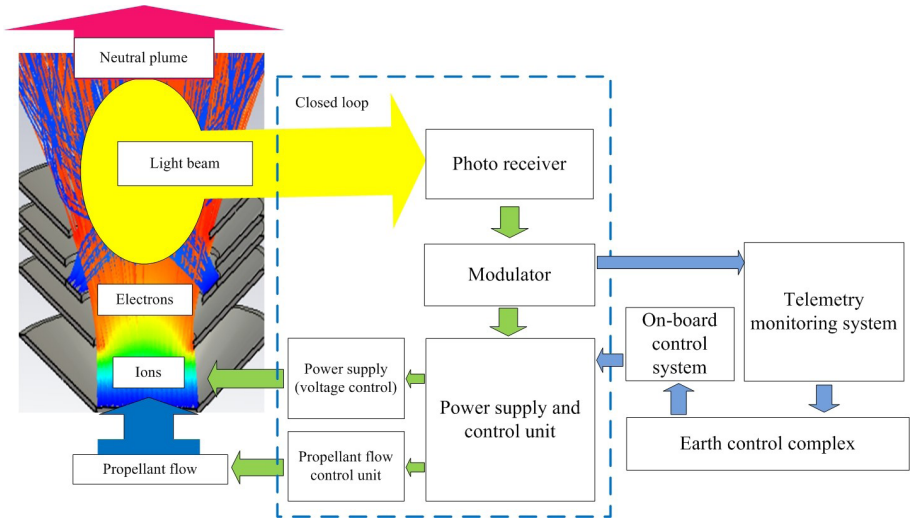

Fig. 1. Block diagram for EPS with closed loop for remote monitoring and control

neous control signal directed to the modulator. Signal from the modulator is transmitted to the PSCU and the telemetric system, which then sends data about the EPS to the mission control center. After the data about the EPS are processed, the mission control center sends control signals to the spacecraft (to the onboard system) whenever necessary. If thrust is unstable and the respective correlated changes occur in plasma radiation, the closed loop for remote monitoring and control provides rapid stabilization by correcting the voltages on the electrodes of the accelerator.

The photodetector has to satisfy several requirements for the EPS to function correctly [13, 14]: it should have small weight and overall dimensions, be reliable, have a long service life, high sensitivity, low noise figure and be equipped with noise protection. The well-known photodiodes do not actually integrate the amplitude-time characteristics of noise and signals, so additional external units with wide dynamic and frequency ranges are required for them to operate as part of the EPS, including preamplifiers, integrators, comparators, etc.

The photodetectors meeting these requirements include the recently developed novel integrated photodetector based on a dynamic *pin* diode-triode, offering several of the necessary functions in a single device [15]. The dynamic *pin* diode-triode with trapped charge carriers and built-in potential barrier generated in the gate is a device with a signal-to-noise ratio $SNR > 1$ and high sensitivity in the wavelength range from 400 to 700 nm. Experimental measurements have shown that the characteristics of the device are satisfactory for using it in an onboard system for remote monitoring and control of the EPS [16, 17]. The output analog signal is proportional to the absorbed energy dose of plasma radiation. Thus, the photodetector serves as a charge integrator/comparator, acting as a dose-to-time converter. Measuring the time delay of the photocurrent, rather than its magnitude, provides a new efficient method for detecting plasma radiation. Noise and other spurious signals are reduced by the averaging effect in the device itself. The magnitude of forward current is controlled only by the forward voltage and does not depend on the radiation intensity.

Conclusions

The closed system for remote control of electrically powered propulsion in spacecraft uses plasma radiation in the ultraviolet, visible and infrared ranges as signal characterizing the operation mode of the EPS. The system must measure the EPS thrust, accurately adjust it and transmit telemetric data to the mission control center. Assuming that the signal $S(\omega, t)$ is proportional to the thrust $F(t)$ of the

EPSP in accordance with relation (5) allows designing a new EPSP with a closed system of remote control, planned to be tested experimentally.

A photodetector based on a pin diode-triode, operating in dynamic mode with the respective properties and parameters, is proposed as a device for obtaining and collecting the initial data. The photodetector developed should make it possible to set the parameters required for the operation of the EPS in remote and automated modes, ensure more precise maneuvering in space, quickly identify errors and malfunctions, control and optimize the consumption of the propellant.

Acknowledgment

The authors are grateful to ActLight SA, Switzerland, for providing a sample pin-diode for the study. This work was supported by State Assignment of the Russian Federation for Basic Research (Project No. FSEG-2020-0024).

REFERENCES

1. **Nauschütt M., Kiefer B., Kunze F., et al.,** Ion thrusters for electric propulsion: Scientific issues developing a niche technology into a game changer, Rev. Sci. Instrum. 91 (6) (2020) 061101.

2. **Levchenko I., Xu S., Mazouffre S., et al.,** Perspectives, frontiers, and new horizons for plasma-based space electric propulsion, Physics of Plasmas. 27 (2) (2020) 020601.

3. **Levchenko I., Bazaka K., Ding Y., et al.,** Space micropropulsion systems for Cubesats and small satellites: From proximate targets to furthermost frontiers, Appl. Phys. Rev. 5 (1) (2018) 011104.

4. **Goebel D.M., Katz I.,** Fundamentals of electric propulsion: Ion and Hall thrusters, John Wiley & Sons, Hoboken, New Jersey, USA (2008) 1–507.

5. **Kurushin A.,** Basic course of design of microwave devices using CST Studio Suite, One-Book, Moscow, 2014.

6. **Dyubo D.B., Tsybin O.Yu.,** A computer model of the contact ionization ion accelerator for the electrically powered spacecraft propulsion, St. Petersburg State Polytechnical University Journal. Physics and Mathematics. 13 (1) (2020) 78–91.

7. **Holste K., Dietz P., Scharmann S., et al.,** Use of emission spectroscopy for real-time assessment of relative wall erosion rate of BHT-200 hall thruster for various regimes of operation, Vacuum. 84 (9) (2010) 1085–1091.

8. **Ferreira J.L., Souza J.H.C., Rego I.S., Ferreira I.S.,** Plasma diagnostics and performance of a permanent magnet Hall thruster, 2004. Access mode: https://hal.archives-ouvertes.fr/hal-00003100

9. **Nishiyama K., Shimizu Y., Funaki I., et al.,** Measurements of the electromagnetic emissions from the MUSES-C ion engine system, Proceedings of the 27th International Electric Propulsion Conference, 15–19 October, 2001, Pasadena, CA. 2001. Paper IEPC-01-112.

10. **Tsybin O.Yu., Makarov S.B., Dyubo D.B., et al.,** An electrically powered ion accelerator with contact ionization for perspective electrically powered thrusters, St. Petersburg Polytechnical State University Journal. Physics and Mathematics. 13 (2) (2020) 99–115.

11. **Penkov M.M., Goncharov P.S., Martynov V.V., Tsybin O.Yu.,** Elektroraketnyy dvigatel [Electrically powered spacecraft propulsion]. Pat. No. 2726152, Russian Federation, MPK H05H 1/54 (2006.01) F03H1/00 (2006.01) B64G 1/54 (2006.01). Mozhaisky Military Space Academy is a declarant and patentee. No. 2019140727; declar. 09.12.2019; publ. 09.07.2020. Bull. No. 19.

12. **Goncharov P.S., Martynov V.V., Shunevich N.A., Tsybin O.Y.,** Use of plasma electromagnetic radiation of an electric rocket thruster, Izvestiya Tula State University. (11) (2020) 197–202.

13. **Kawabata Y., Kawakatsu Y.,** On-board orbit determination using sun sensor and optical navigation camera for deep-space missions, Transactions of the Japan Society for Aeronautical and Space Sciences. 15 (2017) 13–19.

14. **Hufenbach B., Habinc S., Vuilleumier P.,** Space applications for smart sensors, European Space Agency, European Space Research and Technology Centre (1999) 9–16. Access mode: http://microelectronics.esa.int/vhdl/doc/Smart Sensor. pdf.

15. **Okhonin S., Gureev M., Sallin, D., et al.,** A dynamic operation of a *pin* photodiode, Appl. Phys. Lett. 106 (3) (2015) 031115.

16. **Dyubo D.B., Tsybin O.Yu.,** A novel photodiode in on-board micro receiver in 400–800 nm range, Proceedings of the First Joint International Conference on Astrophysics for Young Scientists, Peter the Great St. Petersburg Polytechnic University, Higher School of Applied Physics and Space Technologies (2017) 53–57.

17. **Dyubo D.B., Tsybin O.Yu.,** The relation of volume and surface effects with a charge barrier height in a dynamic *p–i–n*-photodyode, St. Petersburg Polytechnical State University Journal. Physics and Mathematics. 11 (2) (2018) 16–25.

Received 15.06.2021, accepted 06.07.2021.

THE AUTHORS

DYUBO Dmitry B.
Peter the Great St. Petersburg Polytechnic University
29 Politechnicheskaya St., St. Petersburg, 195251, Russian Federation
dyubo_db@spbstu.ru

MAKAROV Sergey B.
Peter the Great St. Petersburg Polytechnic University
29 Politechnicheskaya St., St. Petersburg, 195251, Russian Federation
makarov@cee.spbstu.ru vka@mil.ru

KULESHOV Yuri V.
A.F. Mozhaysky Military-Space Academy
13 Zhdanovskaya St., St. Petersburg, 197198, Russian Federation
vka@mil.ru

GONCHAROV Pavel S.
A.F. Mozhaysky Military-Space Academy
13 Zhdanovskaya St., St. Petersburg, 197198, Russian Federation
vka@mil.ru

SHUNEVICH Nikolay A.
A.F. Mozhaysky Military-Space Academy
13 Zhdanovskaya St., St. Petersburg, 197198, Russian Federation
vka@mil.ru

MARTYNOV Viktor V.
A.F. Mozhaysky Military-Space Academy
13 Zhdanovskaya St., St. Petersburg, 197198, Russian Federation
vka@mil.ru

TSYBIN Oleg Yu.
Peter the Great St. Petersburg Polytechnic University
29 Politechnicheskaya St., St. Petersburg, 195251, Russian Federation
otsybin@rphf.spbstu.ru

СПИСОК ЛИТЕРАТУРЫ

1. **Nauschütt M., Kiefer B., Kunze F., et al.** Ion thrusters for electric propulsion: Scientific issues developing a niche technology into a game changer // Review of Scientific Instruments. 2020. Vol. 91. No. 6. P. 061101.

2. **Levchenko I., Xu S., Mazouffre S., Lev D., Pedrini D., Goebel D., Garrigues L., Taccogna F., Bazaka K.** Perspectives, frontiers, and new horizons for plasma-based space electric propulsion // Physics of Plasmas. 2020. Vol. 27. No. 2. P. 020601.

3. **Levchenko I., Bazaka K., Ding Y., et al.** Space micropropulsion systems for Cubesats and small satellites: From proximate targets to furthermost frontiers // Applied Physics Reviews. 2018. Vol. 5. No. 1. P. 011104.

4. **Goebel D.M., Katz I.** Fundamentals of electric propulsion ion and Hall thrusters. Hoboken, New Jersey, USA: John Wiley & Sons, 2008. Pp. 1–507.

5. **Kurushin A.** Basic course of design of microwave devices using CST Studio Suite. Moscow: One-Book, 2014. 433 p.

6. **Дюбо Д.Б., Цыбин О.Ю.** Компьютерная модель ускорителя ионов с контактной ионизацией для электроракетных двигателей космических летательных аппаратов // Научно-технические ведомости СПбГПУ. Физико-математические науки. 2020. Т. 13. № 1. С. 78–91.

7. **Holste K., Dietz P., Scharmann S., Keil K., Henning T., Zschätzsch D., Reitemeyer C.M., Batishchev O., Martinez-Sanchez M.** Use of emission spectroscopy for real-time assessment of relative wall erosion rate of BHT-200 hall thruster for various regimes of operation // Vacuum. 2010. Vol. 84. No. 9. Pp. 1085–1091.

8. **Ferreira J.L., Souza J.H.C., Rego I.S., Ferreira I.S.** Plasma diagnostic and performance of a permanent magnet Hall thruster. 2004. Режим доступа: https://hal.archives-ouvertes.fr/hal-00003100.

9. **Nishiyama K., Shimizu Y., Funaki I., Kuninaka H., Toki K.** Measurements of the electromagnetic emissions from the MUSES-C ion engine system // Proceedings of the 27th International Electric Propulsion Conference, 15–19 October, 2001, Pasadena, CA. 2001. Paper IEPC-01-112.

10. **Цыбин О.Ю., Макаров С.Б., Дюбо Д.Б., Кулешов Ю.В., Гончаров П.С., Мартынов В.В., Шуневич Н.А.** Электростатический ионный ускоритель с контактной ионизацией для перспективных электрических ракетных двигателей // Научно-технические ведомости СПбГПУ. Физико-математические науки. 2020. Т. 13. № 2. С. 99–115.

11. **Пеньков М.М., Гончаров П.С., Мартынов В.В., Цыбин О.Ю.** Электроракетный двигатель. Патент 2726152 МПК H05H 1/54 (2006.01) F03H 1/00 (2006.01) B64G 1/54 (2006.01). Заявитель и патентообладатель: Федеральное государственное бюджетное военное образовательное учреждение высшего образования «Военно-космическая академия имени А.Ф. Можайского» Министерства обороны Российской Федерации (RU). № 2019140727; заявл. 9.12.2019; опубл. 09.07.2020, Бюлл. № 19.

12. **Гончаров П.С., Мартынов В.В., Шуневич Н.А., Цыбин О.Ю.** Использование электромагнитного излучения плазмы электрического ракетного двигателя // Известия Тульского государственного университета. Технические науки. 2020. № 11. С. 197–202.

13. **Kawabata Y., Kawakatsu Y.** On-board orbit determination using sun sensor and optical navigation camera for deep-space missions // Transactions of the Japan Society for Aeronautical and Space Sciences. 2017. Vol. 15. Pp. 13–19.

14. **Hufenbach B., Habinc S., Vuilleumier P.** Space applications for smart sensors // European Space Agency. European Space Research and Technology Centre. 1999. Pp. 9–16. Режим доступа: http://microelectronics. esa.int/vhdl/doc/ SmartSensor.pdf

15. **Okhonin S., Gureev M., Sallin, D., et al.** A dynamic operation of a *pin* photodiode // Applied Physics Letters. 2015. Vol. 106. No. 3. P. 031115.

16. **Dyubo D., Tsybin O.Yu.** A novel photodiode in on-board micro receiver in 400–800 nm range // Proceedings of the First Joint International Conference on Astrophysics for Young Scientists. Peter the Great St. Petersburg Polytechnic University. Higher school of Applied Physics and Space Technologies. St. Petersburg, 2017. Pp. 53–57.

17. **Дюбо Д.Б., Цыбин О.Ю.** Связь объемных и поверхностных эффектов с высотой зарядового барьера в динамическом *p–i–n*-фотодиоде // Научно-технические ведомости СПбГПУ. Физико-математические науки. 2018. Т. 11. № 2. С. 16–25.

Статья поступила в редакцию 15.06.2021, принята к публикации 06.07.2021.

СВЕДЕНИЯ ОБ АВТОРАХ

ДЮБО Дмитрий Борисович – *инженер Высшей инженерно-физической школы Санкт-Петербургского политехнического университета Петра Великого, Санкт-Петербург, Российская Федерация.*

195251, Российская Федерация, г. Санкт-Петербург, Политехническая ул., 29

dyubo_db@spbstu.ru

МАКАРОВ Сергей Борисович – *доктор технических наук, профессор Высшей школы прикладной физики и космических технологий Санкт-Петербургского политехнического университета Петра Великого, главный научный сотрудник научной лаборатории «Космические телекоммуникационные системы» того же университета, Санкт-Петербург, Российская Федерация.*

195251, Российская Федерация, г. Санкт-Петербург, Политехническая ул., 29

makarov@cee.spbstu.ru

КУЛЕШОВ Юрий Владимирович – *доктор технических наук, профессор, заместитель начальника Военно-космической академии имени А.Ф. Можайского по учебной и научной работе Военно-космической академии имени А.Ф. Можайского, Санкт-Петербург, Российская Федерация.*

197198, Российская Федерация, г. Санкт-Петербург, Ждановская ул., 13

vka@mil.ru

ГОНЧАРОВ Павел Сергеевич – *кандидат технических наук, начальник 12-го отдела Военного института (научно-исследовательского) Военно-космической академии имени А.Ф. Можайского, Санкт-Петербург, Российская Федерация.*

197198, Российская Федерация, г. Санкт-Петербург, Ждановская ул., 13

vka@mil.ru

ШУНЕВИЧ Николай Александрович – *кандидат технических наук, начальник лаборатории, старший научный сотрудник 122-й лаборатории 12-го отдела Военного института (научно-исследовательского) Военно-космической академии имени А.Ф. Можайского, Санкт-Петербург, Российская Федерация.*

197198, Российская Федерация, г. Санкт-Петербург, Ждановская ул., 13

vka@mil.ru

МАРТЫНОВ Виктор Васильевич – *старший научный сотрудник 121-й лаборатории 12-го отдела Военного института (научно-исследовательского) Военно-космической академии имени А.Ф. Можайского, Санкт-Петербург, Российская Федерация.*

197198, Российская Федерация, г. Санкт-Петербург, Ждановская ул., 13

vka@mil.ru

ЦЫБИН Олег Юрьевич – *доктор физико-математических наук, профессор Высшей инженерно-физической школы Санкт-Петербургского политехнического университета Петра Великого, Санкт-Петербург, Российская Федерация.*

195251, Российская Федерация, г. Санкт-Петербург, Политехническая ул., 29

otsybin@rphf.spbstu.ru

DOI: 10.18721/JPM.14310
UDC 621.373.8

A NEW APPROACH TO THE ASSESSMENT OF THE OUTPUT POWER FOR A HELIUM-NEON GAS LASER WITH DIFFERENT CROSS-SECTIONAL GEOMETRY OF THE ACTIVE ELEMENT

V.A. Kozhevnikov, V.E. Privalov, A.E. Fotiadi

Peter the Great St. Petersburg Polytechnic University,
St. Petersburg, Russian Federation

The proposed study continues a series of articles devoted to design methods for the key energy parameters of a helium-neon (He-Ne) gas laser. An application of the previously proposed method for designing the emission power to lasers with the rectangle- and ellipse-shaped cross sections of active elements has been considered. An idea of effective mode volume was used, a calculation algorithm was presented, and a procedure reducing unwieldy calculations was put forward. Varying the parameter values made it possible to get a detailed picture of dependencies of the output laser energy on the geometrical parameters of objects under study. A comparison of the obtained results permitted to find optimal laser parameters for maximum output power. The calculation results of the radiation energy were established to agree well both with those of the laser gain for the given cross sections and those of the experimental data.

Keywords: helium-neon laser, laser power, tube geometry, rectangular and elliptical cross sections

Citation: Kozhevnikov V.A., Privalov V.E., Fotiadi A.E., A new approach to the assessment of the output power for a helium-neon gas laser with different cross-sectional geometry of the active element, St. Petersburg Polytechnical State University Journal. Physics and Mathematics. 14 (3) (2021) 126–138. DOI: 10.18721/JPM.14310

НОВЫЙ ПОДХОД К ОЦЕНКЕ МОЩНОСТИ ИЗЛУЧЕНИЯ ГЕЛИЙ-НЕОНОВОГО ЛАЗЕРА С РАЗЛИЧНОЙ ГЕОМЕТРИЕЙ ПОПЕРЕЧНОГО СЕЧЕНИЯ АКТИВНОГО ЭЛЕМЕНТА

В.А. Кожевников, В.Е. Привалов, А.Э. Фотиади

Санкт-Петербургский политехнический университет Петра Великого,
Санкт-Петербург, Российская Федерация

Предлагаемое исследование продолжает цикл статей, посвященных методам расчета ключевых энергетических параметров гелий-неонового (He-Ne) газоразрядного лазера. Рассмотрено применение предложенного ранее метода расчета мощности излучения к лазерам, обладающим поперечными сечениями активного элемента в виде прямоугольника и эллипса. Использовано представление об эффективном модовом объеме лазера, указан расчетный алгоритм и предложена процедура, снижающая громоздкость расчетов. Варьирование значений лазерных параметров позволило получить развернутую картину зависимости выходной мощности лазерного излучения от геометрических параметров объектов. Сравнение полученных результатов дало возможность выявить оптимальные значения параметров лазеров для достижения максимальной выходной мощности. Установлено, что результаты расчетов мощности излучения хорошо согласуются как с соответствующими результатами по коэффициентам усиления лазера для заданных сечений, так и с экспериментальными данными.

Ключевые слова: гелий-неоновый лазер, мощность лазерного излучения, геометрия сечения трубки

Ссылка при цитировании: Кожевников В.А., Привалов В.Е., Фотиади А.Э. Новый подход к оценке мощности излучения гелий-неонового лазера с различной геометрией поперечного сечения активного элемента // Научно-технические ведомости СПбГПУ. Физико-математические науки. 2021. Т. 14. № 3. С. 126–138. DOI: 10.18721/JPM.14310

Introduction

Elliptical beams (alternatively called Mathieu or Mathieu – Gauss beams) have been the focus of much attention recently: this is one of four (along with the usual Gaussian, Bessel-Gaussian and parabolic beams) fundamental families of non-diffracting solutions of the wave equation. This is due to the potential for their experimental detection and theoretical consideration [1 – 5].

In our previous study [6], we offered a method for estimating the radiation power of a gas-discharge laser with an arbitrary cross-sectional shape of the active element. Let us briefly recall the essence of this method.

An optical resonator with the curvature radius R_e of the corresponding equivalent confocal resonator has the following form of the electric field magnitude E of the fundamental Gaussian mode TEM_{00} in cylindrical coordinates (r, z, φ):

$$E = E_0 \sqrt{\frac{2}{1+\xi^2}} \exp\left[-\frac{kr^2}{R_e\left(1+\xi^2\right)} \right], \tag{1}$$

where $\xi = 2z/R_e$, $k = 2\pi/\lambda$ (the coordinate z is measured from the waist of the Gaussian beam, λ is the laser wavelength); E_0 is the E value for $\xi = 1$ and $r = 0$.

The first approximation of perturbation theory assumes the power of induced radiation to be proportional to the product $E^2\delta N$, where δN is the population inversion of the active medium. The value of δN satisfies the homogeneous Helmholtz equation in the first approximation.

$$\Delta\left(\delta N\right) + \lambda^2 \delta N = 0 \tag{2}$$

with a homogeneous boundary condition

$$\delta N\big|_{\Gamma} = 0, \tag{3}$$

where Γ is the cross-sectional boundary of the active element.

The proposed method introduced the concept of effective mode volume (NMV) as a body bounded by a surface where the magnitude of $|E|^2\delta N$ decreases by e^2 times compared to $E_0^2\delta N_0$ (δN_0 is the population inversion on the axis). Introducing this quantity accounts for both the population inversion and the field distribution in the resonator for arbitrary geometry of the active element.

It was suggested in [6] to estimate the output power of laser radiation using the modal volume NMV by the following formula:

$$P = \iiint\limits_{\mathrm{NMV}} \varepsilon |E|^2 \, \delta N dV, \tag{4}$$

where ε is the corresponding proportionality coefficient.

A three-stage algorithm for finding the laser's radiation power was described for an arbitrary cross-sectional shape of the active element.

Step 1. The population inversion δN of the active medium is calculated by solving Eqs. (2), (3) for a given value of the boundary Γ (for example, by finding an approximate solution of these equations (see our earlier study [7]), allowing to obtain solutions with high accuracy preserving a relatively low computational complexity).

Step 2. The boundary of the effective modal volume (NMV) is found.

Step 3. Direct integration by Eq. (4).

The method for estimating the radiation power was tested (see [6]) for the case of cylindrical geometry, and the calculated results it yielded gave excellent agreement with the experimental data.

We considered rectangular and elliptical cross-sections of the active element in this study.

Rectangular cross-section of active element

Let the sides of the rectangle be equal to a and b, with $b \le a$. If we use the method proposed in [7] for solving the Helmholtz equation with an arbitrary shape of the cross-sectional boundary of the active element, then, due to symmetry, the solution δN of Eqs. (2), (3) in a cylindrical coordinate system (whose origin is in the center of the rectangle, and the polar axis from which the polar angle φ is measured is directed parallel to the larger side) can be represented in the following form:

$$\delta N(r,\varphi) = \delta N_0 \left\{ J_0(\lambda r) + \sum_{m=1}^{s} a_{2m} J_{2m}(\lambda r) \cdot \cos(2m\varphi) \right\},$$

where $J_m(\lambda_r)$ are the Bessel functions of order m.

On the other hand, an exact solution of Eqs. (2), (3) can be found for a rectangle: it is easy to confirm that the function

$$\delta N(r,\varphi) = \delta N_0 \cos(\pi n r \cos\varphi / a) \cos(\pi m r \sin\varphi / b)$$

satisfies homogeneous equation (2) for

$$\lambda_{n,m}^2 = (n^2\pi^2/a^2) + (m^2\pi^2/b^2), \ n = 1, 2, ..., \ m = 1, 2, ...$$

If we consider the main contribution with $n = m = 1$, then the following equation can be obtained to determine the NMV boundary in polar coordinates:

$$\ln\left|\cos\left(\frac{\pi}{a} r\cos\varphi\right)\right| + \ln\left|\cos\left(\frac{\pi}{b} r\sin\varphi\right)\right| + \ln\left(\frac{2R_e}{kw^2(z)}\right) + 2 - \frac{2r^2}{w^2(z)} = 0, \qquad (5)$$

where $w(z) = \sqrt{(R_e + 4z^2/R_e)/k}$.

Eq. (5) can be solved numerically with respect to r for each value of the pair (z, φ), providing the equation for the surface $r(z, \varphi)$ bounding the NMV.

To be definite, we confine ourselves to a plane-sphere resonator; in this case,

$$R_e = 2\{d(R-d)\}^{1/2},$$

where R is the curvature radius of the spherical mirror, d is the distance between the mirrors.

Then the output power of the laser with a rectangular tube cross section is found by the formula:

$$P = \frac{4E_0^2 \delta N_0 \varepsilon}{k} \sqrt{d(R-d)} \iiint\limits_{\text{NMV}} \cos\left(\frac{\pi}{a} r\cos\varphi\right) \cos\left(\frac{\pi}{b} r\sin\varphi\right) \times$$
$$\times \exp\left(\frac{-2r^2}{w^2(z)}\right) \frac{1}{w^2(z)} dz d\varphi r dr. \qquad (6)$$

We performed calculations by Eqs. (5), (6) with different laser parameters. Fig. 1 shows the dependence of the reduced laser power P/α (where the coefficient α is expressed as $\alpha = \varepsilon E_0^2 \delta N_0 / k$) on the ratio of the rectangle sides (a/b) with the following parameter values:

$d = 2.2$ m; $R = 10$ m; $b = 5$ mm;

a varies from 5 to 150 mm; tube length l is 1.2 m;

the active element is located in the center of the resonator.

Given the above laser parameters, the surface $r(z, \varphi)$ bounding the NMV is an ellipse with a small eccentricity. The calculation results show that the eccentricity of this ellipse increases at a fixed z with an increase in the a/b ratio, and the dimensions of the ellipse increase with an increase in z at a fixed value of this ratio.

It seemed interesting to compare the output powers of lasers with the same cross-sectional area of the active element but with different cross sections: circular and rectangular (and, accordingly, with the same volume given the same tube length). The ouput power for the circular cross section was calculated by the method proposed in [6]; the radius of the circular section $r_0 = (ab/\pi)^{1/2}$ and the same values of d, R and l were taken for the given sides a and b of the rectangle; $E_0^2 \delta N_0$ was considered the same for both lasers. The calculations revealed that the power of the laser with a rectangular cross section of the active element was approximately 4 – 6% less than that of the laser with a cylindrical cross section (with the same area).

Notably, our results on estimating the output power of a rectangular laser are in good agreement with both our calculated data on laser gain [8] and with experimental data. It follows from the results obtained in [8] that, firstly, the mean cross-sectional gain of a rectangular laser does not depend on the ratio of the rectangle sides, and, secondly, that it is approximately 6% less than the corresponding coefficient of a cylindrical laser.

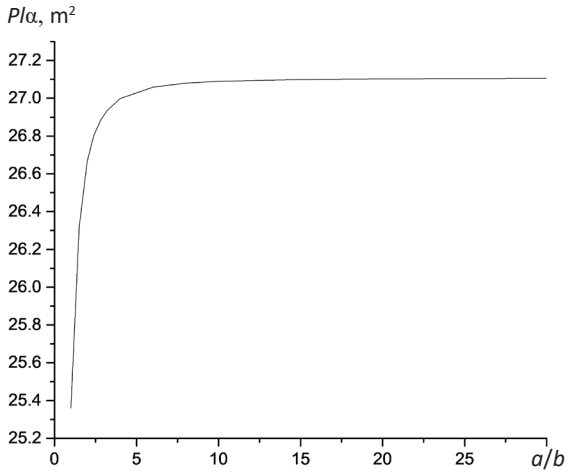

Fig. 1. Dependence of laser output power P/α ($\alpha = \alpha = \varepsilon E_0^2 \delta N_0 / k$) on the ratio of rectangle sides with $d = 2.2$ m, $R = 10$ m, $b = 5$ mm, $l = 1.2$ m

Analyzing the graph in Fig. 1, we can conclude that if the a/b ratio is increased by 30 times, the power only increases by approximately 6.5%; moreover, we can assume that the power practically does not change starting from $a/b \approx 6$. The fact that the power of a laser with a rectangular cross section is about 4 – 6% less than that of a laser with a cylindrical cross section is in agreement with the experimental data obtained in [9]. Therefore, we can assume that the method we propose for calculating the laser output power is correct.

The somewhat unusual ratio between the lengths of the resonator and the active element was chosen because the same lengths were used in the experimental setup in [9]. A question that arises is why the values of the electron and gas temperatures do not appear in the calculations since they of course affect the population inversion. However, this is automatically taken into account in the experiment, as the output power that was measured in [9] includes the population inversion.

Elliptical cross section of active element

Let the semi-axes of the ellipse be equal to a and b ($b < a$). To find the exact solution of homogeneous equation (2) for an ellipse, let us consider it in elliptic coordinates (u, v, z) (their relationship with the Cartesian coordinates is as follows:

$$x = \rho \cdot \mathrm{ch}(u) \cdot \cos v, \;\; y = \rho \cdot \mathrm{sh}(u) \cdot \sin v, \;\; z = z,$$
$$\rho = \mathrm{const} > 0, \;\; u \geq 0, \;\; 0 \leq v < 2\pi.$$

We represent δN as $\delta N = \delta N_0 f(u, v, z)$, and find the function $f(u, v, z)$ using the variable separation method:

$$f(u,v,z) = \varphi(z) \cdot w(u) \cdot g(v).$$

We then obtain a set of three equations:

$$\varphi^{-1} d^2\varphi / dz^2 = -c,$$
$$w^{-1} d^2 w / du^2 + (\lambda^2 - c)\rho^2 \mathrm{ch}(2u)/2 = d,$$
$$-g^{-1} d^2 g / dv^2 + (\lambda^2 - c)\rho^2 \cos(2v)/2 = d,$$

where c, d are separation constants.

Denoting $q = (\lambda^2 - c)\rho^2/4$, we obtain the canonical form of the Mathieu equation from the third equation (we adhere to the notations from [10, 11] for introducing Mathieu functions and related quantities here and below; different authors use different notations):

$$\frac{d^2 g(v)}{dv^2} + (d - 2q\cos(2v))g(v) = 0, \tag{7}$$

and the modified Mathieu equation from the second equation:

$$\frac{d^2 w(u)}{du^2} - (d - 2q\mathrm{ch}(2u))w(u) = 0. \tag{8}$$

Let us choose the value $u = 0$, that is, the center of the elliptical section, as the origin. The separation constant $c = 0$ if it is independent z (it follows then that $q = \lambda^2\rho^2/4$). Because the problem is symmetrical, we are interested in a solution periodic with respect to v. It follows from the theory that

there exists an infinite countable sequence of eigenvalues $d = d_r(q)$, corresponding to even periodic solutions (7). Given a real $q > 0$, these eigenvalues are real, different, and $d_0 < d_1 < d_2 \ldots$. The same as with circular and rectangular cross sections, we consider the fundamental mode with the minimum value of the parameter λ, therefore, the solution (7) that we are concerned with is a Mathieu function of the form $ce_0(v, q)$. Eq. (8) is obtained from (7) by substituting $v = iu$, and the solution we are interested in is a Mathieu function $Ce_0(u, q)$. Thus,

$$f(u,v) = \alpha \cdot Ce_0(u,q) \cdot ce_0(v,q),$$

where α is the normalization factor (since, by definition, $\delta N = \delta N_0 f$, the function f must be normalized to unity in the center of the cross section).

Let the ellipse have semi-axes a and b, then its equation in Cartesian coordinates has the form

$$\left(x^2/a^2\right) + \left(y^2/b^2\right) = 1,$$

and the following expressions hold true for its equation $u = u_0$ in elliptic coordinates:

$$a = \rho \cdot \mathrm{ch}(u_0), \quad b = \rho \cdot \mathrm{sh}(u_0),$$

it follows from here that $\rho = (a^2 - b^2)^{1/2}$ (i.e., ρ is the focal distance),

$$u_0 = \mathrm{Arsh}(b/\rho) = \ln\left[(a+b)/(a-b)\right]/2.$$

The following value should then be taken as α:

$$\alpha = 1/\left(Ce_0(0,q) \cdot ce_0(\pi/2,q)\right).$$

Finally, the solution to the homogeneous Helmholtz equation (2) takes the form

$$\begin{gathered}\delta N = \delta N_0 Ce_0\left(u, \lambda^2\left(a^2 - b^2\right)/4\right) \times \\ \times ce_0\left(v, \lambda^2\left(a^2 - b^2\right)/4\right) \Big/ \left(Ce_0\left(0, \lambda^2\left(a^2 - b^2\right)\right)/4\right) \times \\ \times ce_0\left(\pi/2, \lambda^2\left(a^2 - b^2\right)/4\right).\end{gathered} \tag{9}$$

It follows from homogeneous boundary condition (3) that λ must be such that

$$Ce_0\left(\frac{1}{2}\ln\frac{a+b}{a-b}, \frac{\lambda^2\left(a^2 - b^2\right)}{4}\right) = 0. \tag{10}$$

The equation for determining the NMV in elliptical coordinates can be obtained from here:

$$\ln\left(\frac{2R_e}{kw^2(z)}\right) + 2 - \frac{2\left(a^2 - b^2\right)}{w^2(z)}\left(\mathrm{ch}^2 u \cdot \cos^2 v + \right.$$

$$+\operatorname{sh}^2 u\sin^2 v\Big)-\ln\left[\left|Ce_0\left(0,\frac{\lambda^2}{4}\left(a^2-b^2\right)\right)\right|\right]+$$

$$+\ln\left[\left|Ce_0\left(u,\frac{\lambda^2}{4}\left(a^2-b^2\right)\right)\right|\right]-\ln\left[\left|ce_0\left(\frac{\pi}{2},\frac{\lambda^2}{4}\left(a^2-b^2\right)\right)\right|\right]+$$

$$+\ln\left[\left|ce_0\left(v,\frac{\lambda^2}{4}\left(a^2-b^2\right)\right)\right|\right]=0.$$

Let us rewrite the last equation in cylindrical coordinates to simplify analysis of the NMV shape. It is known [12] that a one-to-one correspondence between points of the plane $0xy$ (except for the semi-axis $(-1, \infty)$) and the region of the plane $0uv$ ($u \geq 0$, $0 \leq v < 2\pi$) is established by assigning parts of the hyperbola

$$\left[x^2/\left(\rho^2\cos^2 v\right)\right]-\left[y^2/\left(\rho^2\sin^2 v\right)\right]=1,$$

belonging to the I, II, III and IV quadrants, the values

$$v,\ \pi-v,\ \pi+v,\ 2\pi-v\ \ (0\leq v\leq \pi/2).$$

Then the equation for determining the NMV boundary in cylindrical coordinates (r, φ, z) takes the form

$$\ln\left(\frac{2R_e}{kw^2(z)}\right)+2-\frac{2r^2}{w^2(z)}-\ln\left[\left|Ce_0\left(0,\frac{\lambda^2}{4}\left(a^2-b^2\right)\right)\right|\right]+$$

$$+\ln\left[\left|Ce_0\left(u(r,\varphi),\frac{\lambda^2}{4}\left(a^2-b^2\right)\right)\right|\right]+$$

$$+\ln\left[\left|ce_0\left(v(r,\varphi),\frac{\lambda^2}{4}\left(a^2-b^2\right)\right)\right|\right]- \qquad (11)$$

$$-\ln\left[\left|ce_0\left(\frac{\pi}{2},\frac{\lambda^2}{4}\left(a^2-b^2\right)\right)\right|\right]=0,$$

where

$$u(r,\varphi)=\operatorname{Arsh}\left\{\left[\left(r^2-\left(a^2-b^2\right)+\left(\left(r^2-\left(a^2-b^2\right)\right)^2+\right.\right.\right.$$

$$\left.\left.\left.+4r^2\left(a^2-b^2\right)\sin^2\varphi\right)^{1/2}\right)\Big/\left(2\left(a^2-b^2\right)\right)\right]^{1/2}\right\},$$

$$v(r,\varphi)=\arccos\left\{\left[\left(r^2+\left(a^2-b^2\right)-\left(\left(r^2+\left(a^2-b^2\right)\right)^2-\right.\right.\right.$$

$$\left.\left.\left.-4r^2\left(a^2-b^2\right)\cos^2\varphi\right)^{1/2}\right)\Big/\left(2\left(a^2-b^2\right)\right)\right]^{1/2}\right\}.$$

Eq. (11) can be solved numerically with respect to r for each value of the pair (z, φ), providing the equation for the surface $r(z, \varphi)$ bounding the NMV.

Next, given that

$$dV = \left(a^2 - b^2\right)\left(\mathrm{sh}^2 u + \sin^2 v\right) du dv dz,$$

we obtain an expression for estimating the output power of the laser with an elliptical cross-section of the active element:

$$\begin{aligned} P = \gamma \iiint\limits_{\mathrm{NMV}(u,v,z)} dz dv du \left(a^2 - b^2\right) \frac{\mathrm{sh}^2 u + \sin^2 v}{w^2(z)} \times \\ \times Ce_0\left(u, \frac{\lambda^2}{4}\left(a^2 - b^2\right)\right) ce_0\left(v, \frac{\lambda^2}{4}\left(a^2 - b^2\right)\right) \times \\ \times \exp\left[\frac{-2\left(a^2 - b^2\right)}{w^2(z)}\left(\mathrm{sh}^2 u + \cos^2 v\right)\right] = \\ = \gamma \iiint\limits_{\mathrm{NMV}(r,\varphi,z)} dz d\varphi r dr \frac{1}{w^2(z)} Ce_0\left(u(r,\varphi), \frac{2}{4}\left(a^2 - b^2\right)\right) \times \\ \times ce_0\left(v(r,\varphi), \frac{\lambda^2}{4}\left(a^2 - b^2\right)\right) \cdot \exp\left(\frac{-2r^2}{w^2(z)}\right), \end{aligned} \tag{12}$$

where $\gamma = \dfrac{2E_0^2 \delta N_0 \varepsilon R_e}{k \cdot Ce_0\left(0, \frac{\lambda^2}{4}\left(a^2 - b^2\right)\right) \cdot ce_0\left(\frac{\pi}{2}, \frac{\lambda^2}{4}\left(a^2 - b^2\right)\right)}$.

Calculating the Mathieu functions is cumbersome, and the actual calculation methods are still the subject of numerous studies (see, for example, [13, 14]). The following series is commonly used to calculate them:

$$ce_0(v, q) = \sum_{k=0}^{\infty} A_{2k}^0(q) \cos(2kv) \tag{13}$$

(the formula for $Ce_0(u, q)$ is obtained by substituting $v = iu$, that is, by replacing the trigonometric cosine with a hyperbolic one), but the coefficients $A_{2k}^0(q)$ are not obtained trivially. The Mathieu functions are found by the following algorithm.

A tabulated set of coefficients for 145 values of q is given in the tables in [15] (notice that the notations introduced in that study and in our work are related:

$$be_0 = d_0 + 2q; \;\; s = 4q; \;\; A \cdot Se_0(s, v) = ce_0(v, q); \;\; A \cdot De_{2k}(s) = A_{2k}(q).$$

We calculated q for the given λ, a, b, and found $d_0(q)$ using the values from [10, 11, 15] (interpolation was introduced for the missing values). Next, we found the coefficients A_{2k} based on the rule: if q is close enough to one of the values in [10, 11, 15], then the coefficients were interpolated, otherwise, the following recurrence relations were used for the coefficients A_{2k}:

$$dA_0 - qA_2 = 0,\ \left(d-4\right)A_2 - q\left(2A_0 + A_4\right) = 0,\ ...,$$
$$\left(d - m^2\right)A_m - q\left(A_{m-2} + A_{m+2}\right) = 0,\ m \geq 3. \tag{14}$$

Finding the values of d and q, all coefficients A_{2k} in terms of A_0 were expressed using Eqs. (14). Next, we used the normalization condition for the Mathieu functions (notably, different authors also introduce different normalization conditions):

$$2A_0^2 + A_2^2 + A_4^2 + A_6^2 + ... = 1. \tag{15}$$

Taking a sufficient number of coefficients A_{2k} in equality (15) and substituting their expressions in terms of A_0, we obtained a formula for finding A_0. Then the coefficients A_{2k} were obtained again from Eqs. (14) and the function $ce_0(v, q)$ was constructed using the expression for series (13) ($Ce_0(u, q)$) was constructed similarly). In addition, we considerably simplified the first step of the algorithm: λ was found with the given a, b using the method in [7], which helped partially avoid the cumbersome calculations. This value of λ was controlled by Eq. (10); this equation was satisfied with good accuracy, which also goes on to confirm that the method from [7] is correct for finding λ. After the functions $ce_0(v, q)$ and $Ce_0(u, q)$ were constructed, it became possible to solve Eq. (11) and then calculate the output power of the laser with an elliptical cross section of the active element by to Eq. (12).

The calculations were performed with varying laser parameters. As an example, Fig. 2 shows the results for the following parameters (they are close to those used in the calculations for a laser with a rectangular cross section described above):

$d = 2.2$ m; $R = 10$ m; $b = 2.5$ mm; $a = 2.75 - 15.0$ mm; $l = 1.2$ m;
the tube is located in the center of the resonator;
the resonator is semi-confocal.

With the given laser parameters, the function $r(z, \varphi)$, which is a solution to Eq. (11), is also an ellipse with a small eccentricity, and the behavior of the dependences is similar to the rectangular case: the eccentricity increases with an increase in the a/b ratio at a fixed z, and the dimensions of the ellipse grow with an increase in z with a fixed value of the a/b ratio.

We also compared the output powers of lasers with elliptical and circular cross sections of the active element with the same area (and the same volume with the same length of the tube): we took

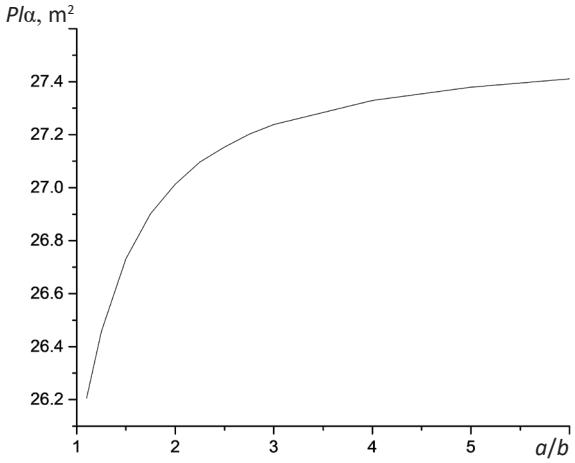

Fig. 2. Dependence of laser output power P/α ($\alpha = \alpha = \varepsilon E_0^2 \delta N_0 / k$)
on the ratio of the ellipse semi-axes with $d = 2.2$ m, $R = 10$ m, $b = 2.5$ mm, $l = 1.2$ m

the radius of the circular section as $r_0 = (ab)^{1/2}$ with the same d, R and l for the given a and b, and calculated the output powers by the method outlined in [6], assuming $E_0^2 \delta N_0$ to be the same for both lasers.

The calculated results for the output power of the laser with an elliptical cross section agree with the calculated results we obtained for the laser gain. The cross-sectional gain of an elliptical laser was obtained in [7] for the ratio of the semiaxes a/b. The gain of the laser with an elliptical cross section was found to be somewhat lower than that with a cylindrical cross section, their difference increasing with an increase in the a/b ratio (recall that an approximate solution was used in [7]). Elliptical beams (Mathieu or Mathieu-Gauss beams), representing one of the four (along with the usual Gaussian, Bessel-Gaussian and parabolic beams) fundamental families of non-diffracting solutions of the wave equation have received much attention lately after they were detected experimentally and described theoretically [1 – 5]. These beams show potential for application in laser processing of materials [16]. However, we did not uncover any descriptions of experiments on measuring the power of gas-discharge lasers with an elliptical cross section of the active element in the literature.

Conclusion

Thus, we have proposed a new method for calculating the output power of a gas-discharge laser with an arbitrary cross-section of the active element. Calculations were performed for the radiation power of a laser with circular (in [6]), rectangular and elliptical cross sections of the active element. The calculated results of the radiation power are in good agreement with the results of previous calculations of laser gains and experimental data. Current research is directed to searching for the optimal shape of the active element cross section with respect to radiation power.

REFERENCES

1. **Gutiérrez-Vega J.C., Iturbe-Castillo M.D., Ramírez G.A., et al.,** Experimental demonstration of optical Mathieu beams, Opt. Commun. 195 (1–4) (2001) 35–40.

2. **Ren Z., Hu H., Peng B.,** Generation of Mathieu beams using the method of 'combined axicon and amplitude modulation', Optics Communications. 426 (1 November) (2018) 226–230.

3. **Ren Z., He J., Shi Y.,** Generation of Mathieu beams using angular pupil modulation, Chin. Phys. B. 27 (12) (2018) 124201.

4. **Julián-Macías I., Rickenstorff-Parrao C., Cabrera-Rosas O.J., et al.,** Wavefronts and caustics associated with Mathieu beams, J. Opt. Soc. Am. A. 35 (2) (2018) 267–274.

5. **Zeylikovich I., Nikitin A.,** The formation and propagation of Mathieu–Gauss type spatial structures on diffraction of a multi segment-shaped laser beam, Eur. Phys. J. D. 74 (9) (2020) 182.

6. **Kozhevnikov V.A., Privalov V.E., Fotiadi A.E.,** The effective mode volume and estimation of helium-neon laser output power, St. Petersburg State Polytechnical University Journal. Physics and Mathematics. 13 (4) (2020) 119–132 (in Russian).

7. **Kozhevnikov V.A., Privalov V.E.,** Laser gain for inhomogeneous boundary conditions, Russian Physics Journal. 63 (9) (2021) 1631–1638.

8. **Kozhevnikov V.A., Privalov V.E., Shemanin V.G.,** Upgrade the evaluation of the contribution of the active element cross section geometry to the He-Ne laser energy characteristics, Opt. Mem. Neural Networks. 28 (3) (2019) 215–221.

9. **Privalov V.E., Khodovoy V.A.,** Eksperimentalnoye issledovaniye He-Ne lazera s razryadnym promezhutkom pryamougolnogo secheniya [An experimental investigation of a He-Ne laser with a rectangular cross-section discharge gap], Optics and Spectroscopy. 37 (4) (1974) 797–799 (in Russian).

10. Handbook of mathematical functions: with formulas, graphs, and mathematical tables, Edited by M. Abramowitz, I.A. Stegun. National Bureau of Standards, Tenth Printing, 1972.

11. **McLachlan N.W.,** Theory and application of Mathieu functions, Oxford University Press, Oxford, 1951.

12. **Bermant A.F.,** Otobrazheniya. Krivolineynyye koordinaty. Preobrazovaniya. Formuly Grina [Mapping. Curvlinear coordinates. Transformations. Green's formulae], Fizmatgiz Publishing, Moscow, 1958 (in Russian).

13. **Frenkel D., Portugal R.,** Algebraic methods to compute Mathieu functions, J. Phys. A. 34 (17) (2001) 3541–3551.

14. **Bibby M.M., Peterson A.F.,** Accurate computation of Mathieu functions, Synthesis lectures on computational electromagnetics #32, Morgan & Claypool Publishers, USA, 2014.

15. Tables relating to Mathieu functions. Characteristic values, coefficients, and joining factors. National Bureau of Standarts, Computation Laboratory, Columbia University Press, New York, 1951.

16. **Orlov S., Vosylius V., Gotovski P., et al.,** Vector beams with parabolic and elliptic cross-sections for laser material processing applications, J. Laser Micro/Nanoeng. 13 (3) (2018) 280–286.

Received 02.07.2021, accepted 02.08.2021.

THE AUTHORS

KOZHEVNIKOV Vadim A.
Peter the Great St. Petersburg Polytechnic University
29 Politechnicheskaya St., St. Petersburg, 195251, Russian Federation
vadim.kozhevnikov@gmail.com

PRIVALOV Vadim E.
Peter the Great St. Petersburg Polytechnic University
29 Politechnicheskaya St., St. Petersburg, 195251, Russian Federation
vaevpriv@yandex.ru

FOTIADI Alexandr E.
Peter the Great St. Petersburg Polytechnic University
29 Politechnicheskaya St., St. Petersburg, 195251, Russian Federation
fotiadi@rphf.spbstu.ru

СПИСОК ЛИТЕРАТУРЫ

1. **Gutiérrez-Vega J.C., Iturbe-Castillo M.D., Ramírez G.A., Tepichín E., Rodrígues-Dagnino R.M., Cháves-Cerda S., New G.H.C.** Experimental demonstration of optical Mathieu beams // Optics Communications. 2001. Vol. 195. No. 1–4. Pp. 35–40.

2. **Ren Z., Hu H., Peng B.** Generation of Mathieu beams using the method of 'combined axicon and amplitude modulation' // Optics Communications. 2018. Vol. 426. 1 November. Pp. 226–230.

3. **Ren Z., He J., Shi Y.** Generation of Mathieu beams using angular pupil modulation // Chinese Physics B. 2018. Vol. 27. No. 12. P. 124201.

4. **Julián-Macías I., Rickenstorff-Parrao C., Cabrera-Rosas O.J., Espíndola-Ramos E., Juárez-Reyes S.A., Ortega-Vidals P., Silva-Ortigoza G., Sosa-Sánchez C.T.** Wavefronts and caustics associated with Mathieu beams // Journal of the Optical Society of America A. 2018. Vol. 35. No. 2. Pp. 267–274.

5. **Zeylikovich I., Nikitin A.** The formation and propagation of Mathieu–Gauss type spatial structures on diffraction of a multi segment-shaped laser beam // The European Physical Journal D. 2020. Vol. 74. No. 9. P. 182.

6. **Кожевников В.А., Привалов В.Е., Фотиади А.Э.** Эффективный модовый объем и оценка мощности выходного излучения гелий-неонового лазера // Научно-технические ведомости СПбГПУ. Физико-математические науки. 2020. Т. 13. № 4. С. 119–132.

7. **Кожевников В.А., Привалов В.Е.** Усиление в лазерах при неоднородных граничных условиях // Известия высших учебных заведений. Физика. 2020. Т. 63. № 9 (730), С. 165–171.

8. **Kozhevnikov V.A., Privalov V.E., Shemanin V.G.** Upgrade the evaluation of the contribution of the active element cross section geometry to the He-Ne laser energy characteristics // Optical Memory and Neural Networks. 2019. Vol. 28. No. 3. Pp. 215–221.

9. **Привалов В.Е., Ходовой В.А.** Экспериментальное исследование He-Ne лазера с разрядным промежутком прямоугольного сечения // Оптика и спектроскопия. 1974. Т. 37. № 4. С. 797–799.

10. Справочник по специальным функциям с формулами, графиками и математическими таблицами. Под ред. М. Абрамовица и И. Стигана. Пер. с англ. М.: Наука, 1979. 832 с.

11. **Мак-Лахлан.** Теория и приложения функций Матьё. Пер. с англ. В.А. Братановского под ред. И.Н. Денисюка. М.: Изд-во ИЛ, 1953. 476 с.

12. **Бермант А.Ф.** Отображения. Криволинейные координаты. Преобразования. Формулы Грина. М.: Физматгиз, 1958, 308 с.

13. **Frenkel D., Portugal R.** Algebraic methods to compute Mathieu functions // Journal of Physics A. 2001. Vol. 34. No. 17. Pp. 3541–3551.

14. **Bibby M.M., Peterson A.F.** Accurate computation of Mathieu functions. Synthesis lectures on computational electromagnetics #32. USA: Morgan & Claypool Publishers, 2014. 124 p.

15. Таблицы для вычисления функций Матье; собственные значения, коэффициенты и множители связи. М.: Вычислительный центр АН СССР, 1967. 279 с.

16. **Orlov S., Vosylius V., Gotovski P., Grabusovas A., Baltrukonis J., Gertus T.** Vector beams with parabolic and elliptic cross-sections for laser material processing applications // Journal of Laser Micro/Nanoengineering. 2018. Vol. 13. No. 3. Pp. 280–286.

Статья поступила в редакцию 02.07.2021, принята к публикации 02.08.2021.

СВЕДЕНИЯ ОБ АВТОРАХ

КОЖЕВНИКОВ Вадим Андреевич – *старший преподаватель кафедры физики Санкт-Петербургского политехнического университета Петра Великого, Санкт-Петербург, Российская Федерация.*

195251, Российская Федерация, г. Санкт-Петербург, Политехническая ул., 29

vadim.kozhevnikov@gmail.com

ПРИВАЛОВ Вадим Евгеньевич – *доктор физико-математических наук, профессор кафедры физики Санкт-Петербургского политехнического университета Петра Великого, Санкт-Петербург, Российская Федерация.*

195251, Российская Федерация, г. Санкт-Петербург, Политехническая ул., 29

vaevpriv@yandex.ru

ФОТИАДИ Александр Эпаминондович – *доктор физико-математических наук, профессор Высшей инженерно-физической школы Санкт-Петербургского политехнического университета Петра Великого, Санкт-Петербург, Российская Федерация.*

195251, Российская Федерация, г. Санкт-Петербург, Политехническая ул., 29

fotiadi@rphf.spbstu.ru

DOI: 10.18721/JPM.14311
UDC 543.51+ 681.2–5

AN ALGORITHM FOR PROCESSING MASS SPECTROMETRIC ANALYSIS DATA FOR INITIAL DIAGNOSTICS OF DISEASES BY EXHALED GASES

V.V Manoilov, L.V. Novikov, A.G. Kuzmin, Yu.A. Titov, I.V. Zarutskii

Institute for Analytical Instrumentation of the Russian Academy of Sciences, St. Petersburg, Russian Federation

An algorithm for processing mass spectra of gases exhaled by patients has been proposed in the paper. The mass spectra are recorded on the MS7-200 quadrupole mass spectrometer, with electronic ionization and with direct capillary injection of the sample. The algorithm is based on transforming an array of spectra (not less than 10) in the space of principal components. The probability of a disease is determined through the Euclidean distance of the patient's coordinates from the centroid. Testing of the algorithm was carried out on the data of mass spectra of gases exhaled by cancer patients. The proposed procedure has several advantages over traditional laboratory methods. The algorithm uses the multidimensional probability density of the distribution of the parameters of the exhaled gases of control groups and the patient being tested and allows to compile an overall picture of the patient's probable diseases in a short time.

Keywords: diagnostics, principal component analysis, multivariate probability density, multivariate data processing

Citation: Manoilov V.V., Novikov L.V., Kuzmin A.G., Titov Yu.A., Zarutskii I.V., An algorithm for processing mass spectrometric analysis data for initial diagnostics of diseases by exhaled gases, St. Petersburg Polytechnical State University Journal. Physics and Mathematics. 14 (3) (2021) 139–149. DOI: 10.18721/JPM.14311

АЛГОРИТМ ОБРАБОТКИ ДАННЫХ МАСС-СПЕКТРОМЕТРИЧЕСКОГО АНАЛИЗА ДЛЯ ПЕРВИЧНОЙ ДИАГНОСТИКИ ЗАБОЛЕВАНИЙ ПО ВЫДЫХАЕМЫМ ГАЗАМ

В.В. Манойлов, Л.В. Новиков, А.Г. Кузьмин, Ю.А. Титов, И.В. Заруцкий

Институт аналитического приборостроения Российской академии наук, Санкт-Петербург, Российская Федерация

В работе предложен алгоритм обработки масс-спектров газов, выдыхаемых пациентами. Масс-спектры регистрируются на квадрупольном масс-спектрометре МС7-200 с электронной ионизацией и прямым капиллярным вводом пробы. Алгоритм основан на преобразовании массива спектров (не менее десяти) в пространство главных компонент. Вероятность заболевания определяется по евклидову расстоянию координат пациента от центроиды. Тестирование алгоритма проведено на данных масс-спектров газов, выдыхаемых больными с онкологическими заболеваниями. Предлагаемая процедура имеет ряд преимуществ перед традиционными лабораторными методами; алгоритм использует многомерную плотность вероятности распределения параметров выдыхаемых газов контрольных групп и тестируемого пациента; позволяет за короткое время составить общую картину вероятных заболеваний.

Ключевые слова: диагностика, метод главных компонент, многомерная плотность вероятности, обработка многомерных данных

Ссылка при цитировании: Манойлов В.В., Новиков Л.В., Кузьмин А.Г., Титов Ю.А., Заруцкий И.В. Алгоритм обработки данных масс-спектрометрического анализа для первичной диагностики заболеваний по выдыхаемым газам // Научно-технические ведомости СПбГПУ. Физико-математические науки. 2021. Т. 14. № 3. С. 139–149. DOI: 10.18721/JPM.14311

Introduction

Exhaled breath analysis is becoming increasingly popular in diagnostics [1, 2]. This technique allows identifying a number of serious diseases, including Alzheimer's disease [3], epilepsy [4], kidney disease [5], cancer [6] and others. The algorithms supporting the devices used for such analysis are an integral component in this type of diagnostics. Software incorporating the given algorithm processes the mass spectra of exhaled gases; the composition of gases is measured using a spectrometer with a quadrupole analyzer. The algorithm is tested by measuring the exhaled gases in cancer patients.

The classical approach to mass spectral analysis involves the so-called initial, or preliminary processing of mass spectra; in this case, mass spectral peaks are detected and their parameters (position on the scale of mass numbers and amplitude, or sometimes area) are assessed. In some cases, initial processing of mass spectra means that the resolution of the device is improved mathematically by separating the superimposed spectral lines [7].

Initial data processing is followed by secondary processing. The algorithm for processing mass spectra described below is run at this stage in offline mode based on the data recorded in computer memory as line spectra. The software that runs the algorithm yields a preliminary estimate of how likely it is that the subjects tested belong to the class of patients with a specific disease or to the class of practically healthy people.

Thus, the algorithm complements the options for classification offered by discriminant and cluster analysis based on multivariate statistical data. Classification of mass spectra of exhaled gases by the methods of discriminant and cluster analysis is described in [8].

The main difference between the mass spectra of exhaled gases in patients with diseases from those in practically healthy people are additional components, for example, with masses of 71, 64, 59 and 55 Da. The presence of these lines in the mass spectrum of the gases exhaled by the examined patient points towards a high probability of disease. Similar to fingerprints, each mass spectrum of exhaled air has its own unique profile (an array of peaks with different intensities), so it can be assumed that different profiles of exhalation ‘fingerprints’ can serve as indicators of a certain disease. After a sufficient amount of such data has been collected, it will be possible to diagnose specific diseases with a very high efficiency, and either prescribe additional tests or immediately start treating the patient.

Basic assumptions

An array of mass spectral data called the ‘healthy’ group forms a matrix. Peak intensities of the mass spectra are recorded for all columns of the matrix, except for the first one, at the given mass values. The first column of the matrix contains the mass spectrum number of exhaled gases of a certain patient, and each of its rows contains data about the intensity of individual mass spectral lines.

We denote such a matrix as $\mathbf{XS} = [x_{ij}]$, where i, j are the numbers of subjects (patients) and attributes (mass numbers), respectively, $i = 1,2,..., I$, $j = 1, 2,..., J$; x_{ij} is the intensity of the j^{th} spectral component of the i^{th} healthy subject.

Similarly, we produce the matrix $I_0 \times J$ for the mass spectra of exhaled gases in diseased subjects. Each row of this matrix contains the intensities of individual lines of the corresponding mass spectrum. We denote this matrix $\mathbf{XI_1} = \left[x_{ij}^0 \right]$, where i, j, J have the same meaning but $i = 1, 2, ..., I_0$; x_{ij}^0 is the intensity of the jth spectral component of the ith diseased subject.

Let us combine the matrices of healthy and diseased subjects, obtaining a common data matrix **X** of size $(I_0 + I) \times J$:

$$\mathbf{X} = \left(\left[\mathbf{XS}; \mathbf{XI}_1 \right] \right).$$

We transform this matrix by the algorithm for constructing the space of principal components (PC) and calculate the score matrix **T**.

Based on clinical examinations of a large number of diseased and healthy subjects, the obtained mass spectra are divided into two sets: control and test groups.

Control groups of mass spectra are the data for subjects with a known diagnosis for their disease and the data for healthy subjects. The situation is different for processing the mass spectra array for the tested group: it is not known whether they belong to healthy or diseased subjects.

The number of mass spectra the gases exhaled by patients in each of the two groups should be at least 30. Each mass spectrum obtained for the breath exhaled by a patient from the control group is represented in the multidimensional space as a point. Such points, collected together from all patients in the group, form a 'cloud' of initial data. The closer to the center (centroid) of the cloud is the point describing the mass spectrum of the breath exhaled by the test patient, the higher the probability that the patient suffers from the disease corresponding to the control group. If the patient is healthy, the probability of their disease is estimated by the control group of healthy subjects; the farther from the center (centroid) of the cloud is the point corresponding to the mass spectrum of the breath exhaled by the test patient, the higher the probability that the patient suffers from a disease

From a mathematical standpoint, the mass spectra of the gases exhaled by subjects from one group make up a data space with some known disease. The probability that a tested subject belongs to one of these groups is estimated sequentially using the formula for the multivariate probability density.

The examination described yields a complete probabilistic picture of the disease in the tested subject. This allows to quickly develop the approaches to further, more thorough examination and subsequent treatment.

Theoretical description of the algorithm

Let x_{ij} be the j^{th} parameter, in the specific case, the intensity of the spectral line for the data of the i^{th} patient from one of the groups, where $i = 1, 2, ..., I$ and $j = 1, 2, ..., J$, and an array of I patients with J recorded spectral lines of exhaled gases is considered. Let us form a matrix of size $I \times J$ from these data. We call this a training matrix and denote it as **X**. The columns of this matrix are denoted as X_j: $\mathbf{X} = [X_1, ..., X_j, ..., X_J]$ [9].

The vector X_j is a random variable. Suppose that this random variable has a normal distribution with the expected value $\overline{X}_j$ and the variance σ_j^2. Matrix elements **X** form a 'cloud' in J dimensional space. We denote this cloud as G, consisting of $I \times J$ points, with the centroid at $\overline{X}$. Its coordinates are expressed as as

$$\overline{X} = \left[\overline{X}_1, \overline{X}_2, ..., \overline{X}_j \right].$$

The subject considered is diseased (or healthy), if the measured vector of parameters of the air they exhale takes the form

$$X_d = \left[X_{d,1}, X_{d,2}, ..., X_{d,j} \right].$$

$X_{i,j}$ is the parameter in J dimensional space G, i.e., $X_d \in G$. This condition is satisfied if the probability P that the point X_d deviates from the centroid $\bar{X}$ does not exceed a certain threshold α. This probability is calculated by constructing a multivariate probability distribution of the event belonging to the space G, assuming that this distribution obeys the normal law [10]:

$$P\left(\mathbf{X}_d\right) = W * \exp\left\{-\frac{1}{2}\left(\mathbf{X}_d - \bar{\mathbf{X}}\right)^T \mathbf{K}_X^{-1}\left(\mathbf{X}_d - \bar{\mathbf{X}}\right)\right\}, \mathbf{X}_d \in G, \quad (1)$$

where $\mathbf{K}_X$ is the covariance matrix, $\mathbf{K}_X = \mathrm{E}\left[\left(\mathbf{X} - \bar{\mathbf{X}}\right) * \left(\mathbf{X} - \bar{\mathbf{X}}\right)^T\right]$ (E is the symbol for the expected value); W is the normalizing factor; $(...)^T$ is the symbol for matrix transposition.

Obviously, the probability P of this event is equal to unity, if it turns out for the next patient examined that $\mathbf{X}_d \equiv \bar{\mathbf{X}}$. This condition is fulfilled if we assume that $W = 1$ in Eq. (1). Then the condition under which the tested patient belongs to the control group takes the form $P(\mathbf{X}_d) < \alpha$, where the quantity α is selected by the method of expert assessment.

Notably, calculating the required probability P by Eq. (1) carries considerable computational difficulties due to a large number of parameters J and correlations between the columns of the matrix $\mathbf{X}$. To compress data and reduce the dimension of the space G, we introduce the orthogonal transformation of data into a space of principal components (the principal components analysis, abbreviated as PCA) [11].

We make a transition to the PC space by generating a new matrix consisting of all rows of the matrix $\mathbf{X}$ and the row $\mathbf{X}_d$. We denote this matrix as $\mathbf{XI}$. In the new coordinate system, we obtain

$$\mathbf{XI} = \mathbf{TP}^T + \mathbf{e} = \sum_{j=1}^{A} t_j \mathbf{p}_j^T + \mathbf{e}, \quad (2)$$

where $\mathbf{p}_j^T$ are the eigenfunctions of the covariance matrix $\mathbf{K}_X$; $\mathbf{T}$ is called the score matrix and is expressed as $\mathbf{T} = [T_1, T_2, ..., T_A]$, its dimension is $I \times A$; $\mathbf{P}^T$ is called the load matrix, its dimension is also $I \times A$; $\mathbf{e}$ is the matrix of residuals (noises), its dimension is $(I \times J)$; the column vectors T_j ($j = 1, 2, ..., A$) are called the principal components (A is the number of principal components).

The magnitude of A is much less than the number of variables J. This circumstance means that almost all primary information about the state of the tested patient is concentrated in the first few PCs. The last row of the matrix (2), the vector T_d, are the coordinates of the patient's parameters in the PC space:

$$\mathbf{T}_d = \left[t_{d,1}, t_{d,2}, ..., t_{d,A} \right].$$

The mean values of the columns in the matrix $\mathbf{T}$ are equal to zero, and the variance is the vector σ^2 with the elements is equal to $\sigma_j^2 = \lambda_j$, i.e., the eigenvalues of the covariance matrix. The expansion in PC is characterized by the variance rapidly decreasing by the fourth PC, while the columns of the matrix $\mathbf{T}$ are not correlated, i.e.,

$$\mathbf{T}_m \mathbf{T}_n' = \begin{cases} 0, \text{with } n \neq m, \\ \lambda_j, \text{with } n = m. \end{cases}$$

In view of this, Eq. (1) takes the following form in the new coordinate system:

$$P(\mathbf{T}_d) = \exp\left\{-\frac{1}{2}\mathbf{T}_d\sigma^{-2}\mathbf{T}_d^{'}\right\} = \exp\left\{-\frac{1}{2}\sum_{j=1}^{A}\frac{t_{d,j}^2}{\sigma_j^2}\right\} \quad (3)$$

and the Euclidean distance from the patient with index d to the centroid of the control group is equal to

$$D(d) = \sqrt{\sum_{j=1}^{A} t_{d,j}^2}. \quad (4)$$

Main steps of the algorithm

The algorithm considered can be divided into two stages, training and diagnostics, executed one after the other.

K matrices $\mathbf{X}^k$ ($k = 1, 2, ..., K$) are formed at the first stage (training) based on the results of clinical examination of a large number of patients, where K is the number of subgroups with the information about the intensity of spectral lines for the exhaled gases corresponding to each type of disease. Notice that the number of rows I^k of each matrix must be greater than the number of columns J^k. Training is performed once, based on the data accumulated on the spectra of gases exhaled by patients (examined in-clinic).

The spectral components of gases exhaled by the tested patients are measured at the second stage of the algorithm (diagnostics), and the probability whether they belong to one of the control groups is calculated in several steps.

Step 1. Use the data on the intensities of the spectral components at the given masses to construct a row vector $\mathbf{X}_d = \{x_{d,1}, x_{d,2}, ..., x_{d,J}\}$.

Step 2. Calculate the matrix $\mathbf{XI}^k = \left[\mathbf{X}^k; \mathbf{X}_d\right]$ with the size $\left(I^k + 1 \times J^k\right)$; the last row in this matrix is the vector X_d.

Step 3. Calculate the normalized values of this matrix. The normalization factor is the maximum value of its elements.

Step 4. Calculate the score matrix $\mathbf{T}^k$ and the eigenvalue vector λ_j^k by the algorithm of the PC method [12].

Step 5. Find the principal components and determine the number A (number of principal components) of the matrix $\mathbf{T}^k$ in such a way that $\sigma_A^k = \sqrt{\lambda_A^k} < \varepsilon$. We can assume that $\varepsilon = (0.001, ..., 0.01)$ without loss of reliability. The last row of the matrix $\sigma_A^k = \sqrt{\lambda_A^k} < \varepsilon$ are the principal components of the parameters characterizing the gases exhaled by the examined patient.

Step 6. Calculate the probability $P\left(T_d^k\right), k = 1, 2, ..., K,$ by Eq. (3).

Step 7. Go back to step 2 ($k = k + 1$) to determine the probability that the examined patient belongs to another group of possible diseases.

Step 8. Analyze the calculated probabilities $P\left(\mathbf{T}_d^k\right), k = 1, 2, ..., K,$ for all K diseases in order to determine the disease with the highest probability.

Testing the developed algorithm

The gases exhaled by the examined patients were injected into a quadrupole mass spectrometer, which has a detection range of 1 – 200 Da, mass number resolution of 0.5 Da, and detection time of up to 15 s for one mass spectrum.

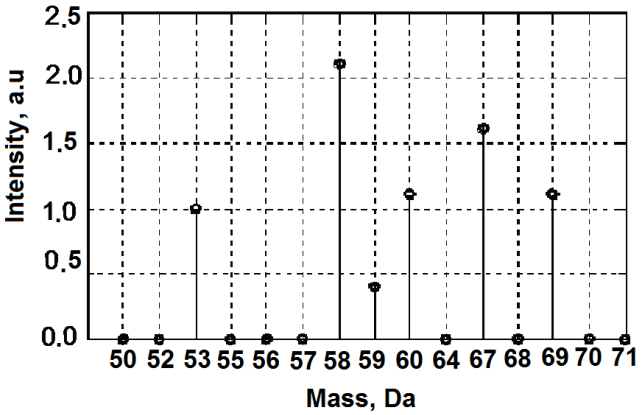

Fig. 1. Mass spectrum of gases exhaled by the patient with a disease

Exhaled gases were measured in 43 patients diagnosed with cancer[1]. These patients were divided into the control group (36 subjects) and the test group (7 subjects). The intensity of the exhaled gas components of the first test patient, for example, coincided with the centroid of the control group. The effectiveness of the algorithm was verified with 10 more tested patients[2] with other types of diseases. Patients from both test groups were assigned serial numbers: $d = (1, 2, ..., 7)$ and $d = (1, 2, ..., 10)$, respectively.

The analyzer recorded the mass spectrum of the gases exhaled by each patient in the range from 50 to 100 Da. Examining a large number of patients and subsequently analyzing the obtained data, we found that the exhaled gases contained spectrum components at masses of 53, ..., 69 Da (12 in total), which are markers of most diseases. A matrix was constructed from the initial data on the control group, containing 12 columns; the intensities of the spectral components serving as markers were located along its rows.

Fig. 1 shows an example for a mass spectrum of the exhaled gases from one of 7 test patients. The mass of singly charged ions in daltons (Da) is plotted along the horizontal axis. The data on exhaled gases of the tested patients were selected sequentially and Steps *1 – 6* of the algorithm were performed. Apparently, it is sufficient to assume that $A = 6$ in the PC space, since $\sigma^k \cong 0$. Eqs. (4) and (3) were used to calculate the Euclidean distance to the centroids of the control group and the probability of diagnosing cancer in each tested patient. These results are given in Table for all tested patients.

Fig. 2,*a* shows the space of the first two principal components of the matrix (PC1 and PC2), with the plotted coordinates of patients in control group 1 (see Table) (o) and seven tested (+) patients. It follows from the data in Table for this group consisting of 7 people that as the coordinates of the mass spectrum of exhaled gases move away from the center of the cloud (centroid), the probability of cancer in these patients decreases but remains high.

Fig. 2,*b* shows the coordinates of patients from control group 2 and 10 tested patients in the space of the first two PCs (PC1 and PC2). As it turned out, all patients (except for the first one) fell outside the cloud of the control group. It is evident from the data for group 2 given in Table that the probability of a different type of cancer is negligible for these patients compared to the type of cancer in group 1 patients.

[1] Data on exhaled gases for this group were provided by the Almazov National Medical Research Centre, St. Petersburg.

[2] Data on exhaled gases for this group were provided by the N.N. Petrov National Medical Research Center of Oncology, St. Petersburg.

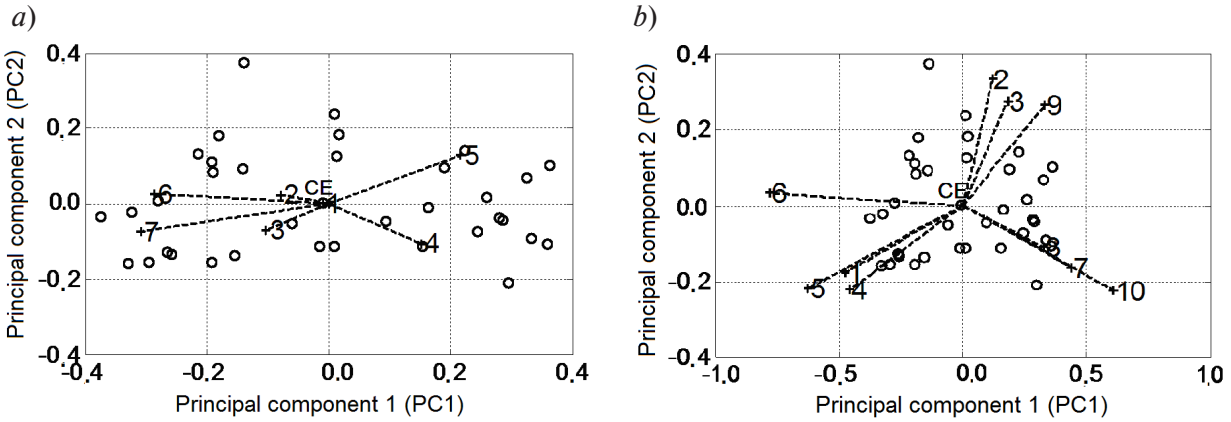

Fig. 2. Examination results in the space of principal components (PC1 and PC2) of the matrix for control groups 1 (*a*) and 2 (*b*) (see Table).
The central points (CE) correspond to the Euclidean center, the rest of the points (o) to the coordinates (mass spectral data) of patients from the corresponding groups. Dashed lines show Euclidean distances to patients (+) who were assigned numbers

Table

Estimated probabilities of cancer in patients from two control groups

Patient no.	Euclidean distance	Probability of disease
Group 1		
1	0.0116	0.9854
2	0.1076	0.1888
3	0.1499	0.2055
4	0.2044	0.1164
5	0.2554	0.2864
6	0.2892	0.3458
7	0.3247	0.1197
Group 2		
1	2.8791	0.0159
4	4.5739	0.0000
3	4.7337	0.0000
2	5.5927	0.0000
5	5.6321	0.0000
8	5.7129	0.0000
9	5.7322	0.0000
6	5.8520	0.0000
10	5.8635	0.0000
7	5.9168	0.0000

Notes. 1. Data for patients from *groups 1 and 2* were obtained from different medical institutions (see footnotes 1 and 2 on page ..., respectively).
2. Patients from *group 2* suffered from cancer of a different type compared with patients from *group 1*.

Conclusion

The medical diagnostics algorithm that we have developed is based on multivariate probability density characterizing the parameter distribution of exhaled gases in the control groups and in patients tested. The algorithm allows to diagnose the most likely diseases for the patient and, if necessary, recommend further tests or treatment. The proposed algorithm and method can also be useful for screening patients, for example, during annual checkups.

Whether the algorithm is applied effectively depends on the size and reliability of the mass spectral data array for healthy controls and the diseased group. The data array for the healthy group should include the data for the detected mass spectra of gases exhaled by the people previously examined by various medical specialists (with high accuracy). These specialists must confirm that no pathologies were found at the time of the experiment on mass spectrometric analysis of exhaled gases. For example, the data array for the healthy group can be compiled from the mass spectra of exhaled gases taken from volunteers in military service, or cadets of military schools and academies who have been thoroughly examined by medical specialists and were found fit for service or training. We have recently carried out experiments on mass spectrometric analysis of exhaled gases in more than 30 cadets of S.M. Kirov Military Medical Academy (St. Petersburg), who were thoroughly examined by medical specialists, making it possible to construct a data array for the healthy group and to refine the test results given in Table.

The data array for the group with diseases was constructed from a large number of mass spectra collected from patients with a well-established diagnosis, for example, a certain type of cancer. This data array was compiled in the course of the study but should be expanded by at least two or three times to improve the reliability of the health decisions made for the patients examined.

The range of capabilities provided by the algorithm can be further extended for processing the data of the mass spectra collected from the exhaled gases not only for devices with quadrupole analyzers but also for devices with other types of analyzers: static, time-of-flight, etc. Studies with such devices can use a system for injecting the sample into the analyzer, similar to the one in our experiments.

The study was performed as part of State Assignment 075-00780-19-02 (registration ID AAAA-A19-11905319-0069-2)

REFERENCES

1. **Li X., Huang D., Zeng J., et al.,** Positive matrix factorization: A data preprocessing strategy for direct mass spectrometry-based breath analysis, Talanta. 192 (15 January) (2019) 32–39.

2. **Li X., Huang L., Zhu H., Zhou Z.,** Direct human breath analysis by secondary nano electrospray ionization ultrahigh resolution mass spectrometry: Importance of high mass resolution and mass accuracy, Rapid Commun. Mass Spectrom. 31 (3) (2017) 301–308.

3. **Tiele A., Wicaksono A., Daulton E., et al.,** Breath-based non-invasive diagnosis of Alzheimer's disease: A pilot study, J. Breath Res. 14 (2) (2020) 026003.

4. **Van Dartel D., Schelhaas H.J., Colon A.J., et al.,** Breath analysis in detecting epilepsy, J. Breath Res. 14 (3) (2020) 031001.

5. **Chen Ch.-Ch., Hsieh J.-Ch., Chao Ch.-H., et al.,** Correlation between breath ammonia and blood ureanitrogen levels in chronic kidney disease and dialysis patients, J. Breath Res. 14 (3) (2020) 036002.

6. **Kononov A., Korotetsky B., Jahatspanian I., et al.,** Online breath analysis using metal oxide semiconductor sensors (electronic nose) for diagnosis of lung cancer, J. Breath Res. 14 (1) (2020) 016004.

7. **Manoilov V.V., Novikov L.V., Belozertsev A.I., et al.,** Processing of mass spectra of exhaled gases based on correlation algorithms, J. Analytical Chem. 75 (13) (2020) 1678–1684.

8. **Manoilov V.V., Novikov L.V., Zarutskii I.V., et al.,** Methods for processing mass spectrometry signals from exhaled gases for medical diagnosis, Biomed. Eng. 53 (5) (2020) 355–359.

9. **Bolshakov A.A., Karimov R.N.,** Metody obrabotki mnogomernykh dannykh i vremennykh ryadov [Methods for processing multivariate data and time series], Goryachaya Liniya-Telekom Publishing, Moscow, 2007 (in Russian).

10. **Shiryayev A.N.,** Probability, Springer-Verlag, New-York, 1996.

11. **Ayvazyan S.A., Bukhshtaber V.M., Enyukov I.S., Meshalkin L.D.,** Prikladnaya statistika. Klassifikatsiya i snizheniye razmernosti [Applied statistics. Classification and dimension reduction], Finance and Statistics Publishing, Moscow, 1989 (in Russian).

12. **Esbensen K.H.,** Multivariate data analysis – in Practice, CAMO, Oslo, 1994 – 2002.

Received 21.06.2021, accepted 19.07.2021.

THE AUTHORS

MANOILOV Vladimir V.
Institute for Analytical Instrumentation of the Russian Academy of Sciences
26, Rizhsky Ave., St. Petersburg, 190103, Russian Federation
manoilov_vv@mail.ru

NOVIKOV Lev V.
Institute for Analytical Instrumentation of the Russian Academy of Sciences
26, Rizhsky Ave., St. Petersburg, 190103, Russian Federation
novik38@mail.ru

KUZMIN Aleksey G.
Institute for Analytical Instrumentation of the Russian Academy of Sciences
26, Rizhsky Ave., St. Petersburg, 190103, Russian Federation
agqz55@rambler.ru

TITOV Yuriy A.
Institute for Analytical Instrumentation of the Russian Academy of Sciences
26, Rizhsky Ave., St. Petersburg, 190103, Russian Federation
toplm@mail.ru

ZARUTSKII Igor V.
Institute for Analytical Instrumentation of the Russian Academy of Sciences
26, Rizhsky Ave., St. Petersburg, 190103, Russian Federation
igorzv@yandex.ru

СПИСОК ЛИТЕРАТУРЫ

1. **Li X., Huang D., Zeng J., Chan Ch.K., Zhou Z.** Positive matrix factorization: A data preprocessing strategy for direct mass spectrometry-based breath analysis // Talanta. 2019. Vol. 192. 15 January. Pp. 32–39.

2. **Li X., Huang L., Zhu H., Zhou Z.** Direct human breath analysis by secondary nano electrospray ionization ultrahigh resolution mass spectrometry: Importance of high mass resolution and mass accuracy // Rapid Communications in Mass Spectrometry. 2017. Vol. 31. No. 3. Pp. 301–308.

3. **Tiele A., Wicaksono A., Daulton E., Ifeachor E., Eyre V., Clarke S., Timings L., Pearson S., Covington J.A., Li X.** Breath-based non-invasive diagnosis of Alzheimer's disease: A pilot study // Journal of Breath Research. 2020. Vol. 14. No. 2. P. 026003.

4. **Van Dartel D., Schelhaas H.J., Colon A.J., Kho K.H., de Vos C.C.** Breath analysis in detecting epilepsy // Journal of Breath Research. 2020. Vol. 14. No. 3. P. 031001.

5. **Chen Ch.-Ch., Hsieh J.-Ch., Chao Ch.-H., Yang W.-Sh., Li X., Cheng H.-T., Chan Ch.-K., Lu Ch.-J., Meng H.-F., Zan H.-W.** Correlation between breath ammonia and blood ureanitrogen levels in chronic kidney disease and dialysis patients // Journal of Breath Research. 2020. Vol. 14. No. 3. P. 036002.

6. **Kononov A., Korotetsky B., Jahatspanian I., et al.** Online breath analysis using metal oxide semiconductor sensors (electronic nose) for diagnosis of lung cancer // Journal of Breath Research. 2020. Vol. 14. No. 1. P. 016004.

7. **Manoilov V.V., Novikov L.V., Belozertsev A.I., Zarutskii I.V., Titov Yu.A., Kuzmin A.G., El-Salim S.Z.** Processing of mass spectra of exhaled gases based on correlation algorithms // Journal of Analytical Chemistry. 2020. Vol. 75. No. 13. Pp. 1678–1684.

8. **Manoilov V.V., Novikov L.V., Zarutskii I.V., Kuzmin A.G., Titov Yu.A.** Methods for processing mass spectrometry signals from exhaled gases for medical diagnosis // Biomedical Engineering. 2020. Vol. 53. No. 5. Pp. 355–359.

9. **Большаков А.А., Каримов Р.Н.** Методы обработки многомерных данных и временных рядов. М.: Горячая линия-Телеком, 2007. 522 с.

10. **Ширяев А.Н.** Вероятность. В 2 кн. 4-е изд., перераб. и доп. Т. 1. Вероятность–1. М.: МЦНМО, 2007. 552 с.

11. **Айвазян С.А., Бухштабер В.М., Енюков И.С., Мешалкин Л.Д.** Прикладная статистика. Классификация и снижение размерности. М.: Финансы и статистика, 1989. 607 с.

12. **Эсбенсен К.** Анализ многомерных данных: избранные главы. Пер. с англ. Под ред. О.Е. Родионовой. Черноголовка.: ИПХФ РАН, 2005. 161 с.

Статья поступила в редакцию 21.06.2021, принята к публикации 19.07.2021.

СВЕДЕНИЯ ОБ АВТОРАХ

МАНОЙЛОВ Владимир Владимирович – *доктор технических наук, заведующий лабораторией автоматизации измерений и цифровой обработки сигналов Института аналитического приборостроения Российской академии наук, Санкт-Петербург, Российская Федерация.*

190103, Российская Федерация, г. Санкт-Петербург, Рижский пр., 26

manoilov_vv@mail.ru

НОВИКОВ Лев Васильевич – *доктор физико-математических наук, ведущий научный сотрудник лаборатории оптики заряженных частиц и математического моделирования Института аналитического приборостроения Российской академии наук, Санкт-Петербург, Российская Федерация.*

190103, Российская Федерация, г. Санкт-Петербург, Рижский пр., 26

novik38@mail.ru

КУЗЬМИН Алексей Георгиевич – *кандидат физико-математических наук, старший научный сотрудник лаборатории экологической масс-спектрометрии Института аналитического приборостроения Российской академии наук, Санкт-Петербург, Российская Федерация.*

190103, Российская Федерация, г. Санкт-Петербург, Рижский пр., 26

agqz55@rambler.ru

ТИТОВ Юрий Алексеевич – *научный сотрудник лаборатории автоматизации измерений и цифровой обработки сигналов Института аналитического приборостроения Российской академии наук, Санкт-Петербург, Российская Федерация.*

190103, Российская Федерация, г. Санкт-Петербург, Рижский пр., 26

toplm@mail.ru

ЗАРУЦКИЙ Игорь Вячеславович – *кандидат технических наук, старший научный сотрудник лаборатории автоматизации измерений и цифровой обработки сигналов Института аналитического приборостроения Российской академии наук, Санкт-Петербург, Российская Федерация.*

190103, Российская Федерация, г. Санкт-Петербург, Рижский пр., 26

igorzv@yandex.ru

DOI: 10.18721/JPM.14312
UDC 539.12

AN ANALYSIS OF φ MESON PRODUCTION IN THE COLLISIONS OF PROTON BEAMS WITH ALUMINUM AND GOLD NUCLEI AT ENERGIES OF 200 GeV

M.M. Mitrankova, E.V. Bannikov, A.Ya. Berdnikov, Ya.A. Berdnikov, A.V. Dubov, D.O. Kotov, Iu.M. Mitrankov

Peter the Great St. Petersburg Polytechnic University,
St. Petersburg, Russian Federation

In the paper, φ meson production in the relativistic collisions at energies of 200 GeV measured by the PHENIX experiment (RHIC) has been studied. Phi mesons' nuclear modification factors were calculated for the mentioned interactions under conditions identical to the experimental ones, using different theoretical models, the results being compared. The accounting for the formation phase of quark-gluon plasma (QGP) in simulation was established to agree well with experiment for the p + Au collisions and disagree for the p + Al ones. This result could indicate an insufficient size of the interaction system of the latter to form QGP at an energy of 200 GeV and the sufficiency of the created minimum conditions for its formation in the former interaction system.

Keywords: quark-gluon plasma, cold nuclear matter effect, nuclear modification factor

Citation: Mitrankova M.M., Bannikov E.V., Berdnikov A.Ya., Berdnikov Ya.A., Dubov A.V., Kotov D.O., Mitrankov Iu.M., An analysis of φ meson production in the collisions of proton beams with aluminum and gold nuclei at energies of 200 GeV, St. Petersburg Polytechnical State University Journal. Physics and Mathematics. 14 (3) (2021) 150–159. DOI: 10.18721/JPM.14312

АНАЛИЗ РОЖДЕНИЯ φ-МЕЗОНОВ В СТОЛКНОВЕНИЯХ ПУЧКОВ ПРОТОНОВ С ЯДРАМИ АЛЮМИНИЯ И ЗОЛОТА ПРИ ЭНЕРГИЯХ 200 ГэВ

М.М. Митранкова, Е.В. Банников, А.Я. Бердников, Я.А. Бердников, А.В. Дубов, Д.О. Котов, Ю.М. Митранков

Санкт-Петербургский политехнический университет Петра Великого,
Санкт-Петербург, Российская Федерация

В работе изучено рождение φ-мезонов в релятивистских столкновениях пучков протонов с ядрами алюминия (p + Al) и золота (p + Au) при энергиях 200 ГэВ, в области малых быстрот. Исследование проведено с помощью детекторной системы «ФЕНИКС» на коллайдере RHIC. С помощью различных теоретических моделей рассчитаны факторы ядерной модификации φ-мезонов в указанных взаимодействиях при условиях, идентичных экспериментальным, проведено сравнение результатов. Установлено, что учет фазы образования кварк-глюонной плазмы (КГП) при моделировании дает хорошее согласие с экспериментом для взаимодействия p + Au и не дает его для p + Al, что может говорить о недостаточности размера системы взаимодействия последнего при энергии 200 ГэВ для формирования КГП, а также достаточности созданных минимальных условий для ее формирования в первом случае.

Ключевые слова: кварк-глюонная плазма, эффект холодной ядерной материи, фактор ядерной модификации

Ссылка при цитировании: Митранкова М.М., Банников Е.В., Бердников А.Я., Бердников Я.А., Дубов А.В., Котов Д.О., Митранков Ю.М. Анализ рождения φ-мезонов в столкновениях пучков протонов с ядрами алюминия и золота при энергиях 200 ГэВ // Научно-технические ведомости СПбГПУ. Физико-математические науки. 2021. Т. 14. № 3. С. 150–159. DOI: 10.18721/JPM.14312

Introduction

Computations in lattice quantum chromodynamics predict a phase transition of hadron gas into such a state of matter as quark-gluon plasma (QGP) at a temperature $T \approx 150$ MeV $\approx 10^{12}$ K (Fig. 1 [1]). QGP is matter consisting of strongly interacting elementary particles, where quarks and gluons are deconfined and can move like quasi-free particles.

Systematic study of collisions of relativistic nuclei presents a unique opportunity to explore the phase transition of quantum chromodynamics (QCD) in laboratory conditions. The experimental program of the PHENIX detector [2] at the Relativistic Heavy Ion Collider (RHIC [3]) includes a wide range of colliding nuclei systems: from basic interactions of proton beams to heavy ion collisions. This allows analyzing different aspects of the conditions necessary to produce QGP.

Experimental signatures of QGP were previously obtained in collisions of such systems as heavy ions of gold (Au + Au) [4], copper and gold (Cu + Au), with the nuclei accelerated to relativistic energy $\sqrt{s_{NN}} = 200$ GeV, and with uranium (U + U) nuclei accelerated at $\sqrt{s_{NN}} = 192$ GeV [5]. As for the dynamics of proton interactions ($p + p$), it is well described by perturbative QCD [1].

Study of elliptical and triangular fluxes of charged hadrons in small interaction systems, such as proton beams with gold nuclei (p + Au), deuterium nuclei with gold nuclei (d + Au), helium-3 nuclei with gold nuclei (^{3}He + Au), made it possible to formulate the hypothesis that the energy density in such collisions is sufficient for producing hot and dense QGP matter [6, 7]. Further experiments are necessary to gain deeper insights into the evolution of the system.

Investigations into the peculiarities of light hadron production are widely carried out for studying the process of QGP generation in the interactions of relativistic nuclei [5].

While there is a wide variety of light hadrons, the φ meson holds particular interest [8], since it contains (anti)strange quarks ($s\bar{s}$), its yields are measurable up to large transverse momenta, and it has a relatively small cross section for hadron interaction, as well as a longer lifetime than that of QGP (~46 fm/c, compared to ~5 fm/c, where c is the speed of light in vacuum [1]).

Study of light hadron production in interactions of relativistic nuclei makes it possible to observe various effects of hot (assuming the generation of QGP) [1] and cold (reflecting the initial and final conditions of interaction) [9] nuclear matter. Phenomena pointing to production of hot and dense matter include collective effects such as increased strangeness yield [10] and the jet quenching effect [11]. The effects of cold nuclear matter include the Cronin effect [12], multiple parton scattering [13], modification of the initial distribution functions of partons in the nucleus [14], etc.

Thus, multiple effects of different nature, indicating either production or absence of QGP, are capable of influencing the production of the φ meson in the interaction of relativistic nuclei. Simulating the interactions under the conditions matching the experimental ones allows obtaining, via different theoretical models, the expected influence from hot and cold nuclear matter on the production of φ mesons.

The minimum conditions for QGP production can be understood by interpreting the experimental data based on comparison with simulation.

The goal of this study consisted in exploring the evolution of collisions of proton beam systems with aluminum and gold nuclei at an energy $\sqrt{s_{NN}} = 200$ GeV by simulating the φ meson production in such collisions and comparing the simulated results with the experiment.

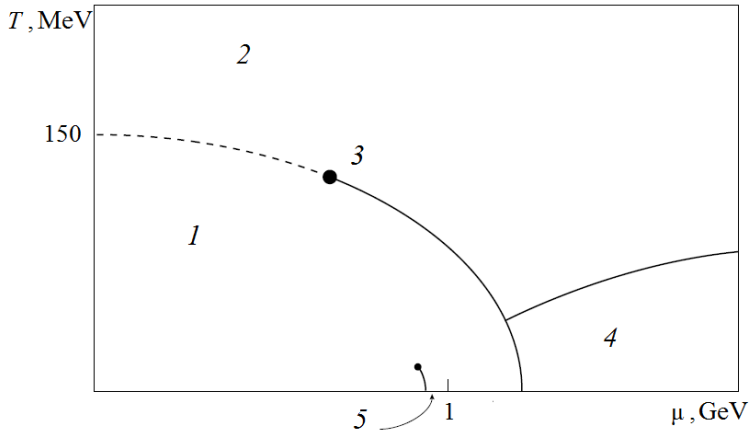

Fig. 1. Theoretical phase diagram of nuclear matter as function of temperature T and baryonic chemical potential μ:
hadron gas *1*, quark-gluon plasma *2*, critical point *3*, color superconductivity *4*, normal nuclear matter *5*. The dashed line indicates the second-order phase transition

The PYTHIA [15] and AMPT [16] software packages with default parameters were used to simulate the evolution of the system without the QGP phase. The AMPT model with string melting was used to consider collective effects (QGP effects).

Measurement method and models used

The experimental datasets used in the analysis were obtained in the PHENIX experiment at RHIC at $\sqrt{s_{NN}} = 200$ GeV in (p + Al) and (p + Au)-interactions near midrapidity ($|\eta| < 0.35$). The production of φ mesons was considered in the decay channel into two unlike-sign K mesons. The values of the φ meson mass, its mean lifetime, and the probability of decay in a given channel (Br) are listed in Table [14].

According to Glauber's model [17], the interaction of relativistic nuclei in the absence of collective effects can be represented as a superposition of elementary nucleon-nucleon interactions. However, various effects of both hot and cold matter can influence the evolution of a system of colliding nuclei. For this reason, nuclear modification factors RAB are used to study the collective effects governing particle production in collisions of ultrarelativistic nuclei [18]. This quantity is calculated as the ratio of invariant hadron yields in $A + B$ collision to the invariant yield of the same hadrons in proton beam collisions ($p + p$) at the same energy, normalized to the number of inelastic nucleon-nucleon collisions (N_{coll}) in $A + B$ system.

The value of Ncoll in Glauber's model is estimated using Monte Carlo simulation.

For deeper analysis of the experimental data obtained, we used the PYTHA and AMPT software packages to simulate the p + Al and p + Au interactions at $\sqrt{s_{NN}} = 200$ GeV, similar to the interactions carried out experimentally. Lund's model of string fragmentation is widely used to describe the hadronization process of ($p + p$) collisions and to perform QCD computations [19].

Table

Main characteristics of φ meson decay

Decay channel	Mass, MeV/c^2	Mean lifetime, fm/c	Br, %
$\varphi \rightarrow K^+K^-$	1019.455 ± 0.020	46.3 ± 0.4	48.9 ± 0.5

The PYTHIA software package was created in 1997 based on this model: its purpose is to simulate the interaction of protons at high energies. We used the latest version of the software package, PYTHIA 8, in our study. However, the computational results related to φ meson production in interactions of proton beams at $\sqrt{s_{NN}}$ = 200 GeV deviate from the experimental data [20]. A new hybrid PYTHIA/Angantyr model was constructed based on PYTHIA to describe the interactions of heavy (heavier than a proton) relativistic nuclei [21]. The interaction of $A + B$ nuclei is described within the framework of this model as a superposition of elementary nucleon-nucleon interactions of different types (elastic, diffraction, absorptive).

Nuclear modification factors of the φ meson were calculated in this study based on the simulated interactions in the PYTHIA software package in accordance with the same procedure that was applied to the experimental data. The values of the nuclear modification factor RAB were calculated as the ratio of invariant φ meson yields in p + Al or p + Au interactions, obtained using the PYTHIA/Angantyr software package, to similar invariant φ meson yields in the interactions of proton beams at the same energy $\sqrt{s_{NN}}$ = 200 GeV, obtained using the standard PYTHIA 8 package. This ratio is normalized to the experimental number of inelastic nucleon-nucleon collisions (N_{coll}) in the p + Al or p + Au system, respectively. This procedure for calculating the nuclear modification factors eliminates the aforementioned discrepancy between the experimental and the calculated data for invariant φ meson yields in proton beam interactions, performed using the PYTHIA 8 package.

Another theoretical model widely used for describing the evolution of relativistic ion collisions is the Multi-Phase Transport Model (AMPT). The software package based on this model makes it possible to comprehensively study the process of potential QGP production. The AMPT model with default parameters describes the evolution of relativistic nuclei interaction without QGP production. This AMPT model configuration includes the following stages:

initial conditions,

parton cascade accounting for the confined state of quarks and gluons;

transition from parton to hadron matter based on Lund's model of string fragmentation;

hadronic interactions.

The extended configuration of the AMPT software package with string melting accounts for the production of the QGP phase: the parton cascade is simulated, followed by partons combining into hadrons by the quark coalescence model [16]. In this case, the nuclear modification factors of the φ meson were calculated as the ratio of their invariant yields in the given interactions, obtained using the AMPT software package, to the experimental value of the similar invariant yield in the interaction of proton beams ($p + p$) at the same energy [22], normalized to the experimental number N_{coll} of inelastic nucleon-nucleon collisions p + Al or p + Au, respectively.

Experimental results and discussion

Fig. 2,*a*,*b* compares the nuclear modification factors of φ mesons in p + Al and p + Au collisions at $\sqrt{s_{NN}}$ = 200 GeV, obtained in the PHENIX experiment, and nuclear modification factors of φ mesons in similar interactions, calculated using the PYTHIA software package. Evidently, the nuclear modification factors of φ mesons calculated with the PYTHIA software package are in good agreement with the experimental results in p + Al collisions at $\sqrt{s_{NN}}$ = 200 GeV. However, the values of RAB calculated using the PYTHIA model turn out to be less than R_{AB} obtained in the experiment in p + Au interactions at $\sqrt{s_{NN}}$ = 200 GeV. Notably, the discrepancy grows with increasing transverse momentum p_T.

Fig. 2,*c*,*d* shows the distributions of the nuclear modification factors R_{AB} over transverse momentum, measured for φ mesons in (p + Al) and (p + Au)-interactions at the same energy $\sqrt{s_{NN}}$ = = 200 GeV at the PHENIX experiment using the AMPT software package. The AMPT model with default parameters describes the experimental results in (p + Al) interactions fairly well, while the

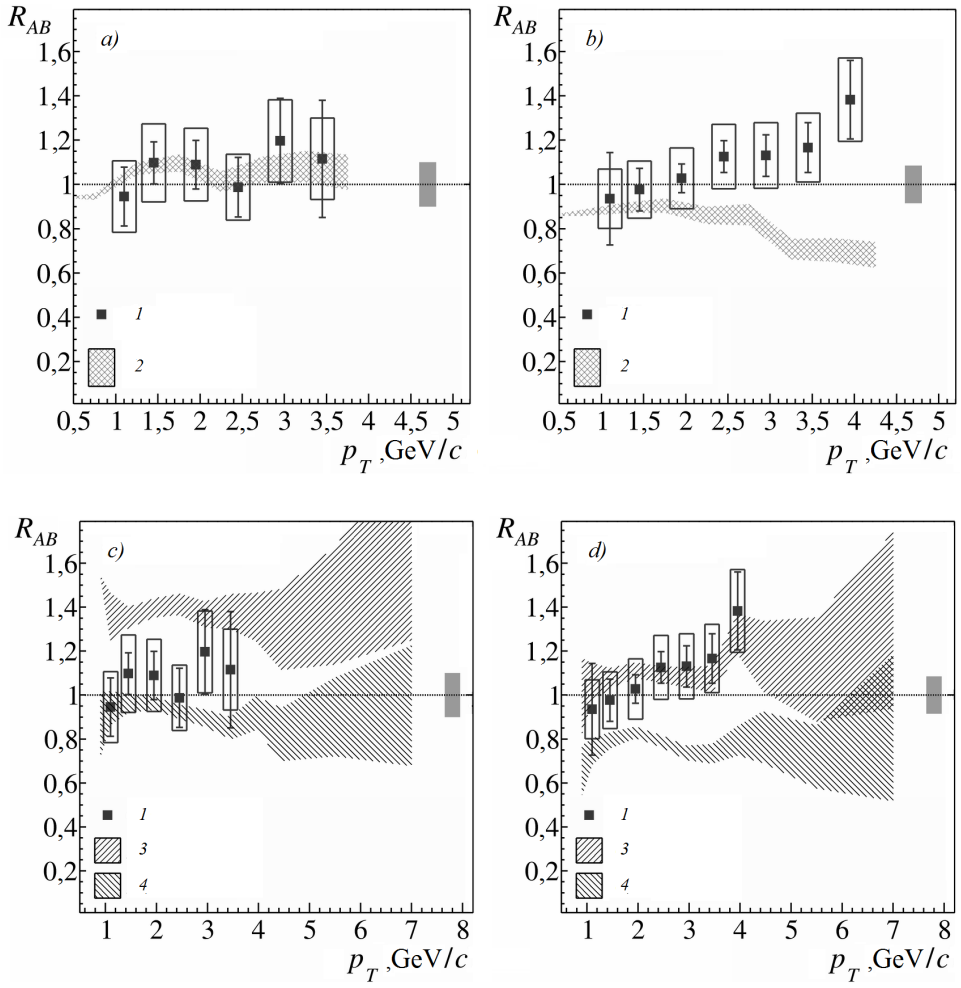

Fig. 2. Distributions of nuclear modification factors of φ mesons over transverse momentum in (p + Al)- (a,c) and (p + Au)- (b,d) interactions at $\sqrt{s_{NN}}$ = 200 GeV; data obtained experimentally (1), using PYTHIA software package (2), AMPT software package, configuration with string melting (3) and with default parameters (4). Bars and boxes correspond to statistical and systematic uncertainties, shaded boxes on the right correspond to normalized uncertainty

AMPT configuration with string melting yields smaller R_{AB} values in (p + Au) interactions. than the experiments. On the other hand, the values of nuclear modification factors of φ mesons calculated using the AMPT model configuration with string melting exceed the experimental ones in (p + Al) interactions, but agree well with those in (p + Au) interactions.

Conclusion

We have analyzed the production of φ mesons in collisions of proton beams with aluminum and gold nuclei at $\sqrt{s_{NN}}$ = 200 GeV at midrapidity. The interactions were simulated under the conditions matching the experimental ones using the PYTHIA and AMPT software packages and comparing the obtained experimental results with the data of theoretical computations.

The distribution of nuclear modification factors of φ mesons in (p + Au) collisions at $\sqrt{s_{NN}}$ = = 200 GeV near midrapidity coincides with the computed results obtained using the AMPT model with string melting, within the uncertainty, while the nuclear modification factors obtained in the

PYTHIA and AMPT software packages with default parameters turned out to be smaller than the experimental values.

Conversely, the distribution of nuclear modification factors of φ mesons in (p + Al) collisions at $\sqrt{s_{NN}}$ = 200 GeV near midrapidity coincides with the computed results obtained using the the PYTHIA and AMPT software packages with default parameters, with the uncertainty, while the nuclear modification factors obtained using the AMPT model with string melting turned out to be larger than the experimental values.

The result obtained may indicate that the mechanism governing the φ meson production at $\sqrt{s_{NN}}$ = 200 GeV in interactions of proton beams with aluminum nuclei is considerably different from that in interactions of proton beams with gold nuclei. The minimum conditions (temperature and baryon density) necessary for QGP production may be achieved in the interactions of proton beams with gold nuclei at $\sqrt{s_{NN}}$ = 200 GeV, while no signatures for QGP production are observed in the interactions of proton beams with aluminum nuclei at the same energy.

The study was carried out within the framework of State Assignment for Basic Research (code 0784-2020-0025).

REFERENCES

1. **Adcox K., Adler S.S., Afanasiev S., et al.,** Formation of dense partonic matter in relativistic nucleus-nucleus collisions at RHIC: experimental evaluation by the PHENIX Collaboration, Nucl. Phys. A. 757 (1–2) (2005) 184–283.

2. **Adcox K., Adler S.S., Aizama M., et al.** (PHENIX Collaboration), PHENIX detector overview, Nucl. Instr. Meth. Phys. Res., A. 499 (2–3) (2003) 469–479.

3. **Harrison M., Ludlam T., Ozaki S.,** RHIC project overview, Nucl. Instr. Meth. Phys. Res., A. 499 (2–3) (2003) 235–244.

4. **Adare A., Afanasiev S., Aidala C., et al.,** Nuclear modification factors of φ mesons in d + Au, Cu + + Cu and Au + Au collisions at $\sqrt{s_{NN}}$ = 200 GeV, Phys. Rev. C. 83 (2) (2011) 024909.

5. **Berdnikov A., Berdnikov Ya., Kotov D., et al.,** Phi meson measurements in Cu + Au collisions at 200 GeV and in U + U collisions at 192 GeV, J. Phys., Conf. Ser. 1135 (1) (2018) 012044.

6. **Aidala C., Akiba Y., Alfred M., et al.** (PHENIX Collaboration), Creation of quark-gluon plasma droplets with three distinct geometries, Nat. Phys. 15 (March) (2019) 214–220.

7. **Nagle J., Zajc W.,** Small system collectivity in relativistic hadronic and nuclear collisions, Ann. Rev. Nucl. Part. Sci. 68 (2018) 211–235.

8. **Shor A.** Phi meson production as a probe of the quark-gluon plasma, Phys. Rev. Lett. 54 (11) (1985) 1122–1125.

9. **Armesto N.,** Small collision systems: theory overview on cold nuclear matter effects, EPJ Web of Conferences. 171 (2018) 11001.

10. **Koch P., Müller B., Rafelski J.,** Strangeness in relativistic heavy ion collisions, Phys. Rep. 142 (4) (1986) 167–262.

11. **d'Enterria D.** (CERN and MIT, LNS), 6.4. Jet quenching, Springer materials (Germany), Ed. by R. Stock, Landolt-Bornstein – Group I – Elementary Particles, Nuclei and Atoms. 23 (Relativistic Heavy Ion Physics) (2010) 471–520.

12. **Kopeliovich B.Z., Nemchik J., Schäfer A., Tarasov A.V.,** Cronin effect in hadron production of nuclei, Phys. Rev. Lett. 88 (23) (2002) 232303.

13. **Arneodo M.,** Nuclear effects in structure functions, Phys. Rep. 240 (5–6) (1994) 301–393.

14. **Nakamura K. et Particle Data Group.,** Review of particle physics, J. Phys. G. 37 (7A) (2010) 075021.

15. **Sjostrand T., Ask S., Christiansen J., et al.,** An introduction to PYTHIA 8.2, Comp. Phys. Comm. 191 (June) (2015) 159–177.

16. **Lin Z.-W., Ko C. M., Li B.-A., et al.,** Multiphase transport model for relativistic heavy ion collisions, Phys. Rev. C. 72 (6) (2005) 064901.

17. **Miller M., Reygers K., Sanders S., Steinberg P.,** Glauber modeling in high energy nuclear collisions, Ann. Rev. Nucl. Part. Sci. 57 (2007) 205–243.

18. **Mitrankova M.M., Berdnikov Ya.A., Berdnikov A.Ya., et al.,** Production of light flavor hadrons in small systems measured by PHENIX at RHIC, Phys. Scr. 96 (8) (2021) 084010.

19. **Andersson B., Mohanty S., Soderberg F.,** Parton fragmentation and string dynamics, Phys. Rep. 97 (2–3) (1983) 31–145.

20. **Adam J., Adamova D., Aggarwal M., et. al.,** $K^*(892)^0$ and φ(1020) meson production at high transverse momentum in *p*-*p* and Pb-Pb collisions at $\sqrt{s_{NN}}$ = 2.76 TeV, Phys. Rev. C. 95 (6) (2017) 064606.

21. **Bierlich C., Gustafson G., Lönnblad L., Shah H.,** The Angantyr model for heavy-ion collisions in PYTHIA 8, J. High Energy Phys. 2018 (10) (2018) 134.

22. **Adare A., Afanasiev S., Aidala C., et al.,** Measurement of neutral mesons in $p + p$ collisions at $\sqrt{s_{NN}}$ = 200 GeV and scaling properties of hadron production, Phys. Rev. D. 83 (5) (2011) 05200422.

Received 20.06.2021, accepted 05.07.2021.

THE AUTHORS

MITRANKOVA Mariia M.
Peter the Great St. Petersburg Polytechnic University
29 Politechnicheskaya St., St. Petersburg, 195251, Russian Federation
mashalario@gmail.com

BANNIKOV Egor V.
Peter the Great St. Petersburg Polytechnic University
29 Politechnicheskaya St., St. Petersburg, 195251, Russian Federation
bannikov.ev.21@gmail.com

BERDNIKOV Alexander Ya.
Peter the Great St. Petersburg Polytechnic University
29 Politechnicheskaya St., St. Petersburg, 195251, Russian Federation
alexber@phmf.spbstu.ru

BERDNIKOV Yaroslav A.
Peter the Great St. Petersburg Polytechnic University
29 Politechnicheskaya St., St. Petersburg, 195251, Russian Federation
berdnikov@spbstu.ru

DUBOV Alexander V.
Peter the Great St. Petersburg Polytechnic University
29 Politechnicheskaya St., St. Petersburg, 195251, Russian Federation
alexanderpolytech@mail.ru

KOTOV Dmitry O.
Peter the Great St. Petersburg Polytechnic University
29 Politechnicheskaya St., St. Petersburg, 195251, Russian Federation
dmitriy.kotov@gmail.com

MITRANKOV Iurii M.
Peter the Great St. Petersburg Polytechnic University
29 Politechnicheskaya St., St. Petersburg, 195251, Russian Federation
mitrankovy@gmail.com

СПИСОК ЛИТЕРАТУРЫ

1. **Adcox K., Adler S.S., Afanasiev S., et al.** Formation of dense partonic matter in relativistic nucleus-nucleus collisions at RHIC: experimental evaluation by the PHENIX Collaboration // Nuclear Physics A. 2005. Vol. 757. No. 1–2. Pp. 184–283.

2. **Adcox K., Adler S.S., Aizama M., et al.** (PHENIX Collaboration). PHENIX detector overview // Nuclear Instruments and Methods in Physics Research. Section A: Accelerators, Spectrometers, Detectors and Associated Equipment. 2003. Vol. 499. No. 2–3. Pp. 469–479.

3. **Harrison M., Ludlam T., Ozaki S.** RHIC project overview // Nuclear Instruments and Methods in Physics Research. A. 2003. Vol. 499. No. 2–3. Pp. 235–244.

4. **Adare A., Afanasiev S., Aidala C., et al.** Nuclear modification factors of φ mesons in d + Au, Cu + + Cu and Au + Au collisions at $\sqrt{s_{NN}}$ = 200 GeV // Physical Review. C. 2011. Vol. 83. No. 2. P. 024909.

5. **Berdnikov A., Berdnikov Ya., Kotov D., et al.** Phi meson measurements in Cu + Au collisions at 200 GeV and in U + U collisions at 192 GeV // J. Phys.: Conf. Ser. 2018. Vol. 1135. No. 1. P. 012044.

6. **Aidala C., Akiba Y., Alfred M., et al.** (PHENIX Collaboration). Creation of quark-gluon plasma droplets with three distinct geometries // Nature Physics. 2019. Vol. 15. March. Pp. 214–220.

7. **Nagle J., Zajc W.** Small system collectivity in relativistic hadronic and nuclear collisions // Annual Review of Nuclear and Particle Science. 2018. Vol. 68. Pp. 211–235.

8. **Shor A.** Phi meson production as a probe of the quark-gluon plasma // Physical Review Letters. 1985. Vol. 54. No. 11. Pp. 1122–1125.

9. **Armesto N.** Small collision systems: theory overview on cold nuclear matter effects // EPJ Web of Conferences. 2018. Vol. 171. P. 11001.

10. **Koch P., Müller B., Rafelski J.** Strangeness in relativistic heavy ion collisions // Physics Reports. 1986. Vol. 142. No. 4. Pp. 167–262.

11. **d'Enterria D.** (CERN and MIT, LNS). 6.4. Jet quenching. Springer materials (Germany). Ed. by R. Stock. Landolt-Bornstein – Group I – Elementary Particles, Nuclei and Atoms. 2010. Vol. 23 (Relativistic Heavy Ion Physics). Pp. 471–520.

12. **Kopeliovich B.Z., Nemchik J., Schäfer A., Tarasov A.V.** Cronin effect in hadron production of nuclei // Physical Review Letters. 2002. Vol. 88. No. 23. P. 232303.

13. **Arneodo M.** Nuclear effects in structure functions // Physics Reports. 1994. Vol. 240. No. 5–6. Pp. 301–393.

14. **Nakamura K. et Particle Data Group.** Review of particle physics // Journal of Physics G. 2010. Vol. 37. No. 7A. P. 075021.

15. **Sjostrand T., Ask S., Christiansen J., Corke R., Desai N., Ilten P., Mrenna S., Prestel S., Rasmussen C., Skands P.** An introduction to PYTHIA 8.2 // Computer Physics Communications. 2015. Vol. 191. June. Pp. 159–177.

16. **Lin Z.-W., Ko C. M., Li B.-A., Zhang B., Pal S.** Multiphase transport model for relativistic heavy ion collisions // Physical Review C. 2005. Vol. 72. No. 6. P. 064901.

17. **Miller M., Reygers K., Sanders S., Steinberg P.** Glauber modeling in high energy nuclear collisions // Annual Review of Nuclear and Particle Science. 2007. Vol. 57. Pp. 205–243.

18. **Mitrankova M.M., Berdnikov Ya.A., Berdnikov A.Ya., Kotov D.O., Mitrankov Iu.M.** Production of light flavor hadrons in small systems measured by PHENIX at RHIC // Physica Scripta. 2021. Vol. 96. No. 8. P. 084010

19. **Andersson B., Mohanty S., Soderberg F.** Parton fragmentation and string dynamics // Physics Reports. 1983. Vol. 97. No. 2–3. Pp. 31–145.

20. **Adam J., Adamova D., Aggarwal M., et. al.** $K^*(892)^0$ and φ(1020) meson production at high transverse momentum in *p-p* and Pb-Pb collisions at $\sqrt{s_{NN}}$ = 2.76 TeV // Physical Review. C. 2017. Vol. 95. No. 6. P. 064606.

21. **Bierlich C., Gustafson G., Lönnblad L., Shah H.** The Angantyr model for heavy-ion collisions in PYTHIA 8 // Journal of High Energy Physics. 2018. Vol. 2018. No. 10. P. 134.

22. **Adare A., Afanasiev S., Aidala C., et al.** Measurement of neutral mesons in $p + p$ collisions at $\sqrt{s_{NN}}$ = 200 GeV and scaling properties of hadron production // Physical Review D. 2011. Vol. 83. No. 5. P. 052004.

Статья поступила в редакцию 20.06.2021, принята к публикации 05.07.2021.

СВЕДЕНИЯ ОБ АВТОРАХ

МИТРАНКОВА Мария Максимовна – *аспирантка Высшей инженерно-физической школы Санкт-Петербургского политехнического университета Петра Великого, Санкт-Петербург, Российская Федерация.*

195251, Российская Федерация, г. Санкт-Петербург, Политехническая ул., 29

mashalario@gmail.com

БАННИКОВ Егор Викторович – *студент магистратуры Института энергетики Санкт-Петербургского политехнического университета Петра Великого, Санкт-Петербург, Российская Федерация.*

195251, Российская Федерация, г. Санкт-Петербург, Политехническая ул., 29

bannikov.ev.21@gmail.com

БЕРДНИКОВ Александр Ярославич – *кандидат физико-математических наук, доцент Высшей инженерно-физической школы Санкт-Петербургского политехнического университета Петра Великого, Санкт-Петербург, Российская Федерация.*

195251, Российская Федерация, г. Санкт-Петербург, Политехническая ул., 29

alexber@phmf.spbstu.ru

БЕРДНИКОВ Ярослав Александрович – *доктор физико-математических наук, профессор Высшей инженерно-физической школы Санкт-Петербургского политехнического университета Петра Великого, Санкт-Петербург, Российская Федерация.*

195251, Российская Федерация, г. Санкт-Петербург, Политехническая ул., 29

berdnikov@spbstu.ru

ДУБОВ Александр Викторович – *аспирант Высшей инженерно-физической школы Санкт-Петербургского политехнического университета Петра Великого, Санкт-Петербург, Российская Федерация.*

195251, Российская Федерация, г. Санкт-Петербург, Политехническая ул., 29

alexanderpolytech@mail.ru

КОТОВ Дмитрий Олегович – *кандидат физико-математических наук, доцент Высшей инженерно-физической школы Санкт-Петербургского политехнического университета Петра Великого, Санкт-Петербург, Российская Федерация.*

195251, Российская Федерация, г. Санкт-Петербург, Политехническая ул., 29

dmitriy.kotov@gmail.com

МИТРАНКОВ Юрий Михайлович – *ассистент Высшей инженерно-физической школы Санкт-Петербургского политехнического университета Петра Великого, Санкт-Петербург, Российская Федерация.*

195251, Российская Федерация, г. Санкт-Петербург, Политехническая ул., 29

mitrankovy@gmail.com

DOI: 10.18721/JPM.14313
UDC 514.13:531.51

THE RELATIVISTIC UNIFORM MODEL: THE METRIC OF THE COVARIANT THEORY OF GRAVITATION INSIDE A BODY

S.G. Fedosin

Perm, Perm Territory, Russian Federation
sergey.fedosin@gmail.com

In the paper, it has been established that the sum of stress-energy tensors of the electromagnetic and gravitational fields, the acceleration and the pressure ones inside a stationary uniform spherical body vanishes within the framework of relativistic uniform model. This fact significantly simplifies a solution of the equation for the metric in the covariant theory of gravitation (CTG). The metric tensor components inside the body were calculated, and then they were combined with those of external metric tensor on the body's surface. The latter procedure also allowed us to exactly determine one of two unknown coefficients in the metric outside the body. The comparison between the CTG metric and the Reissner – Nordström one in general theory of relativity clearly demonstrated their difference caused by discrepancy between equations for the metric and a difference in formulations of the cosmological constant.

Keywords: metric, covariant theory of gravitation, scalar curvature, cosmological constant

Citation: Fedosin S.G., The relativistic uniform model: the metric of the covariant theory of gravitation inside a body, St. Petersburg Polytechnical State University Journal. Physics and Mathematics. 14 (3) (2021) 160–176. DOI: 10.18721/JPM.14313

О МЕТРИКЕ КОВАРИАНТНОЙ ТЕОРИИ ГРАВИТАЦИИ ВНУТРИ ТЕЛА В РЕЛЯТИВИСТСКОЙ ОДНОРОДНОЙ МОДЕЛИ

С.Г. Федосин

г. Пермь, Пермский край, Российская Федерация
sergey.fedosin@gmail.com

В работе доказывается, что сумма тензоров энергии-импульса электромагнитного и гравитационного полей, поля ускорений и поля давления внутри неподвижного однородного сферического тела обращается в нуль в рамках релятивистской однородной модели. Это обстоятельство существенно упрощает решение уравнения для метрики в ковариантной теории гравитации (КТГ). Вычисляются компоненты метрического тензора внутри рассматриваемого тела, а затем на его поверхности они «сшиваются» с компонентами внешнего метрического тензора. Последняя процедура позволяет точно определить один из двух неизвестных коэффициентов в метрике за пределами тела. Сравнение метрики КТГ с метрикой Рейсснера – Нордстрёма в общей теории относительности наглядно показывает их различие, которое обусловлено несовпадением уравнений для метрики, а также различием формулировок космологической постоянной.

Ключевые слова: метрика, ковариантная теория гравитации, скалярная кривизна, космологическая постоянная, релятивистская система

Ссылка при цитировании: Федосин С.Г. О метрике ковариантной теории гравитации внутри тела в релятивистской однородной модели // Научно-технические ведомости СПбГПУ. Физико-математические науки. 2021. Т. 14. № 3. С. 160–176. DOI: 10.18721/JPM.14313

Introduction

In modern physics, the space-time metric of a certain physical system is completely defined by the corresponding metric tensor. The metric definition is of particular importance in the general theory of relativity, where the metric describes an action of gravity. In contrast, in the covariant theory of gravitation (CTG), gravity is an independent physical interaction. In this case, the metric of CTG is required mainly to describe the additional effects, associated with the interaction of electromagnetic waves with the gravitational field in the processes of space-time measurements by means of these waves. Accordingly, the metric form depends significantly on the theory of gravitation used.

Despite the success of the general theory of relativity in describing various gravitational phenomena, the theoretical foundation of this theory is still unsatisfactory. First of all, this is due to the absence of a generally recognized energy-momentum tensor of the gravitational field itself, the search for which has continued to this day [1 – 3]. Accordingly, the energy and momentum of a system becomes ambiguous or not conserved [4 – 6]. Other problems include emerging singularities, the need to interpret the cosmological constant, dark matter, dark energy, etc. In this regard, the search for alternatives to the general theory of relativity remains relevant, in particular, among vector-tensor theories [7 – 9].

The CTG refers to vector theories and has a well-defined energy-momentum tensor of the gravitational field. Outside a fixed spherical body, the metric tensor components within the framework of CTG were determined in Ref. [10]. Only the gravitational and electromagnetic fields exist outside the body, therefore only these fields exert their influence on the space-time metric here. Using this metric, it was possible to calculate the Pioneer effect, which has no explanation in the general theory of relativity [11]. CTG formulas describing the gravitational time dilation, the gravitational redshift of the wavelength, the signal delay in the gravitational field, lead to the same results as the general theory of relativity [12].

Next, we will calculate the metric of CTG inside a spherical body. In the presence of the matter, we should take into account the pressure field, which we consider in a covariant form as a vector field. Similarly, the concept of the vector acceleration field [13, 14] is used to calculate the energy and momentum of the matter, and its contribution into the equation for the metric. It is the representation of these fields in the form of vector fields that made it possible to find a covariant expression for the Navier – Stokes equation [15]. In contrast, in the general relativity, the pressure field and the acceleration one are almost always considered as simple scalar fields. Consequently, we can assume that CTG represents the contribution of the fields to the energy and momentum more accurately, as well as it does to the metric of the system.

In order to simplify the solution of the problem, we will assume that the matter of the body moves chaotically in the volume of the spherical shape, and it is kept from disruption by gravitation. The gravitational force in such macroscopic objects, as planets and stars, is so strong that it is sufficient to form the spherical shapes of them. This force is counteracted by the pressure force in the matter and the force from the acceleration field. One of the manifestations of the force from the acceleration field is the centrifugal force arising from that component of the particles' velocity, which is perpendicular to the radius-vector of the particles. We can also take into account the electromagnetic field and the corresponding force, which usually leads to repulsion of the charged matter in case of the excess charge of one sign. We will also assume that the physical system under consideration is a relativistic uniform system, in which the mass and charge distributions are similar to each other. This will allow us to use the expressions found earlier for the potentials and field strengths.

The need to determine the metric inside the matter arises as a consequence of the fact that the comparison of expressions for the components of the metric tensor inside and outside the matter makes it possible to unambiguously determine one of the unknown coefficients in the external metric. As a result, we obtain a more accurate expression for the CTG metric, suitable for solving more complex problems and considering small gravitational effects.

The equation for the metric

The use of the principle of least action leads to the following equation for the metric in CTG [14]:

$$R_{\alpha}^{\beta} - \frac{1}{4} R \delta_{\alpha}^{\beta} = -\frac{1}{2ck}\left(U_{\alpha}^{\beta} + W_{\alpha}^{\beta} + B_{\alpha}^{\beta} + P_{\alpha}^{\beta}\right), \tag{1}$$

where c is the speed of light; k is the constant, which is part of the Lagrangian in the terms with the scalar curvature R and with the cosmological constant Λ; R_{α}^{β} is the Ricci tensor with the mixed indices; δ_{α}^{β} is the unit tensor (the Kronecker symbol); U_{α}^{β}, W_{α}^{β}, B_{α}^{β} and P_{α}^{β} are the stress-energy tensors of the gravitational, electromagnetic, the acceleration and the pressure ones, respectively.

As was shown in Ref. [16] all the quantities in Eq. (1) should be averaged over the volume of the system's typical particles, if Eq. (1) is used to find the metric inside the body. We will further assume that such averaging has already been carried out in Eq. (1). Another conclusion in Ref. [16] is that, within the framework of the relativistic uniform model, the scalar curvature inside a stationary body with the constant relativistically invariant mass density and charge is a certain constant quantity $\overline{R}$. In this case, the relation $\overline{R} = 2\overline{\Lambda}$ holds in CTG, where $\overline{\Lambda}$ is the averaged cosmological constant for the matter inside the body.

Acting in the same way as we did in Ref. [10], we will use the spherical coordinates

$$x^0 = ct,\ x^1 = r,\ x^2 = \theta,\ x^3 = \varphi,$$

related to the Cartesian coordinates by the relations:

$$x = r\sin\theta\cos\varphi,\ \ y = r\sin\theta\sin\varphi,\ \ z = r\cos\theta.$$

For the static metric, the standard form of the metric tensor of the spherical uniform body is as follows:

$$g_{\alpha k} = \begin{pmatrix} B & 0 & 0 & 0 \\ 0 & -K & 0 & 0 \\ 0 & 0 & -E & 0 \\ 0 & 0 & 0 & -E\sin^2\theta \end{pmatrix}, \tag{2}$$

$$g^{k\beta} = \begin{pmatrix} \frac{1}{B} & 0 & 0 & 0 \\ 0 & -\frac{1}{K} & 0 & 0 \\ 0 & 0 & -\frac{1}{E} & 0 \\ 0 & 0 & 0 & -\frac{1}{E\sin^2\theta} \end{pmatrix}, \tag{3}$$

where B, K, E are the functions of the radial coordinate r only and do not depend on the angular variables.

And there are four nonzero components of the metric tensor:

$$g_{00} = B,\ g_{11} = -K,\ g_{22} = -E,\ g_{33} = -E\sin^2\theta.$$

By definition, the Christoffel coefficients $\Gamma^{\beta}_{\mu\nu}$ are expressed in terms of the metric tensor and its derivatives:

$$\Gamma^{\beta}_{\mu\nu} = \frac{1}{2} g^{\beta\gamma}\left(\partial_{\mu} g_{\gamma\nu} + \partial_{\nu} g_{\gamma\mu} - \partial_{\gamma} g_{\mu\nu}\right). \tag{4}$$

If we denote the derivatives with respect to the radius r by primes, then the nonzero Christoffel coefficients, expressed in terms of the functions B, K, E in the metric tensors (2) and (3), are equal, according to Eq. (4), to the following:

$$\begin{gathered}\Gamma^{0}_{01} = \Gamma^{0}_{10} = \frac{B'}{2B},\ \Gamma^{1}_{00} = \frac{B'}{2K},\ \Gamma^{1}_{11} = \frac{K'}{2K},\ \Gamma^{1}_{22} = -\frac{E'}{2K},\ \Gamma^{1}_{33} = -\frac{E'\sin^2\theta}{2K},\\ \Gamma^{2}_{12} = \Gamma^{2}_{21} = \Gamma^{3}_{13} = \Gamma^{3}_{31} = \frac{E'}{2E},\ \Gamma^{2}_{33} = -\sin\theta\cos\theta,\ \Gamma^{3}_{23} = \Gamma^{3}_{32} = \operatorname{ctg}\theta.\end{gathered} \tag{5}$$

With the help of coefficients (5) we will calculate the components of the Ricci tensor with the covariant indices using the standard formula:

$$R_{\mu\nu} = \partial_{\alpha}\Gamma^{\alpha}_{\mu\nu} - \partial_{\nu}\Gamma^{\alpha}_{\mu\alpha} + \Gamma^{\alpha}_{\mu\nu}\Gamma^{\beta}_{\alpha\beta} - \Gamma^{\alpha}_{\mu\beta}\Gamma^{\beta}_{\alpha\nu}.$$

This will give four nonzero components:

$$\begin{gathered}R_{00} = \frac{B''}{2K} - \frac{B'^2}{4BK} - \frac{B'K'}{4K^2} + \frac{B'E'}{2KE},\ R_{11} = -\frac{B''}{2B} + \frac{B'^2}{4B^2} - \frac{E''}{E} + \frac{E'^2}{2E^2} + \frac{B'K'}{4BK} + \frac{K'E'}{2KE},\\ R_{22} = -\frac{E''}{2K} + \frac{E'K'}{4K^2} - \frac{E'B'}{4BK} + 1,\ R_{33} = \sin^2\theta\, R_{22}.\end{gathered} \tag{6}$$

Eq. (1) contains the components of the Ricci tensor with the mixed indices, which can be found by multiplying the components of this tensor with the covariant indices by the metric tensor using the $R^{\beta}_{\alpha} = R_{\alpha\mu} g^{\mu\beta}$ formula. By application of components (6) and metric tensor (3), we find:

$$\begin{gathered}R_0^{\ 0} = \frac{B''}{2BK} - \frac{B'^2}{4B^2K} - \frac{B'K'}{4BK^2} + \frac{B'E'}{2BKE},\\ R_1^{\ 1} = \frac{B''}{2BK} - \frac{B'^2}{4B^2K} - \frac{B'K'}{4BK^2} + \frac{E''}{KE} - \frac{E'^2}{2KE^2} - \frac{K'E'}{2K^2E},\\ R_2^{\ 2} = \frac{E''}{2KE} + \frac{B'E'}{4BKE} - \frac{K'E'}{4K^2E} - \frac{1}{E},\ R_3^{\ 3} = R_2^{\ 2}.\end{gathered} \tag{7}$$

Using formulas (6) and (3), we will calculate the scalar curvature as follows:

$$R = R_{\mu\nu} g^{\mu\nu} = \frac{B''}{BK} - \frac{B'^2}{2B^2K} - \frac{B'K'}{2BK^2} + \frac{B'E'}{BKE} + \frac{2E''}{KE} - \frac{E'^2}{2KE^2} - \frac{K'E'}{K^2E} - \frac{2}{E}. \tag{8}$$

The field tensors

The stress-energy tensors of the gravitational field [17, 18], the electromagnetic, the acceleration and the pressure ones [14], located on the right-hand side of the Eq. (1) for the metric, can be expressed as follows:

$$\begin{aligned}
U_{\alpha}^{\ \beta} &= -\frac{c^2}{4\pi G} g^{\mu\kappa}\left(-\delta_{\alpha}^{\lambda} g^{\sigma\beta} + \frac{1}{4}\delta_{\alpha}^{\beta} g^{\sigma\lambda}\right)\Phi_{\mu\lambda}\,\Phi_{\kappa\sigma},\\
W_{\alpha}^{\ \beta} &= \varepsilon_0 c^2\, g^{\mu\kappa}\left(-\delta_{\alpha}^{\lambda} g^{\sigma\beta} + \frac{1}{4}\delta_{\alpha}^{\beta} g^{\sigma\lambda}\right)F_{\mu\lambda}\,F_{\kappa\sigma},\\
B_{\alpha}^{\ \beta} &= \frac{c^2}{4\pi\eta} g^{\mu\kappa}\left(-\delta_{\alpha}^{\lambda} g^{\sigma\beta} + \frac{1}{4}\delta_{\alpha}^{\beta} g^{\sigma\lambda}\right)u_{\mu\lambda}\,u_{\kappa\sigma},\\
P_{\alpha}^{\ \beta} &= \frac{c^2}{4\pi\sigma} g^{\mu\kappa}\left(-\delta_{\alpha}^{\lambda} g^{\sigma\beta} + \frac{1}{4}\delta_{\alpha}^{\beta} g^{\sigma\lambda}\right)f_{\mu\lambda}\,f_{\kappa\sigma}.
\end{aligned} \tag{9}$$

Here $\Phi_{\mu\lambda}$, $F_{\mu\lambda}$, $u_{\mu\lambda}$ and $f_{\mu\lambda}$ are the tensors of the gravitational, the electromagnetic, the acceleration and the pressure fields, respectively; G, ε_0, η and σ are the gravitational, the electric, the acceleration and the pressure fields' constants, respectively.

The stress-energy tensors in Eqs. (9) were derived from the principle of the least action under the assumption that all the physical fields in the system under consideration were described as vector fields that had their own 4-potentials [13]. Due to the fact that the field tensors have the same form, it was possible to combine all the fields into a single general field [19, 20].

Let us express the 4-potentials of the fields in terms of the corresponding scalar and vector potentials of these fields:

$$D_{\lambda} = \left(\frac{\psi}{c}, -\mathbf{D}\right) \text{ for the gravitational field,}$$

$$A_{\lambda} = \left(\frac{\varphi}{c}, -\mathbf{A}\right) \text{ for the electromagnetic field,}$$

$$U_{\lambda} = \left(\frac{\vartheta}{c}, -\mathbf{U}\right) \text{ for the acceleration field,}$$

$$\pi_{\lambda} = \left(\frac{\wp}{c}, -\mathbf{\Pi}\right) \text{ for the pressure field.}$$

The gravitational tensor is defined as the 4-curl of the 4-potential [17]. Similarly, the electromagnetic tensor, the acceleration tensor and the pressure field tensor [14] are calculated and have the following form:

$$\begin{aligned}
\Phi_{\mu\lambda} &= \nabla_{\mu} D_{\lambda} - \nabla_{\lambda} D_{\mu} = \partial_{\mu} D_{\lambda} - \partial_{\lambda} D_{\mu},\ F_{\mu\lambda} = \nabla_{\mu} A_{\lambda} - \nabla_{\lambda} A_{\mu} = \partial_{\mu} A_{\lambda} - \partial_{\lambda} A_{\mu},\\
u_{\mu\lambda} &= \nabla_{\mu} U_{\lambda} - \nabla_{\lambda} U_{\mu} = \partial_{\mu} U_{\lambda} - \partial_{\lambda} U_{\mu},\ f_{\mu\lambda} = \nabla_{\mu}\pi_{\lambda} - \nabla_{\lambda}\pi_{\mu} = \partial_{\mu}\pi_{\lambda} - \partial_{\lambda}\pi_{\mu}.
\end{aligned} \tag{10}$$

In the system under consideration, the vector potentials **D**, **A**, **U** and **Π** of all the fields are close to zero because of the random motion of the matter's particles. This is due to the fact that the vector potentials of individual particles are directed along the particles' velocities, and therefore they change each time as a result of interactions.

The global vector potential of each field inside the body is calculated as the vector sum of the corresponding vector potentials of the particles. At each time point, most of the particles in the system have oppositely directed velocities and vector potentials, so that the vector sum of these potentials tends to zero on the average. The more particles are present in the system, the more exactly the equality to zero holds for the global vector potentials of the fields. We will not also take into account the proper vector potentials of individual particles. As was shown in Ref. [21], the energy of the particles' motion arises due to all these potentials, which is approximately equal to their kinetic energy. Thus the inaccuracy, arising from equating the vector potentials **D**, **A**, **U** and **Π** to zero, does not exceed the inaccuracy in the case when only the rest energy is taken into account in the system's energy and the kinetic energy of the particles is neglected.

As for the scalar field potentials ψ, φ, ϑ and $\wp$, in the static case for a stationary spherical body, they must depend only on the current radius r and must not depend on either time or angular variables.

Assuming that $\mathbf{D} \approx 0$ and neglecting the contribution of the vector potential **D**, in the spherical coordinates

$$x^0 = ct,\ x^1 = r,\ x^2 = \theta,\ x^3 = \varphi$$

we find, from tensors (10) and (3), the nonzero components of the gravitational tensor:

$$\Phi_{01} = -\Phi_{10} = -\frac{1}{c}\frac{\partial \psi}{\partial r} - \frac{1}{c}\frac{\partial D_r}{\partial t} \approx -\frac{1}{c}\frac{\partial \psi}{\partial r}. \tag{11}$$

In Eq. (11) the quantity D_r in the spherical coordinates is the projection of the vector potential on the radial component of the 4-dimensional coordinate system. In this case, the quantity

$$\Gamma_r = c\Phi_{01} = -\frac{\partial \psi}{\partial r} - \frac{\partial D_r}{\partial t}$$

is the projection of the gravitational field strength on the radial component of the coordinate system.

The nonzero components of the electromagnetic field tensor, the acceleration one, and the pressure field tensor are obtained similarly to Eq. (11):

$$\begin{gathered} F_{01} = -F_{10} = -\frac{1}{c}\frac{\partial \varphi}{\partial r} - \frac{1}{c}\frac{\partial A_r}{\partial t} \approx -\frac{1}{c}\frac{\partial \varphi}{\partial r},\ u_{01} = -u_{10} = -\frac{1}{c}\frac{\partial \vartheta}{\partial r} - \frac{1}{c}\frac{\partial U_r}{\partial t} \approx -\frac{1}{c}\frac{\partial \vartheta}{\partial r}, \\ f_{01} = -f_{10} = -\frac{1}{c}\frac{\partial \wp}{\partial r} - \frac{1}{c}\frac{\partial \Pi_r}{\partial t} \approx -\frac{1}{c}\frac{\partial \wp}{\partial r}. \end{gathered} \tag{12}$$

In the Minkowski space-time, the special theory of relativity is valid, so that the potentials and the field strengths can be calculated exactly. For the case of the relativistic uniform model, the field strengths, which are part of the field tensors' components inside a spherical body, in the static case have the following form [22]:

$$
\begin{aligned}
c\Phi_{01} &= -\frac{Gc^2\gamma_c}{\eta r^2}\left[\frac{c}{\sqrt{4\pi\eta\rho_0}}\sin\left(\frac{r}{c}\sqrt{4\pi\eta\rho_0}\right) - r\cos\left(\frac{r}{c}\sqrt{4\pi\eta\rho_0}\right)\right] \approx -\frac{4\pi G\rho_0\gamma_c r}{3},\\
cF_{01} &= \frac{\rho_{0q}c^2\gamma_c}{4\pi\varepsilon_0\rho_0\eta r^2}\left[\frac{c}{\sqrt{4\pi\eta\rho_0}}\sin\left(\frac{r}{c}\sqrt{4\pi\eta\rho_0}\right) - r\cos\left(\frac{r}{c}\sqrt{4\pi\eta\rho_0}\right)\right] \approx \frac{\rho_{0q}\gamma_c r}{3\varepsilon_0},\\
cu_{01} &= \frac{c^2\gamma_c}{r^2}\left[\frac{c}{\sqrt{4\pi\eta\rho_0}}\sin\left(\frac{r}{c}\sqrt{4\pi\eta\rho_0}\right) - r\cos\left(\frac{r}{c}\sqrt{4\pi\eta\rho_0}\right)\right] \approx \frac{4\pi\eta\rho_0\gamma_c r}{3},\\
cf_{01} &= \frac{\sigma c^2\gamma_c}{\eta r^2}\left[\frac{c}{\sqrt{4\pi\eta\rho_0}}\sin\left(\frac{r}{c}\sqrt{4\pi\eta\rho_0}\right) - r\cos\left(\frac{r}{c}\sqrt{4\pi\eta\rho_0}\right)\right] \approx \frac{4\pi\sigma\rho_0\gamma_c r}{3}.
\end{aligned}
\tag{13}
$$

In Eqs. (13) γ_c is the Lorentz factor of the typical particles that are moving at the center of the body; ρ_0 and ρ_{0q} denote the invariant mass and charge densities of the typical particles, respectively.

These mass and charge densities are obtained in the reference frames, which are comoving with the particles. It follows from Eqs. (10) – (13) that the field tensors inside the body are proportional to each other:

$$
-\frac{\Phi_{\mu\lambda}}{G} = \frac{4\pi\varepsilon_0\rho_0 F_{\mu\lambda}}{\rho_{0q}} = \frac{u_{\mu\lambda}}{\eta} = \frac{f_{\mu\lambda}}{\sigma}. \tag{14}
$$

Let us sum up all the stress-energy tensors in formulas (9) and use Eq. (14):

$$
\begin{aligned}
&U_\alpha^\beta + W_\alpha^\beta + B_\alpha^\beta + P_\alpha^\beta =\\
&= \frac{c^2}{4\pi\eta^2}\left(-G + \frac{\rho_{0q}^2}{4\pi\varepsilon_0\rho_0^2} + \eta + \sigma\right) g^{\mu\kappa}\left(-\delta_\alpha^\lambda g^{\sigma\beta} + \frac{1}{4}\delta_\alpha^\beta g^{\sigma\lambda}\right) u_{\mu\lambda}\, u_{\kappa\sigma}.
\end{aligned}
\tag{15}
$$

As was found in Ref. [23] from the equation of the particles' motion and in Ref. [24] from the generalized Poynting theorem, the following condition holds for the sum of the field coefficients inside the body:

$$
-G + \frac{\rho_{0q}^2}{4\pi\varepsilon_0\rho_0^2} + \eta + \sigma = 0. \tag{16}
$$

Substituting condition (16) into Eq. (15) we find out that the sum of the stress-energy tensors inside the body, which is in equilibrium, becomes equal to zero:

$$
U_\alpha^\beta + W_\alpha^\beta + B_\alpha^\beta + P_\alpha^\beta = 0. \tag{17}
$$

Relation (17) was also derived in Ref. [24]. Will the result of Eq. (17) change if we consider the situation in the curved space-time? In the physical system in the form of a spherical body, the space-time metric is static and depends only on the radial coordinate. Since the vector field potentials are assumed to be zero, the tensor of each field contains only two nonzero components, which are equal in the absolute value. Taking into account the metric of the curved space-time leads to the fact that the tensors' components of each field in Eq. (13) must be multiplied by the same function Z that depends on the metric tensor components. Just as the metric tensor components, this function will depend

only on the radial coordinate. In the flat Minkowski space-time this function must be equal to unity, $Z = 1$, so that Eq. (13) is satisfied, which does not contain Z function.

Indeed, the equations for calculating the tensors of all the vector fields coincide with each other in their form, according to Refs. [13, 18, 25], and hence, the field tensors can differ from each other only by the constant coefficients at constant mass density ρ_0 and charge density ρ_{0q}. Therefore, if we multiply the tensor of each field, found in the Minkowski space-time, by the same function Z, in order to find this tensor in the curved space-time, relation (14) would not change, and an additional factor would appear on the right-hand side of Eq. (15). Since condition (16) always holds true, then, in the system under consideration, the sum of the stress-energy tensors in Eqs. (15) and (17) will also be zero in the curved space-time.

Calculation of the metric inside the body

Eq. (1) for the metric, in view of Eq. (17), is significantly simplified:

$$R_\alpha^\beta - \frac{1}{4} R \delta_\alpha^\beta = 0.$$

Substituting here (7) and (8), we get three equations:

$$\frac{B''}{2BK} - \frac{B'^2}{4B^2K} - \frac{B'K'}{4BK^2} + \frac{B'E'}{2BKE} - \frac{E''}{KE} + \frac{E'^2}{4KE^2} + \frac{K'E'}{2K^2E} + \frac{1}{E} = 0, \tag{18}$$

$$\frac{B''}{2BK} - \frac{B'^2}{4B^2K} - \frac{B'K'}{4BK^2} - \frac{B'E'}{2BKE} + \frac{E''}{KE} - \frac{3E'^2}{4KE^2} - \frac{K'E'}{2K^2E} + \frac{1}{E} = 0, \tag{19}$$

$$\frac{B''}{2BK} - \frac{B'^2}{4B^2K} - \frac{B'K'}{4BK^2} - \frac{E'^2}{4KE^2} + \frac{1}{E} = 0. \tag{20}$$

Substituting Eq. (20) in Eqs. (18) and (19) gives the same equation:

$$\frac{E''}{KE} - \frac{E'^2}{2KE^2} - \frac{B'E'}{2BKE} - \frac{K'E'}{2K^2E} = 0, \text{ or } \frac{E''}{E'} - \frac{E'}{2E} - \frac{B'}{2B} - \frac{K'}{2K} = 0. \tag{21}$$

If we subtract Eq. (18) from (19), we will get Eq. (21) again. The latter can be easily integrated, because each term represents the derivative of the natural logarithm of the corresponding function:

$$E' = C_1 \sqrt{BKE}, \tag{22}$$

where C_1 is a certain constant.

We will now use the condition obtained in Ref. [16], according to which the scalar curvature inside the body must be a constant value $\overline{R} = C_2$. With the help of the scalar curvature (8) we obtain an expression:

$$\frac{B''}{BK} - \frac{B'^2}{2B^2K} - \frac{B'K'}{2BK^2} + \frac{B'E'}{BKE} + \frac{2E''}{KE} - \frac{E'^2}{2KE^2} - \frac{K'E'}{K^2E} - \frac{2}{E} = C_2. \tag{23}$$

The sum of Eqs. (23) and (18) gives the following one:

$$\frac{B''}{BK}-\frac{B'^2}{2B^2K}-\frac{B'K'}{2BK^2}+\frac{B'E'}{BKE}=\frac{C_2}{2}.$$

Comparing this expression with Eq. (20), we obtain:

$$\frac{E'^2}{4KE^2}-\frac{1}{E}+\frac{B'E'}{2BKE}=\frac{C_2}{4}.$$

Next, we will substitute here the value of $K=\frac{E'^2}{C_1^2BE}$ according to Eq. (22):

$$\frac{E'}{E}=\frac{2C_1^2B'}{4+C_2E-C_1^2B}. \tag{24}$$

Now we need K from Eq. (22) and the relation $\frac{K'}{K}$ from Eq. (21):

$$K=\frac{E'^2}{C_1^2BE},\ \frac{K'}{K}=\frac{2E''}{E'}-\frac{B'}{B}-\frac{E'}{E}. \tag{25}$$

Let us substitute expressions (25) into Eq. (20):

$$B''-\frac{B'E''}{E'}+\frac{B'E'}{2E}-\frac{BE'^2}{2E^2}+\frac{2E'^2}{C_1^2E^2}=0. \tag{26}$$

Eqs. (24) and (26) together form a system of two differential equations in the functions B and E. Direct substitution shows us that the system of these equations has the following solution:

$$E=r^2,\ B=\frac{C_3}{r}+\frac{4}{C_1^2}+\frac{C_2r^2}{3C_1^2}.$$

Indeed, in the weak gravitational field, when the curved space-time turns into the Minkowski one, it should be $E=r^2$, $B=K\approx 1$ in the spherical coordinates.

In order to ensure that the function B is not infinitely large at the center at $r=0$, the constant C_3 must be equal to zero. From the condition $B\approx 1$ it follows that $C_1=2$, and from Eq. (22) we get the equality $BK=1$. In addition, the constant C_2 must be sufficiently small. As a result, for the metric tensor components we can write the following:

$$\begin{gathered}B=g_{00}=1+\frac{C_2r^2}{12},\ E=-g_{22}=r^2,\\ K=-g_{11}=\frac{1}{B}=\frac{1}{1+\frac{C_2r^2}{12}},\ g_{33}=-r^2\sin^2\theta.\end{gathered} \tag{27}$$

The constant C_2 in expressions (27) represents the value of the scalar curvature, averaged over the volume of a typical particle, which is constant inside the body, so that $\overline{R} = C_2$.

In Ref. [16] we found the relation for the value of the cosmological constant $\overline{\Lambda}$ averaged over the volume of a typical particle:

$$-ck\overline{\Lambda} = \frac{G\rho_0}{a}\left[\frac{c^3\gamma_c}{\eta\sqrt{4\pi\eta\rho_0}}\sin\left(\frac{a}{c}\sqrt{4\pi\eta\rho_0}\right) - m_g\right] -$$

$$-\frac{\rho_{0q}}{4\pi\varepsilon_0 a}\left[\frac{\rho_{0q}c^3\gamma_c}{\eta\rho_0\sqrt{4\pi\eta\rho_0}}\sin\left(\frac{a}{c}\sqrt{4\pi\eta\rho_0}\right) - q_b\right] + \rho_0\wp_c - \frac{\sigma\rho_0 c^2\gamma_c}{\eta}.$$

Expanding the sine by the rule

$$\sin x \approx x - \frac{x^3}{6},$$

in view of Eq. (16), we find:

$$\begin{aligned} -ck\overline{\Lambda} &\approx -\frac{Gm_g\rho_0}{a} - \frac{Gm\rho_0\gamma_c}{2a} + \rho_0 c^2\gamma_c + \frac{q_b\rho_{0q}}{4\pi\varepsilon_0 a} + \frac{q\rho_{0q}\gamma_c}{8\pi\varepsilon_0 a} + \rho_0\wp_c, \\ C_2 = \overline{R} = 2\overline{\Lambda} &\approx -\frac{2}{ck}\left(\rho_0\psi_a - \frac{Gm\rho_0\gamma_c}{2a} + \rho_0 c^2\gamma_c + \rho_{0q}\varphi_a + \frac{q\rho_{0q}\gamma_c}{8\pi\varepsilon_0 a} + \rho_0\wp_c\right), \end{aligned} \tag{28}$$

where k is the factor,

$$k = -\frac{c^3}{16\pi G\beta} \tag{29}$$

(β is a certain constant of the order of unity);

$\psi_a = -\dfrac{Gm_g}{a}$ is the scalar potential of the gravitational field on the surface of the body at $r = a$;

$\varphi_a = \dfrac{q_b}{4\pi\varepsilon_0 a}$ is the scalar potential of the electric field (a is the radius of the body); m_g, q_b are the gravitational mass and the total charge of the body; γ_c is the Lorentz factor of the particles at the center of the body; $\wp_c$ is the potential of the pressure field at the center of the sphere; the mass $m = \dfrac{4\pi a^3\rho_0}{3}$ and the charge $q = \dfrac{4\pi a^3\rho_{0q}}{3}$ are auxiliary quantities.

In the brackets, on the right-hand side of Eq. (28), there is the sum of the volumetric energy densities of the particles in the scalar field potentials: the first and second terms are from the gravitational field, the third one is from the acceleration field, the fourth and fifth terms are from the electric field, and the sixth one is from the pressure field.

The third term is the greatest, it is proportional to the rest energy density of the body. If we take into account only this term, then, in the first approximation, the constant C_2 will be equal to

$$C_2 \approx \frac{32\pi G\rho_0\gamma_c\beta}{c^2}.$$

Comparison of the metric tensor components inside and outside the body

At $r = a$ the current radius reaches the surface of the spherical body, and here the internal metric becomes equal to the external one. It means that we can equate the components of the corresponding metric tensors at $r = a$. According to Ref. [10], the metric tensor components outside the body in the covariant theory of gravitation are equal to

$$g_{00} = 1 + \frac{A_3}{r} + \frac{1}{16\pi ckr^2}\left(Gm_g^2 - \frac{q_b^2}{4\pi\varepsilon_0}\right),\ g_{22} = -r^2,$$
$$g_{11} = -\frac{1}{1 + \frac{A_3}{r} + \frac{1}{16\pi ckr^2}\left(Gm_g^2 - \frac{q_b^2}{4\pi\varepsilon_0}\right)},\ g_{33} = -r^2\sin^2\theta. \tag{30}$$

Comparison of Eqs. (30) and (27) shows that the components g_{22} and g_{33} coincide both inside and outside the body.

Equating g_{00} in Eqs. (27) and (30) under condition that $r = a$, taking into account Eqs. (28) and (29), we find the constant A_3:

$$A_3 \approx \frac{2G\beta}{c^4}\left[mc^2\gamma_c + \left(m - \frac{1}{2}m_g\right)\psi_a - \frac{Gm^2\gamma_c}{2a} + \left(q - \frac{1}{2}q_b\right)\varphi_a + \frac{q^2\gamma_c}{8\pi\varepsilon_0 a} + m\wp_c\right]. \tag{31}$$

According to Ref. [22], the gravitational mass m_g of the body and the total electric charge q_b are determined as follows:

$$m_g = \int \rho_0\gamma' dV =$$
$$= \frac{c^2\gamma_c}{\eta}\left[\frac{c}{\sqrt{4\pi\eta\rho_0}}\sin\left(\frac{a}{c}\sqrt{4\pi\eta\rho_0}\right) - a\cos\left(\frac{a}{c}\sqrt{4\pi\eta\rho_0}\right)\right] \approx m\gamma_c\left(1 - \frac{3\eta m}{10ac^2}\right).$$
$$q_b = \int \rho_{0q}\gamma' dV =$$
$$= \frac{\rho_{0q}c^2\gamma_c}{\eta\rho_0}\left[\frac{c}{\sqrt{4\pi\eta\rho_0}}\sin\left(\frac{a}{c}\sqrt{4\pi\eta\rho_0}\right) - a\cos\left(\frac{a}{c}\sqrt{4\pi\eta\rho_0}\right)\right] \approx q\gamma_c\left(1 - \frac{3\eta m}{10ac^2}\right). \tag{32}$$

Since $\gamma_c > 0$, it turns out that $m_g > m$ and $q_b > q$.

Now we will substitute Eq. (31) into the expression for g_{00} (see Eq. (30)) and take into account Eq. (29):

$$g_{00} = -\frac{1}{g_{11}} \approx 1 + \frac{2Gm\gamma_c\beta}{c^2 r} +$$
$$+ \frac{2G\beta}{c^4 r}\left[m\psi_a + \frac{1}{2}m_g(\psi - \psi_a) - \frac{Gm^2\gamma_c}{2a} + q\varphi_a + \frac{1}{2}q_b(\varphi - \varphi_a) + \frac{q^2\gamma_c}{8\pi\varepsilon_0 a} + m\wp_c\right]. \tag{33}$$

In this expression $\psi = -\frac{Gm_g}{r}$ and $\varphi = \frac{q_b}{4\pi\varepsilon_0 r}$ denote the scalar potentials of the gravitational and electric fields outside the body, respectively.

We can also determine the quantities γ_c and $\wp_c$ more exactly. In Ref. [21] we found the expression for the square of the particles' velocities v_c^2 at the center of the spherical body; using it we can estimate the value of the Lorentz factor in Eq. (33):

$$\gamma_c = \frac{1}{\sqrt{1-v_c^2/c^2}} \approx 1+\frac{v_c^2}{2c^2}+\frac{3v_c^4}{8c^4} \approx 1+\frac{3\eta m}{10ac^2}\left(1+\frac{9}{2\sqrt{14}}\right)+\frac{27\eta^2 m^2}{200a^2c^4}\left(1+\frac{9}{2\sqrt{14}}\right)^2.$$

According to Ref. [26], the scalar potential of the pressure field at the center of the body is approximately equal to

$$\wp_c \approx \frac{3\sigma m}{10a}\left(1+\frac{9}{2\sqrt{14}}\right),$$

while the acceleration field constant η and the pressure field constant σ are given by the formulas

$$\eta = \frac{3}{5}\left(G-\frac{\rho_{0q}^2}{4\pi\varepsilon_0\rho_0^2}\right),\ \sigma = \frac{2}{5}\left(G-\frac{\rho_{0q}^2}{4\pi\varepsilon_0\rho_0^2}\right).$$

In Eq. (33) we see the complex structure of the metric tensor components, in which additional terms appear as compared to the Minkowski spacetime metric, where in the spherical coordinates

$$g_{00} = -\frac{1}{g_{11}} = 1.$$

The main addition in Eq. (33) is the term

$$\frac{2Gm\gamma_c\beta}{c^2 r},$$

and if we take into account Eq. (32), then this addition will become approximately equal to $-\frac{2\psi\beta}{c^2}$.

The second important addition includes square brackets in Eq. (33), which, by the order of magnitude, determines the energy of the gravitational and electric fields, as well as the pressure one. In these brackets, we can also use the approximate relation of the masses in expression (32). For the metric tensor components outside the body all this leads to the following expression:

$$g_{00} = -\frac{1}{g_{11}} \approx 1-\frac{2\psi\beta}{c^2}+\frac{2G\beta}{c^4 r}\left(m\psi_a+\frac{1}{2}m_g\psi+\frac{3\eta m^2\gamma_c}{10a}+q\varphi_a+\frac{1}{2}q_b\varphi+m\wp_c\right). \qquad (34)$$

On the right-hand side of Eq. (34), in the round brackets, there are quantities with the dimension of energy. For large cosmic bodies, the main quantity here is the negative energy associated with gravitation. In this case we can see that the third term, containing c^4 in the denominator, is distinguished by a sign from the second term, containing c^2 in the denominator.

Comparison with the metric of the general theory of relativity

In order to compare with the metric tensor components (30) and (34), we will consider the Reissner – Nordström metric in the spherical coordinates, which describes the static gravitational field around a charged spherical body in the general theory of relativity. We will use our notation for the field potentials:

$$g_{00} = 1 + \frac{2\psi}{c^2} + \frac{Gq_b\varphi}{c^4 r},\ g_{11} = -\frac{1}{1 + \frac{2\psi}{c^2} + \frac{Gq_b\varphi}{c^4 r}},\ g_{22} = -r^2,\ g_{33} = -r^2 \sin^2\theta. \quad (35)$$

As we can see, the second and third terms in the component g_{00} in the Reissner – Nordström metric (35) differ significantly from the corresponding terms in the component g_{00} in the CTG metric (34) outside the body. For example, we can see that the metric in Eq. (35) does not reflect the energy of the pressure field inside the body in any way, whereas in Eq. (34) the energy $m_\delta \wp_c$ is associated with the pressure field and makes its contribution to the metric. Taking into account Eq. (28), the energy $m_\delta \wp_c$ also defines the metric (27) inside the body.

This difference in the form of the metric is due to the difference in the equations for determining the metric in both theories. While Eq. (1) is used in CTG, the equation for the metric with the cosmological constant Λ in the general theory of relativity has the following form in the matter with the stress-energy tensor T_α^β :

$$R_\alpha^\beta - \frac{1}{2} R\,\delta_\alpha^\beta + \Lambda\,\delta_\alpha^\beta = \frac{8\pi G}{c^4} T_\alpha^\beta. \quad (36)$$

According to the approach of the general theory of relativity, the action of gravitation must be described by the metric tensor, and therefore T_α^β does not include the stress-energy tensor of the gravitational field. There is no matter and no pressure field outside the charged body; only the electromagnetic field is left on the right-hand side of Eq. (36), so that we have $T_\alpha^\beta = W_\alpha^\beta$. As a rule, the term with the cosmological constant Λ in Eq. (36) is neglected due to its smallness, and then the solution for the metric (35) is obtained.

Since the cosmological constant is taken into account in CTG fully, it turns out that the solution of Eq. (27) in view of (28) for the CTG metric inside the body and the solution of Eq. (33) outside the body are more precise and informative than the solution of Eq. (35) in the Reissner – Nordström metric. Moreover, in CTG, the cosmological constant $\overline{\Lambda}$ is not equal to zero and is proportional to the potentials of all the fields acting inside the body. If in Eq. (28) only the main term with rest energy density is taken into account, then with the relation (29) we can estimate the value $\overline{\Lambda}$:

$$\overline{\Lambda} \approx -\frac{\rho_0 c \gamma_c}{k} \approx \frac{16\pi G \rho_0 \beta \gamma_c}{c^2}. \quad (37)$$

If we substitute here the average mass density of the cosmic space matter of the observable universe, we shall obtain the value $\overline{\Lambda} \approx 10^{-52}$ m^{-2}. The smallness of the cosmological constant $\overline{\Lambda}$ inside cosmic bodies is associated with the large factor (29) in Eq. (37). To this end we recall that the issue of the cosmological constant in the general theory of relativity has not yet been resolved unambiguously [27], especially with respect to correlation with vacuum energy. Here it is implied that a very large vacuum energy makes little contribution to the metric for some reason and to the small cosmological constant.

In CTG, the greater is the mass density in Eq. (37), the larger is Λ inside the body. However if we distribute the matter of all cosmic bodies over the space, then the mass density will be very low, which leads to insignificantly small value $\overline{\Lambda} \approx 10^{-52}$ m^{-2}. We should also pay attention to the fact that the cosmological constant outside the body is assumed to be zero due to its gauging in CTG [16]. Inside the bodies, as well as inside the observable universe as some global body, $\overline{\Lambda}$ has a certain value. In the approximation of the relativistic uniform body model, $\overline{\Lambda}$ is determined in Eq. (28).

In contrast, in the general theory of relativity, in Eq. (36), the nonzero value of the cosmological constant outside the body is admitted. The latter follows from the possibility of influence of the zero vacuum's energy on the metric through the cosmological constant.

Summary

In Section 3 we have shown that the sum of the stress-energy tensors of all the four fields inside the body is zero. With this in mind, the metric tensor components were calculated as functions of the current radius in Eq. (27). As a result, on the surface of the body at $r = a$ it became possible to compare the metric inside and outside the body and to determine the unknown coefficient A_3 in the external metric (30).

The metric tensor components g_{00} and g_{11} outside the fixed spherical body in the covariant theory of gravitation (CTG), that were presented in Eq. (30), were specified by us in Eqs. (33) and (34). It turns out that these components are the functions of the scalar potentials of all the fields, so that, for example, the pressure field inside the body also influences the metric outside the body. However, the main contribution to the metric is made by the scalar potential of the gravitational field $\psi = -\frac{Gm_g}{r}$. Apparently this is due to the fact that the expression for the scalar potential ψ includes the gravitational mass m_g that characterizes the source of the field and the gravitation force. At the same time the relativistic energy is proportional to the inertial mass M, while for an external observer the mass M is the rest mass and characterizes the system with respect to the forces acting on it. Both of these masses differ from each other by the mass-energy of the particles' binding by means of the fields [26]. As for the electromagnetic field, its contribution is secondary. The body's charge is only indirectly included in the rest mass of the body and is not directly included in the gravitational mass. The electric field potentials vanish in neutral bodies in Eq. (34). Thus, the gravitational field is the main factor that distinguishes the curved space-time metric from the Minkowski flat one.

Our calculations allowed us to calculate the metric CTG inside the body and to refine the metric outside the body, but there was one more unknown adjustable coefficient β in the metric tensor components. Its appearance can be due to the assumption that the coefficient (29) has an exact value, so that the coefficient β is intended to ensure the correct value of the metric. The value of the coefficient β can be determined in the gravitational experiments, in which the space-time metric should be taken into account.

REFERENCES

1. **Sharif M., Fatima T.,** Energy-momentum distribution: a crucial problem in general relativity, Intern. J. Mod. Phys. A. 20 (18) (2005) 4309.

2. **Cooperstock F.I., Sarracino R.S.,** The localization of energy in general relativity, J. Phys. A. 11 (5) (1975) 877.

3. **Rüster S.B.,** The fundamental conservation law in the theory of general relativity: an unconventional approach is feasible and correct? Parana J. Sci. Educ. 6 (9) (2020) 1–11.

4. **Denisov V.I., Logunov A.A.,** The inertial mass defined in the general theory of relativity has no physical meaning, Theor. Math. Phys. 51 (2) (1982) 421–426.

5. **Khrapko R.I.,** The truth about the energy-momentum tensor and pseudotensor, Gravit. Cosmol. 20 (4) (2014) 264–273.

6. **Dirac P.A.M.,** General theory of relativity, A Wiley-Interscience Publication, O.H.N. Wiley & Sons, New York, London, Sydney, 1975.

7. **Dale R., Sáez D.,** Testing vector-tensor gravity with current cosmological observations, J. Phys. Conf. Ser. 600 (1) (2015) 012044.

8. **Momeni D., Faizal M., Myrzakulov K., Myrzakulov R.,** Compact stars in vector–tensor-Horndeski theory of gravity, Eur. Phys. J. C. 77 (1) (2017) 77.

9. **Heisenberg L., Bartelmann M.,** Kinetic field theory applied to vector-tensor gravity, Phys. Lett. B. 796 (10 Sept.) (2019) 59–64.

10. **Fedosin S.G.,** The metric outside a fixed charged body in the covariant theory of gravitation, Int. Front. Sci. Lett. 1 (1) (2014) 41–46.

11. **Fedosin S.G.,** The pioneer anomaly in covariant theory of gravitation, Canad. J. Phys. 93 (11) (2015) 1335–1342.

12. **Fedosin S.G.,** The physical theories and infinite hierarchical nesting of matter, Vol. 2, LAP LAMBERT Academic Publishing, Republic of Moldova, 2015.

13. **Fedosin S.G.,** The procedure of finding the stress-energy tensor and vector field equations of any form, Adv. Studies Theor. Phys. 8 (18) (2014) 771–779.

14. **Fedosin S.G.,** About the cosmological constant, acceleration field, pressure field and energy, Jordan J. Physics. 9 (1) (2016) 1–30.

15. **Fedosin S.G.,** Four-dimensional equation of motion for viscous compressible and charged fluid with regard to the acceleration field, pressure field and dissipation field, Int. J. Thermodynamics. 18 (1) (2015) 13–24.

16. **Fedosin S.G.,** Energy and metric gauging in the covariant theory of gravitation, Aksaray Univ. J. Sci. Eng. 2 (2) (2018) 127–143.

17. **Fedosin S.G.,** Fizika i filosofiia podobiia ot preonov do metagalaktik [Similarity physics and philosophy from prequarks up to metagalaxies], Stil-MG Publishing, Perm, 1999 (in Russian).

18. **Fedosin S.G.,** The principle of least action in covariant theory of gravitation, Hadronic J. 35 (1) (2012) 35–70.

19. **Fedosin S.G.,** The concept of the general force vector field, OALib J. 3 (3) (2016) e2459, 1–15.

20. **Fedosin S.G.,** Two components of the macroscopic general field, Rep. Adv. Phys. Sci. 1 (2) (2017) 1750002.

21. **Fedosin S.G.,** The virial theorem and the kinetic energy of particles of a macroscopic system in the general field concept, Continuum Mech. Thermodyn. 29 (2) (2016) 361–371.

22. **Fedosin S.G.,** Relativistic energy and mass in the weak field limit, Jordan J. Phys. 8 (1) (2015) 1–16.

23. **Fedosin S.G.,** Estimation of the physical parameters of planets and stars in the gravitational equilibrium model, Canad. J. Phys. 94 (4) (2016) 370–379.

24. **Fedosin S.G.,** The generalized Poynting theorem for the general field and solution of the 4/3 problem, Int. Front. Sci. Lett. 14 (2019) 19–40.

25. **Fedosin S.G.,** Fizicheskie teorii i beskonechnaia vlozhennost' materii [Physical theories and infinite matter nesting], Sergey Fedosin Publishing, Perm, 2009 (in Russian).

26. **Fedosin S.G.,** The binding energy and the total energy of a macroscopic body in the relativistic uniform model, Middle East J. Sci. 5 (1) (2019) 46–62.

27. **Martin J.,** Everything you always wanted to know about the cosmological constant problem (but were afraid to ask), Comptes Rendus Physique. 13 (6–7) (2012) 566–665.

Received 06.03.2021, accepted 22.06.2021.

THE AUTHOR

FEDOSIN Sergey G.
22–27, Architect Sviyazev St., Perm, Perm Territory, 614088, Russian Federation
sergey.fedosin@gmail.com

СПИСОК ЛИТЕРАТУРЫ

1. **Sharif M., Fatima T.** Energy-momentum distribution: a crucial problem in general relativity // International Journal of Modern Physics. A. 2005. Vol. 20. No. 18. P. 4309.

2. **Cooperstock F.I., Sarracino R.S.** The localization of energy in general relativity // Journal of Physics. A. 1978. Vol. 11. No. 5. P. 877.

3. **Rüster S.B.** The fundamental conservation law in the theory of general relativity: an unconventional approach is feasible and correct? // Parana Journal of Science and Education. 2020. Vol. 6. No. 9. Pp. 1–11.

4. **Денисов В.И., Логунов В.А.** Инертная масса, определенная в общей теории относительности, не имеет физического смысла // Теоретическая и математическая физика. 1982. Т. 51. № 2. С. 163–170.

5. **Khrapko R.I.** The truth about the energy-momentum tensor and pseudotensor // Gravitation and Cosmology. 2014. Vol. 20. No. 4. Pp. 264–273.

6. **Дирак П.А.М.** Общая теория относительности. Пер. с англ. Под ред. чл.-кор. АН СССР Д.И. Блохинцева. М.: Атомиздат, 1978. 64 с.

7. **Dale R., Sáez D.** Testing vector-tensor gravity with current cosmological observations // Journal of Physics: Conference Series. 2015. Vol. 600. No. 1. P. 012044.

8. **Momeni D., Faizal M., Myrzakulov K., Myrzakulov R.** Compact stars in vector–tensor-Horndeski theory of gravity // The European Physical Journal. C. 2017. Vol. 77. No. 1. P. 37.

9. **Heisenberg L., Bartelmann M.** Kinetic field theory applied to vector-tensor gravity // Physical Letters B. 2019. Vol. 796. 10 September. Pp. 59–64.

10. **Fedosin S.G.** The metric outside a fixed charged body in the covariant theory of gravitation // International Frontier Science Letters. 2014. Vol. 1. Pp. 41–46.

11. **Fedosin S.G.** The pioneer anomaly in covariant theory of gravitation // Canadian Journal of Physics. 2015. Vol. 93. No. 11. Pp. 1335–1342.

12. **Fedosin S.** The physical theories and infinite hierarchical nesting of matter. Vol. 2. Republic of Moldova: LAP LAMBERT Academic Publishing, 2015. 420 p.

13. **Fedosin S.G.** The procedure of finding the stress-energy tensor and vector field equations of any form // Advanced Studies in Theoretical Physics. 2014. Vol. 8. No. 18. Pp. 771–779.

14. **Fedosin S.G.** About the cosmological constant, acceleration field, pressure field and energy // Jordan Journal of Physics. 2016. Vol. 9. No. 1. Pp. 1–30.

15. **Fedosin S.G.** Four-dimensional equation of motion for viscous compressible and charged fluid with regard to the acceleration field. Pressure field and dissipation field // International Journal of Thermodynamics. 2015. Vol. 18. No. 1. Pp. 13–24.

16. **Fedosin S.G.** Energy and metric gauging in the covariant theory of gravitation // Aksaray University Journal of Science and Engineering. 2018. Vol. 2. No. 2. Pp. 127–143.

17. **Федосин С.Г.** Физика и философия подобия от преонов до метагалактик. Пермь: Стиль-МГ, 1999. 544 с.

18. **Fedosin S.G.** The principle of least action in covariant theory of gravitation // Hadronic Journal. 2012. Vol. 35. No. 1. Pp. 35–70.

19. **Fedosin S.G.** The concept of the general force vector field // Open Access Library Journal. 2016. Vol. 3. No. 3. P. e2459. Pp. 1–15.

20. **Fedosin S.G.** Two components of the macroscopic general field // Reports in Advances of Physical Sciences. 2017. Vol. 1. No. 2. P. 1750002.

21. **Fedosin S.G.** The virial theorem and the kinetic energy of particles of a macroscopic system in the general field concept // Continuum Mechanics and Thermodynamics. 2016. Vol. 29. No. 2. Pp. 361–371.

22. **Fedosin S.G.** Relativistic energy and mass in the weak field limit // Jordan Journal of Physics. 2015. Vol. 8. No. 1. Pp. 1–16.

23. **Fedosin S.G.** Estimation of the physical parameters of planets and stars in the gravitational equilibrium model // Canadian Journal of Physics. 2016. Vol. 94. No. 4. Pp. 370–379.

24. **Fedosin S.G.** The generalized Poynting theorem for the general field and solution of the 4/3 problem // International Frontier Science Letters. 2019. Vol. 14. Pp. 19–40.

25. **Федосин С.Г.** Физические теории и бесконечная вложенность материи. Пермь: Изд. Сергей Федосин, 2009–2013. 635 с.

26. **Fedosin S.G.** The binding energy and the total energy of a macroscopic body in the relativistic uniform model // Middle East Journal of Science. 2019. Vol. 5. No. 1. Pp. 46–62.

27. **Martin J.** Everything you always wanted to know about the cosmological constant problem (but were afraid to ask) // Comptes Rendus Physique. 2012. Vol. 13. No. 6–7. Pp. 566–665.

Статья поступила в редакцию 06.03.2021, принята к публикации 22.06.2021.

СВЕДЕНИЯ ОБ АВТОРЕ

ФЕДОСИН Сергей Григорьевич – *физик-исследователь, г. Пермь, Пермский край, Российская Федерация*.

614088, Российская Федерация, г. Пермь, Пермский край, ул. Архитектора Свиязева, 22, кв. 79.

sergey.fedosin@gmail.com